Investigations of Planet Formation in Circumstellar Discs Around Young Stars

Raeesa Parker

A thesis submitted in partial fulfilment
of the requirements for the degree of
Doctor of Philosophy

Jeremiah Horrocks Institute for Maths, Physics and Astronomy
University of Central Lancashire

February 2022

Declaration

Type of Award: Doctor of Philosophy

School: Physical Sciences and Computing

I declare that while registered as a candidate for the research degree, I have not been a registered candidate or enrolled student for another award of the University or other academic or professional institution.

I declare that no material contained in the thesis has been used in any other submission for an academic award and is solely my own work.

No proof-reading service was used in the compilation of this thesis.

Raeesa Parker

February 2022

Abstract

Submillimetre observations of protoplanetary discs have revealed a wide range of complex substructures in the dust continuum. Rings, gaps, and cavities, are now a common sight in many discs. In this thesis we study the dust morphology of protoplanetary discs observed with ALMA. We then model the substructure using gravitationally unstable discs, and conclude by comparing our models to actual data.

We look at 794 protoplanetary discs observed with ALMA during Cycles 0–5. We find that only 56 discs show resolvable substructure; 7% of the sample. We sort the discs into four categories: Rim, Ring, Spiral, and Horseshoe, based upon the most prominent morphology seen in the dust continuum.

We derive stellar ages and masses using isochrones and evolutionary tracks. We find no trends in each category relating to the stellar age or mass. We find that a rim of material is the most populous substructure seen in protoplanetary discs, followed by concentric rings of dust and gaps. A horseshoe–like concentration of material and spiral arms are rare substructures seen only in relatively old and young systems, respectively.

We confirm the ubiquitous nature of rims and cavities in protoplanetary discs by showing that the majority of discs that have a rim in submillimetre emission, also features the same in scattered light. We also find that all discs classified as horseshoe show spiral arms in scattered light, indicating that the same mechanism may be responsible for the formation of these two morphologies.

We find that the majority of protoplanetary discs in the ALMA Archive have

been observed at resolutions insufficient to resolve substructure. For the discs observed at high resolutions of $\lesssim$0.1", we find that 42% of discs show substructure. This increases to 60% for the discs observed at 'ultra–high' resolutions of $\lesssim$0.04". Thus, the fraction of discs observed by ALMA showing substructure may increase from 7% up to 60% provided 'ultra–high' resolution observations are used for all observations.

Smooth particle hydrodynamic simulations are used to model the substructure seen in discs of three protostars using gravitational instabilities. The initial conditions used are based upon actual ALMA observations. We are only able to create substructure in the disc of HD 36112 - where the surface density is found to be sufficiently high.

Synthetic observations are run to determine the robustness of our models. We are able to recreate the spiral arm seen in the ALMA observations of HD 36112. This has not been done in previous modellings of this protostar. We find that multiple mechanisms are required in order to fully recreate all substructure components seen in the complex disc surrounding HD 36112.

We show that synthetic observations are unable to resolve all of the structure present in our disc models. This results in outer disc radii being truncated, as well as an overestimation of central cavity extents. We also find that artificial substructures can be created in synthetic observations as a result of spiral arms in disc models being smeared. We thus confirm that the populous rim substructure seen in ALMA disc observations may be a resolution effect.

The surface densities required to form substructure within protoplanetary discs via gravitational instabilities are much higher than is currently observed. Therefore, we are either missing a substantial fraction of disc masses when making observations, or we are missing a key aspect of physics when modelling the substructure within protoplanetary discs.

Contents

List of Tables

List of Figures

Abbreviations

`CASA`	Common Astronomy Software Applications	57
2MASS	Two Micron All-Sky Survey	88
ACD	Amplitude Calibration Device	50
AEM	Alcatel Alenia Space European Industrial Engineering MT Aerospace	47
ALMA	Atacama Large Millimetre / sub–Millimetre Array	40
DSHARP	Disc Substructures at High Angular Resolution Project	86
FITS	Flexible Image Transport System	62
FT	Fourier Transform	43
Gaia	Global Astrometric Interferometer for Astrophysics	89
GMC	Giant Molecular Cloud	2
ISM	Interstellar Medium	2
MG	Moving Group	93
PDI	Planet-Companion Disc Interactions	199
PI	Principal Investigator	48
PMS	Pre-Main Sequence	141
PWV	Precipitable Water Vapour	211
QA	Quality Assurance	62
RMS	Root Mean Square	66

SED	Spectral Energy Distribution	3
SFR	Star Forming Region	88
SPH	Smooth Particle Hydrodynamics	vi
sub-mm	Submillimetre	10
VLA	Very Large Array	177
WVR	Water Vapour Radiometer	50
YSO	Young Stellar Object	1
ZAMS	Zero Age Main-Sequence	94

Acknowledgements

First and foremost I would like to thank my supervisor, Professor Derek Ward-Thompson, for giving me the chance to carry out this research, and for the guidance and knowledge imparted along the way. Being your student has not only allowed me to grow as a researcher, but as a person as well.

Thank you to Dr. Jason Kirk and Dr. Dimitris Stamatellos for their continued help; and for always answering my questions, no matter how trivial. Thanks to the star formation research group at the Jeremiah Horrocks Institute, for the endless good advice and support. Particular thanks to Saul Phiri; without whom the journey of becoming a radio astronomer would not have been nearly as much fun.

Thank you to Dr. Anita Richards at the University of Manchester for teaching me the black magic that is radio interferometry. Additionally, this thesis could not have been conducted without the workshops provided by the UK ALMA Arc Node. I would like to acknowledge the Science and Technology Funding Council, as their gracious studentship has allowed me to pursue my passion of astronomy.

To my husband, Ahmad, whom I met along this wondrous journey. Thank you for always supporting me. Here's to many more adventures together. And my sisters, who never let me give up no matter how much I wanted to. My world is surely a more exciting place to live in with you, guys, by my side.

Finally, and most importantly, my thanks and love to my parents; to whom this thesis is dedicated. You are the strongest people I know, and without whom this doctorate would not have been possible.

Chapter 1

Introduction

Since the discovery of the first planet orbiting stars other than our Sun (Wolszczan & Frail 1992), there has been a dramatic increase in the diverse nature of planetary systems. These extra-solar planets have been discovered to orbit stars with a range of stellar types (Johnson et al. 2007; Mulders et al. 2015) and metallicity (Buchhave et al. 2012). As well as orbiting single star systems, extra-solar planets have been found to orbit both binary systems (Doyle et al. 2011) and higher multiplicity stellar systems (Wagner et al. 2016). A theory of planet formation is therefore not only needed to explain the origin of our own Solar System, but that of the thousands of other systems discovered thus far.

Planets form in the circumstellar discs surrounding Young Stellar Objects (YSO). The disc that initially surrounds the protostar is known as a *protostellar disc*; rich in both dust and gas. During its evolution, the disc accretes a substantial fraction of its mass onto the protostar. This leaves behind a *protoplanetary disc*, within which planets can begin to form. The work presented in this thesis focuses on protoplanetary discs around young stars and the substructures that exist therein.

I begin this chapter by giving a brief overview of both protostellar and protoplanetary disc formation. I then go on to describe the theoretical structure of protoplanetary discs as well as the processes governing the evolution of the dust

population. I then discuss various mechanisms of planet formation and their limitations. Lastly, I introduce some of the main substructures that have been observed in protoplanetary discs thus far.

1.1 A Brief Overview of Protostellar Evolution

The Interstellar Medium (ISM) has been modelled to have three phases (McKee & Ostriker 1977). Regions of hot, ionised gas are called the Hot ISM and typically have temperatures of $\sim 10^6$ K. The Warm ISM is made up of partially ionised gas with a temperature of $\sim 10^4$ K. And lastly, the Cold ISM is comprised of mainly molecular and atomic gas with temperatures $< 10^3$ K.

Star and planet formation takes place within so-called Giant Molecular Clouds (GMCs) in the ISM. Compared to the average temperature of the ISM, these clouds are relatively cool ($T < 10^2$ K) and dense. This allows the clouds to gravitationally collapse, hence triggering star formation. The stability of the cloud depends upon the balance between its internal energy and its gravitational potential energy. The internal, outward pressure is provided by turbulence, as well as thermal and magnetic pressures. The collapse of the cloud can only occur once its gravitational potential energy dominates over these other supports.

Regions of dust and gas within the GMC can further fragment and collapse to form starless cores. These cores continue to accrete mass from the surrounding cloud until they reach a point of gravitational stability; they are then known as prestellar cores (Ward-Thompson et al. 1994). An object can observationally be defined as a prestellar core provided it has a number density of $n(H_2) > 10^4$ cm^{-3} which is not detected in near-infrared emission (Beichman et al. 1986).

The continued accretion of material by the prestellar core leads to further collapse until a hydrostatic central object forms. At this stage the object is considered to be a protostar, and evolves through four stages, Class 0–I–II–III, before arriving at the

Main Sequence.

These low-mass ($< 8M_{\odot}$) pre-main sequence stars are often classified based upon their current evolutionary state. Three stages of protostar evolution were first proposed by Lada (1987): Class I, Class II and Class III, with Class I being the least evolved and Class III the most. Andre et al. (1993) later introduced an additional stage, Class 0, which precedes the Class I stage. Figure 1.1 depicts the stages of protostellar evolution.

To determine the evolutionary state of a protostar, its Spectral Energy Distribution (SED) is looked at. This describes how the flux distribution of a protostar varies with frequency or wavelength. Protostars are surrounded by an envelope of dust and gas, as well as a circumstellar disc at later stages. The dust and gas absorb the stellar radiation emitted from the protostar and re-emit this at longer wavelengths. Therefore, compared to the SED of a blackbody or star, the infrared region (between the wavelengths of 2–25μm) of a protostar's SED will feature an excess. The slope of this excess is known as the spectral index and is given by

$$\alpha = \frac{dlog(\lambda F_{\lambda})}{dlog(\lambda)} \ , \tag{1.1}$$

where F_{λ} is the flux density at wavelength λ.

The spectral index of a protostar can determine its class (Wilking et al. 1989; Andre et al. 1993; Andre 1994). Sources with a flat spectral index were later classified to lie between Class I and Class II protostars (Greene et al. 1994).

1.1.1 Class 0

Protostars that are not yet main sequence stars are known as Young Stellar Objects. Class 0 YSOs are the youngest protostars and are surrounded by an envelope of dust and gas. Class 0 objects are defined as such if the mass of the central hydrostatic

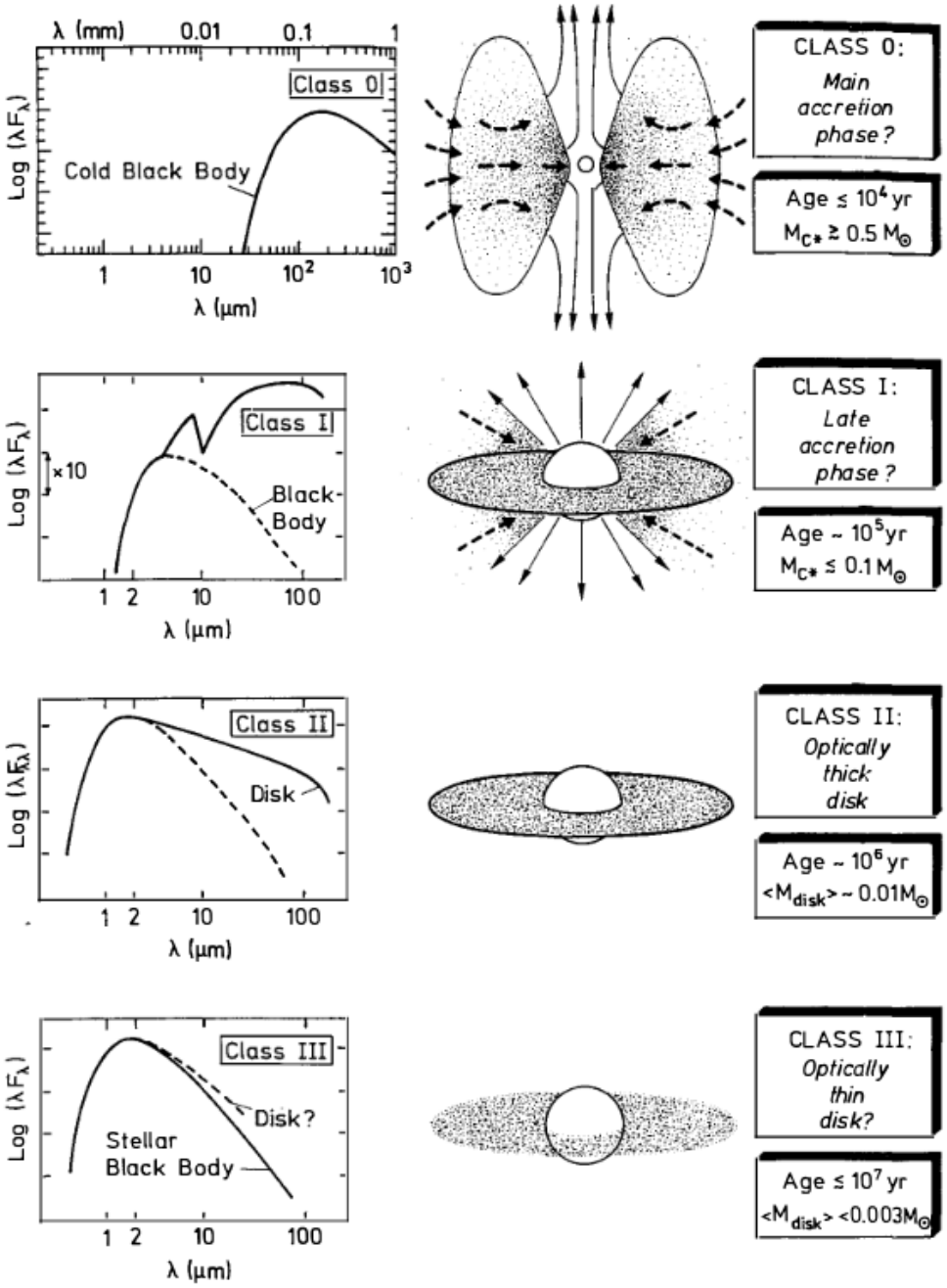

Figure 1.1: The evolutionary sequence of protostars proposed by Lada (1985) and Andre et al. (1993). Figure from Andre (1994).

object is less than that of the surrounding envelope (Andre et al. 1993). The material from this envelope rapidly accretes onto the central object (Pudritz et al. 1996), resulting in the main accretion phase of the protostar's evolution. Material is also lost from the system via strong bipolar outflows (Snell et al. 1980; Lada 1985; Walker et al. 1988; Bachiller 1996) and jets (Pudritz & Norman 1983, 1986). Therefore, this is the shortest phase of protostellar evolution, with a lifetime of the order 10^4–10^5 years (Barsony 1994; Dunham et al. 2014).

The majority of the emission observed from these objects is due to the radiation re-emitted by the envelope of dust and gas surrounding the central protostar. The emission from the envelope is typically at far-infrared or millimetre wavelengths, and the system has a bolometric temperature < 70 K. This results in a spectral index very similar to that of a Class I object. Therefore, in order to distinguish between these two stages, the ratio of the bolometric luminosity to the sub-mm luminosity is looked at. Class 0 objects have very low L_{bol}/L_{sub-mm} values (Andre et al. 1993).

1.1.2 Class I

Class I YSOs are defined as having a spectral index $\alpha > 0$ (Lada 1987). At this stage, the protostar is still surrounded by an envelope; its temperature, however, has now increased beyond 70 K. This is due to the increase in temperature of the central protostar. Therefore, Class I objects are visible in the mid-infrared, and their SED features a rise in emission at $\lambda > 2\mu$m. This contrasts to the SED of a Class 0 object which features no excess. The typical age of Class I objects is $\sim 10^4$–10^5 years.

The accreting envelope does not fall directly onto the protostar. As its mass decreases, it rotates more rapidly and conservation of angular momentum causes the infalling material to flatten out into a disc. Material in the disc now moves inwards to be accreted onto the protostar. Viscosity and gravitational torques create an angular momentum transport to the outer regions of the disc. This results in the

majority of the disc material moving inwards, with some moving outwards in order to conserve angular momentum. This can a create circumstellar disc with radii of $\sim$ 1000au (Hartmann et al. 1998).

1.1.3 Class II

The protostar then evolves into a Class II young stellar object. Lower mass ($< 3M_{\odot}$) Class II protostars are known as Classical T–Tauri stars (Joy 1945; Herbig 1962), after the archetypical T–Tauri. Whilst higher mass YSOs ($3M_{\odot} <$M$< 8M_{\odot}$) are known as Herbig Ae/Be stars (Herbig 1960). These stars have a spectral index of $-1.5 < \alpha < 0$ (Lada 1987) and typically have an age of $\sim 10^6$years.

During this phase, most of the material has been accreted onto the circumstellar disc, and the envelope has mostly dissipated. The near and mid-infrared excesses are both now provided by the optically thick circumstellar disc; with the SED showing a broader distribution than that of a blackbody, with a flat or decreasing emission spectrum longward of 2μm.

The protostar has now acquired the bulk of its mass, however it may still accrete some material at a reduced rate (Hartmann et al. 1998). Various processes, such as photoevaporation and radial drift, are believed to remove material from the disc during this phase. These will be discussed in Section 1.3. The majority of planet formation is thought to occur in the Class II stage.

1.1.4 Class III

The last phase of protostellar evolution features Class III protostars. These stars have a spectral index of $\alpha > 1.5$ (Lada 1987). These objects have similar lifetimes to that of Classical T–Tauri stars ($\sim 10^6$years) (Wilking et al. 1989), however accretion onto the protostar has now stopped.

The presence of an accretion disc is often inferred by the presence of strong Hα

line emission (Kenyon & Hartmann 1990). Therefore, Classical T-Tauri stars are often shown to have Hα equivalent widths greater than 10Å (Alcala et al. 1993). Objects with a smaller equivalent width than this are often called Weak-line T-Tauri stars. These YSOs are assumed to be more evolved than the Classical T-Tauri young stellar objects (Duvert et al. 2000).

Due to various dust and gas processes, the gaseous disc has now dissipated leaving behind a disc composed primarily of larger dust grains (Bryden et al. 2009). This optically thin debris disc provides the slight infrared excesses seen in Class III SEDs, and they can be modelled using a reddened blackbody (e.g. Wilking et al. (1989)). Following this phase, the protostar contracts to become a main sequence star.

1.2 The Protoplanetary Disc

The protoplanetary disc is the disc of gas and dust surrounding a young stellar object. This is the location of where planet formation takes place in a protostellar system. There are currently two major theories on the formation of planets; the core accretion model and gravitational fragmentation.

The core accretion model focuses on the collision and subsequent agglomeration of dust grains in the disc (Safronov & Zvjagina 1969; Goldreich & Ward 1973; Greenberg et al. 1978; Hayashi et al. 1985; Lissauer 1993). These go on to form planetesimals (dust aggregates with sizes ∼m–km), and eventually rocky planets. Once a planet is massive enough, a period of rapid gas accretion follows (Pollack et al. 1996). Thus allowing the formation of gas giant planets.

Gravitational fragmentation is the result of particularly massive and cold regions of the disc becoming gravitationally unstable (Kuiper 1951; Cameron et al. 1978; Boss 1997). These regions can go on to form dense clumps which then collapse to form bound objects.

This thesis focusses solely on protoplanetary discs surrounding young stellar

objects, and the substructures developing therein. In this section we first consider the observational constraints of observing protoplanetary discs. We follow with an overview of the structure and evolution of the dust components of the disc. We end by outlining some of the constraints involved in the core accretion method of planet formation.

1.2.1 Observations of Protoplanetary Discs

Observations of young stellar objects can reveal a great deal about the protoplanetary disc's structure, temperature, and composition. Although the disc is composed primarily of gas (∼99% of the disc mass), it is highly transparent and difficult to observe. The majority of the disc's opacity comes from the ∼1% dust mass. This makes the disc optically thick at wavelengths shorter than the far infrared.

The dust absorbs the radiation emitted from the central protostar and re-emits the radiation at wavelengths between infrared and submillimetre (∼1–100 μm). This leads to an emission bump in the SED of the young stellar object compared to the emission from the protostar alone. As excesses at different wavelengths correspond to different emission temperatures, the SED can be used to map different components of the protoplanetary disc; this is depicted graphically in Figure 1.2.

The inner-most region of the disc is likely to be puffed up to a larger surface area (Dullemond et al. 2001). Therefore, the emission from this region is highly energetic and provides up to half the total infrared flux. The mid-infrared excess is thought to originate from the disc surface. Whereas the far-infrared excess is likely due to the disc midplane. This region is cooler than other regions of the disc as it is shielded from direct stellar radiation. Dust in the midplane is instead heated from the re-emission of radiation from layers above.

Observations at millimetre wavelengths probe the SED in the Rayleigh-Jeans domain. The dust here exists in the cold outer regions of the disc and can be

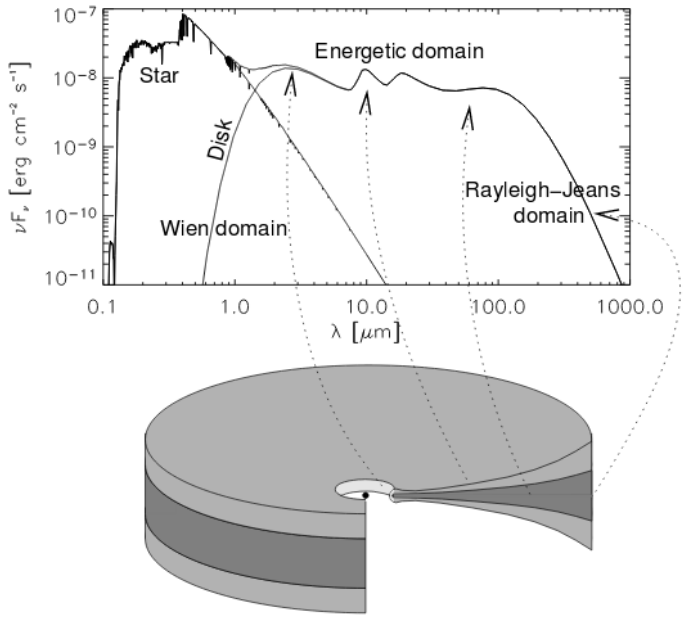

Figure 1.2: An SED of a young stellar object showing the blackbody emission from the protostar and infrared excess from the protoplanetary disc (Dullemond et al. 2007). Each excess (above the standard emission from a blackbody), shown by the dotted arrows, corresponds to a different component of the protoplanetary disc.

described by the Rayleigh-Jeans law

$$\nu F_\nu \approx \frac{\nu \kappa_\nu B_\nu(T) M_d}{D^2} \ , \tag{1.2}$$

where ν represents the frequency, κ_ν is the dust mass opacity, $B_\nu(T)$ is the Planck function at temperature T, M_d is the dust mass, and D is the distance to the young stellar object.

It is advantageous to observe the protoplanetary disc at millimetre wavelengths as is it optically thin. Thus estimates of the disc mass can be made (Weintraub et al. 1989). Previous studies have shown them to lie in the range of 0.005–0.14$M_\odot$ (Andrews et al. 2009). Current instrumentation also allows for high angular resolution observations to be made at millimetre wavelengths, allowing the disc to be spatially resolved as well as being able to detect substructure within the disc.

The dust size distribution can also be estimated from submillimetre (sub-mm) observations of protoplanetary discs. We can understand the properties of dust absorption from laboratory experiments (Koike et al. 1980; Wright 1987; Blanco et al. 1991; Mennella et al. 1995, 1998; Jager et al. 1998; Zubko et al. 2004), and compare these results to the dust distribution in discs. We assume that the dust mass opacity follows

$$\kappa_\nu \propto \nu^\beta \ , \tag{1.3}$$

where β is dependant upon the grain size distribution and is known the opacity spectral index. The observed flux, F_ν from Equation 1.2, thus follows $F_\nu \propto \nu^{\beta+2}$.

As shown in Equation 1.1, the gradient of an SED can be used to predict the spectral index of a protostellar system. By using the relation for the observed flux above, and Equation 1.1, we can see that the flux follows $F_\nu \propto \nu^\alpha$, where α is

the spectral index. Therefore, observations at millimetre wavelengths, coupled with Equation 1.2, allow us to make direct estimations of the grain size distribution in protoplanetary discs (Draine 2006; Natta et al. 2007).

Numerous studies have been performed to find the opacity spectral index of the grain size distributions in protoplanetary discs. Beckwith & Sargent (1991) found that discs usually have an index of $0 < \beta < 1$. An opacity spectral index of $\beta \approx 0.5$ was assumed to be due to centimetre–sized dust grains in the disc of TW Hya (Calvet et al. 2002). A similar result was found for the disc surrounding CQ Tau, where $\beta \approx 0.6 \pm 0.1$ was attributed to grain growth (Testi et al. 2003). A larger opacity spectra index of $\beta \approx 1$, however, was found by Andrews & Williams (2005) who studied the SEDs for 44 protoplanetary discs in the Taurus-Auriga star forming region.

1.2.2 Protoplanetary Disc Structure

We have previously discussed how the SED of a protostar can be used to map different regions of a protoplanetary disc. Each component contains a different dust population and can be observed using different observational techniques. The structure of the disc is shown on the right in Figure 1.3.

Protoplanetary discs are flared with a vertical scale height that increases with radius. This was first suggested by Kenyon & Hartmann (1987) who found that the SEDs of T–Tauri discs do not match a profile for a flat disc. The surface of the disc absorbs more radiation from the protostar than that of a flat disc, resulting in the infrared excess seen in the SED in Figure 1.2.

The inner regions of the protoplanetary disc ($\sim$ a few au from the protostar) are comprised of hot μm–sized dust grains and can be probed by mid- and near-infrared observations. The temperature of the disc at these radii can reach up to 1500 K, thus causing the sublimation of dust grains (Hillenbrand et al. 1992). Exterior to this

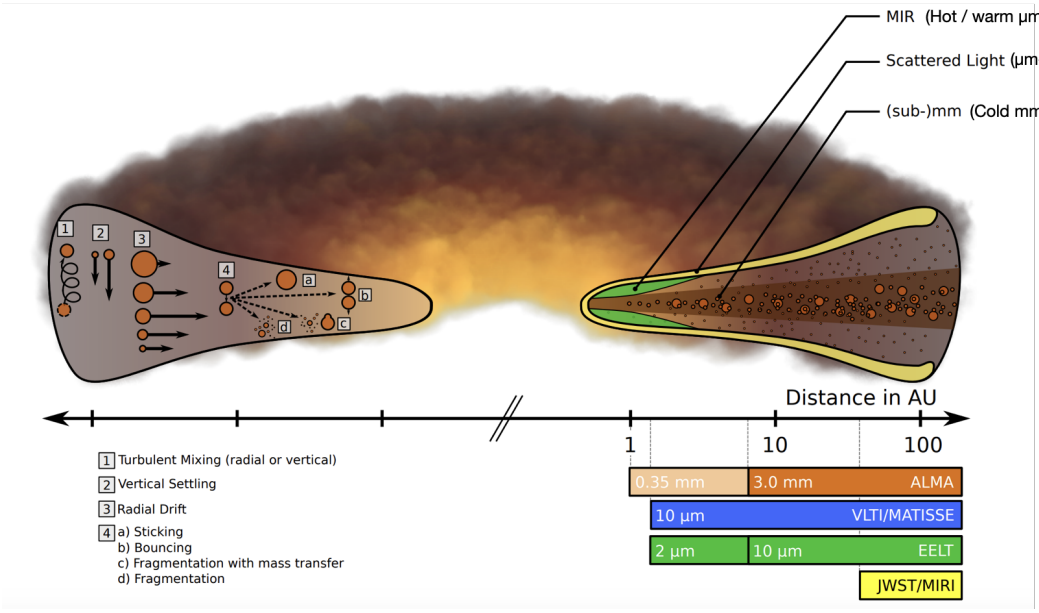

Figure 1.3: An illustration of the disc structure, grain evolution processes and observational techniques. The left shows the main grain growth transport and collision mechanisms. The arrows indicate the velocity of the grains, with longer arrows representing higher velocities. On the right, the different areas of the protoplanetary disc can be seen, along with the various techniques needed to probe them, and the dust population in each region. The horizontal bars on the right show the maximum resolution that can be achieved when observing each coloured section, along with the current/upcoming instrument available for observation. Adopted from Testi et al. (2014).

sublimation point, the disc is exposed directly to stellar radiation, and is therefore, much hotter than the colder midplane regions of the disc (Natta et al. 2001; Tuthill et al. 2001). This creates an optically thick 'puffed-up' inner wall at this sublimation point.

The surface of the disc is comprised of small μm–sized dust grains which originate from the ISM (Draine 2003). These grains reflect the radiation emitted by the protostar. Therefore, scattered light observations of protoplanetary discs can reveal the surface density of the dust grains. As the μm–sized dust grains grow in size, they settle towards the midplane of the disc.

The midplane is comprised of solid dust grains with a range of sizes (μm–cm–sized). This region of the disc is assumed to be optically thin; thus submillimetre observations of the disc can reveal the bulk of its material. The midplane of the protoplanetary disc is the densest region and is thought to be the location of the majority of the dust growth processes. As the midplane is shielded from the stellar radiation by the upper layers of the disc, this region is particularly cold. This aids in the growth of the dust grains as gasses can condensate onto the dust grains thus providing a sticky, outer coating (Goldreich & Ward 1973).

The distribution of mass within a protoplanetary disc is characterised by the surface density, Σ. Analytical solutions for viscous discs, derived by Lynden-Bell & Pringle (1974) and Hartmann et al. (1998), describe the surface density as a tapered power law given by

$$\Sigma(R) = (2-\gamma)\,\frac{M_{disc}}{2\pi R_c^2}\,\left(\frac{R}{R_c}\right)^{-\gamma}\,exp\left[-\left(\frac{R}{R_c}\right)^{2-\gamma}\right]\,, \tag{1.4}$$

where M_{disc} is the total disc mass and γ is a radial viscosity power index (where the viscosity has the relation $\upsilon \propto R^{\gamma}$). The disc radius is given by R. The characteristic radius, R_c, is the radius at which the surface density deviates from a power law and

instead begins to decline steeply. Hughes et al. (2008) find characteristic radii in the the range R_c= 30–200 au.

1.3 Dust Evolution

Although the protoplanetary disc comprises of just 1% of its mass in dust, it is this component that affects the structure of the disc greatly through its opacity to the stellar radiation. Studying the dust evolution, therefore, is key to understanding the planet formation process as it reveals how the dust behaves with regards to the gas in the disc; along with its growth from micron–sized grains to fully formed planets.

The dust found in protoplanetary discs originate from the diffuse interstellar medium. They are mainly composed of silicates with sizes $r \lessapprox 0.1$ μm (Draine 2003). As they advance through the interstellar medium, cold molecular clouds, and eventually arrive at the protoplanetary disc, gas molecules from the surrounding medium freeze onto the grain surfaces producing icy mantles (Bergin & Tafalla 2007; Pontoppidan et al. 2005).

A relative motion can exist between the dust grains in the disc and the gas. The gas in the disc travels at sub-Keplerian velocities, with small dust grains being well-coupled to the gas. However, as the dust grains grow in size, they begin to decouple and travel in Keplerian orbits. This results in a relative motion between the larger dust grains and the gas. Therefore, the dust feels a friction along its orbit. The magnitude of the force felt by the dust grains depends both on its relative motion to the gas as well as the particle size.

Dust grains in the disc can be smaller than the mean free path of the gas molecules. The drag force affecting these grains can be considered as the result of individual collisions with the gas molecules (see e.g. Baines et al. (1965)). This is known as the Epstein regime (Whipple 1972; Weidenschilling 1977). If the particles of dust are larger than the mean free path of the gas molecules, the dust grains

are said to be in the Stokes regime (Whipple 1972; Weidenschilling 1977). In this regime, a flow structure can be considered to develop around the dust grains and the gas should be treated as a fluid (see e.g. Stepinski & Valageas (1996)).

The motion of the dust particles are often described using the stopping time, τ_s. This is the characteristic time for the acceleration or deceleration of the dust particles and is given by

$$\tau_s = \frac{m_p v}{f} \ , \tag{1.5}$$

where m_p and v are the particle mass and velocity, and f is the drag force. Particles of different shapes, sizes, and composition, are affected by the drag force differently. The dimensionless parameter called the Stokes number is widely used to describe dust grains as particles with the same Stokes number have identical aerodynamical behaviour regardless of mass, size, composition, or the environment. The Stokes number can be defined as

$$St = \Omega_K \tau_s \ , \tag{1.6}$$

where τ_s is the stopping time of the particle and Ω_K is the orbital period. Particles with Stokes numbers < 1 are well coupled to the gas, whereas particles with Stokes numbers > 1 travel due to their own inertia.

The drag force felt by the dust particles causes them to radially drift towards smaller radii (Whipple 1972; Adachi et al. 1976; Weidenschilling 1977). This force is felt greatest by particles with St$\sim$1. The radial drift of dust grains can cause the particles to be accreted onto the central star or even stunt the growth of dust grains (see Section 1.3.3). Grains can also pile up at specific locations in the innermost regions of the disc where the gas to dust ratio drops significantly.

Collisions between dust grains as they orbit the YSO, as well as radially drift, may cause coagulation. This would increase both the size and mass of the dust grains. As the particles grow, they decouple from the gas and begin to settle towards the midplane of the disc (Safronov & Zvjagina 1969; Goldreich & Ward 1973). This would eventually form a progressively thinner midplane layer in the protoplanetary disc. This mechanism has previously thought to be a way of growing dust grains (Weidenschilling 1980; Nakagawa et al. 1986).

Weidenschilling (1980) showed that the continuous settling of dust grains is problematic and unrealistic. Similarly, observations of protoplanetary discs have detected grains above the midplane. The mechanism counteracting the vertical settling of dust grains is thought to be turbulence (Dubrulle et al. 1995). Small grains in the midplane, the result of destructive collisions, can replenish the small dust population in the upper disc layers via vertical mixing caused by turbulence (Dullemond & Dominik 2005; Birnstiel et al. 2009; Zsom et al. 2011). Grains in the upper layers can also be replenished via the continuous infall of material from the protostellar envelope (Mizuno et al. 1988; Dominik & Dullemond 2008).

The transport mechanisms of the dust grains previously discussed lead to both vertical and radial motion of the dust particles. These lead to collisions which may promote either the growth of dust grains, or their destruction. The outcome of the collision is dictated by various particles parameters such as size, mass, and collisional velocity. We now discuss the various grain growth processes in Section 1.3.1, as well as the outcomes of various collisions in Section 1.3.2. We conclude the section by discussing the numerous barriers to grain growth in Section 1.3.3.

1.3.1 Grain Growth Processes

There are various processes that can lead to the collision, and subsequent growth of dust grains. The mechanisms leading to growth depend upon the size, mass, and

composition of the dust grains, as well as their location in the protoplanetary disc. Here we discuss the various processes that can lead to the growth of dust grains from sub–μm–sized up to metre–sized aggregates.

Brownian motion: The early protoplanetary disc features sub–μm dust particles embedded in the gas disc. The dust grains are well coupled to the gas, therefore the drift between dust grains is very small. Brownian motion dominates the collisions between the micrometre–sized dust population. The dust grains move with an average thermal velocity relative to the gas at rest at

$$v_t = \sqrt{\frac{3\kappa T}{m_p}} \ , \tag{1.7}$$

where κ denotes the Boltzmann constant, T is the temperature of the gas, and m_p is the mass of the dust particle.

The relative motions between the dust grains induced by Brownian motion cause the dust grains to collide (Kusaka et al. 1970), where they are able to combine via the van der Waals force. This weak, short-range force arises between adjacent particles due to the induced electrical dipoles in the neighbouring layers of contact. Although Brownian motion becomes negligible as the dust grains grow in size, it is the dominating source of relative motion for particles of the order sub–μm.

Relative velocities: Relative velocities can exist between the dust grains in the protoplanetary disc. This can cause them to collide and coagulate, thus increasing the size of the dust aggregate. Relative motion, however, can also result in the fragmentation of dust aggregates (see Section 1.3.2 below for the various outcomes of dust collisions). Although Brownian motion dominates relative motion of sub–μm grains, other mechanisms are responsible for dust populations comprised of larger aggregates.

As the dust grains grow in size, they begin to settle vertically as well as radially drift. This can cause relative velocities to form between the dust grains (Nakagawa et al. 1986; Weidenschilling & Cuzzi 1993; Brauer et al. 2008). Both radial drift velocities and vertical settling velocities peak at St$\sim$1. This gravitational sedimentation allows for further coagulation as the dust density in the midplane increases. It is in the midplane of the protoplanetary disc where grain growth is thought to occur rapidly. The radial drift of dust grains can lead to dust traps forming. Here the gas to dust ratio dramatically decreases causing grain growth to increase. The dust traps can lead to substructures forming in the disc (see Section 1.4).

Relative motions can also exist between the dust grains due to the turbulent nature of the protoplanetary disc (Voelk et al. 1980; Markiewicz et al. 1991; Cuzzi & Hogan 2003; Ormel & Cuzzi 2007). Relative velocities induced by turbulence increase with the Stokes number until St=1. The turbulence also provides some degree of vertical mixing of dust grains (Dullemond & Dominik 2005). This can also aid in the growth of dust grains as larger grains from the midplane can easily coagulate with smaller grains near the surface of the disc.

Relative velocities can also exist between dust grains in the azimuthal direction if there are regions of high pressure (Birnstiel et al. 2013). This mechanism relies on the relative motion between gas and dust. The relative velocities are small for particles with Stokes numbers less than unity. They do, however, reach a high for particles with Stokes values > 1 and increase with the Stokes number.

We have outlined four mechanisms that cause relative motions to exist between dust grains in the protoplanetary disc; Brownian motion, turbulence, radial drift, and azimuthal over-pressures. These mechanisms affect the populations of different sized dust grains. As well as this, they operate over different regions of the protoplanetary disc. Figure 1.4 shows the dominant contribution to the relative velocities in protoplanetary discs. The plot was generated for a $1M_{\odot}$ protostar with

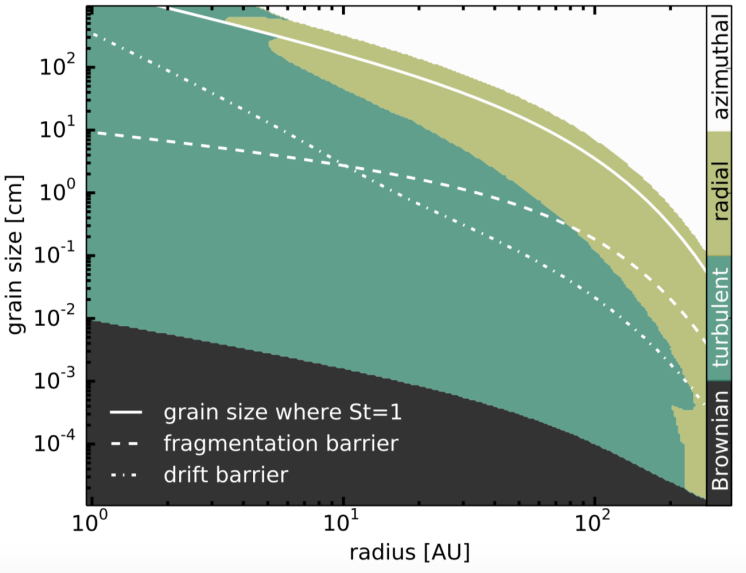

Figure 1.4: The particle sizes and regimes of relative velocities in the dust of protoplanetary discs. The solid white line represents a dust particle with a Stokes number of St=1 (where the effects of radial drift and settling are greatest). The dashed line indicates the the size barrier to fragmentation whilst the dashed-dotted line indicates the radial drift barrier. The coloured sections denote the dominating source of relative velocities for a particles given size and radius (Testi et al. 2014).

a disc mass of 1% the stellar mass.

Condensation: Gas in the cold, outer regions of the protoplanetary disc can condense onto small dust grains giving them an outer, sticky mantle. The dust grains are then able to stick upon collisions and are able to grow in size (Goldreich & Ward 1973). This is not, however, an efficient form of dust growth as there is not enough material in the gas phase to grow a macroscopic icy mantle on every microscopic dust grain.

As the dust grains grow in size, they are also affected by radial drift. Crossing the snowline - the radius at which the icy mantle melts - causes the dust grains to lose their sticky, outer coating. Therefore, collisions no longer result in coagulation, but rather fragmentation. Drifting too close to the central protostar can also increase

the temperature of the dust grains dramatically, which may result in sublimation.

Although Ros & Johansen (2013) were able to grow decimetre–sized particles via condensation, the particles consisted entirely of ice, and radial drift was not considered. Therefore, it is still unclear if condensation is a viable dust growth mechanism under realistic disc conditions.

1.3.2 Dust Collisional Outcomes

The collision between grains of dust, and the subsequent outcome, depends on a large number of parameters, including: the grain size, mass, porosity, composition, and structure. The outcome is also dependant upon the impact velocity and angle (Blum & Wurm 2008). Due to vertical settling, collisions between two dust grains involve a wide range of impact velocities as well as initial sizes. Therefore, it is extremely challenging to study the outcome of collisions experimentally or numerically, and thus make predictions of the grain growth process.

Nonetheless, collisional models of protoplanetary dust have been developed, beginning with the pioneering work of Blum & Munch (1993). Experiments involving millimetre–sized dust aggregates comprised of μm– or nm–sized grains were made to collide with a range of velocities. Since then, there has been a considerable increase in dust collisional models covering a wide parameter space (see Blum & Wurm (2008) for review) (Güttler et al. 2010; Gundlach et al. 2015; Musiolik et al. 2016a,b).

Laboratory-based protoplanetary dust models have been based upon two scenarios; outcomes for collisions involving similar–sized aggregates, and outcomes when small projectiles hit larger aggregates. Here we briefly describe the different outcomes of dust collisions, with a graphical representation of each outcome shown in Figure 1.5.

Outcomes for collisions between similar–sized aggregates

Sticking: For two particles which collide with an energy less than the individual

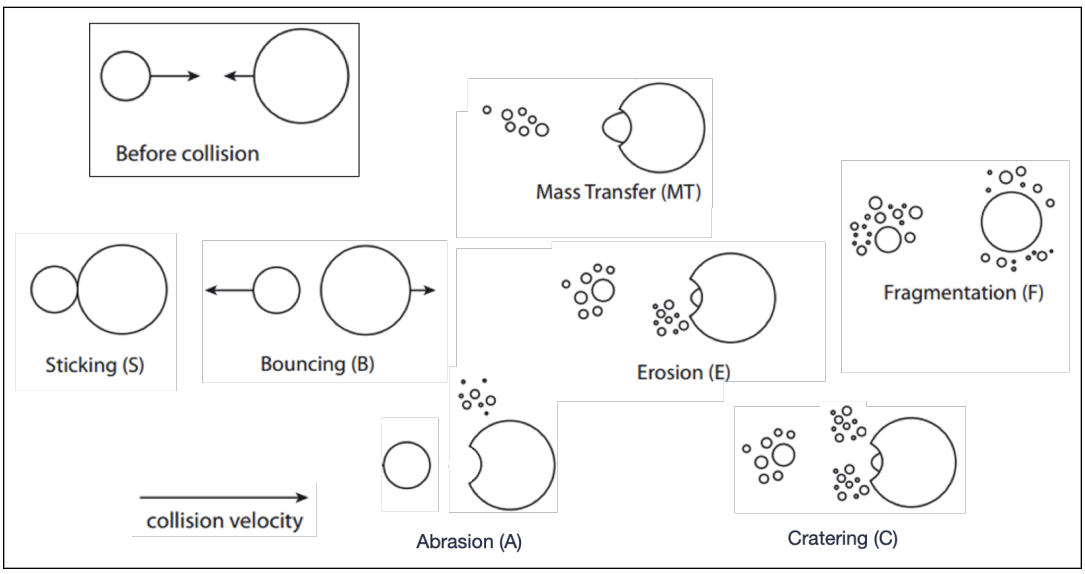

Figure 1.5: Outcomes for dust collisions in protoplanetary discs. Sticking, Mass Transfer, and Erosion lead to a positive net growth of one aggregate; whereas Abrasion, Cratering, and Fragmentation, lead to a negative net growth for one or both aggregates. Adopted from Windmark et al. (2012).

van der Waals binding energy, sticking will occur if the collision is at least partially inelastic (Dominik & Tielens 1997). For collisional energies greater than the binding energy of the particles, the degree of inelasticity determines the outcome of the collision.

There are three possible process that lead to the complete transfer of material from one dust aggregate to another. These were first outlined in Güttler et al. (2010). For very small impact velocities, the aggregates can hit and completely stick to each other. Two aggregates may collide and stick, however there may be some deformation or compaction of either one or both aggregates. Lastly, an aggregate that is slightly smaller than its collisional partner may be deeply embedded into the larger target resulting in cohesion between the two aggregates.

The results by Güttler et al. (2010) are supported by both previous and later works (see references within the review by Blum & Wurm (2008), as well as

Weidling et al. (2012); Kothe et al. (2013); Weidling & Blum (2015); Brisset et al. (2016, 2017); Whizin et al. (2017)).

Bouncing: If the energy dissipation upon the collision of two aggregates is insufficient to allow the sticking, however, is still not large enough to result in negative growth outcomes (see below), bouncing occurs (Blum & Munch 1993; Heißelmann et al. 2007; Zsom et al. 2010; Weidling et al. 2012; Kothe et al. 2013; Landeck 2016; Brisset et al. 2016, 2017). The bouncing of aggregates may lead to the halting of growth, and experiments by Weidling et al. (2009) show that bouncing may lead to the compaction of dust aggregates.

Fragmentation: Aggregates that collide at high velocities may lead to a negative growth of either one or both aggregates. This can occur for relative velocities $\Delta\nu \gtrsim 1$ ms^{-1} (Güttler et al. 2010). These collisions may also lead to the complete fragmentation of both aggregates involved in the collision (Blum & Munch 1993; Beitz et al. 2011; Schräpler et al. 2012; Deckers & Teiser 2013; Bukhari Syed et al. 2017).

Abrasion: Two dust aggregates that collide with a relative velocity smaller than the velocity required for fragmentation may suffer a small mass loss. Experiments have recently shown that abrasion does not occur for velocities below $\sim$0.1 ms^{-1}, and increased in strength with increasing velocities (Kothe 2016).

Outcomes for collisions between a small projectile and large dust aggregates

Mass transfer: A small dust aggregate colliding with a larger aggregate at a velocity greater than its fragmentation velocity may transfer some of its mass to the target

(Wurm et al. 2005; Teiser & Wurm 2009b,a; Deckers & Teiser 2013; Bukhari Syed et al. 2017). The small dust aggregate fragments with up to a 50% chance of transferring material to the target (Teiser et al. 2011).

Cratering: If the projectile aggregate is larger than in the mass transfer case, the target aggregate may lose some mass during the collision. Although there may be some mass transfer between the smaller projectiles and the target, the projectile excavates more mass than it transfers and hence leads to a negative growth for the larger target (Wurm et al. 2005; Paraskov et al. 2007). Subsequent cratering collisions may result in the complete fragmentation of the larger dust aggregate.

Erosion: If the projectile is larger than in the mass transfer case, but not so large that the collision results in cratering, erosion occurs for the target aggregate. Some mass is transferred to the target aggregate, as well as some material fragmenting from the target. The mass loss, however, is to a lesser degree than in the cratering case, as the overall growth of the target aggregate may be positive. This has been shown both experimentally (Schräpler & Blum 2011; Schräpler et al. 2018) as well as in numerical simulations (Seizinger et al. 2013; Krijt et al. 2015).

The collisional outcomes between dust aggregates of different radii are shown in Figure 1.6. The green sections represent when collisions between aggregates result in the positive growth of the dust grains. The orange and red sections indicate when collisions result in a negative growth. From Figure 1.6 we can see that it is likely for collisions to result in some loss of material, thereby making the growth of dust aggregates difficult.

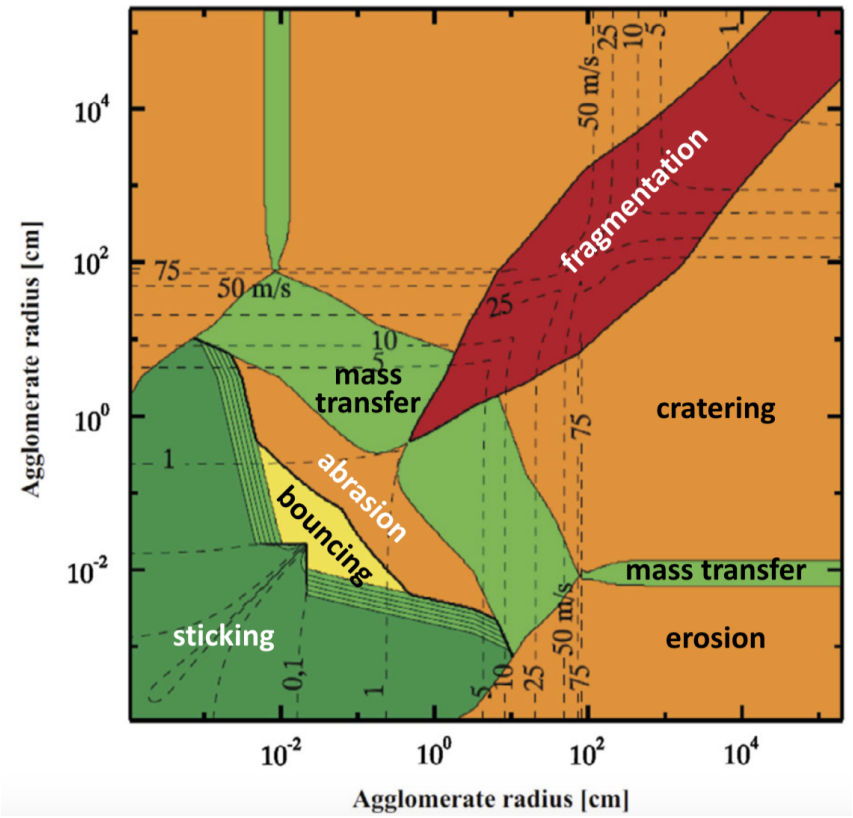

Figure 1.6: Collisional outcomes between dust grains of different radii in a proto-planetary disc. Different outcomes are coloured and labelled. Dashed contours mark the mean collision velocities in units of ms^{-1} from laboratory experiments (Blum 2018).

1.3.3 Barriers to Grain Growth

Here we discuss the mechanisms that can inhibit the growth of dust grains to beyond mm–sized.

Radial Drift: The small (sub–μm) dust grains close to the surface of the disc are highly coupled to the gas disc. The dust grains are supported via gravity and the centrifugal force. The gas is additionally supported by an outwards pressure which results in it orbiting the YSO with sub–Keplerian rotation. As the dust grains grow in size, they decouple from the gas and travel in inclined Keplerian orbits. The difference in velocity causes the dust grains to feel a headwind as they orbit the protostar. As a result, the dust grains decelerate, begin to lose angular momentum, and consequently drift to smaller radii (Whipple 1972; Adachi et al. 1976; Weidenschilling 1977).

The velocity of the inward drift component contributes only a fraction to the total orbital velocity. However inward drift speeds of $\sim$50 ms^{-1} can be reached by dust grains with St$\sim$1. At a radius of 1 au, radial drift can cause cm and m–sized bodies to spiral inwards and may be accreted onto the central protostar (Weidenschilling 1977; Nakagawa et al. 1986). This can happen on the timescale of a few hundred orbits. As this process halts the growth of the dust grains beyond metre–sized aggregates, it has been coined the metre-barrier.

From Figure 1.6, we can see that collisions involving dust grains travelling at $\sim$50 ms^{-1} often result in a negative overall growth. Therefore, the fragmentation and radial drift of dust grains can efficiently prevent the growth of dust above $\sim$1–100 cm. However, in order to reach the gravitational regime, where dust aggregates can gravitationally collapse, bodies that are roughly nine orders more massive are needed.

Bouncing Barrier and Fragmentation: We have previously introduced the concept of bouncing and fragmentation in Section 1.3.2 when discussing the various outcomes of dust collisions. From Figure 1.6 we can see that collisions with impact velocities $v \gtrapprox 25$ ms^{-1} often result in a negative growth of the dust aggregates. As dust grains grow in size, their velocity increases due to their radial drift. Therefore, collisions become more destructive as the dust grains increase in size (Chokshi et al. 1993).

Models by Zsom et al. (2010) were able to show that the dust grains in protoplanetary discs are able to grow via the hit-and-stick method until such a point where the majority of the collisions result in bouncing. The models ended with a deadlock where all the particles were of similar size and all collisions led to bouncing. Thus the growth of dust grains stopped. This is known as the bouncing barrier.

Similarly, ignoring the bouncing barrier and assuming that dust collisions transition from hit-and-stick to fragmentation/erosion, a point is reached where all collisions result in fragmentation (Brauer et al. 2008; Windmark et al. 2012). Thus the dust grains are stopped from further growing in size. A steady state can be reached in which dust grains undergo numerous cycles of growth and subsequent fragmentation (Birnstiel et al. 2011).

Protoplanetary disc models run by Dullemond & Dominik (2008) were able to remove small grains ($r < 100\mu$m) from the disc within 10^4 years via coagulation processes. However, this is inconsistent with observations of protoplanetary discs which have revealed the presence of small grains of dust in evolved discs (Malfait et al. 1998; Bouwman et al. 2003). Therefore, the negative growth process of fragmentation may be required in order to keep the delicate balance between grain growth and grain destruction in the protoplanetary disc (Dullemond & Dominik 2008).

Turbulence: Protoplanetary discs have some degree of turbulence, both radially and

vertically (Voelk et al. 1980; Markiewicz et al. 1991; Cuzzi & Hogan 2003; Ormel & Cuzzi 2007). The relative velocities between the dust particles caused by turbulence may lead to the growth of dust grains (Nakagawa et al. 1986). Contrary to this, if the degree of turbulence is relatively high, collisions between dust grains may result in fragmentation rather than coagulation. The relative velocities caused by turbulence increases with the Stokes number of the dust grains, and peaks at St=1. The maximum turbulent velocity in protoplanetary discs, first derived by Ormel & Cuzzi (2007), is given by

$$\Delta v_{turb} = c_s \left(\frac{9\alpha_t}{2} \right)^{1/2} , \tag{1.8}$$

where $c_s = \sqrt{\kappa_B T / \mu m_p}$ is the isothermal sound speed and α_t is the Shakura-Sunyaev parameter which specifies the degree of turbulence in the disc (Shakura & Sunyaev 1973).

1.3.4 The Formation of Planetesimals

As discussed in the previous section, the growth of the dust grains in protoplanetary discs is severely affected by a number of barriers. Dust grains have successfully been shown to grow up to centimetre and metre–sized aggregates. However, planetesimals, of the order ∼km–sized, are needed in order to gravitationally collapse and form terrestrial planets (or the cores of giant planets).

The core accretion method of planet formation also suffers from a time scale constraint. The destructiveness of planet formation via core accretion results in planets forming on time scales of a few millions years. This is longer than the average disc lifetime (Haisch et al. 2001; Cieza et al. 2007). By the time the planetesimals have formed, the dispersal of the gas disc is already underway. Therefore, forming gas giant planets proves to be difficult via the core accretion theory. This has led

to other mechanisms of planet formation being proposed.

Here we introduce some mechanisms that have been proposed to circumvent the constraints of the core accretion method of planet formation. Although these mechanisms discuss the formation of planetesimals, the topic still remains debated. One limitation of planetesimal formation studies is the observational constraints. Current facilities do not allow for high resolution detections of planetesimals which may aid in producing robust models of their formation.

1.3.4.1 Streaming Instabilities

The streaming instability has been suggested to form planetesimals in protoplanetary discs. First proposed by Johansen & Youdin (2007), this mechanism is caused by the effect of the dust grains onto the gas distribution in the disc. Although the mass of the disc is provided predominantly by the gas, regions of the disc will have a similar relative density between the dust and gas populations. Therefore, the gas will feel a feedback effect from the dust (Youdin & Goodman 2005). This can lead to highly concentrated regions of dust grains in the protoplanetary disc, which can then gravitationally collapse to form planetesimals. In order for streaming instability to occur, however, a high density of dust grains needs to be decoupled from the gas. For this to occur a large number of particles would need to be relatively large with a Stokes number of St$\sim$0.1–1 (Bai & Stone 2010). The growth barriers mentioned above may, however, limit the sizes of the dust population in the disc. As well as this, the canonical gas-to-dust ratio of 100:1 may not be low enough in order for the dust grains to reach the high densities required for the streaming instability to kick in.

1.3.4.2 Gravitational Instabilities

Planetesimals were first thought to form via gravitational instabilities in the midplane of the protoplanetary disc (Safronov & Zvjagina 1969; Goldreich & Ward 1973). As the dust grains settle towards the disc midplane, a progressively thinner dust layer would form. Once the density of this thin dust disc is high enough, gravitational instabilities in the dust would cause the collapse and subsequent formation of planetesimals. This mechanism was shown to be ineffective at forming planetesimals by Weidenschilling (1980). As the dust settles in the disc, turbulence is generated via the Kelvin-Helmholtz instability. The dust is thus prevented from fully settling in the midplane and forming the densities required for gravitational collapse.

Since the work of Weidenschilling (1980), the mechanism of gravitational instabilities to form planetesimals has been expanded to study the formation of objects such as planets and brown dwarfs via the direct collapse of the protoplanetary disc.

The stability of a protoplanetary disc depends upon the balance between three mechanisms; gravity, and the combination of rotational and thermal support. The instabilities in the disc can contribute to the transport of angular momentum (Tomley et al. 1994; Bodenheimer 1995; Ruden 1995; Durisen et al. 2007; Forgan et al. 2011; Armitage 2011; Rice et al. 2011). And an unstable disc may go on to gravitationally fragment to form planetesimals (Rice et al. 2006), gas giant planets (Mayer et al. 2004; Boss 2011, 2012), brown dwarf companions (Matzner & Levin 2005), and binary stars (Laughlin & Rozyczka 1996).

The stability of a protoplanetary disc can be expressed by the Toomre stability criterion, Q (Toomre 1964), where

$$Q = \frac{K c_s}{\pi G \Sigma} \ . \tag{1.9}$$

The epicyclic frequency of the disc, K, represents the rotational support present in the disc. This is often approximated to the Keplerian frequency, Ω_K. The thermal support is represented by the sound speed, c_s, which we have defined above. The surface density of the disc, Σ, represents the gravitational support. This acts to destabilise the disc.

The disc is thought to become gravitationally unstable for Toomre values of $Q < 1$. However, this assumes the disc is razor-thin, which was shown to be an incorrect assumption by Weidenschilling (1980). Durisen et al. (2007) were able to show that the critical Toomre value may be $Q < 1.4$, with discs being able to fragment provided $Q < 0.6$ (Takahashi & Inutsuka 2016).

Approximations on the stability of the disc can also be made by looking at the disc-to-star mass ratio; where a small value is indicative of a stable disc. Thus the disc may undergo gravitational instabilities if the mass of the disc is comparable to the mass of the young stellar object. Dong et al. (2015a) were able to show that a disc can become gravitationally unstable if the disc-to-star mass ratio, q, is greater than 0.25. This mass ratio is only achievable at the earlier stages of protostellar evolution (i.e. in the Class 0 or Class I phase). During these phases the protostellar system is still embedded in its parent molecular cloud, from which it actively accretes. Thus there is a continuous supply of material to the protoplanetary disc, allowing it to be sufficiently massive enough to undergo gravitational instability. This does, however, lead to difficulties in observing discs that may be gravitationally unstable as they are surrounded by an envelope. Nonetheless, observations have been made of particularly massive discs around very young protostars (Osorio et al. 2003; Rodríguez et al. 2005; Eisner et al. 2005).

Spiral arms are thought to be generated in protoplanetary discs as a result of gravitational instabilities (Toomre 1964; Boss 1997). They act as a way of transferring angular momentum outward of the disc, resulting in material migrating radially

inward and ultimately accreting on to the protostar.

Spiral arms may go on to gravitationally fragment to form bound objects such as brown dwarfs (Matzner & Levin 2005) and planets (Mayer et al. 2004; Boss 2011, 2012). This can happen when the local Toomre value obeys $Q < 1$, and the region is sufficiently cold such that $t_{cool} < (0.5 - 2)t_{orb}$ (Gammie 2001; Johnson & Gammie 2003; Rice et al. 2003, 2005). Here t_{cool} is the cooling rate and t_{orb} is the local orbital period. A dense clump may form in a region satisfying these two conditions and subsequently gravitationally collapse.

The formation of bound objects via gravitational instability is of great importance as it may be a mechanism of forming massive planets, brown dwarfs, and low-mass stars (Whitworth & Stamatellos 2006; Boley 2009; Stamatellos & Whitworth 2009a; Kratter & Lodato 2016). The process of gravitational fragmentation would allow these objects to form in shorter timescales than the core accretion method of planet formation. Thus circumventing the problem of the quick dispersal of the gas disc in the core accretion model.

1.4 Substructures in Protoplanetary Discs

The forces in a protoplanetary disc that govern the gas flow are a balance between gravity, rotation, and pressure support. The planet formation barrier of radial drift, first discussed in Section 1.3, occurs due to the fact that the gas in the disc is supported by a pressure force whereas the dust is not. Therefore, the gas orbits the disc at sub-Keplerian velocities. Dust grains, which travel at Keplerian velocity, feel a headwind and subsequently decouple from the gas. This causes the dust to migrate inwards towards the pressure maximum at the inner disc edge.

Contrary to the assumption of a smooth, monotonic pressure gradient, local maxima may be present in the disc. Exterior to the local maxima, the gas continues to travel at sub-Keplerian velocities causing particles to drift inwards. Just interior

to the maxima, however, the gas travels at super-Keplerian velocity. This causes the particle of dust to be pushed outwards. The perturbed gas flow thus causes the dust grains to converge towards the local pressure maximum, where the gas orbits at Keplerian velocity. This process can effectively 'trap' solids by slowing or halting their migration.

Localised pressure maxima may solve the barriers of planetesimal formation as the dust grains can be stalled in the disc. This can alleviate the problem of radial drift (Pinilla et al. 2012b, 2013). As well as this, the high concentration of dust grains may bring the dust-to-gas ratio closer to unity (e.g. Yang et al. (2017)). Thus creating favourable conditions for planetesimal formation via the onset of the streaming instability (see Section 1.3.4) (Youdin & Goodman 2005; Johansen & Youdin 2007). The high concentrations of dust grains may also lead to the localised gravitational collapse of the disc (Goldreich & Ward 1973; Youdin & Shu 2002). Substructures may form at these pressure maxima as a result of these processes.

The pressure maxima can be formed in a number of different ways, with the subsequent structures appearing in different grain size distributions (therefore probed using different wavelength observations). This thesis focusses on substructures seen in the dust continuum of protoplanetary discs at submillimetre wavelengths. Therefore, the following section introduces the different substructures, and their formation mechanisms, that are observable at submillimetre wavelength only.

There are four main substructures that have been observed in protoplanetary discs thus far; rims and cavities, rings and gaps, asymmetrical dust traps, and spiral waves. Recent high resolution observations of protoplanetary discs have been able to resolve the substructures down to milliarcsecond resolutions (Andrews et al. 2018a). The formation mechanisms for each substructure are shown in Figure 1.7. We discuss each substructure in more detail below.

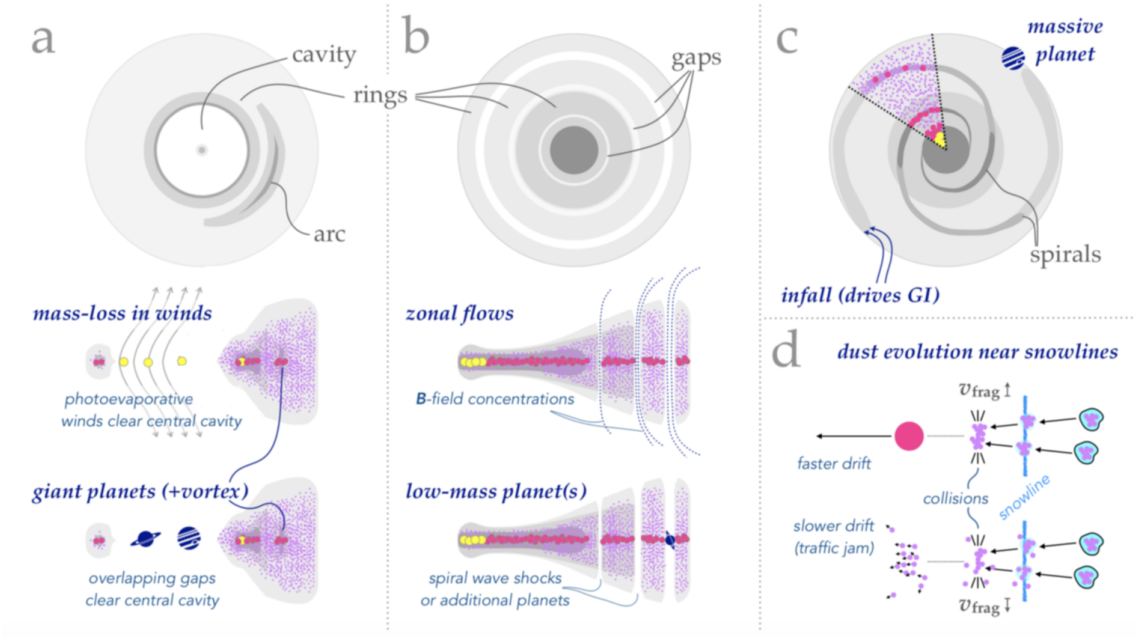

Figure 1.7: An illustration of the substructures formed via various mechanisms. The greyscale denotes the gas distribution in the disc. Coloured symbols and points represent solid densities such as planets and dust grains. (a) A schematic diagram showing the possible formation mechanisms of a rim/cavity and an asymmetric dust trap. The side views of the disc show a cavity being formed due to winds (top) or giant planets (bottom). Each mechanism causes the dust density to decrease in the cavity, with a sharp edge causing a pile-up of dust grains. This can also form a vortex causing a asymmetric arc-shaped structure. (b) A schematic diagram showing the processes that can cause the formation of rings/gaps in disc. Below shows the side view of a disc where rings/gaps can form due to zonal flows (top) or low-mass planets (bottom). (c) The formation of spiral waves in a disc can either be due to gravitational instabilities or by massive planets external to the disc. (d) The outcomes of icy dust grains as they cross a condensation front in the protoplanetary disc. The top diagram shows the effects of critical velocity needed for fragmentation, v_{frag}, increasing, thus promoting dust growth and drift. The bottom diagram shows the effects of v_{frag} decreasing, resulting in a pile-up of small dust grains. Image from Andrews (2020).

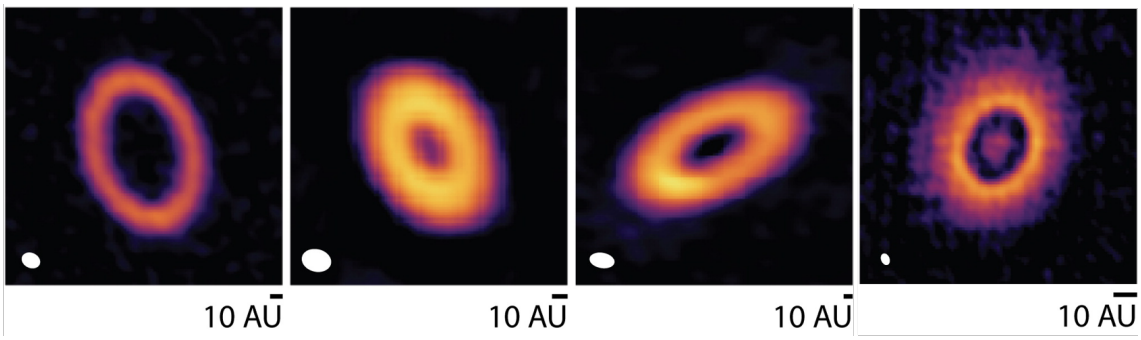

Figure 1.8: Examples of protoplanetary discs featuring a rim and cavity substructure. All discs have been observed with ALMA and depict the submillimetre continuum emission. The beams are shown in the lower left corners, with a 10 au scale–bar in the lower right. From left to right: SZ 91 (Tsukagoshi et al. 2019), EM* SR 24S (Pinilla et al. 2017a), HD 34282 (van der Plas et al. 2017), and DM Tau (Kudo et al. 2018). Figures from Andrews (2020).

1.4.1 Rims and Cavities

A common substructure seen in the protoplanetary discs observed with ALMA is a cavity of some sort surrounded by a rim of material. This could be in the form of the inner cavities seen in transition discs or the depletion of dust and gas in different regions of a protoplanetary disc (Piétu et al. 2007; Brown et al. 2009; Andrews et al. 2011). Examples of protoplanetary discs featuring a rim and cavity can be seen in Figure 1.8.

This type of substructure can be formed in one of two ways: mass-loss due to protostellar winds and the evolution of giant planets (see Figure 1.7(a)). Mass can be lost from the system via winds caused by photoevaporation (Hollenbach et al. 1994; Pollack et al. 1996; Hardy et al. 2015).

Photoevaporation occurs when the gas in the disc is sufficiently heated by ultraviolet or X-ray photons emitted by the central protostar. The molecules dissociate, or are ionised, causing them to become unbound. The pressure gradient in the disc

causes the gas to accelerate away in the form of a thermally driven wind. Models of photoevaporation effects in protoplanetary discs show the formation of ring-shaped pressure maxima at ∼tens of au (Alexander et al. 2014; Ercolano & Pascucci 2017). Inner cavities may exist interior to these maxima, depleted, or completely void, of material.

The interaction between the protoplanetary disc and companions are also able to form the rim/cavity substructure seen in protoplanetary discs. A sufficiently massive planet may be able to interact with the disc causing spiral shocks. These shocks can transfer angular momentum and repel disc material away from the orbit of the companion (Lin & Papaloizou 1979, 1986; Goldreich & Tremaine 1980; Baruteau et al. 2014; Dong et al. 2015b). The width and depth of the cavity cleared depend upon the mass of the companion and the local thermal structure of the disc (Kley & Nelson 2012). The pressure maximum exterior to this cavity has been shown to trap drifting dust grains (Rice et al. 2006; Paardekooper & Mellema 2006; Zhu et al. 2012).

The existence of multiple giant planets can cause multiple overlapping gaps that deplete the dust surface density over a wide radial range (see Figure 1.7a) (Dodson-Robinson & Salyk 2011; Zhu et al. 2011). The planets may also excite vortices in the disc leading to azimuthal asymmetries in the pressure structure. This may cause dust to pile up in other regions of the protoplanetary disc (Kley & Dirksen 2006; Ataiee et al. 2013; Zhu et al. 2014).

1.4.1.1 Asymmetrical Dust Traps

The modulations of the pressure gradient caused by photoevaporation and the orbits of companions do not have to be axisymmetric. Arc–like dust substructures at the edge of large cavities have be seen in protoplanetary discs (Casassus et al. 2013; van der Marel et al. 2013); they are, however, a rare substructure. These structures can

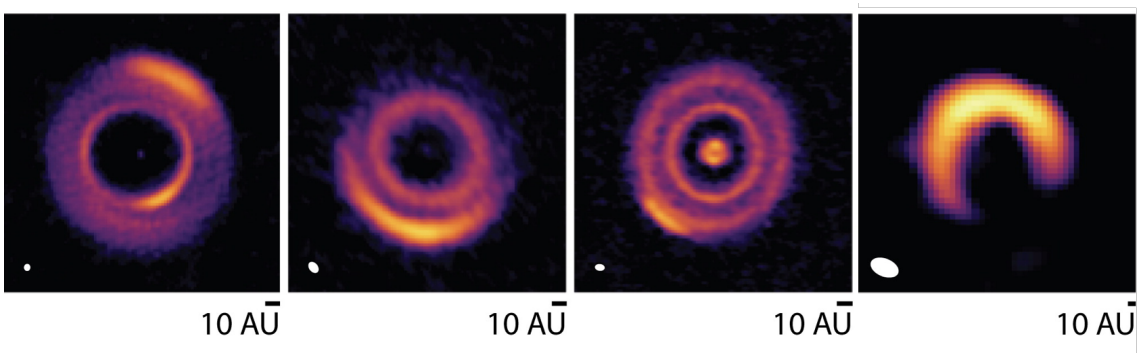

Figure 1.9: Examples of protoplanetary discs featuring an asymmetrical dust trap. All discs have been observed with ALMA and depict the submillimetre continuum emission. The beams are shown in the lower left corners, with a 10 au scale–bar in the lower right. From left to right: HD 36112 (Dong et al. 2018a), SAO 206462 (Cazzoletti et al. 2018), HD 143006 (Pérez et al. 2018), and HD 142527 (Casassus et al. 2013). Figures from Andrews (2020).

form alongside rim/cavity substructures (Marino et al. 2015; van der Marel et al. 2016b; Kraus et al. 2017; Boehler et al. 2018) or in a gap (Isella et al. 2018; Pérez et al. 2018). Examples of protoplanetary discs featuring an asymmetrical dust trap can be seen in Figure 1.9.

1.4.2 Rings and Gaps

Multiple dust rings, separated by gaps void of dust, have also been seen in protoplanetary discs. Although similar to the rim/cavity substructure, rings/gaps feature multiple concentric rims. Examples of protoplanetary discs featuring rings and gaps can be seen in Figure 1.10. The rings (and gaps) can be formed in a number of mechanisms including due to low-mass planets and zonal flows (see Figure 1.7(b)).

Turbulence in protoplanetary discs caused by its magnetic field may lead to the formation of coherent features in its pressure distribution. Asymmetric pressure structures can be formed when the gas distribution is modified by spontaneous

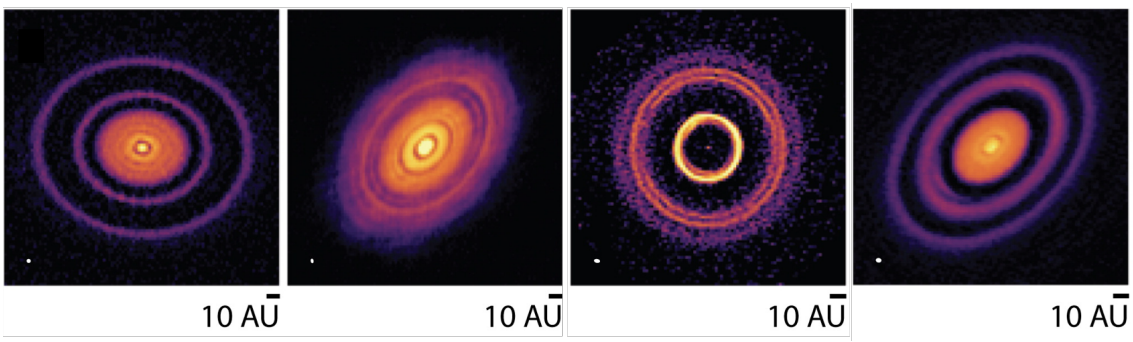

Figure 1.10: Examples of protoplanetary discs featuring rings and gaps. All discs have been observed with ALMA and depict the submillimetre continuum emission. The beams are shown in the lower left corners, with a 10 au scale–bar in the lower right. From left to right: AS 209 (Guzmán et al. 2018), HL Tau (ALMA Partnership et al. 2015), HD 169142 (Pérez et al. 2019), and HD 163296 (Isella et al. 2018).

concentrations of magnetic flux (Johansen et al. 2009; Dittrich et al. 2013). This may repel gas from regions of peak magnetic flux to neighbouring regions (Uribe et al. 2011; Bai & Stone 2014; Simon & Armitage 2014; Béthune et al. 2016; Suriano et al. 2017a,b). These zonal flows cause gaps to form in both the gas and dust distributions of the protoplanetary disc. This in turn causes dust to pile up at the edge of the pressure maxima, thus forming concentric ringed structures.

The interaction of a planet with a disc is commonly thought to be the origin mechanism for forming ring-like structures seen in protoplanetary discs. Similar to the rim/cavity substructure, low mass planets can also weakly interact with the pressure distribution of the disc, thus forming concentric rings of dust (Dipierro et al. 2016; Rosotti et al. 2016). Fedele et al. (2018) were able to show that multiple gaps in a disc may be formed by single or multiple planets.

Grain growth via condensation fronts was first introduced in Section 1.3.1. The crossing of the condensation front by the dust grains, and the subsequent sublimation of their icy mantles, may go on to form substructures in the protoplanetary disc. The loss of an icy mantle reduces the mass of the dust grains, thus the dust surface

density is dramatically decreased past the snowline (Stammler et al. 2017). The newly sublimated gas is able to travel back past the snowline and is able to re-condense onto dust grains (Stevenson & Lunine 1988; Cuzzi & Zahnle 2004; Ros & Johansen 2013; Ros et al. 2019). This enhances the growth rate of the dust grains, thus a concentration of solid material can be built exterior to the snowline.

The critical velocity required for fragmentation, v_{frag}, can either increase or decrease as dust grains cross the snowline; this in turn leads to different grain evolutions (see Figure 1.7(d)). A decrease in the fragmentation velocity leads to more destructive collisions, and therefore a higher population of smaller dust trains. The smaller fragments suffer a small radial drift which then leads to a pile-up of dust grains at smaller radii (Birnstiel et al. 2010; Saito & Sirono 2011). An increase in the fragmentation velocity leads to less destructive collisions, therefore an enhancement in the dust growth (Pinilla et al. 2017b). This does, however, lead to a faster radial drift of the dust grains. The dust may go on to accrete onto the protostar or cross the snowline of a different molecule.

1.4.3 Spiral Waves

The last type of substructure seen in protoplanetary discs are spiral arms (Pérez et al. 2016). Examples of discs featuring spiral arms can be seen in Figure 1.11. These structures are rarely seen in submillimetre light, contrary to the numerous population of discs featuring spiral arms at near-infrared wavelengths. The spiral arms seen at submillimetre wavelengths are thought to be excited by either planet-disc interactions (Zhu et al. 2015; Dong et al. 2015b), gravitational instabilities (Dong et al. 2015a) or a combination of both (Pohl et al. 2015) (see Figure1.7(c)).

We have previously discussed the stability of a protoplanetary disc in Section 1.3.4.2. Instabilities in the disc can lead to the formation of spiral arms (Toomre 1964; Boss 1997); these act as a way of transferring angular momentum outward of

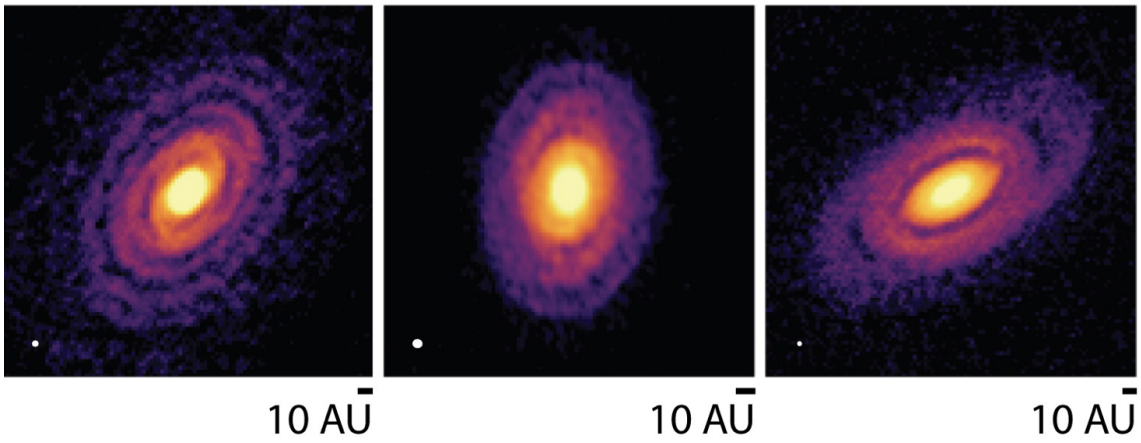

Figure 1.11: Examples of protoplanetary discs featuring spiral arms. All discs have been observed with ALMA and depict the submillimetre continuum emission. The beams are shown in the lower left corners, with a 10 au scale–bar in the lower right. From left to right: IM Lup, Wa Oph 6, and Elias 2–27 (Huang et al. 2018).

the disc. The regions of maximum pressure in the spiral arms lead to the concentration, and subsequent enhanced growth, of drifting dust grains (Rice et al. 2004; Dipierro et al. 2015). For the disc to become gravitationally unstable, it is required to be unusually massive and cool (Toomre 1964; Gammie 2001). Therefore, it is thought that the formation of spiral arms due to gravitational instabilities occurs in very young systems where the discs are sufficiently massive.

Giant planets orbiting a protostar at large disc radii may be able to invoke large-scale arms interior to their orbits (Dong et al. 2015b; Zhu et al. 2015). These planets need to be sufficiently massive in order to cause spiral shocks to form in the disc. The transfer of angular momentum repels material away from the planet's orbit (Lin & Papaloizou 1979, 1986; Goldreich & Tremaine 1980; Baruteau et al. 2014; Dong et al. 2015b), causing dust to be trapped at the pressure maximum formed (Rice et al. 2006; Paardekooper & Mellema 2006; Zhu et al. 2012).

1.5 Thesis Outline

This thesis focusses on the formation and detectability of dust substructures observed in protoplanetary discs using submillimetre continuum observations.

We begin with Chapter 2 where we discuss the observational techniques involved in radio astronomy. We introduce the telescope used to take the protoplanetary disc observations presented in this work, and subsequent data reduction and cleaning processes.

Chapter 3 introduces the computational techniques used here, namely describing the basics of smooth particle hydrodynamic simulations. We follow this by introducing the modelling code utilised in this work and the computational package used to visualise the simulations.

Chapter 4 discusses the dust substructures seen in protoplanetary discs observed using the Atacama Large Millimetre / submillimetre Array (ALMA). We categorise the substructures based on the morphology seen in the dust continuum. We follow this by calculating the stellar masses and ages of the host stars, which we then use to explore trends relating the disc morphology to stellar parameters.

Chapter 5 discusses the modelling of three protoplanetary discs. We aim to determine if substructure can be formed via gravitational instabilities in the disc. The discs modelled have stellar masses of very low, solar, and intermediate mass, and we explore the substructures seen as the disc mass is varied.

We compare synthetic disc observations to actual ALMA observations in Chapter 6. We run synthetic ALMA observations using the disc models and the observational parameters used in the original observation. We then compare the substructures seen in the synthetic observations to the substructures in the original observations. This is done to determine if the substructures formed during protoplanetary disc modelling are representative of the current substructures seen in protoplanetary

discs.

We explore the main findings of this thesis in Chapter 7. We begin by discussing the representativeness of our sample compared with the current disc population. We then explore the dependence of observed substructure with observational resolution. We lastly discuss how accurately the substructure present in protoplanetary discs may be resolved using current observational techniques and how this may affect how protoplanetary discs are modelled.

We conclude with Chapter 8, where we summarise our main findings and explore the various ways in which the work presented in this thesis may be extended.

Chapter 2

Radio Astronomy and Instrumentation

2.1 An Introduction to Radio Astronomy

A radio interferometer is a collection of small radio telescopes that combine the signal they each receive to simulate a large, single, radio telescope dish. In contrast to optical telescopes where the maximum resolution is determined by the diameter of the dish, the limiting factor for the resolution of an interferometer is given by the maximum separation between each radio dish.

Interferometers in radio astronomy use a different frame of reference when viewing celestial objects. The separation between two antenna is given by the baseline length, $\overline{b}$. An individual antenna observing an object with right ascension, x, and declination, y, will point to the object in the direction given by the unit vector $\overline{s}$. The coordinates, $\overline{u}$ and $\overline{v}$ are used to represent the east–west and north–south components of the baseline between two antennae on the Fourier plane. This alternate coordinate space is shown in Figure 2.1.

Processing radio interferometric observations requires many steps. As well as the

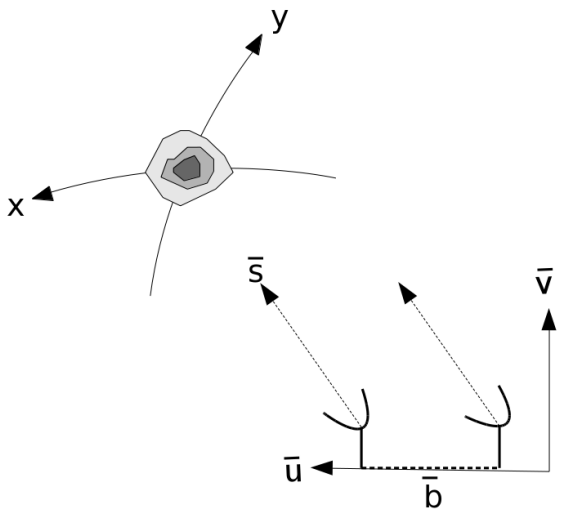

Figure 2.1: The relationship between the (u, v) plane and image plane. $\overline{s}$ is a unit vector in the direction of the source from each antennae. $\overline{b}$ is the baseline length between any two antennae in the array. $\overline{u}$ and $\overline{v}$ represent the east-west and north-south components of the baseline between two antennae.

unit conversion from (u, v) space to real-world coordinates, each antenna measures the Fourier Transform (FT) of the sky brightness distribution. The observations need to be converted into an intensity, with which science can be performed. The signals received are first processed through the front–end and back–end of each antenna. The data are then sent along optical fibres to the correlator, where the signals from each antenna are correlated to produce a product ready to be processed.

An object being observed by the interferometer, in direction $\overline{s}$, will have the intensity, $I(\overline{s})$. Wavefronts from this source will not arrive at each antenna simultaneously due to their separation. Therefore a geometric delay is added to each antenna's signal to ensure the wavefronts received by each antenna are added correctly. This delay is given by

$$\tau_g = \frac{\overline{b} \cdot \overline{s}}{c}\,, \tag{2.1}$$

where c is the speed of light and $\overline{s}$ is a unit vector in the direction of the object (Burke & Graham-Smith 1997). Signals from each antenna are added by the correlator. As the signals from each antenna do not reach the correlator at the same time, there is also an instrumental delay, τ_i, applied to each wavefront.

If we consider a two element array, the signals received by each antenna are outputted as voltages given by

$$V_1 \propto v_1 cos[2\pi\nu(t-\tau_g)] + isin[2\pi\nu(t-\tau_g)]\,, \tag{2.2}$$

$$V_2 \propto v_2 cos[2\pi\nu t] + isin[2\pi\nu t]\,, \tag{2.3}$$

where v_1 and v_2 are the voltage amplitudes, τ_g is the geometric delay, and ν is the frequency of the observations (Rohlfs & Wilson 2000).

The voltages from each antenna are passed through the correlator where they are cross multiplied and time averaged, giving

$$R_c \propto \frac{v_1 v_2}{2} cos[2\pi\nu\tau_g] + isin[2\pi\nu\tau_g]\,, \tag{2.4}$$

For a source of intensity $I(\overline{s})$ observed using antennae of collecting area $A(\overline{s})$, the output of the correlator is given by

$$R = A(\overline{s})I(\overline{s})\{cos[2\pi\nu\tau] + isin[2\pi\nu\tau]\}d\overline{s}d\nu\,, \tag{2.5}$$

where τ is the difference between the geometric and instrumental delays (Rohlfs & Wilson 2000). Integrating over $\overline{s}$, the total response of the correlator is given by:

$$R = \iint_{\overline{s}} A(\overline{s})I(\overline{s})\{cos[2\pi\nu\tau] + isin[2\pi\nu\tau]\}d\overline{s}d\nu\,, \tag{2.6}$$

The field of view of an interferometric observation is centred on the phase tracking centre, $\overline{s_0}$ (Thompson 1989). This is given by

$$\overline{s} = \overline{s_0} + \overline{\sigma}\,, \tag{2.7}$$

Substituting Equation 2.7 into Equation 2.6 and replacing τ_g with Equation 2.1 yields

$$R = exp\Big[i2\pi\nu\Big(\frac{\overline{b}\cdot\overline{s_0}}{c} - \tau_i\Big)\Big]d\nu \iint\limits_{\overline{s}} A(\overline{\sigma})I(\overline{\sigma})exp\Big[i2\pi\nu\Big(\frac{\overline{b}\cdot\overline{\sigma}}{c}\Big)\Big]d\sigma\,, \tag{2.8}$$

where the integral in Equation 2.8 is known as the Complex Visibility function, V (Rohlfs & Wilson 2000).

The van Cittert-Zernike theorem can be used to relate the visibility function measured in (u, v) space to the intensity distribution given in (x, y) space (van Cittert 1934; Zernike 1938). This function is described by

$$V(u,v) = \int\int I(x,y)e^{-2\pi i(ux+vy)}dxdy\,, \tag{2.9}$$

where $I(x, y)$ is the intensity distribution. Therefore, the visibility that an interferometer measures is the Fourier transform of the intensity distribution on the sky.

The visibility is sampled on discrete points on the (u, v) plane. A delta function gives unity to all the sampled positions and zero everywhere else. This function is known as the Sampling Function, $S(u, v)$. The Dirty Image of an interferometer is the Fourier Transform of the Complex Visibility with the Sampling Function. It is given by

$$I^D(x,y) = \int\int V(u,v)\cdot S(u,v)e^{2\pi i(ux+vy)}dudv\,, \tag{2.10}$$

The convolution theorem states that the product of any two FTs is equal to the FT of their convolution. Therefore, the Dirty Image can also be written as

$$I^D(x,y) = S(x,y) \circledast I(x,y), \tag{2.11}$$

where $S(x,y)$ is the FT of the sampling function and is given by

$$S(x,y) = \int\int S(u,v)e^{2\pi i(ux+vy)}dudv\,, \tag{2.12}$$

This is known as the Dirty Beam (Clark 1989). This is analogous to the Point Spread Function for conventional telescopes. In order to measure the intensity distribution of the source, $I(x,y)$ (given by 2.11), the Dirty Beam ($S(x,y)$) needs to be deconvolved from the Dirty Image (outputted by the correlator).

2.2 The Atacama Large Millimetre / submillimetre Array

The Atacama Large Millimetre / submillimetre Array is an interferometer located on the Chajnantor plain of the Chilean Andes (lat. = 23.02917°m long. = -67.754649°). The extremely dry and clear sky conditions are optimal for millimetre and submillimetre interferometry. ALMA operates at a range of frequencies in this regime and is capable of performing continuum, spectral line, and polarimetric observations. The first observations were conducted in 2011 and the telescope became fully operational in 2013.

2.2.1 Arrays

ALMA is made-up of 66 antennae used in two arrays; the 12–m Array and the Atacama Compact Array (also known as the Morita Array). Fifty of the antennae have a diameter of 12–m and are used in the 12–m Array. These allow for sensitive, high-resolution imaging to be conducted. The compact array is comprised of 12

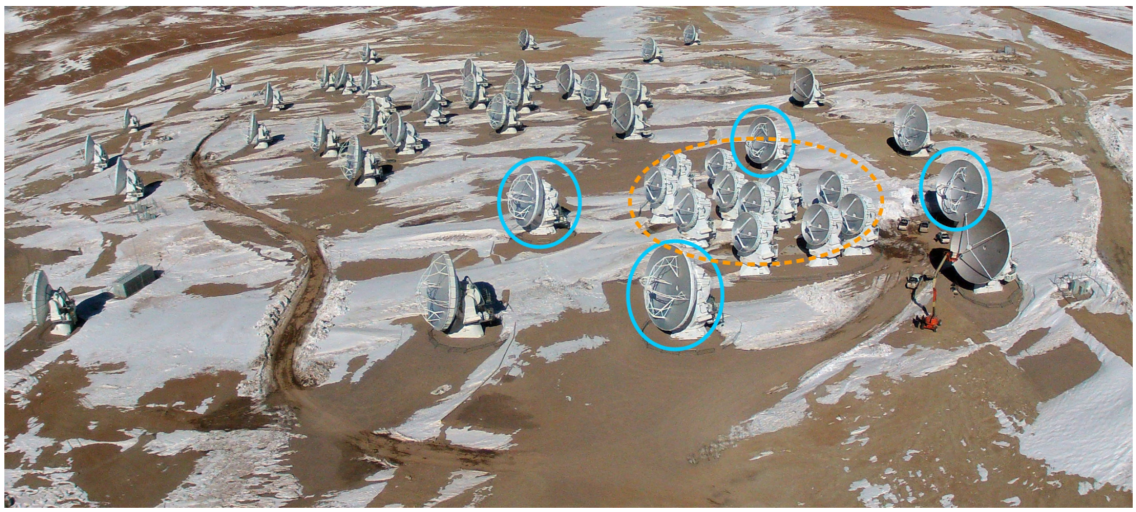

Figure 2.2: The ALMA interferometer, located on the Chajnantor plain of the Chilean Andes. The 50 antennae in the 12–m array are located on the left and are un–circled The 12 7–m dishes in the ALMA Compact Array (within the orange dashed circle) and four single-dish 12–m dishes (blue circles) can be seen on the right (Remijan et al. 2020).

7–m antennae as well as four 12–m antennae. The 7–m dishes are closely spaced, whilst the four 12–m dishes conduct single-dish observations. This is done in order to enhance the wide-field imaging of extended sources. The arrays in the ALMA interferometer are shown in Figure 2.2.

The observations conducted in this work were conducted with the 12–m array. Therefore, we provide further details on this array only.

The 12–m Array consists of 50 antennae; 25 VertexRSI antennae and 25 Alcatel Alenia Space European Industrial Engineering MT Aerospace (AEM) antennae. Figure 2.3 shows the two types of antennae using the 12–m Array. Each type of antenna was built according to strict ALMA antenna performance specifications, and therefore, operate in the same way.

Figure 2.3: The two types of antennae used in the 12–m array. Right shows the VertexRSI antenna whilst left is the AEM antenna. Image adapted from Remijan et al. (2020).

2.2.1.1 Configurations

The ALMA antennae are not fixed in place. Distributed over the Chajnantor and Pampa la Bola plateaus are 192 antenna stations. The antennae can be moved using the two special purpose ALMA antennae transporters. This allows for different array configurations. The location of the stations allow for baselines ranging from 15 m (limited by the size of the antennae) to $\sim$ 16 km. This enables ALMA to produce high quality images with high spatial resolutions.

The desired angular resolution of an observation, indicated by the Principle Investigator PI, dictates the most extended array configuration, whilst the largest angular scale dictates the most compact array. ALMA allows for ten different configurations of the 12–m array; C43-1 to C43-10. The configurations are shown in Figure 2.4. Not all of these configurations may be used during a cycle, nor all of the antennae. This may be due to maintenance of the antennae stations or the antennae themselves.

The different configurations allow for a range of angular resolutions to be achieved. The maximum resolution, as well maximum recoverable scale for each

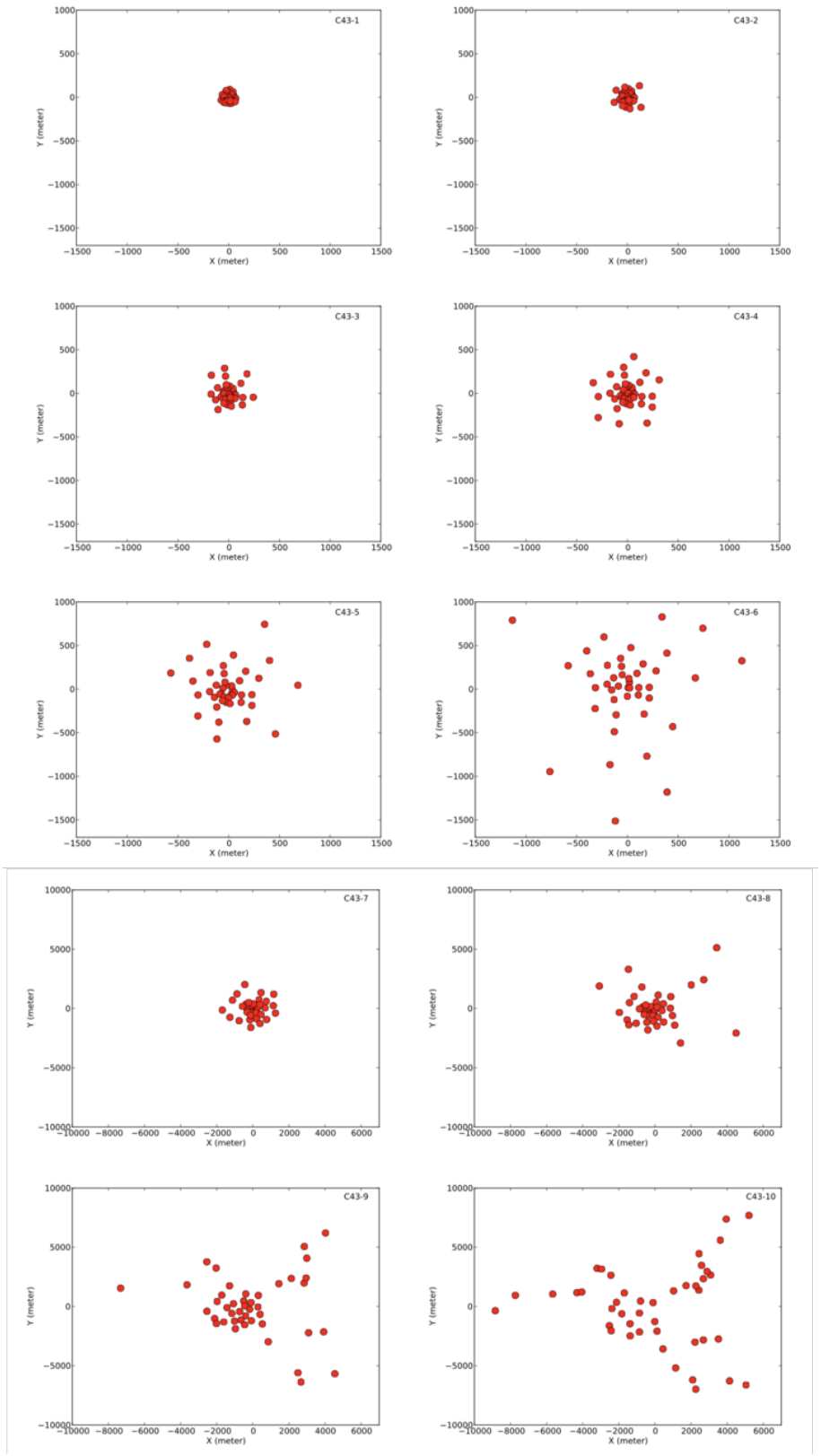

Figure 2.4: The array configurations for the ALMA 12–m array. Not all of these will be available during a cycle (Remijan et al. 2020).

configuration is shown in Table 2.1. The maximum resolution of an interferometer is measured by the longest baseline. However for a more robust measure for the angular resolution, ALMA uses the 80th percentile of the *uv* distances. Similarly, the 5th percentile of the *uv* distances are used to determine the maximum recoverable scale.

2.2.2 Observing with ALMA

Observations from ALMA go through many steps before being science-ready. Signals are first processed at the front–end where they are down converted to intermediate frequencies. They are then fed through the back–end where they are converted into the ALMA digital format (Recoquillon et al. 2005). Finally they are put through the correlator where the signals are transformed into a format that can be used to produce a science usable image (see Section 2.1). Figure 2.5 outlines the stages involved in making an ALMA observation. Below we discuss each of these steps in more detail.

2.2.2.1 Receivers

The front–end of each antenna contains a cryostat, water vapour radiometer (WVR), and amplitude calibration device (ACD). It also contains up to 10 receiver bands operating at a range of frequencies. We outline the role of each below:

Cryostat : The role of the cryostat is to keep the receivers at extremely cold temperatures ($\sim$ 4 K). The cryostat can hold up to 10 receiver bands; each covering one of the ALMA observing frequency bands. ALMA only observes at one band at any one time, however three receivers can be switched on simultaneously.

WVR : The resolutions of millimetre and submillimetre observations are limited by atmospheric fluctuations caused by water vapour. Although ALMA is located in an area with exceptionally dry conditions, phase fluctuations still need to be

Table 2.1: Angular resolutions (θ_{res}) and maximum recoverable scale (θ_{MRS}) for the ALMA 12–m array configurations, in each frequency band. All values are given in arcseconds.

Config. ↓	Band →	3	4	5	6	7	8	9	10
C43-1	θ_{res}	3.83	2.25	1.83	1.47	0.98	0.735	0.52	0.389
	θ_{MRS}	28.5	19.0	15.4	12.4	8.25	6.19	4.38	3.27
C43-2	θ_{res}	2.30	1.53	1.24	0.99	0.66	0.499	0.353	0.264
	θ_{MRS}	22.6	15.0	12.2	9.81	6.54	4.9	3.47	2.59
C43-3	θ_{res}	1.42	0.943	0.765	0.615	0.41	0.308	0.218	0.163
	θ_{MRS}	16.2	10.8	8.73	7.02	4.68	3.51	2.48	1.86
C43-4	θ_{res}	0.918	0.612	0.496	0.399	0.266	0.2	0.141	0.106
	θ_{MRS}	11.2	7.5	6.08	4.89	3.26	2.44	1.73	1.29
C43-5	θ_{res}	0.545	0.363	0.295	0.237	0.158	0.118	0.0838	0.0626
	θ_{MRS}	6.7	4.47	3.62	2.91	1.94	1.46	1.03	0.77
C43-6	θ_{res}	0.306	0.204	0.165	0.133	0.0887	0.0665	0.0471	0.0352
	θ_{MRS}	4.11	2.74	2.22	1.78	1.19	0.892	0.632	0.472
C43-7	θ_{res}	0.211	0.141	0.114	0.0917	0.0612	0.0459	0.0325	0.0243
	θ_{MRS}	2.58	1.72	1.4	1.12	0.749	0.562	0.398	0.297
C43-8	θ_{res}	0.096	0.064	0.0519	0.0417	0.0278	-	-	-
	θ_{MRS}	1.42	0.974	0.768	0.618	0.412	-	-	-
C43-9	θ_{res}	0.057	0.038	0.0308	0.0248	0.0165	-	-	-
	θ_{MRS}	0.814	0.543	0.44	0.354	0.236	-	-	-
C43-10	θ_{res}	0.042	0.028	0.0227	0.0183	0.0122	-	-	-
	θ_{MRS}	0.496	0.331	0.268	0.216	0.144	-	-	-

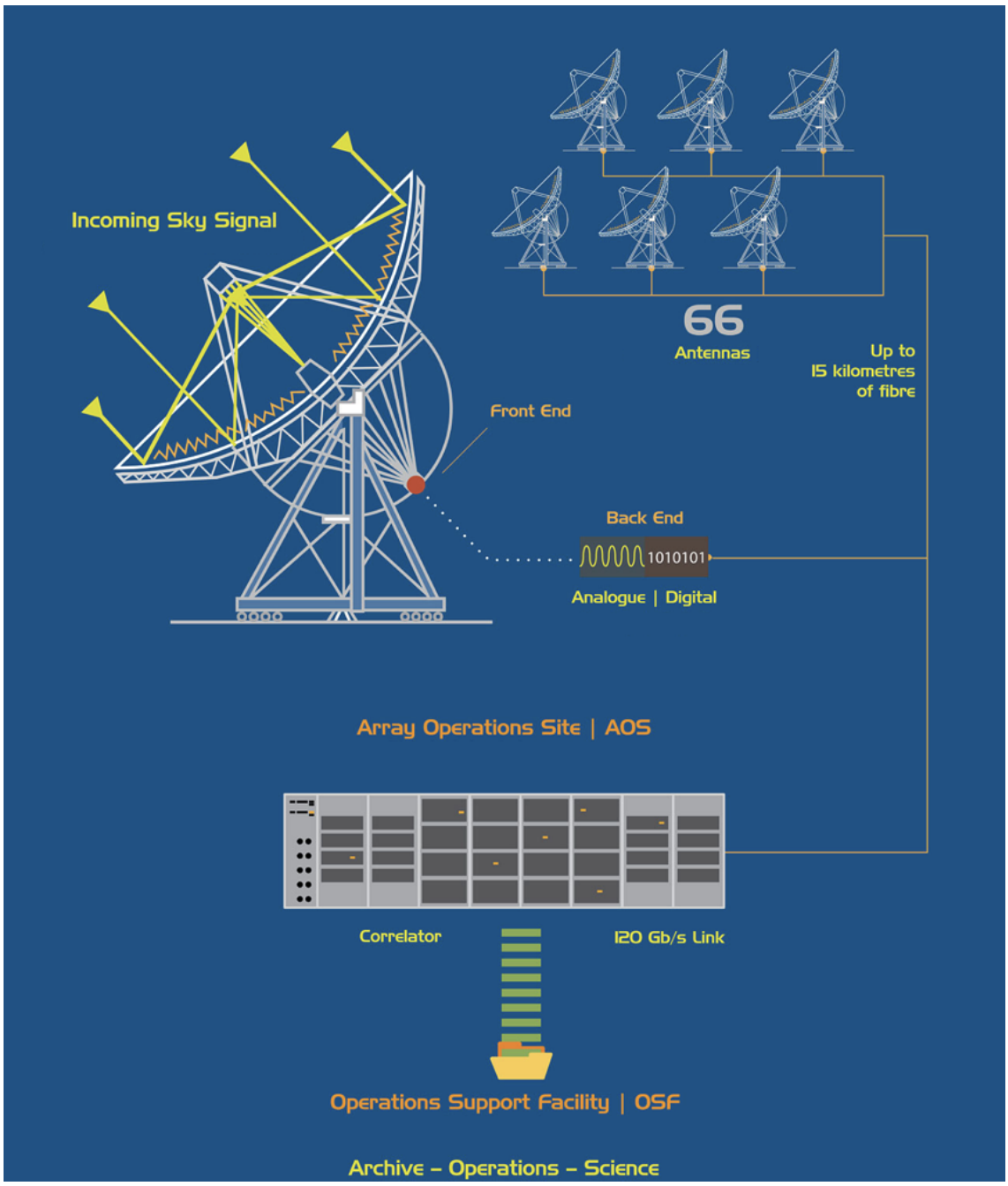

Figure 2.5: A schematic diagram showing how the signals received by ALMA are processed. The signals are first processed at the front–end and are then digitised at the back–end. They are transmitted towards the Array Operations Site Technical Building where they are then fed through the correlator (ESO 2015). The data are then sent to the Operations Support Facility to be quality checked and archived. Image credit : ESO (2015).

corrected. The water vapour radiometer on each antenna is used for this.

Amplitude calibration device : The ACD is used to measure the receiver temperature and sky emission. This is done by comparing the signals on the sky to cold and hot loads. To calibrate the observations to a temperature scale, the brightness of the two loads have to be known.

Receiver bands : Each antenna can hold up to 10 receiver bands operating at different wavelengths. Each ALMA observing band covers a range of frequencies, each tailored to where the transmission from the atmosphere is the greatest. Figure 2.6 shows the frequency range for each observing band.

The deep, broad, absorption features, seen in Figure 2.6, are due to H_2O in the atmosphere, as well as O_2. The narrower, shallow features are due to O_3 in the stratosphere, transitions of CO, and other absorption lines. The bands have been strategically placed to allow for the greatest transmission as well as to allow for spectral line observations to be made.

To date, eight out of the ten proposed observing bands are operational on each antenna; bands 3-10. Band 1 receivers are currently under construction, whilst band 2 receivers may be added in the future. We outline the frequency range for each band in Table 2.2.

2.2.2.2 The Back–End

The signals produced by the front–end electronics of the antenna are analogue signals. Before they can be passed to the correlator, they have to be digitised. This is done through the back–end of the antenna.

The Data Transmission System in each antenna first digitises the frequency signals from the front–end. This converts them to a format that can be transmitted along an optical fibre. The data are sent to the Array Operations Site Technical Building, where they are converted to electrical signals (Baudry et al. 2006). The

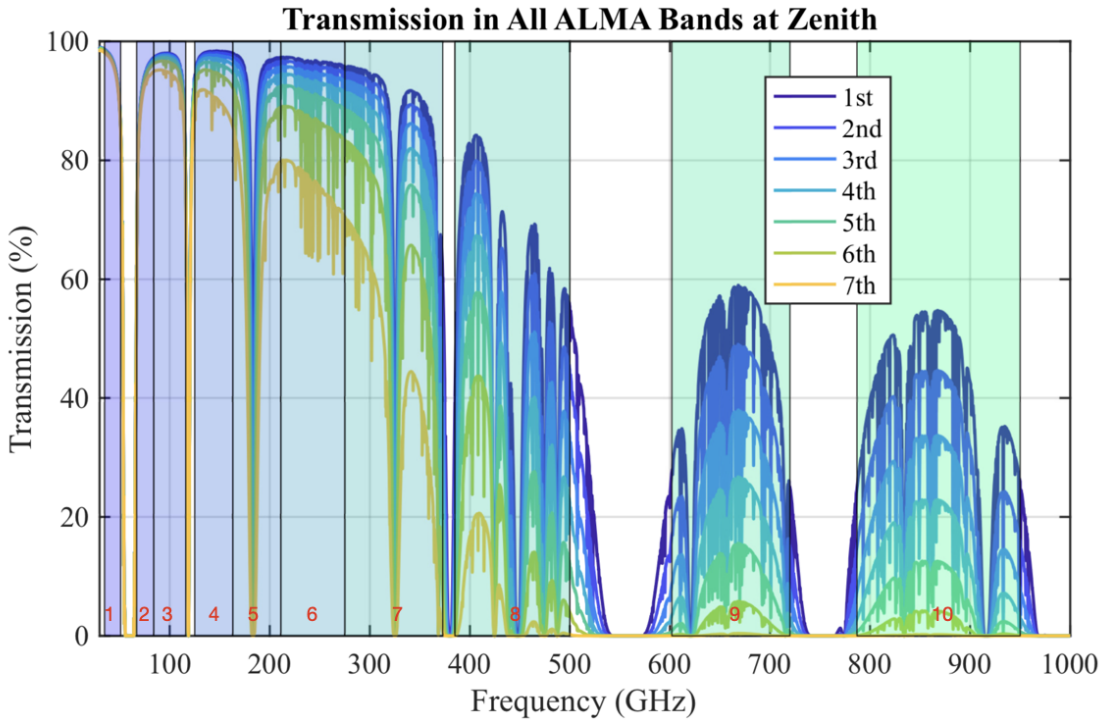

Figure 2.6: The atmospheric transmission measured at zenith at the Array Operation Site for the first seven octiles of observing conditions at ALMA. The best observing condition, where the principle water vapour is the lowest, is the first octile. The 7th octile is the transmission in the worst ALMA observing condition. The frequency coverage for each of the ten receiver bands is shown as a shaded box and is indicated, by red, at the bottom of the plot (Remijan et al. 2020).

Table 2.2: Frequency and wavelength ranges of ALMA receiver bands. To date, only bands 3-10 are operational.

Band	Frequency Range (GHz)	Wavelength Range (mm)
1	35 - 50	6.0 - 8.5
2	67 - 91	3.3 - 4.5
3	84 - 116	2.6 - 3.6
4	125 - 163	1.8 - 2.4
5	158 - 211	1.4 - 1.9
6	211 - 275	1.1 - 1.4
7	275 - 373	0.80 - 1.1
8	385 - 500	0.6 - 0.8
9	602 - 720	0.4 - 0.5
10	787 - 950	0.32 - 0.38

Figure 2.7: The ALMA 64-input Correlator used by the 12–m array. This is located in the ALMA Array Operations Site Technical Building. Image credit : ALMA (ESO/NAOJ/NRAO), S. Argandoña.

signals are now ready to be processed by the ALMA correlator.

2.2.2.3 Correlator

The data from the 12–m array are processed by the 64-input Correlator (also known as the Baseline Correlator), shown in Figure 2.7. The correlator receives the voltage-based signals from each individual antenna, where, first, a delay is applied to the signals. This is to account for the difference in arrival time of wavefronts from different antennae. The correlator then multiplies and averages the voltage signals to produce what is known as the Dirty Image. In order to obtain the sky distribution, the Dirty Beam needs to be deconvolved from the Dirty Image (see Section 2.1).

2.2.3 Calibrating and Imaging ALMA Data

The process of calibrating and imaging an ALMA dataset is outlined in Figure 2.8. Calibration and imaging of radio astronomy data is typically performed in the *Python*-based *Common Astronomy Software Applications* (`CASA`) package (Jaeger 2008). All data in this work were calibrated and imaged using `CASA`.

2.2.3.1 Calibrating ALMA Data

The response of an antenna to an incoming radio signal may not be perfect. Therefore, before deconvolution of the Dirty Image can be performed, the data need to be calibrated. There are several steps that need to be performed; including:

- Primary Calibration
- Initial Calibration
- Phase Calibration
- Delay Calibration
- Bandpass Calibration
- Flux Calibration
- Gain Calibration

Primary Calibration : The antennae measure the sky brightness distribution in units of *Kelvin*. This, however, needs to be converted into science–usable units of *Jansky*. To convert the data to an accurate temperature scale, the data first need to be calibrated in the front–end. The amplitude calibration device corrects for any differences in the atmospheric transmission between the target source and the amplitude calibrators (for which the sky brightness distribution is known). The

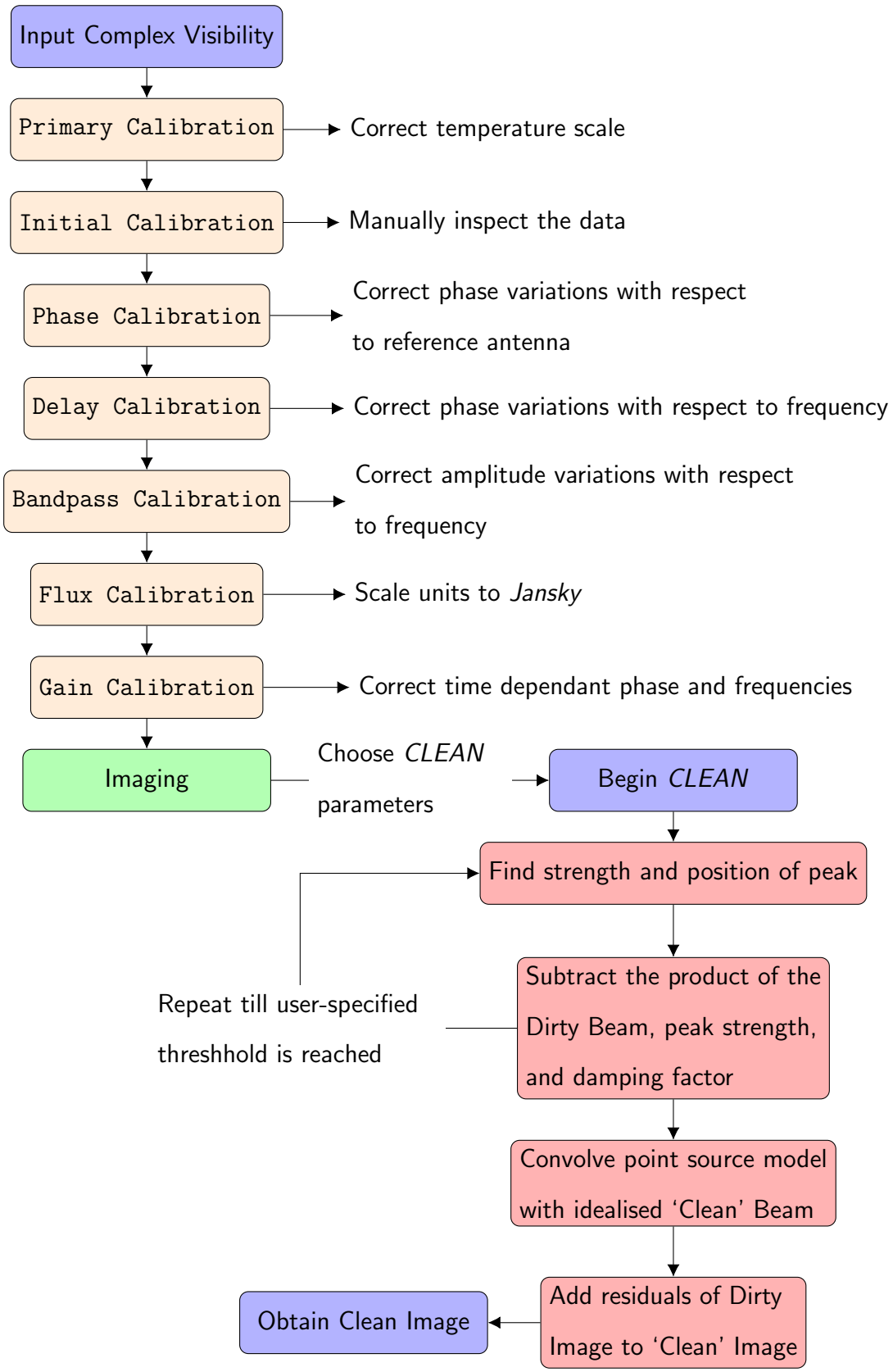

Figure 2.8: The steps needed to calibrate and image an ALMA dataset.

calibrated data will later be scaled to units of *Jansky* during the flux calibration step.

Initial Calibration : The data are then manually inspected and edited. This is done to remove any obvious bad data caused by individual antennae, baselines, or frequencies.

The first time-steps from the data are removed to account for any initial pointing delays. This is also known as *quacking*. Time-steps may also be removed if there were malfunctions in the correlator.

The radio window is also allocated to services other than radio astronomy; this includes aeroplane communications, satellite downlink, and digital broadcasts. Interference from these sources may also affect the observations, reducing the sensitivity of the image. Therefore, individual antennae, time-steps, frequencies, and baselines may need to be removed.

Data from an individual antenna may need to be removed if the antenna itself was broken. A shadow caused by one antenna may affect the performance of another. Therefore, data from the antenna located in a shadow would have to be removed for the time range its performance is affected. The removal of an individual antenna will, however, reduce the sensitivity of the observation.

Phase Calibration : A reference antenna is chosen for each observation, for which the phase is set to zero at all times over a set of frequency channels. Phase calibration involves correcting any phase differences between each antennae and the reference antenna.

Delay Calibration : Interferometers operate over large bandwidths. The phase response of an antenna may not always be constant over the frequency range. Therefore, delay calibration needs to be done. As well as this, inaccuracies in the positions of each antenna will cause the phase to vary as a function of frequency. To correct for this, observations of an isolated, point source are needed to determine

the phase slope with regards to frequency.

Bandpass Calibration : Each antenna will have a different amplitude and phase response to incoming radio signals. Therefore bandpass calibration is performed to correct any errors that occur in the amplitude with respect to the frequency. A bright point source will need to be observed in order to perform bandpass calibrations.

Flux Calibration : Flux calibration is needed to scale the measured amplitudes and convert the signals to conventional units such as Janskys (1 Jy = $10^{-26}\mathrm{Wm}^{-2}\mathrm{Hz}^{-1}$). A point source, with a known flux density, will need to be observed. The relative amplitudes from the interferometer can then be converted to absolute amplitudes.

Gain Calibration : The antenna response can be affected by the atmosphere as well as by the instrument themselves. Gain calibration is performed to correct any errors in the time dependant phase and frequencies. Observations of a source close to the target, with a known structure and moderate intensity, need to be made frequently. This will allow the determination of atmospheric phase changes to the line of sight of the target. An example of gain calibration targets include quasars and planets.

The response of an antenna may also be affected by several factors such as opacity of the atmosphere and aperture illumination. Therefore, all of the calibration targets need to be located close to the target source.

Once the data has been calibrated, the deconvolution of the Dirty Beam from the Dirty Image, (in order to obtain the intensity distribution of the source) can be performed. This is done using the *CLEAN* algorithm in `CASA`.

2.2.3.2 *CLEAN*

The *CLEAN* algorithm was first introduced by Jan Högbom in 1974 (Högbom 1974). Its purpose is to perform the deconvolution of images made in radio astronomy observations. Although variations have been proposed since then (Clark 1980; Schwab 1984), the method developed by Högbom (1974) is still widely used today.

To deconvolve the Dirty Image, interpolation or reconstruction of missing values in the (u, v) plane need to be made. The *CLEAN* algorithm assumes the sky is made up of a series of point sources. It first finds the brightest pixel in the Dirty Image and measures its brightness and position. The next step involves subtracting the product of the Dirty Beam, peak brightness, and damping factor, from the Dirty Image, at the position of the peak. The damping factor, γ, is usually ≤ 1 and is called the *loop gain*.

These steps are repeated until the remaining peaks are below some user-specified level. The accumulated point source models are then convolved with an idealised 'Clean Beam'. The residuals of the Dirty Image are then re-added to the Clean Image. These steps are outlined in Figure 2.8.

This process can be conjectural as the 'Cleaning' is often done manually. Under-cleaning results in not recovering all the source flux. Whereas, over-cleaning will result in some 'clean components' being, in fact, noise.

The nature of radio interferometry is such that the resolution of the image is based upon the baseline length between any two antennae. Therefore, a large baseline resolves small structures, whereas small baselines resolve extended emission. Depending on the aim of the observation, a *uv*-taper can be applied to the image during the 'Cleaning' process. This changes the *uv*-range of the visibilities or applies an outer *uv*-taper. This allows the observers to increase the sensitivity to either extended or small sources.

The Clean Image can be improved by adding a data weighting during the Cleaning process. A weight is given to each visibility sample depending on the desired output. This can be done to improve the spatial resolution and/or sensitivity of the image. The three most common weightings are the Uniform, Natural, and Briggs weighting. We outline the characteristics of each in Table 2.3.

2.2.4 The ALMA Archive

The ALMA Science Archive contains all the propriety and public data of Principal Investigator proposal observations. Proposals are divided into two project types; regular and large. All data have a propriety period of 12 months, after which they are publicly available. The archival data for a publicly available program includes a number of directories, the contents of which are as follows :

- The 'calibration' directory containing the calibration tables.
- The 'log' directory contains the `CASA` log files from running the calibration scripts.
- The 'products' directory contains the final Flexible Image Transport System (FITS) images.
- The 'qa' directory contains the Quality Assurance 2 (QA2) reports.
- The 'script' directory contains the calibration and imaging scripts used to process the raw data into the final FITS products.
- The 'raw' directory contains the raw data.
- The 'calibrated' directory contains the raw data after calibration has been performed.

Table 2.3: The data weightings that can be applied when cleaning radio data using the *CLEAN* algorithm.

	Uniform	Briggs	Natural
Weightings	The weights are calculated as in the 'Natural' weighting. The data is then gridded to a number of *uv*-cells and re-weighted to have a 'Uniform' weighting	Parametrised by the *Robust* parameter, where the value of *Robust*=0 results in a good trade-off between sensitivity and resolution	Weighted only by data weights, given by the inverse noise variance on the visibility.
Benefit	High Resolution	Good sensitivity and resolution	High sensitivity
Limitation	High Noise	May result in unresolved and faint emission	Low Resolution
Robust Parameter	-2	0	2

All processed ALMA data, available in the archive, have been through a Quality Assurance process. The aim of this process is to ensure that the data-products in the archive are 'Science Ready' (Stoehr et al. 2020), with very little need for reprocessing. The products are processed to meet the expected quality standards outlined, by the PI, in the science goals of the project proposal.

The data go through three Quality Assurance steps, QA0-2, which we outline below in Section 2.2.4.1. All archival data are QA2 approved.

2.2.4.1 Quality Assurance Process

QA0 : The first stage of the Quality Assurance process takes place during, and just after, an observation. The calibration and overall performance of the observations are monitored. These checks are done in real time by the astronomer on duty at the time of the observation.

The signal received by each antenna is studied for errors; from its path from the atmosphere, to its input into the correlator. The observations are checked and corrected for atmospheric effects as well as front–end, antenna, connectivity, correlator, and observation issues. These are outlined further in Table 2.4.

After accounting for the issues outlined in Table 2.4 for QA0, the data are classified as either; Pass, Semi–pass or Fail. These are the same resulting categories for QA1 and QA2. Fail datasets are those that have unusable data and are deemed as being of no scientific value. They are not made available to PIs. Semi–pass datasets are those that contain some issues but may have some scientific value. They are not used to produce final data products, however they are still available to the PI in the ALMA Archive. Pass QA0 datasets have no issues remaining and advance to further QA checks.

QA1 : The performance of the array, as well as individual antenna, are tracked during the observations. The performance of these elements can vary very slowly

Table 2.4: The parameters inspected at the Quality Assurance 0 stage of an ALMA observation Remijan et al. (2020). Any errors are flagged and corrected before the data are sent to the QA1 stage.

Parameter	Notes
Atmospheric Effects	Weather parameters, sky opacity, system temperature, phase fluctuations, WVR outputs.
Antenna issues	Antenna delays, shadowing, antenna positions.
front–end issues	Bandpass instability, receiver temperatures, phase variations.
Connectivity issues	System temperatures, unusual relative phase or amplitude variations between spectral windows, interference.
Correlator issues	Bandpass shapes, delays.
Observation issues	Calibrator fluxes, incomplete datasets, incomplete mapping.

(on timescales typically longer than one week) and can affect the quality of the data (Remijan et al. 2020).

The antennae in the array are set to a non–integrated state and are no longer used for science observations. Antenna and array calibrations are then performed. These involve :

- Array calibrations including baseline and antenna position measurements.
- Antenna calibrations including pointing models, beam patterns and front–end delay measurements.
- Source calibrations including the monitoring of standard flux targets.

Similar to the QA0 process, the data are classified according to three categories: Pass, Semi–pass, or Fail. If the antenna and array calibrations result in no issues and the quality of the science observations are not affected, they Pass (or Semi–pass) the QA1 stage and proceed to the QA2 stage.

QA2 : The ALMA data are then ready to be calibrated and imaged. During this process various issues and parameters are checked to ensure they meet the QA2 standards and are fit to be sent to the PI.

Calibration issues, such as the bandpass quality are checked. The quality of the flux scale calibration are also checked to make sure that the flux accuracy is better than 5% for Bands 3,4 and 5; 10% for Bands 6,7 and 8; and 20% for Bands 9 and 10 (Stoehr et al. 2020).

The noise Root Mean Square (RMS) of the target images are checked to ensure the level is of a comparable scale to the level requested by the PI. The spatial resolution is also checked to ensure it meets the science requirements for the goals of the project. Other parameters such as *uv*-coverage, time on target, and contamination of the target by bright objects outside the field-of-view are also used to assess the quality of the data.

Chapter 3

Computational Methods

3.1 Smooth Particle Hydrodynamics

The processes of star and planet formation are dictated by equations of fluid dynamics. Smooth Particle Hydrodynamics (SPH henceforth) is a Lagrangian method that can be utilised to solve these equations.

First developed by Gingold & Monaghan (1977) and Lucy (1977), this method assumes that the fluid is represented by a number of particles. These are interpolation points known as SPH particles which follow the properties of the fluid. An SPH particle represents a small portion of the fluid, and is smoothed over a scale size, h, and a weighting function, $W(r, h)$. These are referred to as the smoothing length and smoothing function, respectively.

A particle i interacts hydrodynamically with all the other SPH particles that lie inside a length of $2h$. These particles are referred to as the neighbours of i.

The number of neighbours is usually set to $\approx$50. Although increasing the number of neighbours can lead to a more accurate estimate for the density distribution, particles have been shown to form pairs when the number of neighbours increase >55–58 (Dehnen & Aly 2012; Price 2012). Similarly, a low level of neighbours results in an inaccurate density estimate. Therefore, using $\approx$50 neighbours allows for a good

compromise between an accurate density estimate and the pairing instability.

As the spatial resolution is determined by the smoothing length, a sphere containing 50 particles is found. The radius of this sphere is then taken to be $2h$. The changing radius of this sphere allows for the resolution to automatically adapt to the local conditions. The smoothing function determines the shape for the interpolation approximation of the SPH particles as well as the width of their influencing area. It is often taken to be a cubic spline and is used when calculating the density of an SPH particle. This density is given by

$$\rho_i = \sum_{j=1}^{N} m_i W(r_{ij}, h_i), \tag{3.1}$$

where $r_{ij} \equiv r_i - r_j$, and the summation includes particle i itself. This equation also represents the continuity equation for SPH. We can take the spatial derivative of Equation 3.1 to give

$$\frac{\partial \rho_i}{\partial r_i} = \sum_{j=1}^{N} m_j \nabla_i W(r_{ij}, h). \tag{3.2}$$

We have made the substitution of $r_{ij} = r_i - r_j$ and $\nabla_i = \partial / \partial r_i$.

The Euler-Lagrange equations are used to derive the SPH fluid equations. This is to ensure conservation of energy, momentum, and angular momentum. Using the continuity equation above, the basic forms of the SPH momentum and energy equations are given by

$$\frac{\mathrm{d}\nu_i}{\mathrm{d}t} = -\sum_{j=1}^{N} m_j \left(\frac{P_i}{\rho_i^2} + \frac{P_j}{\rho_j^2} \right) \nabla W(r_{ij}, h), \tag{3.3}$$

and

$$\frac{\mathrm{d}u_i}{\mathrm{d}t} = \frac{P_i}{\rho_i^2} \sum_{j=1}^{N} m_j \nu_{ij} \cdot \nabla W(r_{ij}, h), \tag{3.4}$$

respectively. The pressure of particle i is given by P_i, whilst $\nabla W(r_{ij}, h)$ is the gradient of the smoothing function at the position of particle i. These forms of the SPH fluid equations do not take into account gravity. They also assume a constant smoothing length and no dissipation.

The method of conducting Smooth Particle Hydrodynamic simulations in this work, and solving the SPH fluid equations, were conducted using the code `SEREN`. Below we introduce this code as well as discuss the features of `SEREN` implemented and utilised in this work.

3.2 SEREN

`SEREN` is a Smooth Particle Hydrodynamic code designed to solve hydrodynamical problems. First devised by Hubber et al. (2011), the numerical code was mainly written to solve problems in star and planet formation, however it can also be used in other branches of astrophysics. The code is available on the source control service, GitHub [1].

3.2.1 Features of SEREN

`SEREN` is designed in a modular style, thus allowing for a number of options to be selected or disabled with relative ease. We now describe the features of `SEREN` utilised in the simulations run in this work.

[1] `SEREN` available at `https://github.com/dhubber/seren`.

3.2.1.1 ∇h SPH

A particle in a dense area would have a small smoothing length. As it moves to a less dense area, neighbouring particles may not be captured within its small area of influence. Therefore a constant smoothing length is not suitable for systems which have a large density range. A variable smoothing length for each particle allows the resolution of the simulation to be increased (Hernquist & Katz 1989; Benz 1990).

The smoothing length in `SEREN` is set to be a function of the SPH particle density (Springel & Hernquist 2002; Price & Monaghan 2004) and is given by

$$h_i = \eta \left(\frac{m_i}{\rho_i} \right)^{\frac{1}{D}}, \tag{3.5}$$

where m_i is the mass of particle i, ρ_i is the SPH density at the position of particle i, D is the spatial dimensionality, and η is a parameter that controls the mean number of neighbours. We can see from Equations 3.5 and 3.1 that the smoothing length and density are dependant on each other. Therefore, h_i and ρ_i are calculated iteratively in `SEREN`.

The temporal variability of the smoothing length is given by

$$\frac{\mathrm{d}h_i}{\mathrm{d}t} = -\frac{h_i}{\rho_i D} \frac{\mathrm{d}\rho_i}{\mathrm{d}t}. \tag{3.6}$$

This can be used to calculate the Lagrangian time derivative of the density function (given by Equation 3.1) which results in

$$\frac{\mathrm{d}\rho_i}{\mathrm{d}t} = \frac{1}{\Omega_i} \sum_{j=1}^{N} m_j \nu_{ij} \cdot \nabla_i W(r_{ij}, h_i). \tag{3.7}$$

The factor Ω_i has the form

$$\Omega_i = 1 - \frac{\partial h_i}{\partial \rho_i} \sum_{j=1}^{N} m_j \frac{\partial W_{ij}}{\partial h_i}(r_{ij}, h_i). \tag{3.8}$$

This is a dimensionless quantity that corrects for the spatial variability of h.

Equation 3.7 can then be used to derive the momentum and energy SPH equations taking into account the variability of the smoothing length. These equations were derived by Springel & Hernquist (2002) and are the following

$$\frac{\mathrm{d}\nu_i}{\mathrm{d}t} = -\sum_{j=1}^{N} m_j \left(\frac{P_i}{\Omega_i \rho_i^2} \nabla_i W(r_{ij}, h_i) + \frac{P_j}{\Omega_j \rho_j^2} \nabla_i W(r_{ij}, h_i) \right), \tag{3.9}$$

and

$$\frac{\mathrm{d}u_i}{\mathrm{d}t} = \frac{P_i}{\Omega_i \rho_i^2} \sum_{j=1}^{N} m_j \nu_{ij} \cdot \nabla W(r_{ij}, h). \tag{3.10}$$

3.2.1.2 Kernel-Softened Gravity

Gravitational accelerations are required in SPH simulations. When two SPH particles get close together their mutual gravity forces may become very large. To avoid this situation the gravity is 'softened', i.e. the mass of each particle is considered to be distributed within $2h$.

The gravitational forces of the SPH particles are smoothed over in a similar manner to that in which the discrete particle masses are smoothed into a continuous density function. Thus, the continuous gravitational potential of the SPH particles are given by Poisson's equation

$$\nabla^2 \Phi = 4\pi G \rho \tag{3.11}$$

We invoke the kernel-softened gravity in SEREN, which utilises the equations of self-gravitating SPH derived by Price & Monaghan (2007). The authors introduce two new smoothing functions similar to the density smoothing function, $W(r,h)$. The gravitational acceleration function, ϕ', and gravitational potential function, ϕ, are given by

$$\phi'(r,h) = \frac{4\pi}{r^2}\int_0^r W(r',h)r'^2 dr', \tag{3.12}$$

and

$$\begin{aligned}\phi(r,h) = 4\pi\Bigg(&-\frac{1}{r}\int_0^r W(r',h)r'^2 dr' + \int_0^r W(r',h)r' dr' \\ &- \int_0^{\mathcal{R}h} W(r',h)r' dr'\Bigg)\end{aligned} \tag{3.13}$$

respectively. The integral limit of $\mathcal{R}h$ defines the extent of the smoothing function, $W(r',h)$. Here we have used the M4 cubic spline function with $\mathcal{R} = 2$ (Monaghan & Lattanzio 1985) .

Using these two functions for gravitational acceleration and potential, Price & Monaghan (2007) were able to show that the momentum equation taking into account gravity is given by

$$\begin{aligned}\left.\frac{\mathrm{d}\nu_i}{\mathrm{d}t}\right|_{grav} = &-G\sum_{j=1}^{N} m_j \frac{\phi'(r_{ij},h_i) + \phi'(r_{ij},h_j)}{2}\hat{r}_{ij} \\ &-\frac{G}{2}\sum_{j=1}^{N} m_j\left[\frac{\xi_i}{\Omega_i}\nabla_i W(r_{ij},h_i) + \frac{\xi_j}{\Omega_j}\nabla_i W(r_{ij},h_j)\right].\end{aligned} \tag{3.14}$$

This form of the SPH momentum equation takes into account both the adaptive

smoothing lengths (see Section 3.2.1.1) and gravitational acceleration. The factor ξ is similar to that of Ω (see Equation 3.8) in that it is a dimensionless parameter to account for the spatial variability of h. It is given by

$$\xi_i = \frac{\partial h_i}{\partial \rho_i} \sum_{j=1}^{N} m_j \frac{\partial \phi_{ij}}{\partial h_i}(r_{ij}, h_i). \tag{3.15}$$

The gravitational potential at the position of particle i due to all other particles is given by

$$\Phi_i = G \sum_{j=1}^{N} m_j \frac{\phi(r_{ij}, h_i) + \phi(r_{ij}, h_j)}{2}. \tag{3.16}$$

3.2.1.3 Artificial Viscosity

Viscosity in SPH simulations is responsible for converting kinetic energy to heat. Converging particle streams need to form a contact discontinuity rather than interpenetrating as this may cause the conversion from kinetic energy to heat to be represented incorrectly. To do this, artificial viscosity is utilised in `SEREN`. This modifies the momentum and energy SPH equations to

$$\left.\frac{\mathrm{d}\nu_i}{\mathrm{d}t}\right|_{visc} = -\sum_{j=1}^{N} m_j \Pi_{ij} \nabla_i W(r_{ij}, h_i), \tag{3.17}$$

and

$$\left.\frac{\mathrm{d}u_i}{\mathrm{d}t}\right|_{visc} = \sum_{j=1}^{N} m_j \Pi_{ij} \nu_{ij} \cdot \nabla_i W(r_{ij}, h_i), \tag{3.18}$$

respectively.

We invoke the standard (α, β) formulation (Monaghan & Gingold 1983) for artificial viscosity, where the artificial viscosity term, Π_{ij}, is given by

$$\Pi_{ij} = \frac{-\alpha \bar{c}_{s,ij} \mu_{ij} + \beta \mu_{ij}^2}{\bar{\rho_{ij}}}. \tag{3.19}$$

In the equation above, α and β are dimensionless viscosity terms, $\bar{\rho_{ij}} = \frac{1}{2}(\rho_i + \rho_j)$, and $\bar{c}_{s,ij} = \frac{1}{2}(c_{s,i} + c_{s,j})$, where c_s is the isothermal sound speed. The parameter μ_{ij} is given by

$$\mu_{ij} = \begin{cases} \frac{h_i \nu_{ij} \cdot r_{ij}}{|r_{ij}|}, & \text{if } \nu_i \cdot r_{ij} < 0; \\ 0, & \text{otherwise.} \end{cases} \tag{3.20}$$

This method by Monaghan & Gingold (1983) smears out shocks by modifying the acceleration and heating/cooling rate of the particles. α and β are free parameters controlling the strength of the viscous terms. In this work we invoke α and β values of 1 and 2, respectively.

We use the time-dependant viscosity (Morris & Monaghan 1997). In this method, each particle has its own value of α, which evolves over time (Monaghan 1997).

3.2.1.4 Integration Scheme

To temporally evolve the fluid, an integration scheme needs to be implemented. For the simulations conducted in this thesis, we utilise the 2nd order Runge–Katta integration scheme available in `SEREN`. This scheme calculates the next position of an SPH particle after a chosen timestep, Δt via

$$x_{n+1} = \frac{1}{2}(k_1 + k_2)\Delta t, \tag{3.21}$$

where

$$k_1 = f(t_n, x_n), \tag{3.22}$$

and

$$k_2 = f(t_{n+1}, x_n + k_1 \delta t). \tag{3.23}$$

Each coefficient, k_n, represents a slope estimation.

3.2.1.5 Sink Particles

The gravitational collapse of SPH particles lead to high densities, short smoothing lengths, high accelerations, and short timesteps. This can be computationally unfeasible and therefore considerably slows down the temporal evolution of the simulation.

Following Bate et al. (1995), dense condensations of SPH particles are replaced with sink particles. These particles possess the collective properties of the condensation it represents (i.e. mass, momentum, and position). They do not, however, retain information on the condensation's structure and evolution. They interact gravitationally and radiatively, not hydrodynamically, with other sink and SPH particles. Thus allowing for a longer temporal evolution.

3.2.1.6 Approximate radiative Transfer

We use the radiative cooling scheme available in `SEREN`; based on the work of Stamatellos et al. (2007). Studying the radiative transport of the energy in an SPH simulation can be computationally expensive. Therefore, an estimate is made using underlying assumptions.

The method by Stamatellos et al. (2007) estimates the optical depth for each particle. This is done by using the local opacity and estimating the column density through which the heating and cooling happens. This is then used to obtain an approximate cooling rate, which is used to determine the thermal evolution of the gas. This method includes effects from dust sublimation, ice melting, bound-free,

free-free, and electron scattering interactions.

The opacities are based on the Bell & Lin (1994) parametrisation where

$$\kappa(\rho, T) = \kappa_0 \rho^a T^b \tag{3.24}$$

κ, a, and b are constants that depend upon the species that contribute to the local opacity at a given density and temperature.

The radiation heating/cooling rate of a particle i is set to

$$\left.\frac{\mathrm{d}u_i}{\mathrm{d}t}\right|_{rad} = \frac{4\sigma_{SB}(T_O^4(r_i) - T_i^4)}{\bar{\Sigma}_i^2 \bar{\kappa}_R(\rho_i, T_i) + \kappa_P^{-1}(\rho_i, T_i)}, \tag{3.25}$$

where σ_{SB} is the Stefan-Boltzmann constant and $\bar{\Sigma}_i$ is the mass-weighted mean column density. $\bar{\kappa}_R(\rho, T)$ and κ_P are the pseudo-mean Rosseland- and Planck- mean opacities, respectively (see Stamatellos et al. (2007)). $T_O^4(r_i)$ represents the radiative heating due to the background radiation field with effective temperature $T_O(r_i)$.

3.2.2 SEREN Tests

`SEREN` has been extensively tested and we briefly discuss the results of these tests both with regards to the hydrodynamical and gravitational aspects of the code as well as the tests performed for protoplanetary discs. The following tests, as well as more information about them, can be found on the `SEREN` webpage [2] or Hubber et al. (2011).

3.2.2.1 Adiabatic Sod Shocktube Test

In order to demonstrate that `SEREN` correctly models shocks, the Sod test (Sod 1978) has been carried out. This test is performed using both the ∇h SPH method as well

[2] `SEREN` webpage - `https://dhubber.github.io/seren/seren.html`.

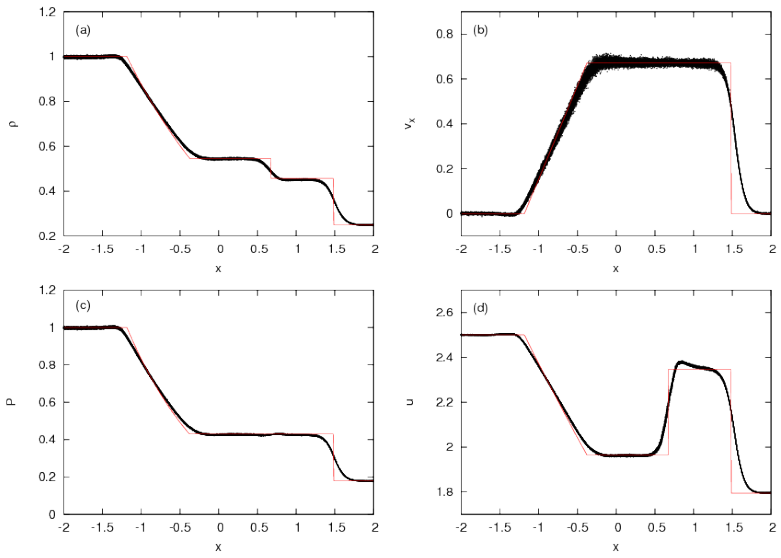

Figure 3.1: Results of the adiabatic Sod shocktube test showing (a) the density, (b) the x-velocity, (c) the thermal pressure, (d) the specific internal energy. The black dots represent the results from the SPH simulation and the red lines show the analytic solutions. Figure from Hubber et al. (2011).

as the standard (α, β) formulation for artificial viscosity (Monaghan & Gingold 1983).

The computational domain is set to $-4 \leq x \leq +4$. The left side of the domain contains a high-density, high-pressure gas represented by 64,000 particles, whilst the right-hand side contains a low-density, low-pressure gas represented by 16,000 particles. The gas is assumed to be adiabatic and the momentum and energy equations are solved.

The results of the test simulation is shown in Figure 3.1, where the density, x-velocity, thermal pressure, and specific internal energy profiles of the SPH particles can be seen (black dots). The plots show the interval between $|x| < 2$. The 1-D analytic solution to the fluid equations can be seen as the red lines. From these plots we can see that `SEREN` reproduces well the analytic solutions to the momentum and energy equations.

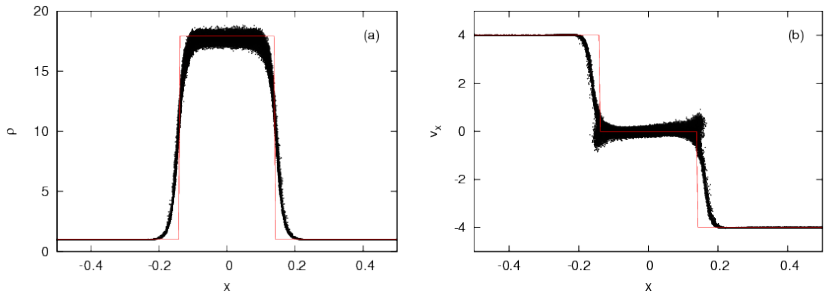

Figure 3.2: Results of the colliding flows shocktube test using time-dependant artificial viscosity (Morris & Monaghan 1997). Figure (a) shows the density and (b) the x-velocity. The black dots represent the results from the SPH simulation and the red lines show the analytic solution. Figure from Hubber et al. (2011).

3.2.2.2 Colliding Flows Shocktube Test

A shocktube test is conducted in order to confirm that the code can correctly model shocks formed by two colliding flows. This is done by confirming that artificial viscosity can effectively suppress particle interpenetration and capture shocks.

The same computational domain used in Section 3.2.2.1 above is utilised for this test. The gas particles in both the right and left side of the computational domain have uniform density, however they have equal but opposite velocities. Artificial viscosity is used in the simulation using the time-dependant variation (Morris & Monaghan 1997). As the gas is isothermal, the energy equation is not solved.

The results of the simulation are shown in Figure 3.2. The SPH density and x-velocity as a function of of position x (black dots), as well as the analytic solution, have been plotted. As we can see from Figure 3.2, the peak density and width of the shock are in agreement with the analytic solution. Thus confirming that `SEREN` can effectively capture shocks.

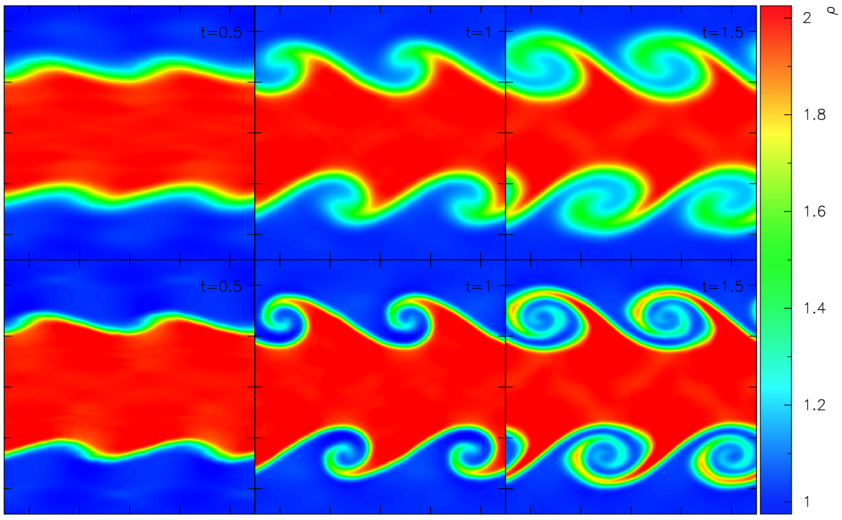

Figure 3.3: Results of the Kelvin-Helmholtz instability test for the low-resolution case (top) and high-resolution case (bottom). The plots show the evolution of the density field (colour-bar on right) at dimensionless times of t= 0.5, 1.0 and 1.5 (left, middle, and right columns respectively). Figure from Hubber et al. (2011).

3.2.2.3 Kelvin-Helmholtz Instability

The Kelvin-Helmholtz instability occurs when there is a velocity difference across the interface between two moving fluids. This results in the two fluids interpenetrating and developing a vortex that mixes the two fluids. `SEREN` has also been tested to determine if the Kelvin-Helmholtz instability is able to form correctly in the simulations.

The computational domain is set with two fluids with a relative velocity between them. The growth of the instability is followed for a total dimensionless time of $t = 1.5$. The simulation is performed at both low (12,242 particles) and high (98,290 particles) resolution. The evolution of the density field at different times can be seen in Figure 3.3. The instability evolves at roughly the same rate in both the low and high-resolution cases and clear vorticity can be seen in the last snapshots of the simulations.

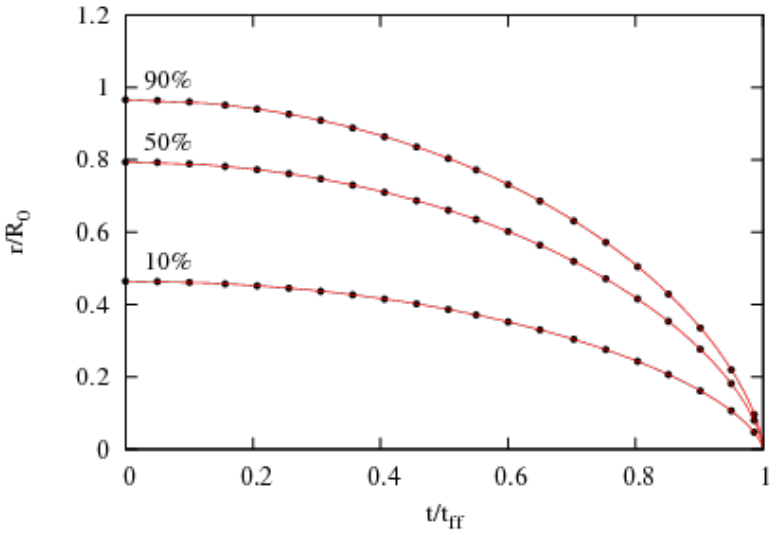

Figure 3.4: Results of the freefall collapse test of a uniform-density sphere. The radial position of three particles at 90%, 50%, and 10% mass radii (dots) as well as the analytic solution (red line) is shown. Figure from Hubber et al. (2011).

3.2.2.4 Freefall Collapse Test

In order to test the accuracy of the gravitational forces, a simulation of the freefall collapse of a uniform-density sphere has been carried out by Hubber et al. (2011).

The test starts with a static, uniform-density sphere with mass M_0, initial radius R_0, and initial density $\rho_0 = 3M_0/4\pi R_0^3$. A shell of the sphere which is initially ($t = 0$) at r_0 collapses, and is at subsequent times at radius, r. The uniform-density sphere is comprised of 100,000 SPH particles and its subsequent evolution is followed. The sphere is expected to homologously collapse to a singularity on a timescale of t_{ff}.

The results from the test are shown in Figure 3.4. The plot compares the 90%, 50%, and 10% of the sphere mass as a function of time (dots). The simulation matches well the analytic solution (red line).

3.2.2.5 Boss-Bodenheimer Test

The Boss-Bodenheimer test (Boss & Bodenheimer 1979) is a standard test used for star formation codes. It investigates the non-axisymmetric collapse and fragmentation of a rotating, self-gravitating gas cloud. The cloud collapses under self-gravity and forms a bar-like structure with dense condensations at each end of the bar.

The simulation starts with a uniform-density sphere (comprised of 50,000 SPH particles) of total mass $M = 1.0\mathrm{M}_{\odot}$, radius $R = 3.2 \times 10^{16}$ cm, and density $\rho_0 = 1.44\times10^{-17}$ g cm^{-3}. A sinusoidal, azimuthal density perturbation is added and the simulation is run for a total of $t = 100$ kyr.

The gas initially collapses under self-gravity to form a thin 'bar' with two dense condensations at either end. The dense concentrations of gas are able to collapse further to form two sinks. This occurs when the density reaches $\rho_{sink}=2\times10^{-12}$g cm^{-3} and is shown in Figure 3.5(a). The gas surrounding the sinks still retain some angular momentum relative to the sinks and form two discs which are connected together by the bar (Figure 3.5) The two sinks continue to follow eccentric orbits. The continual close encounters lead to more mass loading onto the discs - from both the surrounding gas and the bar (Figure 3.5(c)). This leads to a period of rapid accretion, followed by a quiet period. As the sinks move towards apastron, the accretion rate drops off.

3.2.2.6 SEREN Code Comparison

`SEREN` has been specifically designed for star and planet formation problems using smooth particle hydrodynamics. However, other codes (both SPH and not) have also been used to simulate protoplanetary discs and the process of star and planet formation.

A recent study by Fletcher et al. (2019) compared seven codes that have previously been used in star and planet formation studies. Five SPH codes - `PHANTOM`

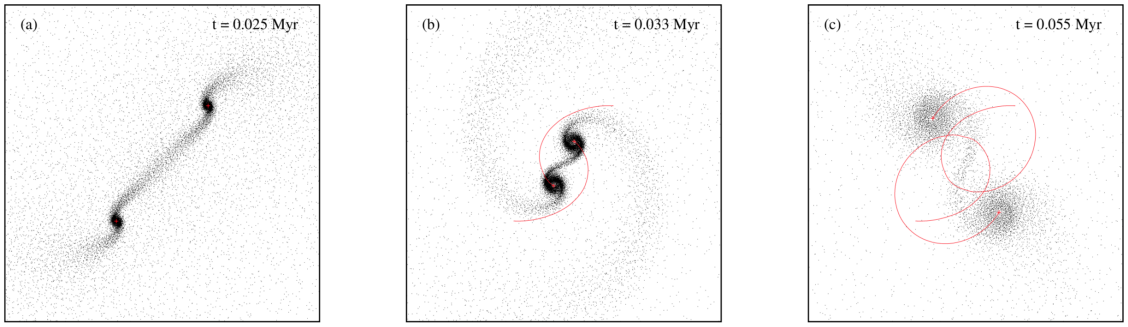

Figure 3.5: Results of the Boss-Bodenheimer test showing the SPH and sink particle plots at times of (a)t =0.025 Myr, (b) $t = 0.033$ Myr, and (c) $t = 0.055$ Myr. SPH particles are represented by black dots and the position and motion of the sink particles are shown by the red lines. Figure from Hubber et al. (2011).

(Price et al. 2018), `GADGET` (Springel 2005), `SPHINX` (Dehnen & Aly 2012), `SEREN` (Hubber et al. 2011), and `SPHNG` (Benz 1990) - are compared in the study. Results from the Meshless Finite Mass code `GIZMO` (Hopkins 2015), as well as the 2D fixed cylindrical grid finite differencing code `FARGO` (Masset 2000), are also studied and compared.

This paper compares the evolution of a planet that has formed in the disc using these different codes. They find that all codes give qualitative similar results with relatively small quantitative differences regarding the planet mass growth and migration. This study shows that `SEREN` provides similar results with other well-established hydrodynamic codes.

3.3 Splash

In order to visualise the data we make use of `Splash` (Price 2007). This utility is specifically designed for the visualisation of the outputs from astrophysical simulations using Smooth Particle Hydrodynamics. It is able to visualise data in one, two and three dimensions. This *Fortran* program uses the custom-built back–end

graphics library, `giza`, to do the actual plotting.

We use `Splash` in Chapter 5 in order to visualise the outputs of the SPH simulations run. By utilising `Splash`, we are able to produce rendered plots rather than simple particle plots. Each particle can be plotted using a third quantity (column density in this thesis), rather than just by its position. Thus allowing us to fully analyse the results produced in the simulations.

3.4 Summary

In this chapter we have introduced the Lagrangian method of Smooth Particle Hydrodynamics that can be used to solve the fluid dynamic equations of star and planet formation.

The continuity equation for SPH is given by

$$\rho_i = \sum_{j=1}^{N} m_i W(r_{ij}, h_i), \tag{3.26}$$

and can be used to derive the energy and momentum equations for the SPH particles.

In this work we utilise a ∇hSPH model which assumes a variable smoothing length for each particle. We also consider self-gravity in our simulations in order to avoid unphysically large accelerations when SPH particles get close to each other. We invoke the standard (α, β) formulation for artificial viscosity in order to smear out any shocks. This is done by modifying the heating/cooling rate of the particles.

Thus the basic energy and momentum equations, given by Equations 3.3 and 3.4, respectively, are transformed to:

The momentum equation

$$\frac{\mathrm{d}\nu_i}{\mathrm{d}t} = -\sum_{j=1}^{N} m_j \left(\frac{P_i}{\Omega_i \rho_i^2} \nabla_i W(r_{ij}, h_i) + \frac{P_j}{\Omega_j \rho_j^2} \nabla_i W(r_{ij}, h_i) + \Pi_{ij} \nabla_i W(r_{ij}, h_i) \right) + \left. \frac{\mathrm{d}\nu_i}{\mathrm{d}t} \right|_{grav}, \tag{3.27}$$

the energy equation

$$\frac{\mathrm{d}u_i}{\mathrm{d}t} = \sum_{j=1}^{N} m_j \left(\frac{P_i}{\Omega_i \rho_i^2} \nu_{ij} \cdot \nabla W(r_{ij}, h) + \frac{P_j}{\Omega_j \rho_j^2} \nu_{ij} \cdot \nabla W(r_{ij}, h) + \Pi_{ij} \cdot \nabla_i W(r_{ij}, h_i) \right). \tag{3.28}$$

The gravitational contribution is given by

$$\left. \frac{\mathrm{d}\nu_i}{\mathrm{d}t} \right|_{grav} = -G \sum_{j=1}^{N} m_j \frac{\phi'(r_{ij}, h_i) + \phi'(r_{ij}, h_j)}{2} \hat{r}_{ij} - \frac{G}{2} \sum_{j=1}^{N} m_j \left[\frac{\xi_i}{\Omega_i} \nabla_i W(r_{ij}, h_i) + \frac{\xi_j}{\Omega_j} \nabla_i W(r_{ij}, h_j) \right]. \tag{3.29}$$

The viscosity terms are

$$\Pi_{ij} = \frac{-\alpha \bar{c}_{s,ij} \mu_{ij} + \beta \mu_{ij}^2}{\bar{\rho}_{ij}}; \qquad \mu_{ij} = \begin{cases} \frac{h_i \nu_{ij} \cdot r_{ij}}{|r_{ij}|}, & \text{if } \nu_i \cdot r_{ij} < 0; \\ 0, & \text{otherwise.} \end{cases} \tag{3.30}$$

and the correction terms to account for the variability of h are given by

$$\Omega_i = 1 - \frac{\partial h_i}{\partial \rho_i} \sum_{j=1}^{N} m_j \frac{\partial W_{ij}}{\partial h_i}(r_{ij}, h_i) \qquad \xi_i = \frac{\partial h_i}{\partial \rho_i} \sum_{j=1}^{N} m_j \frac{\partial \phi_{ij}}{\partial h_i}(r_{ij}, h_i). \tag{3.31}$$

The star and planet formation code `SEREN` (Hubber et al. 2011) is used to solve these equations. We also use the radiative cooling scheme based on Stamatellos et al. (2007) to run the simulations produced in this work. The package `Splash` (Price 2007) is used in order to visualise the outputs from `SEREN`. The simulations produced in this thesis are introduced and discussed in Chapter 5.

Chapter 4

The Evolution of Protoplanetary Discs Observed with ALMA

4.1 Introduction

ALMA observations of protoplanetary discs have revealed a multitude of different, complex substructures. These include horseshoe-like structures (Casassus et al. 2013), spiral arms (Pérez et al. 2016), inner cavities, (van der Marel et al. 2015) and discs featuring bright, concentric dust rings (ALMA Partnership et al. 2015). There has also been an increase in the amount of theoretical work being undertaken in order to explain the origin of these disc features (Dong et al. 2015b; Takahashi & Inutsuka 2016; Gonzalez et al. 2017).

Substructures have been observed in the protoplanetary discs surrounding stars with a wide range of different stellar parameters. Previous works have mostly focused on individual objects. More recently, Long et al. (2019) targeted 32 compact discs in the Taurus star-forming region. ALMA observations, at a high resolution ($\sim 0.12''$), were made in order to detect dust structures in the disc. Just under half of the discs were revealed to have dust gaps and rings.

The study conducted by van der Marel et al. (2019) focused solely on stars surrounded by protoplanetary discs featuring multiple rings. Archival ALMA observations of 16 protoplanetary discs were obtained. The morphology and gap locations of the discs were compared and any relations to the stellar age and luminosity were investigated.

The Disk Substructures at High Angular Resolution Project (DSHARP), is a deep, high resolution (~ 0.035") survey of 20 nearby, bright, and large protoplanetary discs (Andrews et al. 2018a). The location, sizes, and amplitudes of the small-scale substructures in the disc material were studied in order to asses how they might relate to the planet formation process. The young stellar objects in the sample cover a wide range of stellar luminosities and ages. A gap, and some sort of substructure were found in all discs in the sample.

In this work we study the different substructures found in 56 protoplanetary discs observed with ALMA. There are a range of substructures seen in the discs and the stars studied cover a wide parameter range of both intermediate and low-mass stars. In Section 4.2 we present our sample. We introduce a new classification scheme for protoplanetary substructures in Section 4.3. The stellar ages and masses of the host stars in the sample are then derived in Section 4.4. In Sections 4.5 and 4.6 we study the trends relating the disc substructure to various stellar parameters. We discuss the main results of this work in Section 4.7, and finally summarise in Section 4.8.

4.2 Archival Disc Observations

The ALMA Archive has been searched to find protoplanetary discs that feature different morphological structures seen in the millimetre dust continuum. The continuum product images of observations from Cycles 0 to 5 were looked at. The full sample of observations we have looked at is shown in Table A.1 in Appendix A.

The continuum product files available in the ALMA Archive are considered 'Science Ready' (Stoehr et al. 2020). However, they are often of a slightly lower quality than the final published data. Upon comparing the product files to the published data on each source, we find that the quality of the data, with regards to the final RMS–error and recovered total flux improves by less than an order of magnitude. No additional substructure is revealed between the archival product files and the published data. The slightly higher quality published data may better constrain the various properties of the substructure seen in the disc. However, since we are merely interested in detecting the presence of substructure in the disc, additional processing has not been done in order to improve the quality of the product files.

Protoplanetary discs that are spatially resolved and show clear substructure in millimetre dust were chosen. In order to be classified as having substructure, the discs had to feature either a cavity or gap of some sort or a pile-up of dust grains. We are interested in asymmetric substructure that may be seen in the dust continuum of the mm-dust disc. Therefore, we ignore discs, such as IRS48. Although a crescent-shaped structure can be seen in the disc, the crescent nature of the substructure is only visible when compared to multi-wavelength dust observations (van der Marel et al. 2013). We are solely interested in substructure that can be seen in the millimetre dust continuum, alone.

We have chosen to exclude debris discs from our sample; including the well-studied discs surrounding HR 4796A, HD 107146 and HD 181327. These discs are much older than the discs in our sample and the ALMA Archive is much less complete for these older discs. Similarly, we have excluded young, embedded discs such as Elias 2–24 and HL Tau as they may still be surrounded by an envelope. We have only obtained the final, calibrated continuum products of each observation and any observations that have undergone further processing will be discussed in Section 4.3.1.

Thus we have a complete sample of the protoplanetary discs in the ALMA Archive, observed during Cycles 0 to 5, that currently show resolvable substructure. We acknowledge that our sample is not complete with regards to all protoplanetary discs featuring substructure as some discs in the Archive may have substructure that remains unresolved. It is, however, complete in terms of those observed with ALMA and present in the archive.

The sample that we are left with consists of 56 protoplanetary discs across the first six cycles of ALMA observations. The observations for each disc were conducted at either Band Six or Band Seven (1.3 mm or 0.8 mm respectively) with two exceptions. Observations of 2MASS J16152023–3255051 (hereafter J16152023) were conducted at Band Nine (0.4 mm), whilst observations of HD 163296 were conducted at Band Eight (0.6 mm).

The sample of discs is shown in Table 4.1. A literature search has been conducted to obtain the temperature and luminosity of each host star. The luminosities have been scaled to the new Gaia DR2 distances (Gaia Collaboration et al. 2018). Where the error is not given in the literature for the temperature, we make an estimate of the uncertainty. The typical error on the quoted values from the literature is 6%, therefore we use this and make a conservative estimated error of 10% for temperatures without an uncertainty value. We also find, from literature, each Star Forming Region (SFR) that each object is located in.

Objects belonging to the Two Micron All-Sky Survey (2MASS) are displayed as '2MASS J##+## or '2MASS J##'–##' , where ## is its unique identity number. From this point on, the prefix '2MASS' will be removed. To query these objects in astronomical databases, such as `Simbad`, the prefix '*2MASS*' should be readded.

The 56 host stars have luminosities spanning from $0.1L_{\odot}$ to $90L_{\odot}$ and temperatures from 3400 to 12000 K, covering a wide parameter range of low and

intermediate–mass stars. Host stars with mass, M_* <1.8$M_\odot$, we refer to as low–mass objects. Intermediate objects are defined as those with mass 1.8$M_\odot$ <M< 8$M_\odot$, while objects with mass greater than 8$M_\odot$ are referred to as high–mass objects. The lower mass limit of 1.8$M_\odot$ for the intermediate stars comes from Simon et al. (2002). The lower mass limit for high–mass stars (8$M_\odot$) originates from the minimum mass required to produce a type II supernova (Zinnecker & Yorke 2007).

The stars in our sample are located in a number of different star forming regions and at a range of distances. Gaia DR2 distances are available for all sources except for the young stellar object J05052286+2531312. We make a distance estimate of 140.0 ± 14.0 pc for this object based on its location in the Taurus molecular cloud. We have assumed a conservative error estimate of 10% for this distance. The estimated Gaia distance to the Class II T–Tauri star RY Tau has changed drastically, from 140 pc (Agra-Amboage et al. 2009) to 177 pc in Gaia DR1 and to 443.1 ± 47.0 pc in Gaia DR2 (Gaia Collaboration et al. 2018). This discrepancy was discussed by Garufi et al. (2019). Therefore, we adopt their value of 133^{+55}_{-30} pc obtained from HIPPARCOS data (ESA 1997). The majority of the discs observed with ALMA are located in well-surveyed star forming regions and have distances less than $\sim$ 200pc.

The new Gaia distances agree to within 20% of the previous literature values for the majority of sources. The new distance to HD 169142 was determined to be 114.0 pc compared to its previous distance of 145.0 pc (Manoj et al. 2006). Other examples include SZ111, which changed from 200.0 to 158.3pc and CQ Tau (100 to 163 pc).

Table 4.1: Literature properties of the sample studied in this work. The references correspond to the luminosity and temperature, respectively. Both the luminosity and temperature have been obtained from the same source where one reference is provided. All distances have been obtained from Gaia DR2 (Gaia Collaboration et al. 2018) with the exceptions of J05052286+2531312 and RY Tau which were obtained from Kenyon et al. (2008) and Garufi et al. (2019), respectively (see text for details).

ID	Name	Luminosity ($L_\odot$)	T_{eff} (K)	Distance (pc)	SFR	Ref.
1	AA Tau	0.8 ± 0.3	4000 ± 400	137.2 ± 2.4	Taurus	(1)(2)
2	AB Auriga	89.6 ± 35.7	9800 ± 980	162.9 ± 1.5	Taurus	(3)(4)
3	AS 209	1.4 ± 0.7	4300 ± 300	121.0 ± 0.9	Ophiuchus	(5)
4	CI Tau	0.8 ± 0.3	4100 ± 190	158.7 ± 1.2	Taurus	(5)
5	CQ Tau	10.0 ± 7.6	6900 ± 640	163.1 ± 2.2	Taurus	(5)
6	CS Cha	1.9 ± 0.2	4800 ± 480	176.0 ± 2.0	Chameleon	(6)
7	DM Tau	0.2 ± 0.0	3700 ± 170	145.1 ± 1.1	Taurus	(5)
8	DoAr25	1.0 ± 0.4	4300 ± 300	138.5 ± 1.5	Upper Scorpius	(5)
9	DoAr44	1.8 ± 0.8	4800 ± 220	145.9 ± 1.0	Ophiuchus	(5)
10	DS Tau	0.3 ± 0.1	3800 ± 380	159.0 ± 1.0	Taurus	(7)
11	Elias 2–27	0.9 ± 0.3	3700 ± 370	118.5 ± 13.1	Ophiuchus	(8)

Table 4.1: - continued.

ID	Name	Luminosity ($L_\odot$)	T_{eff} (K)	Distance (pc)	SFR	Ref.
12	EM* SR 21A	12.9 ± 5.9	5800 ± 400	138.4 ± 1.1	Ophiuchus	(5)
13	EM* SR 24S	3.8 ± 1.8	5000 ± 350	114.4 ± 4.5	Ophiuchus	(5)
14	EM* SR 4	1.2 ± 0.5	5100 ± 190	134.6 ± 0.8	Upper Scorpius	(5)
15	GG Tau	1.8 ± 2.0	4000 ± 400	150.3 ± 24.2	Taurus	(9)(10)
16	GM Auriga	1.6 ± 0.4	4800 ± 220	159.6 ± 2.1	Taurus	(5)
17	GO Tau	0.7 ± 0.1	3800 ± 110	144.0 ± 3.0	Taurus	(5)
18	GW Lup	0.3 ± 0.2	3600 ± 170	155.9 ± 1.3	Lupus	(5)
19	HD 100453	6.2 ± 2.6	7300 ± 250	104.2 ± 0.4	Lower Centaurus Crux	(11)
20	HD 100546	36.5 ± 7.2	10400 ± 600	110.0 ± 0.6	Chameleon	(12)
21	HD 142527	20.6 ± 8.2	6600 ± 100	157.3 ± 1.2	Lupus	(13)
22	HD 142666	9.5 ± 6.5	7500 ± 250	148.3 ± 1.2	Upper Scorpius	(11)
23	HD 143006	3.8 ± 1.3	5600 ± 260	166.1 ± 4.0	Upper Scorpius	(14)
24	HD 163296	17.0 ± 11.7	9300 ± 650	101.5 ± 1.2	Upper Scorpius	(5)
25	HD 169142	9.5 ± 2.0	8400 ± 820	114.0 ± 0.8	Lupus	(15)
26	HD 34282	10.7 ± 8.9	9500 ± 250	311.6 ± 4.6	Orion	(11)
27	HD 36112	9.8 ± 4.5	7600 ± 500	160.2 ± 1.7	Taurus	(5)

Table 4.1: - continued.

ID	Name	Luminosity ($L_\odot$)	T_{eff} (K)	Distance (pc)	SFR	Ref.
28	HD 97048	42.9 ± 12.0	10000 ± 1000	184.8 ± 1.3	Chameleon	(12)
29	IM Lup	2.6 ± 1.1	4400 ± 200	158.5 ± 1.3	Lupus	(5)
30	IP Tau	0.4 ± 0.2	3900 ± 90	130.0 ± 2.0	Taurus	(5)
31	LkCa15	1.1 ± 0.4	4400 ± 300	158.9 ± 1.2	Taurus	(5)
32	J05052286+2531312	0.1 ± 0.1	3600 ± 360	140.0 ± 14.0	Taurus	(6)
33	J16042165–2130284	0.6 ± 0.2	4900 ± 340	150.1 ± 1.3	Upper Scorpius	(5)
34	J16152023–3255051	0.9 ± 0.4	4400 ± 300	157.7 ± 0.9	Lupus	(5)
35	J16230923–2417047	1.0 ± 0.1	6000 ± 600	160.5 ± 1.4	Ophiuchus	(5)
36	MWC 480	17.4 ± 2.0	8500 ± 850	162.0 ± 2.0	Taurus	(7)
37	PDS 70	0.8 ± 0.7	4400 ± 440	113.4 ± 0.5	Lupus	(16)
38	PDS 99	1.1 ± 0.1	4200 ± 420	155.0 ± 2.0	Corona Australis	(6)
39	RU Lup	1.5 ± 0.7	4100 ± 190	159.6 ± 1.7	Lupus	(5)
40	RXJ1842.9–3532	0.8 ± 0.1	4800 ± 480	154.0 ± 1.0	Corona Australis	(6)
41	RXJ1852.3–3700	0.6 ± 0.1	4800 ± 480	146.0 ± 1.0	Corona Australis	(6)
42	RY Lup	1.9 ± 0.9	4900 ± 230	159.1 ± 1.8	Lupus	(5)
43	RY Tau	6.0 ± 4.0	5100 ± 510	443.1 ± 47.0	Taurus	(17)

Table 4.1: - continued.

ID	Name	Luminosity ($L_\odot$)	T_{eff} (K)	Distance (pc)	SFR	Ref.
44	SAO 206462	7.2 ± 3.3	6600 ± 460	178.9 ± 1.2	Lupus	(5)
45	SZ 111	0.2 ± 0.1	3700 ± 170	158.3 ± 0.8	Lupus	(5)
46	SZ 129	0.4 ± 0.2	4100 ± 190	161.7 ± 1.3	Lupus	(5)
47	SZ 91	0.2 ± 0.1	3700 ± 170	159.1 ± 1.6	Lupus	(5)
48	T Cha	1.3 ± 0.1	5600 ± 560	110.0 ± 1.0	Chameleon	(6)
49	TW Hya	0.3 ± 0.2	4100 ± 280	60.1 ± 0.2	TW Hya Assoc.	(5)
50	UX Tau	1.9 ± 0.8	4900 ± 230	139.4 ± 1.9	Taurus	(5)
51	V1094 Sco	1.7 ± 0.2	4200 ± 420	150.0 ± 1.0	Upper Scorpius	(18)
52	V1247 Ori	14.3 ± 2.1	7300 ± 780	398.4 ± 10.1	Orion	(19)
53	V4046 Sgr	0.5 ± 0.1	4100 ± 410	72.0 ± 1.0	β Pic MG	(6)
54	V892 Tau	38.0 ± 18.0	12000 ± 1200	117.4 ± 1.6	Taurus	(20)(21)
55	Wa Oph 6	2.9 ± 1.3	4200 ± 290	123.9 ± 0.7	Ophiuchus	(5)
56	WSB 60	0.2 ± 0.1	3400 ± 100	137.0 ± 4.0	Ophiuchus	(5)

References : (1) Grosso et al. (2007), (2) Schneider et al. (2015), (3) Monnier et al. (2006), (4) Isella et al. (2006) , (5) Andrews et al. (2018b), (6) Francis & van der Marel (2020), (7)Long et al. (2018), (8) Isella et al. (2009), (9) White et al. (1999), (10) Dutrey et al. (2016), (11) Fairlamb et al. (2015), (12) van den Ancker et al. (1997), (13) Mendigutía et al. (2014), (14) Andrews et al. (2018a), (15) Fedele et al. (2017), (16) Metchev et al. (2004), (17) Bertout et al. (2007), (18) van Terwisga et al. (2018), (19) Kraus et al. (2013), (20) Berrilli et al. (1992), (21) Manoj et al. (2006).

The archival ALMA observations were taken at a range of resolutions, all sub-arcsecond. We further discuss the detectability of substructure in Section 4.7.2. The smallest angular scale we can resolve in our sample is in the DM Tau disc, with a resolution of 0.02" (2.9 au at 145 pc), whilst we can only resolve down to a resolution of 0.77" (123.6 au at 160 pc) in the disc of J16230923–2417047. In addition to this, the discs are located at a range of distances and the observations were conducted with varying sensitivities. As a result, any statement on the detectability of substructure based on flux would be meaningless.

An HR diagram of the sample has been plotted in Figure 4.1. It is evident in the diagram that our sample uniformly covers both stellar luminosity and temperature. The Zero Age Main-Sequence (ZAMS) has also been plotted on the HR Diagram (ZAMS from Siess et al. (2000)). The discs have been plotted with different symbols according to the classification they have been given in this work. This will be discussed further in Section 4.3.

All but five systems in our sample are single star systems. UX Tau A and HD 100453 both have companions orbiting at a radius > 100 au and are surrounded by a circumprimary disc (Tanii et al. 2012; Wagner et al. 2018). A circumbinary disc surrounds HD 142527 (Fukagawa et al. 2006), CS Cha (Guenther et al. 2007) and GG Tau; with GG Tau being a triple star system (Di Folco et al. 2014). With such a limited sample of multiple star systems, we have not investigated trends relating to disc morphology and multiplicity.

4.3 Classification Scheme

Garufi et al. (2018) studied the appearance of protoplanetary discs (in morphology and spatial extent) in scattered light. Stellar and disc properties were calculated and related to seven categories defined in their study; Ring, Spiral, Giant, Rim, Inclined, Faint, and Small discs. Following a similar approach, we classify our discs into four

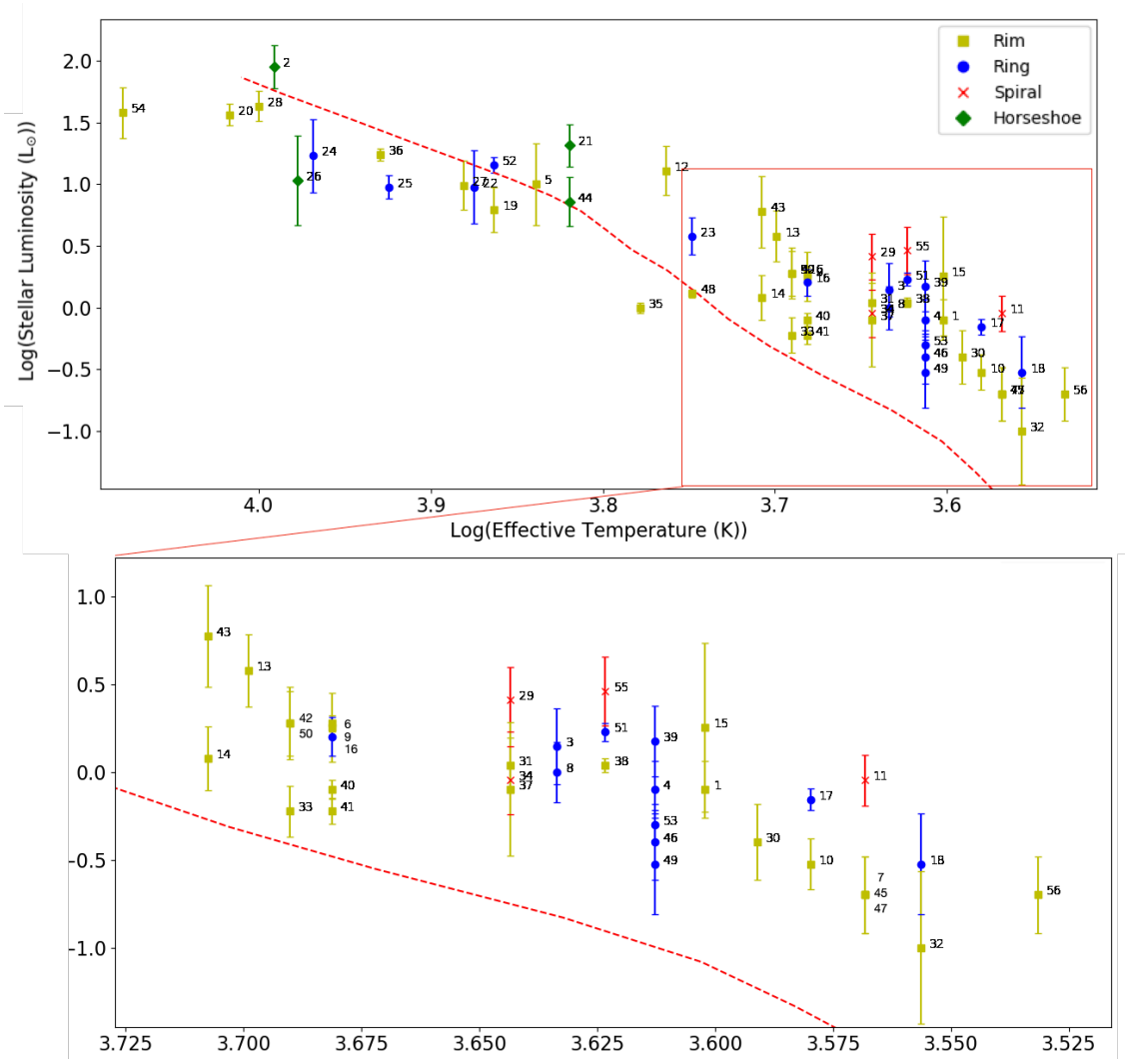

Figure 4.1: An HR diagram of the sources in our sample. The red dashed line marks the Zero Age Main-Sequence using the model of Siess et al. (2000). The discs have been labelled and their identities can be found in Table 4.1. The coloured markers indicate the category assigned to each protoplanetary disc (see Section 4.3).

categories based upon their appearance and morphology. The characteristics of the four categories are outlined below and summarised in Figure 4.2.

Rings: Protoplanetary discs that feature bright, concentric rings have been classified as ringed discs. Between the rings are gaps devoid of gas and/or dust. A minimum of two concentric rings need to be seen in order for a disc to be classified as ringed. Examples of these discs that have been observed with ALMA include GM Auriga (Macías et al. 2018) and HD 169142 (Fedele et al. 2017). These discs may also feature a central cavity, as can be seen in GM Auriga.

Rims: The majority of the discs that have been studied in this work feature a single bright rim at the edge of a large disc cavity. These rims have been seen around both intermediate–mass and low–mass protostars including DM Tau, LkCa15, and J16042165–2130284 (Pinilla et al. 2018). Disc rims can also be seen in protoplanetary discs that have been classified as ring or horseshoe. However since the rim is not the most prominent feature, these discs have been sorted in other categories. We are only focusing on the continuum emission from the protoplanetary disc, thus the cavity needs to be void of only dust in order to be classified as a rim.

Horseshoe: Horseshoe shaped discs are similar to rim discs; a single ring of dust surrounding a large cavity. However, the majority of the dust in horseshoe discs is located in a small region of the disc. An example of a system containing a horseshoe shaped protoplanetary disc is HD 142527 (Casassus et al. 2015), where the dust in the protoplanetary disc resembles a crescent or horseshoe shape.

Spiral: Discs which feature spiral like arms of continuum emission are classified as spiral discs. This structure has rarely been seen in protoplanetary discs as of yet, the first being Elias 2–27 (Pérez et al. 2016).

All of our chosen discs are resolved and show substructure, therefore we have omitted the Faint category of discs used by Garufi et al. (2018). We have also not used the Small disc category as all of our discs have a radius larger than 20 au.

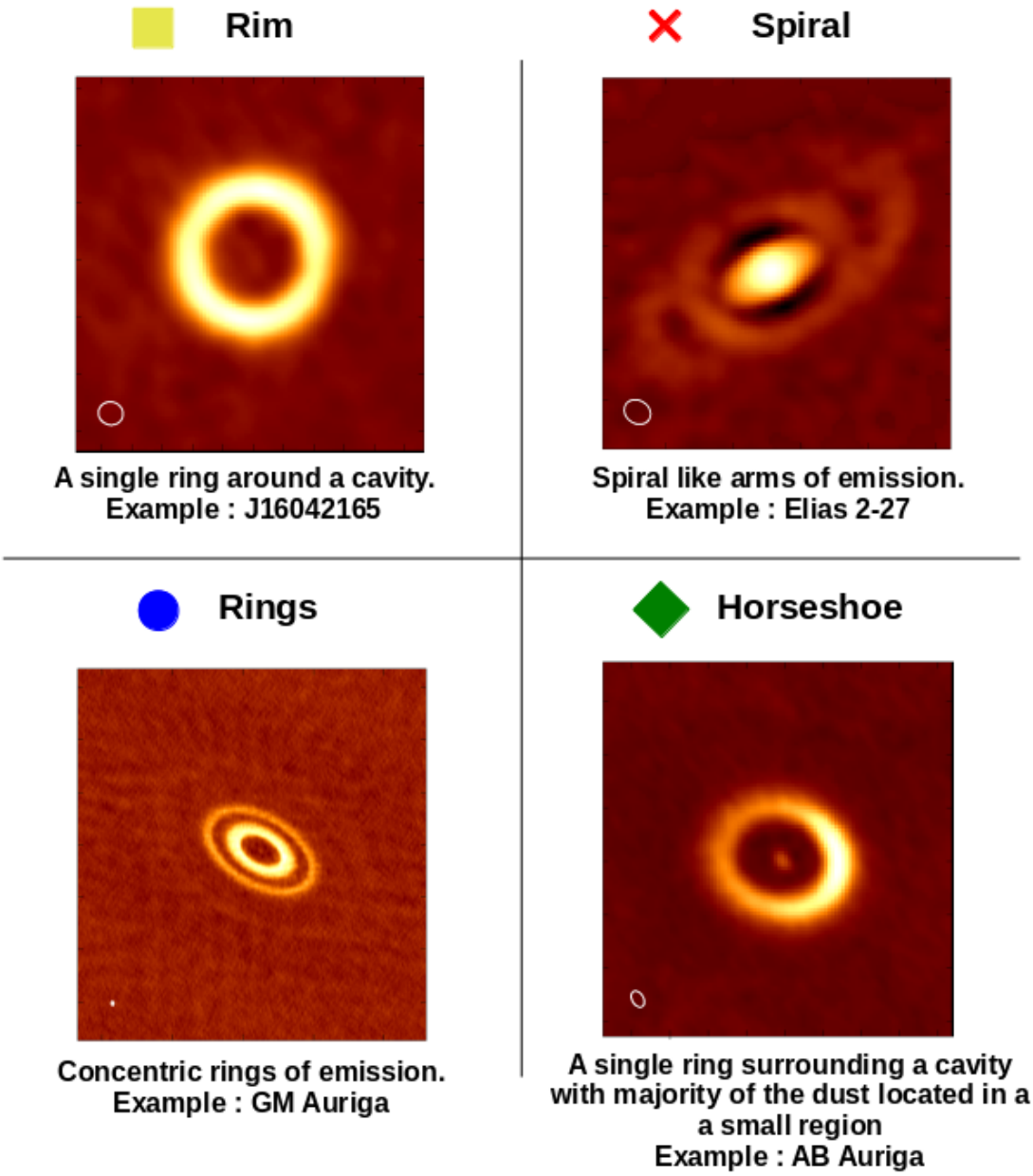

Figure 4.2: Examples of protoplanetary discs from each category defined in this work. Further details about each category is given in the text. The technique of unsharp masking filtering has been applied to the image of Elias 2-27 (see section 4.3.1).

Garufi et al. (2018) define discs that show faint arm-like structures on large scales as Giant. These structures are only seen in discs with a radial extent $\gg$100 au. The structures seen in these discs are faint and could even be attributed to broken rings rather than spiral arms. Therefore, we have removed the Giant category and introduced the Horseshoe category which has been outlined above.

The discs have been classified based on the most prominent morphological feature seen in the sub-mm dust emission. Some discs like CQ Tau could be defined as either a horseshoe disc or a rim disc. We have chosen to classify this disc as a rim disc since this is the most prominent feature. RY Lup also appears to have a horseshoe-like morphology. However this disc is nearly edge on with an inclination angle of $\approx$70 $^{\circ}$ (Langlois et al. 2018). Therefore the horseshoe-like morphology may just be an observational effect. Therefore, we have placed this disc in the Rim category. We do acknowledge that some discs can fit into multiple classifications and the classification for each source can be found in Table 4.2.

Table 4.2: The values derived in this work. Columns 3 and 4 show the stellar ages and masses derived using the stellar tracks from Siess et al. (2000) and Baraffe et al. (2015). Column 5 shows the classification assigned to the protoplanetary disc. The radius of the disc that contains 68% of the total disc flux is shown in Column 6.

ID #	Name	Age (Myr)	M_* ($M_\odot$)	Classification	$R_{68\%F}$ (au)
1	AA Tau	1.5 $\pm$ 0.8	0.8 $\pm$ 0.2	Rim	55 $\pm$ 5
2	AB Auriga	3.0 $\pm$ 0.5	2.7 $\pm$ 0.6	Horseshoe	163 $\pm$ 8
3	AS 209	1.5 $\pm$ 0.9	0.9 $\pm$ 0.2	Rings	97 $\pm$ 4
4	CI Tau	2.0 $\pm$ 1.0	0.8 $\pm$ 0.2	Rings	127 $\pm$ 5
5	CQ Tau	10.0 $\pm$ 4.9	1.7 $\pm$ 0.4	Rim	60 $\pm$ 8
6	CS Cha	4.0 $\pm$ 3.0	1.4 $\pm$ 0.2	Rim	46 $\pm$ 3
7	DM Tau	5.0 $\pm$ 3.0	0.6 $\pm$ 0.2	Rim	29 $\pm$ 1

Table 4.2: - continued.

ID #	Name	Age (Myr)	M_* ($M_\odot$)	Classification	$R_{68\%F}$ (au)
8	DoAr25	2.5 ± 1.0	1.0 ± 0.2	Rings	97 ± 5
9	DoAr44	3.0 ± 1.0	1.4 ± 0.3	Rim	54 ± 7
10	DS Tau	4.0 ± 1.0	0.7 ± 0.1	Rim	59 ± 2
11	Elias 2–27	0.5 ± 0.1	0.5 ± 0.1	Spirals	59 ± 7
12	EM* SR 21A	4.0 ± 1.2	2.2 ± 0.4	Rim	62 ± 10
13	EM* SR 24S	4.0 ± 1.7	1.9 ± 0.4	Rim	26 ± 1
14	EM* SR 4	12.0 ± 6.0	1.2 ± 0.2	Rim	24 ± 1
15	GG Tau	0.9 ± 0.2	0.6 ± 0.1	Rim	225 ± 36
16	GM Auriga	8.0 ± 5.0	1.4 ± 0.3	Rings	61 ± 4
17	GO Tau	1.0 ± 0.5	0.5 ± 0.1	Rings	96 ± 10
18	GW Lup	2.0 ± 1.5	0.4 ± 0.1	Rings	47 ± 2
19	HD 100453	13.0 ± 3.1	1.7 ± 0.3	Rim	31 ± 1
20	HD 100546	20.0 ± 4.0	2.5 ± 0.5	Rim	29 ± 2
21	HD 142527	6.0 ± 1.0	1.9 ± 0.4	Horseshoe	186 ± 10
22	HD 142666	10.3 ± 8.5	1.7 ± 0.3	Rings	37 ± 1
23	HD 143006	10.0 ± 2.0	1.5 ± 0.3	Rings	68 ± 8
24	HD 163296	4.0 ± 1.0	2.1 ± 0.4	Rings	56 ± 11
25	HD 169142	8.0 ± 0.5	1.9 ± 0.4	Rings	52 ± 3
26	HD 34282	7.0 ± 2.0	2.1 ± 0.4	Horseshoe	187 ± 14
27	HD 36112	10.0 ± 5.0	1.9 ± 0.5	Rim	80 ± 4
28	HD 97048	5.4 ± 0.4	2.5 ± 0.5	Rim	139 ± 43
29	IM Lup	0.8 ± 0.2	1.0 ± 0.2	Spirals	87 ± 4
30	IP Tau	3.0 ± 1.5	0.6 ± 0.1	Rim	26 ± 2
31	LkCa15	3.0 ± 2.0	1.1 ± 0.2	Rim	79 ± 5

Table 4.2: - continued.

ID #	Name	Age (Myr)	M_* ($M_\odot$)	Classification	$R_{68\%F}$ (au)
32	J05052286+2531312	12.0 ± 10.0	0.6 ± 0.1	Rim	42 ± 4
33	J16042165–2130284	20.0 ± 8.0	1.0 ± 0.2	Rim	98 ± 5
34	J16152023–3255051	6.0 ± 4.0	1.0 ± 0.2	Spirals	63 ± 3
35	J16230923–2417047	30.0 ± 6.0	1.1 ± 0.2	Rim	32 ± 5
36	MWC 480	9.0 ± 1.0	2.2 ± 0.4	Rim	50 ± 4
37	PDS 70	5.0 ± 4.0	1.1 ± 0.2	Rim	68 ± 2
38	PDS 99	2.0 ± 1.0	0.8 ± 0.2	Rim	62 ± 5
39	RU Lup	0.6 ± 0.1	0.7 ± 0.1	Rings	37 ± 2
40	RXJ1842.9–3532	13.0 ± 4.0	1.0 ± 0.2	Rim	71 ± 3
41	RXJ1852.3–3700	17.0 ± 4.0	1.1 ± 0.2	Rim	47 ± 2
42	RY Lup	4.0 ± 2.0	1.4 ± 0.3	Rim	72 ± 4
43	RY Tau	3.0 ± 1.0	2.2 ± 0.5	Rim	133 ± 14
44	SAO 206462	14.0 ± 5.5	1.5 ± 0.3	Horseshoe	120 ± 21
45	SZ 111	5.0 ± 3.0	0.5 ± 0.1	Rim	52 ± 8
46	SZ 129	6.0 ± 6.0	0.3 ± 0.1	Rings	36 ± 1
47	SZ 91	5.0 ± 3.0	0.6 ± 0.1	Rim	80 ± 7
48	T Cha	20.0 ± 4.0	1.2 ± 0.2	Rim	44 ± 2
49	TW Hya	10.0 ± 5.0	0.8 ± 0.2	Rings	36 ± 0
50	UX Tau	6.5 ± 3.5	1.5 ± 0.3	Rim	42 ± 4
51	V1094 Sco	0.8 ± 0.3	0.8 ± 0.2	Rings	135 ± 5
52	V1247 Ori	9.0 ± 0.9	1.8 ± 0.3	Rings	131 ± 17
53	V4046 Sgr	4.0 ± 2.0	0.8 ± 0.2	Rings	37 ± 3
54	V892 Tau	10.0 ± 0.0	2.7 ± 0.5	Rim	35 ± 2
55	Wa Oph 6	0.5 ± 0.1	0.8 ± 0.2	Spirals	50 ± 1

Table 4.2: - continued.

ID	Name	Age	M_*	Classification	$R_{68\%F}$
#		(Myr)	($M_\odot$)		(au)
56	WSB 60	2.0 ± 1.0	0.3 ± 0.1	Rim	36 ± 5

4.3.1 Unsharp Masking Filtering

ALMA observations of Elias 2–27 by Pérez et al. (2016) revealed spiral density waves in the protoplanetary disc. The technique of Unsharp Masking Filtering was performed on the observations in order to remove the large–scale disc emission and highlight the spiral structure of the disc. We utilise the same technique on the ALMA Archive observation of Elias 2–27, as well as three other discs: IM Lup, J16152023, and Wa Oph 6.

Substructure can be seen in all four discs. However, the conditions of the observations may not have been sufficient in order to clearly resolve the substructure. Therefore, the Filtering was performed in order to highlight the structure that can faintly be seen in the disc; this then allowed us to accurately classify these protoplanetary discs. No other science was performed using these filtered observations.

Following Pérez et al. (2016), the original archival observation of Elias 2–27 was smoothed with a 2-D Gaussian of 0.33" FWHM. This image was then scaled by a factor of 0.87 before subtracting it from the original image. Figure 4.3 shows the observation before and after the filtering process.

We applied a similar process to the ALMA observations of IM Lup, J16152023, and Wa Oph 6 as faint spiral substructure could be seen. The discs were smoothed with Gaussians of FWHM 0.33". J16152023 was then scaled by a factor of 0.87, whilst the discs of Wa Oph 6 and IM Lup were scaled by 0.67. Figures 4.3 and show the original ALMA observations and the post-filtered images for these protoplanetary discs.

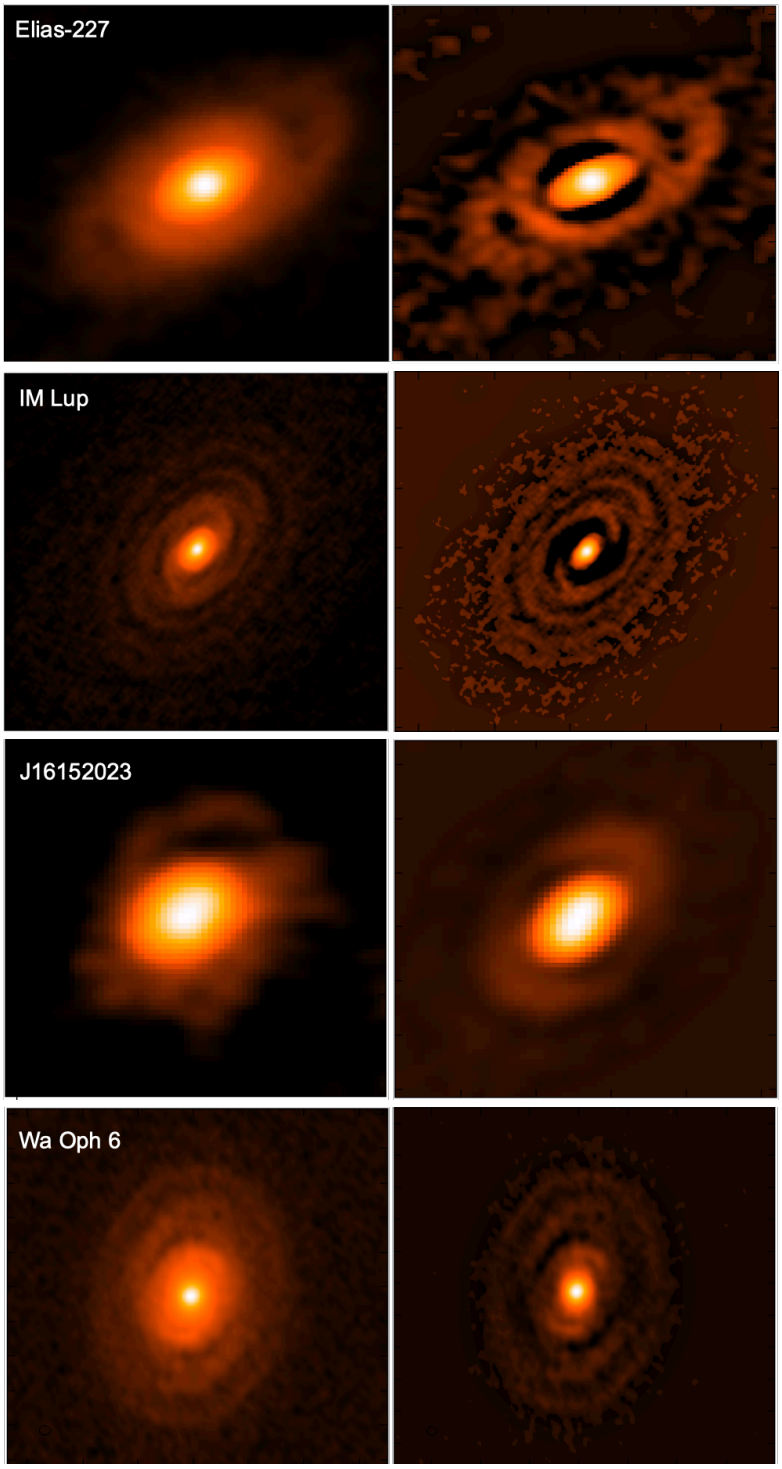

Figure 4.3: Protoplanetary discs surrounding Elias-227, IM Lup, J1615202, and Wa Oph 6 before (left) and after (right) the unsharp masking filtering process. Each disc has been smoothed with a Gaussian and subsequently scaled (see text for further details).

4.4 Stellar Evolutionary and Isochronal Tracks

Individual stellar masses were determined for the host stars using the new luminosities, and the models of Siess et al. (2000) and Baraffe et al. (2015). The models of Baraffe et al. (2015) are only applicable for stars $< 1.4M_{\odot}$, therefore we use the models of Siess et al. (2000) for any star with a mass larger than this. Stellar tracks were plotted onto the HR diagram (Figure 4.1) and the stellar masses were interpolated. Errors on the masses are derived using the associated luminosity error for each star.

Figures 4.4 and 4.5 display the HR diagram shown in Figure 4.1 with the addition of stellar tracks from the models of Baraffe et al. (2015) and Siess et al. (2000). A line marking the Zero Age Main-Sequence (ZAMS) has also been over–plotted using the model of Siess et al. (2000). These diagrams have been used to determine the stellar masses of the sources in our sample, the values of which can be found in Table 4.2. Reddening has been accounted for when obtaining the literature values for the temperature and luminosity of these objects.

We calculate the stellar ages for the host stars following the same method. Isochrones from Baraffe et al. (2015) and Siess et al. (2000) were plotted onto the HR Diagram shown in Figure 4.1, and stellar ages were interpolated. We, again, use the models of Baraffe et al. (2015) for stars with mass $<1.4\mathrm{M}_{\odot}$, and the models of Siess et al. (2000) for any star with a mass larger than this. Errors on the ages are derived using the associated luminosity error for each star.

The HR Diagrams featuring the isochrones are shown in Figures 4.6 and 4.7. The stellar ages are given in Table 4.2.

It should be noted that this method of determining the ages and masses of pre-main sequence stars is quite uncertain. This is due to the luminosities of some stars having large errors, resulting in a large uncertainty range for the ages and masses.

Therefore, the derived values from this method are only an estimate and should be treated with caution. The estimates of the stellar ages are later used to organise the protoplanetary discs according to age (see Section 4.5).

We compare the ages derived here to the estimated age of the star forming region each star belongs to. We find that the ages we have derived generally agree with the estimated ages of the star-forming region within 3σ. The ages of the star forming regions can be found in Table A.2 in Appendix A.

The derived ages of the objects that do not agree with the age of the star forming region we find to be either very young or very old objects. Therefore, the stellar isochrones may be underestimating or overestimating the ages for these stars (Jørgensen & Lindegren 2005). Undetected stellar companions in a system would lead to different observational parameters being determined for an individual young stellar object. For systems with two objects of comparable masses, the magnitude of the binary has been shown to be 0.75 times brighter than the corresponding single star. This leads to a considerable overestimation of the stellar age (Jørgensen & Lindegren 2005). Isochrones in part of the HR diagram overlap, this can be seen in Figure 4.7. Therefore, the multiple possible solutions for the age of the object may lead to either an overestimation or and underestimation of the true age of the young stellar object.

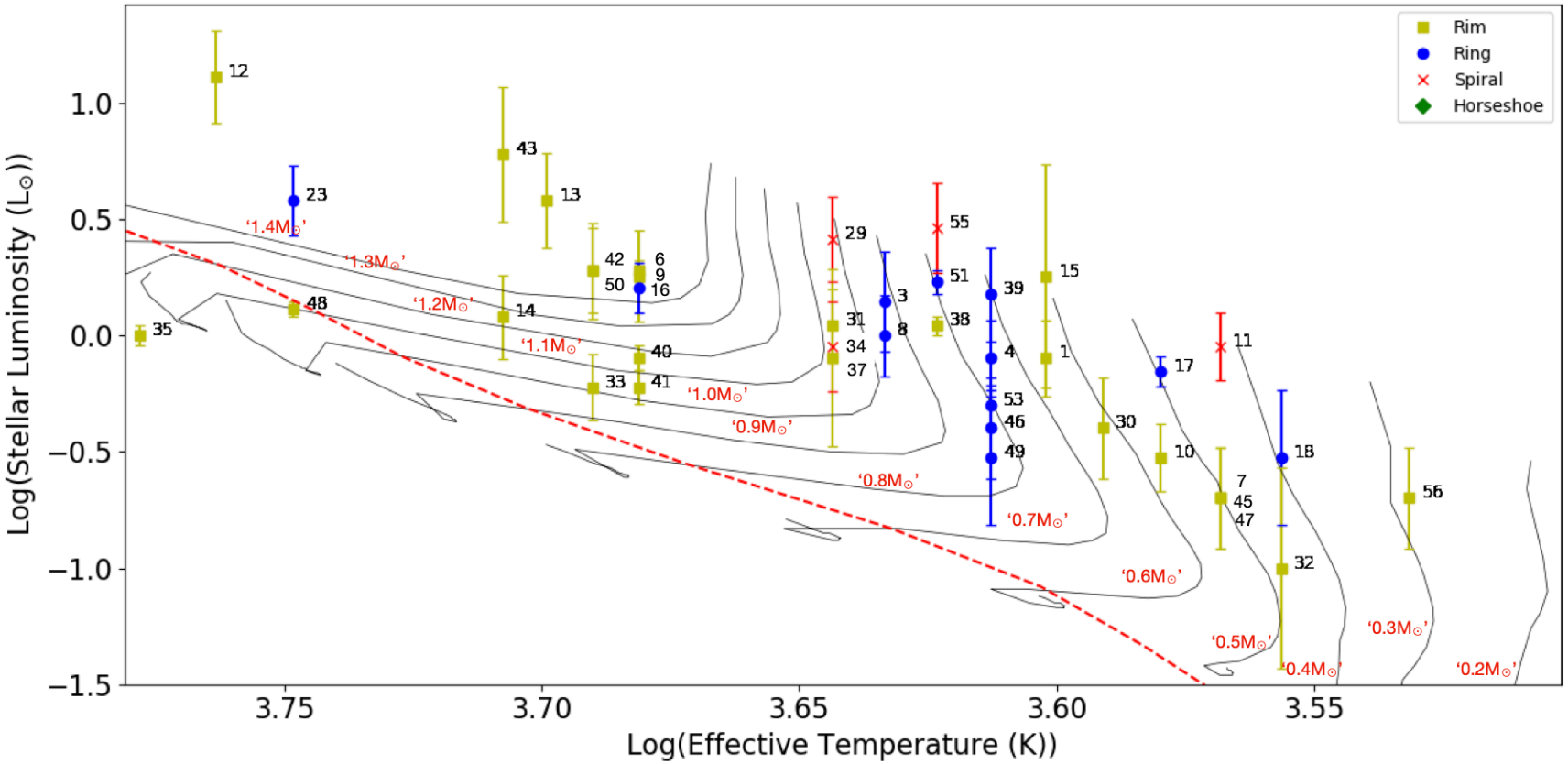

Figure 4.4: An HR diagram of the low–mass (<1.4$M_{\odot}$) sources studied in this work. The red dashed line marks the Zero Age Main-Sequence (ZAMS) using the model of Siess et al. (2000). Stellar tracks for a range of masses have been over–plotted as black lines from the models of Baraffe et al. (2015). The discs have been labelled and their identities can be found in Table 4.1.

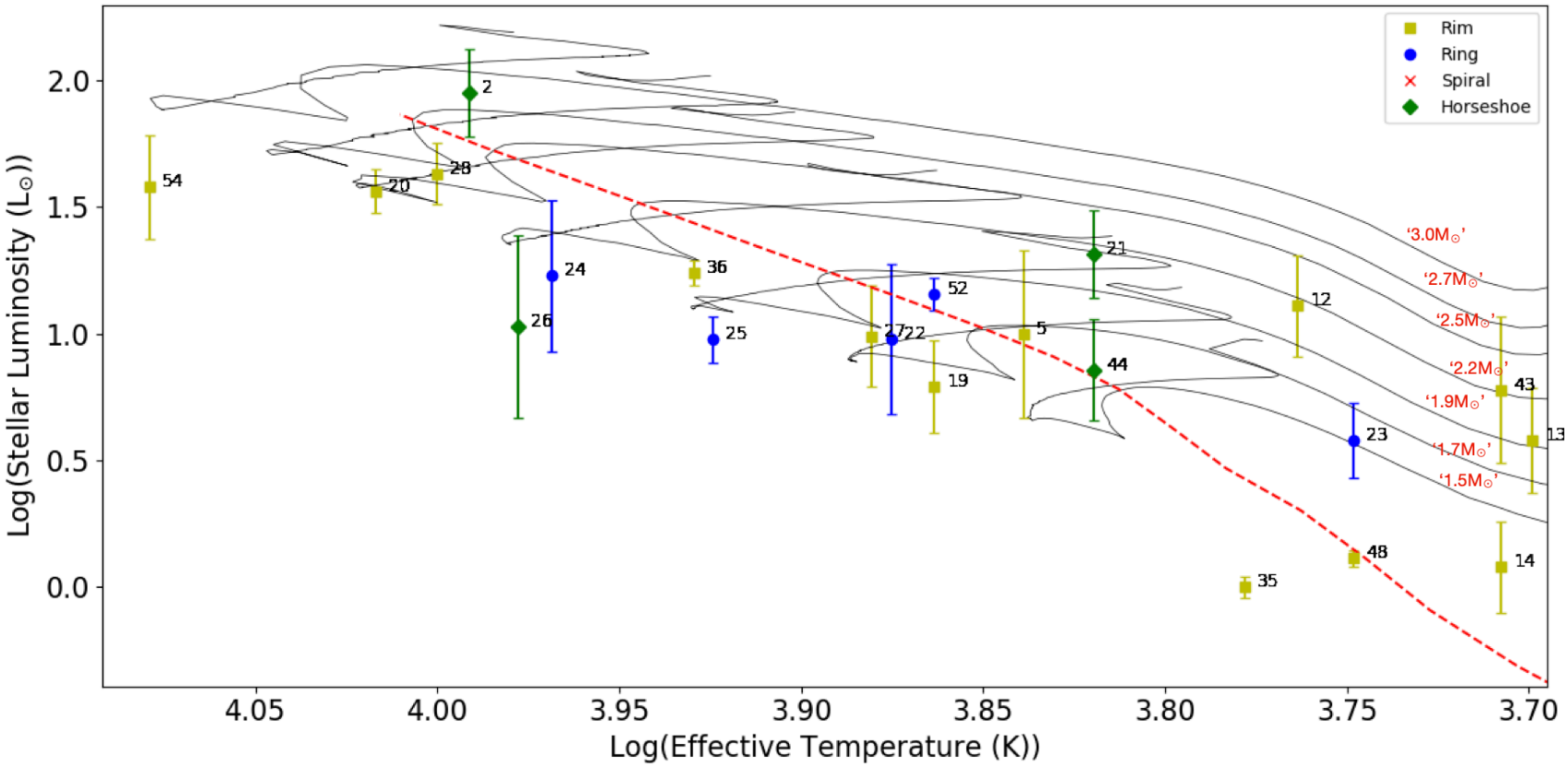

Figure 4.5: An HR diagram of the intermediate–mass (>1.4$M_{\odot}$) sources studied in this work. The red dashed line marks the ZAMS using the model of Siess et al. (2000). Stellar tracks for a range of masses have been over–plotted as black lines from the models of Siess et al. (2000). The discs have been labelled and their identities can be found in Table 4.1.

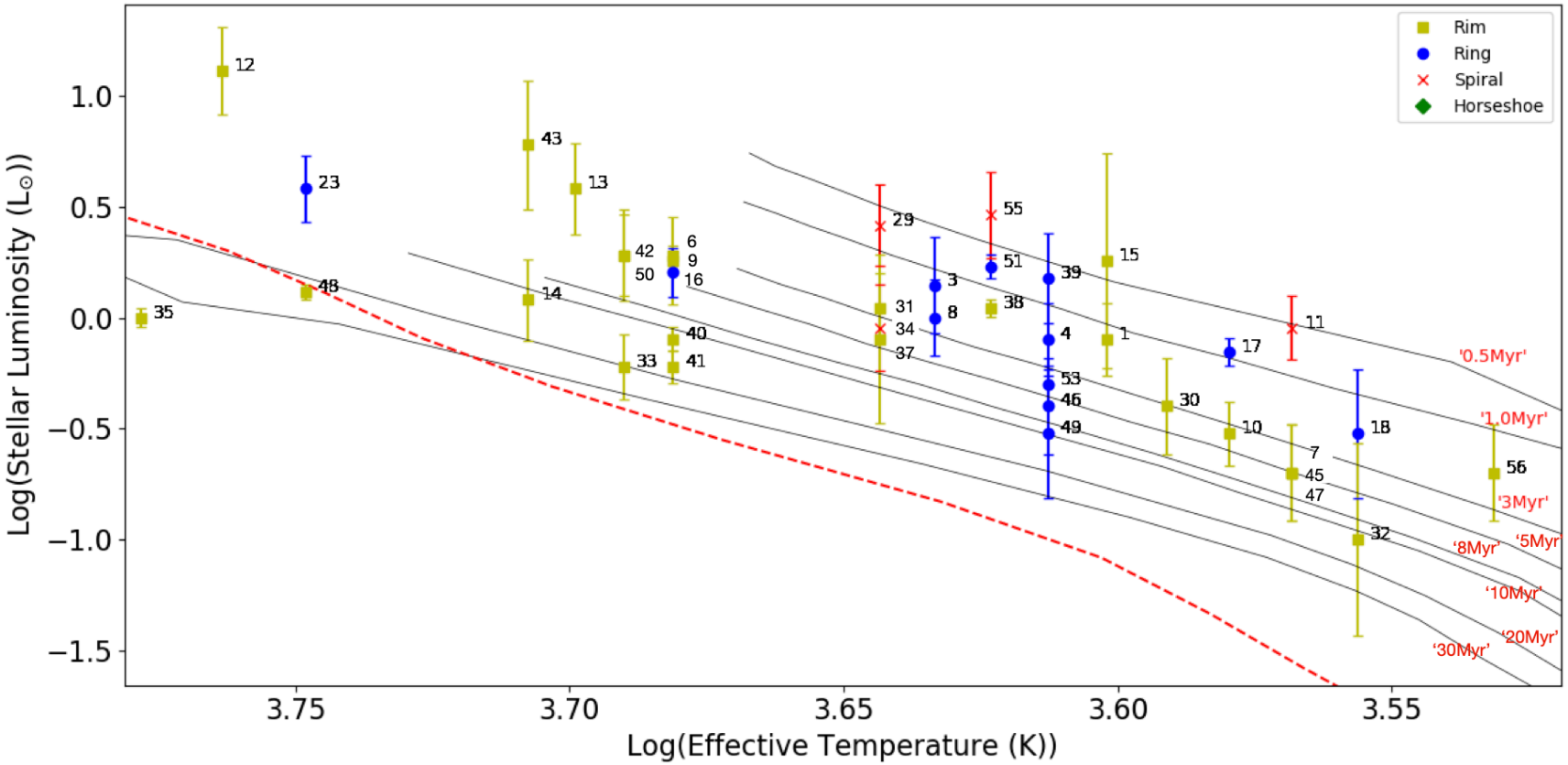

Figure 4.6: An HR diagram of the low–mass (<1.4$M_{\odot}$) sources studied in this work. The red dashed line marks the ZAMS using the model of Siess et al. (2000). Isochrones for a range of ages have been over–plotted as black lines from the models of Baraffe et al. (2015). The discs have been labelled and their identities can be found in Table 4.1.

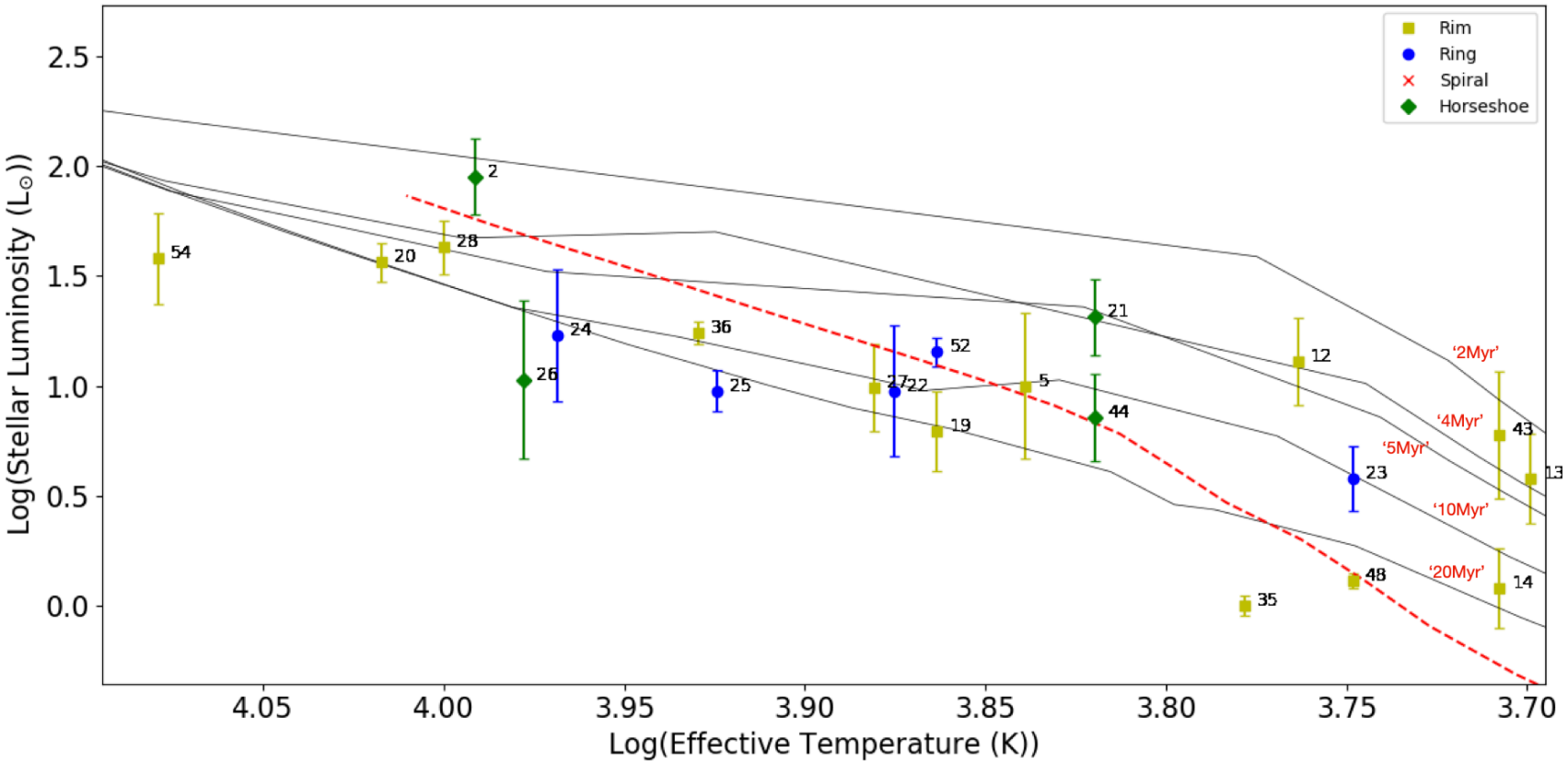

Figure 4.7: An HR diagram of the intermediate–mass (>1.4$M_{\odot}$) sources studied in this work. The red dashed line marks the ZAMS using the model of Siess et al. (2000). Isochrones for a range of ages have been over–plotted as black lines from the models of Siess et al. (2000). The discs have been labelled and their identities can be found in Table 4.1.

4.5 Disc Evolution

To study whether the morphological structures seen in protoplanetary discs evolve with age, we have ordered the discs studied in this work according to age. We have used the ages derived in Section 4.4 using the evolutionary tracks from Siess et al. (2000) and Baraffe et al. (2015). Figures 4.8, 4.9, 4.10, and 4.11 show the Rim, Ring, Horseshoe, and Spiral discs ordered according to age. The images of the observations show a 500×500au field–of–view. Stars with a † symbol in the lower left corner, show an area of 1000×1000 au. This has been done to allow comparisons between the radial extent of the discs.

4.5.1 Disc Radii

The ALMA observations were taken with a range of resolutions and sensitivities. Therefore, the radial extent of each disc cannot be compared with each other. The most robust way to compare the radial extent of the discs is to determine the radius containing 68% of the total flux (see work by Tripathi et al. (2017) , Ansdell et al. (2018) and Long et al. (2019)). This parameter can then be compared across the sample to study its behaviour with regards to stellar mass and age. This also allows for a more quantitative analysis of the substructure in the protoplanetary discs.

The radius that contains 68% of the total flux from each disc is obtained using `CASA`. This is done by fitting a 2-dimensional Gaussian to each protoplanetary disc to determine the radius that contains 100% of the total flux. We then iteratively fit smaller Gaussians until a radius containing 68% of the flux is obtained. The radii values can be found in Table 4.2. We compare our derived radii to literature values of the radii containing 68% of the total flux for the discs where this has been calculated. We find that the radii calculated here agree with the literature values within 3σ (Tripathi et al. 2017; Ansdell et al. 2018; Long et al. 2019). We do not

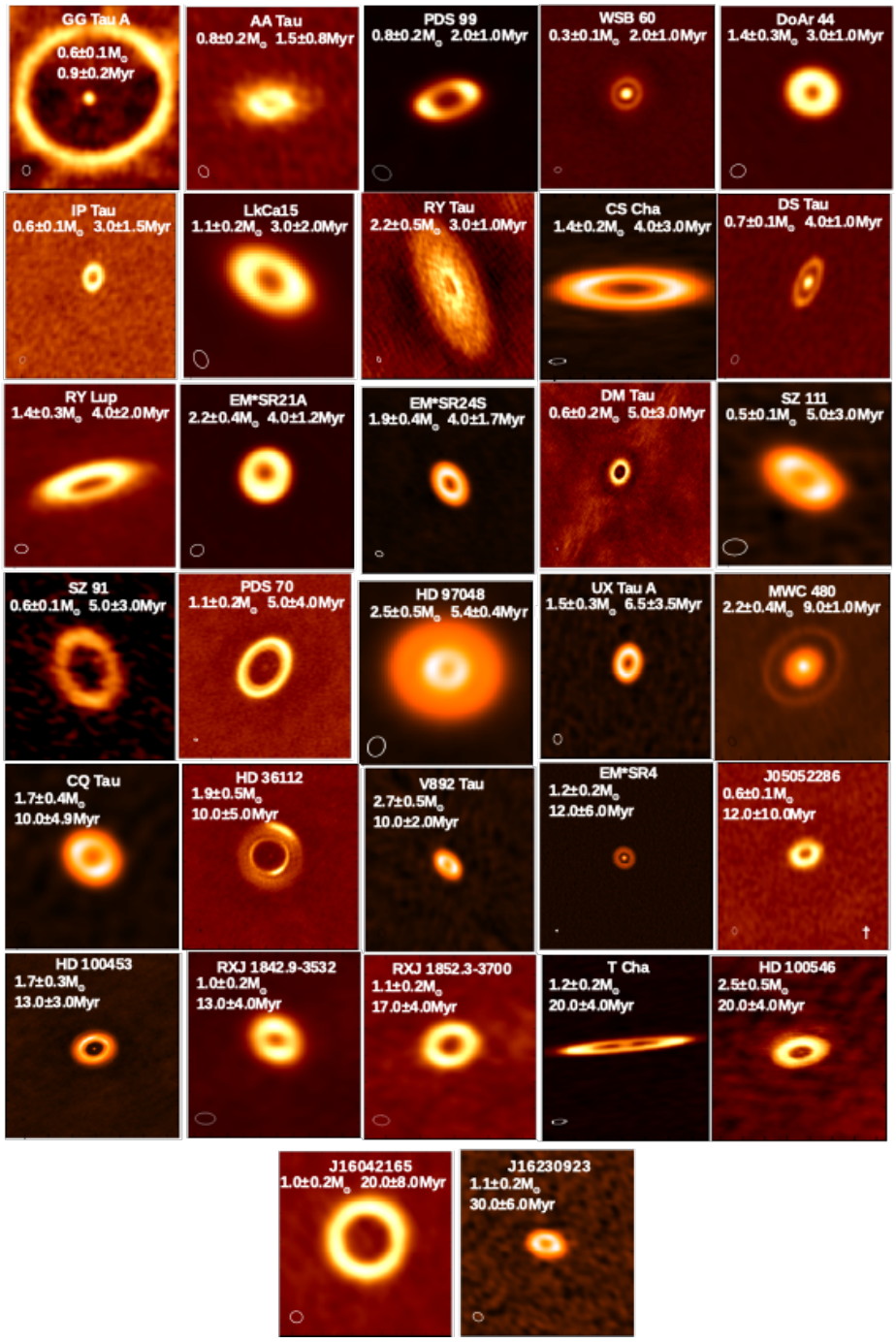

Figure 4.8: Images of the protoplanetary discs classified as Rims in this study. The discs are ordered by age with the top left (GG Tau) being the youngest and the lower right (J160230923) showing the oldest. The beam sizes used in each observation can be seen in the lower left of each image. All images show a 500×500 au field–of–view with the exception of the discs labelled with a † in the lower right. These images have a field–of–view of 1000×1000 au.

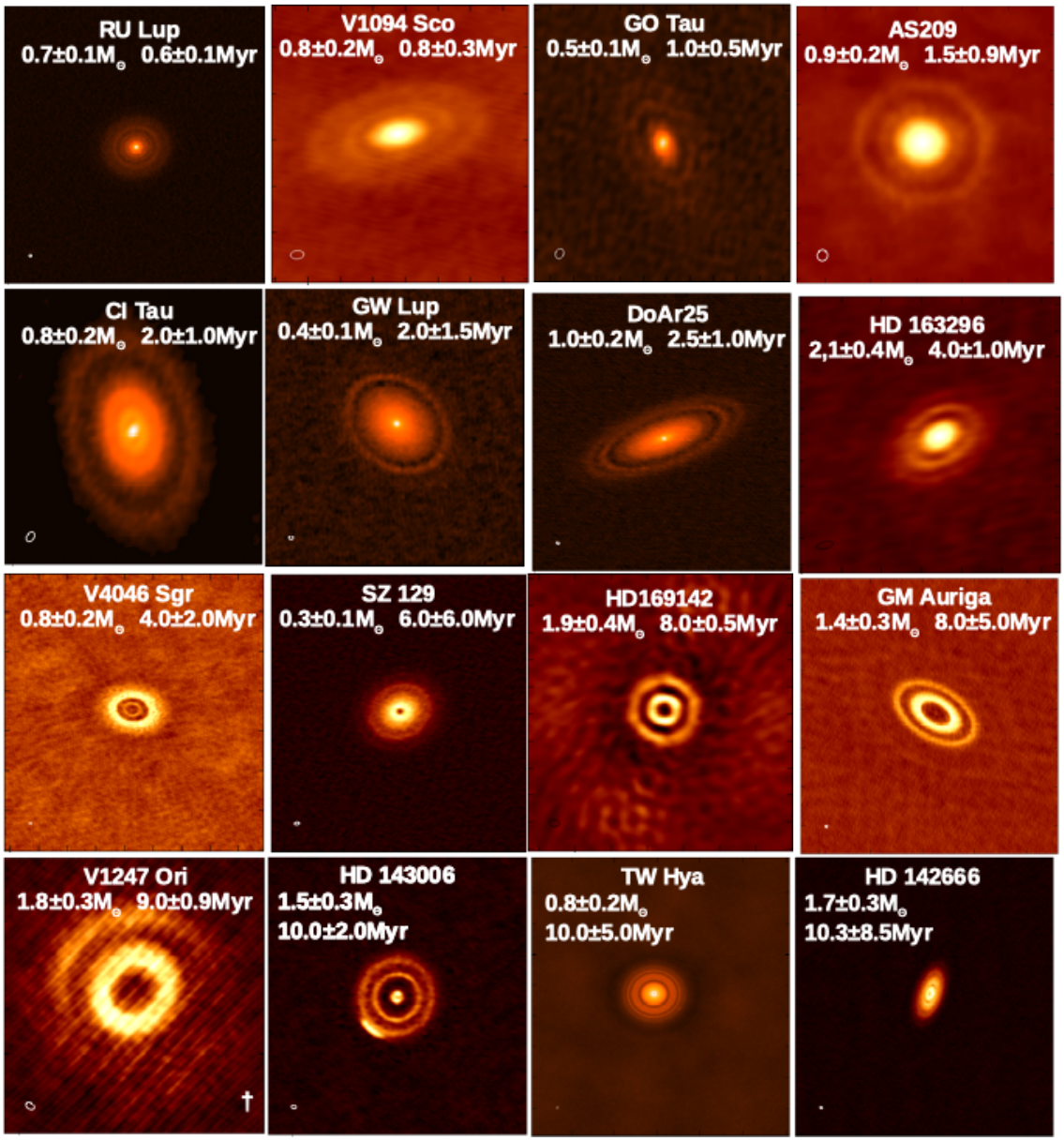

Figure 4.9: Images of the protoplanetary discs classified as Rings in this study. The discs are ordered by age with the top left (RU LUP) being the youngest and the lower right (HD 142666) showing the oldest. The beam sizes used in each observation can be seen in the lower left of each image. All images show a 500×500 au field–of–view with the exception of the discs labelled with a † in the lower right. These images have a field–of–view of 1000×1000 au.

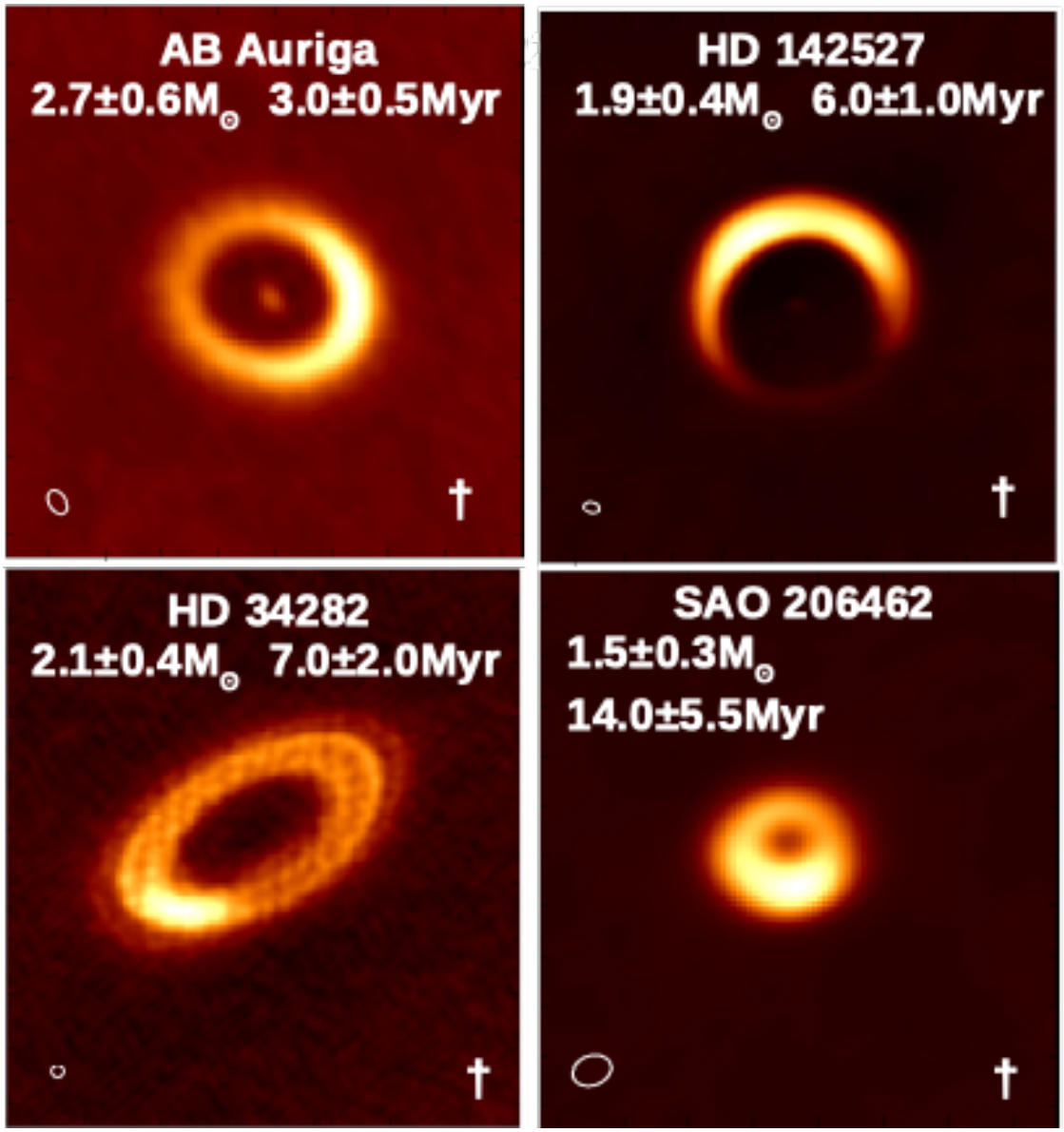

Figure 4.10: Images of the protoplanetary discs classified as Horseshoe in this study. The discs are ordered by age with the top left (AB Auriga) being the youngest and the lower right (SAO 206462) showing the oldest. The beam sizes used in each observation can be seen in the lower left of each image. These images of these discs, marked with the † in the lower right, have a field–of–view of 1000×1000 au.

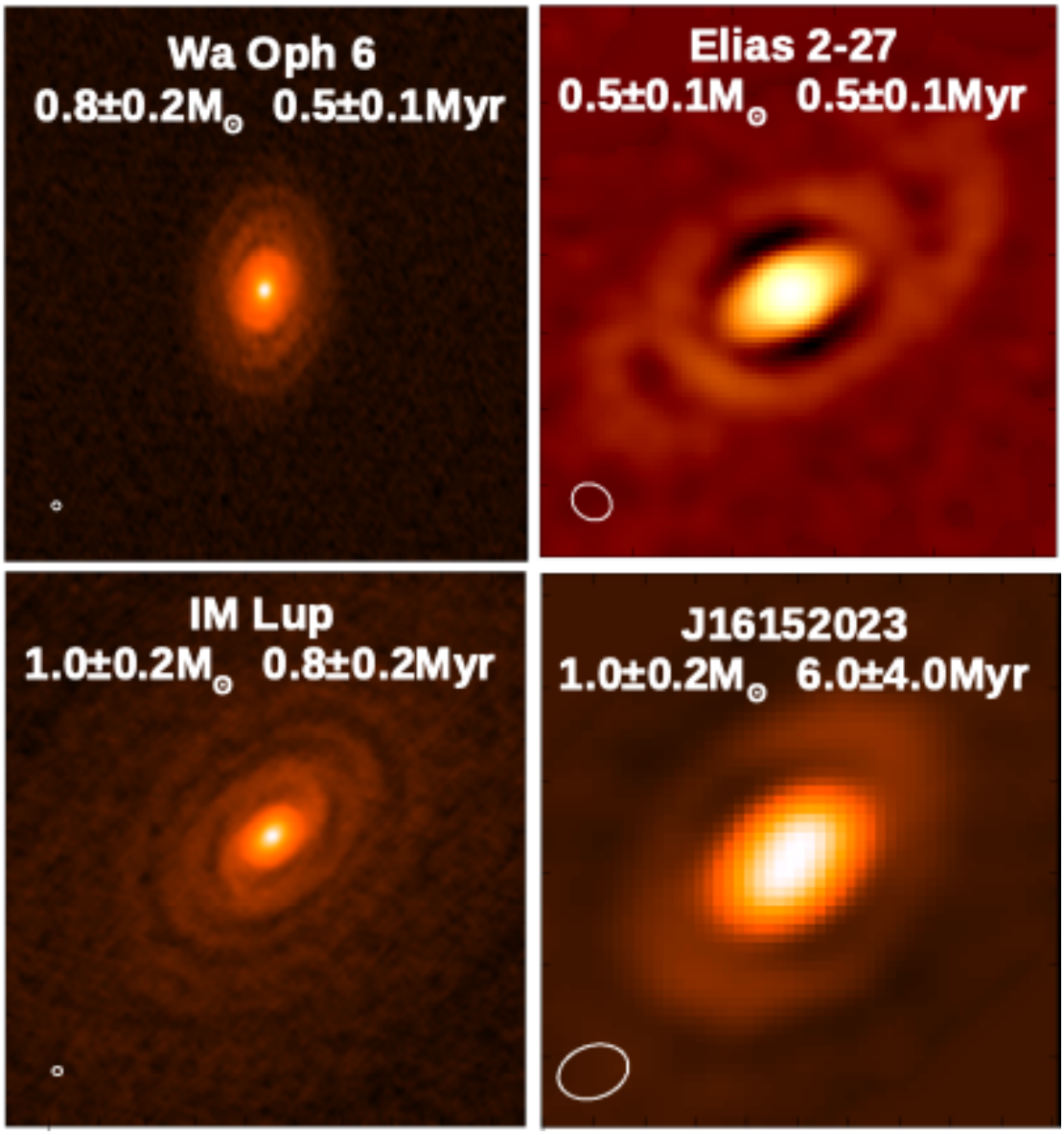

Figure 4.11: Images of the protoplanetary discs classified as Spiral in this study. The discs are ordered by age with the top left (Wa Oph 6) being the youngest and the lower right (J16152023) showing the oldest. The beam sizes used in each observation can be seen in the lower left of each image. Each image has a field–of–view of 500×500 au.

make use of the derived radii for the Horseshoe and Spiral discs in further analysis as there are only four discs in each category; an insufficient sample to derive meaningful relationships.

To study if the spatial extent of the Rim and Ring discs are correlated with age, we plot the disc radii against the derived stellar ages. This can be found in Figure 4.12. It should be noted that we have also excluded circumbinary discs from this analysis.

We fit the relation of the disc radius to age using the Bayesian linear regression method of Kelly (2007), *linmix*. This is done for the Rim and Ring discs independently. The *linmix* method of linear regression takes into account errors on both axes.

For the Rim discs, we find a negative trend relating the disc radius to the age of the system, with a slope of -1.3±1.0. This is shown by the yellow fit line in Figure 4.12. The large error on the slope may be due to the large errors associated with the calculated ages.

To assess the strength of this radius-age relation, we calculate a Pearson correlation coefficient for the trend. We find a slightly negative relationship with an r–value of -0.22. We measure a p–value of 0.24, indicating that this slight negative trend is not statistically significant. This result is in agreement with the work done by van der Marel et al. (2019) who showed that there was no correlation between the radius of the disc and the age of the system. Although they did show a negative trend for the oldest discs in the sample.

The relation of the disc radius of the Ring discs with age is studied in a similar manner. The blue fit in Figure 4.12 shows the regression fit for the Ring discs derived using *linmix*. A slightly negative trend with a slope of -2.1±4.0 is found for the Ring discs of our sample. We investigate the significance of this relationship by calculating a correlation coefficient. A slight negative correlation is found, similar

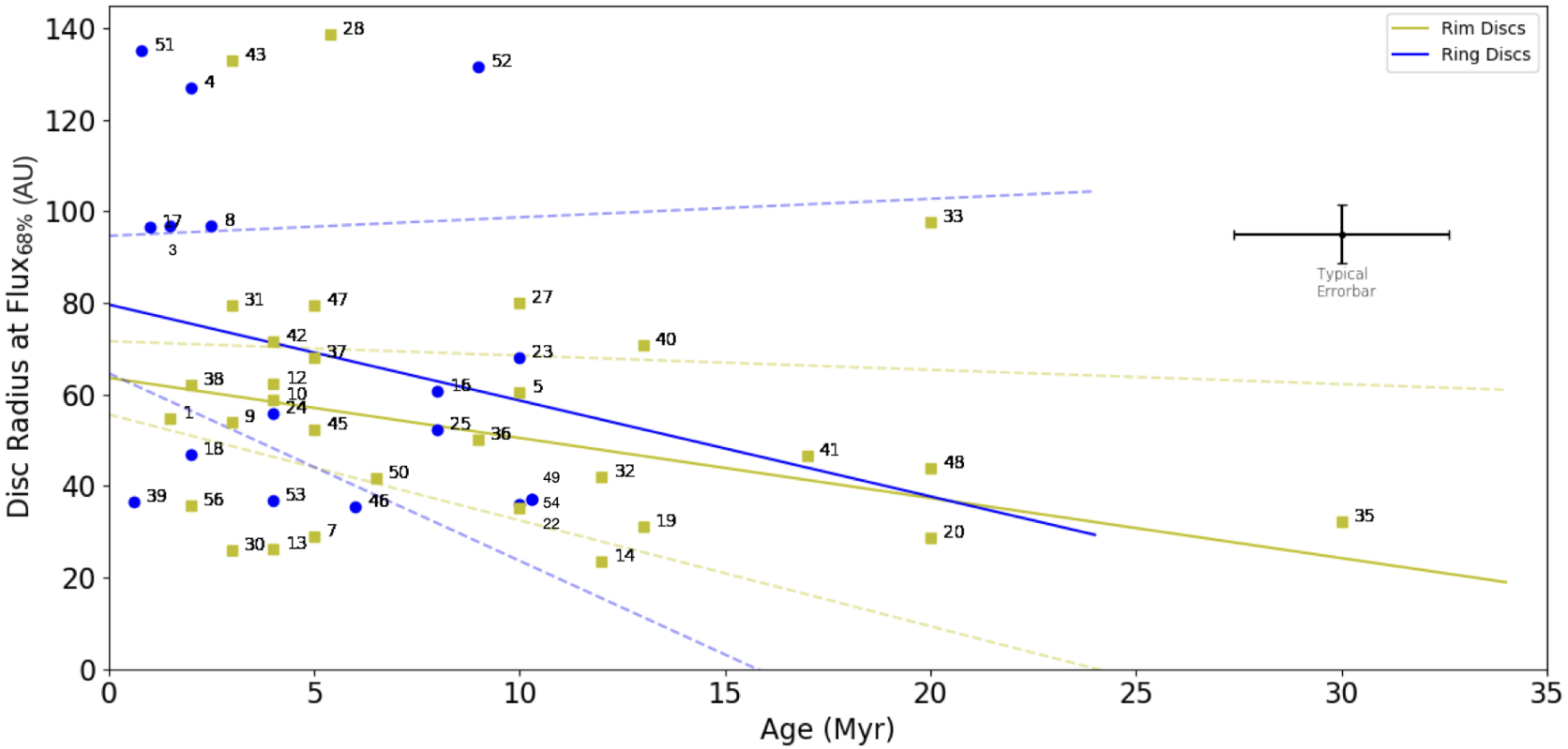

Figure 4.12: The radii of the protoplanetary discs containing 68 % of the total flux against the stellar age. The yellow markers indicate the Rim discs while the blue indicate the Ring discs. The trendlines have been calculated using the linear regression package *linmix* by Kelly (2007) and are depicted by the solid colour. The dashed lines represent the upper and lower bounds of the uncertainties on the trendlines for the Rim (yellow) and Ring (blue) discs.

to the Rim discs, with an r–value of -0.33. However, we again find that this result is not statistically significant as a p–value of 0.21 is derived. Therefore, we conclude that there is no correlation between the radial extent of the ring discs and the age of the system. This supports the conclusions reached by van der Marel et al. (2019) who found no trends relating the locations of gaps and rings to the age of the system.

4.6 Disc Radius - Stellar Mass Relation

The dependence of the disc radial extent with the stellar mass has also been investigated. The stellar masses have been calculated in Section 4.4 and can be found in Table 4.2. Figures 4.13, 4.14, 4.15, and 4.16 show the Rim, Ring, Horseshoe, and Spiral discs ordered according to stellar mass, respectively. The images of the observations of the low–mass stars show a field–of–view of 500×500au, while the stars, with a † symbol, are 1000×1000au. This again was again done to allow comparisons of the spatial extents of the discs.

In order to study if the radial extent of the discs depend on the stellar mass, we follow the same method adopted when studying the relation between the radius of the disc and the age of the system (Section 4.5). A graph relating the mass of the star and the radius of the disc can be seen in Figure 4.17. We have not examined trends for the Horseshoe and Spiral discs as we only have a small sample of discs. The trend relating to the Rim discs are shown in yellow, whilst the Ring discs are shown in blue.

We find positive trends relating the mass of the star to the outer radius of the disc for both the Rim and Ring discs. However, the large errors associated with the determination of the stellar mass make these trends uncertain.

The Rim discs have a slope of 5.3±10.9. We confirm that this is a weak relationship by calculating a correlation coefficient for the trend. We find an r–value of 0.24 with a p–value of 0.21 for the trend relating the stellar mass of the system to

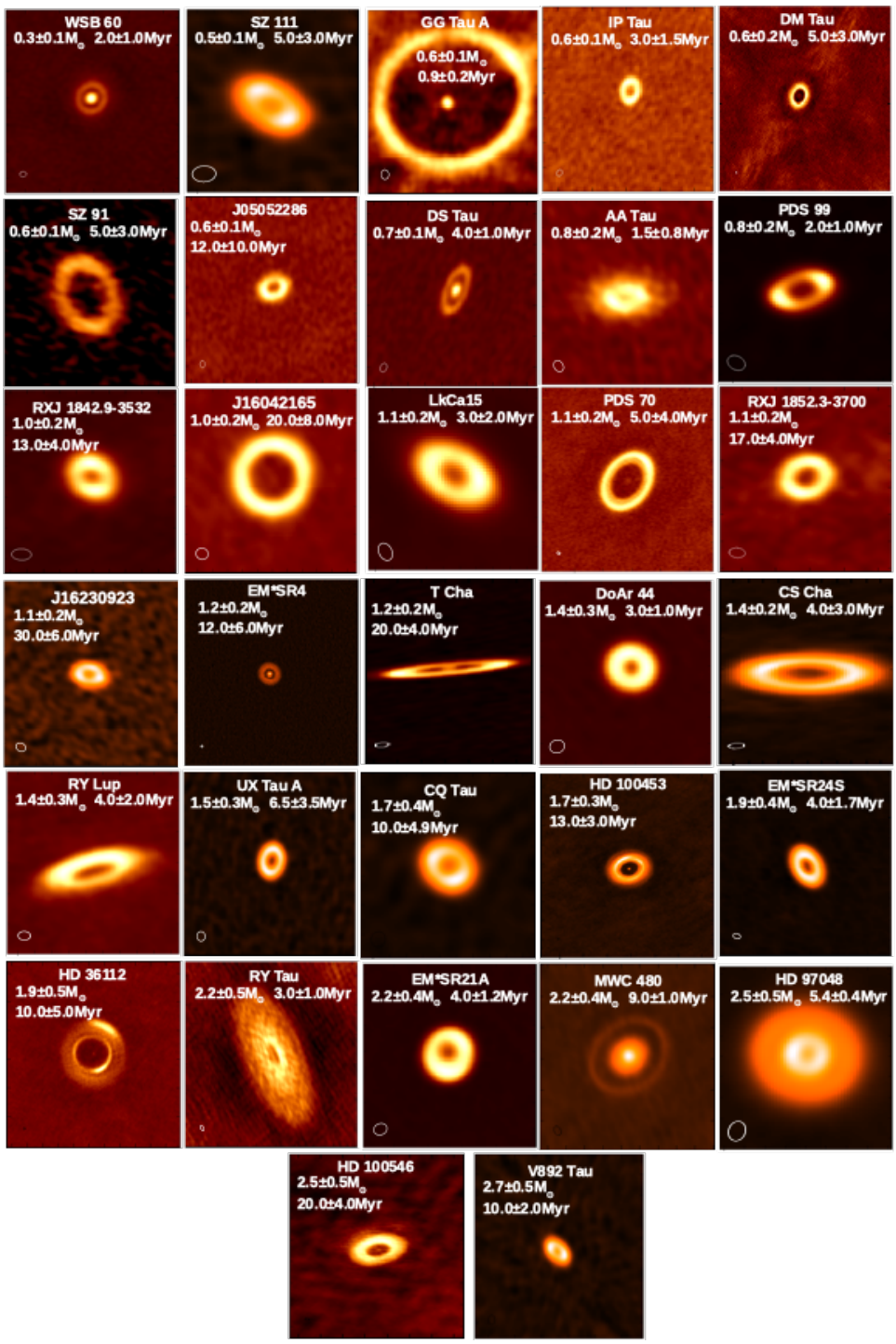

Figure 4.13: The Rim protoplanetary discs have been ordered according to stellar mass. WSB 60 has the lowest stellar mass of M_*=0.3$M_\odot$ whilst V892 Tau has a stellar mass of M_*= 2.7$M_\odot$. All images show a 500×500 au field–of–view with the exception of the discs labelled with a † in the lower right. These images have a field–of–view of 1000×1000 au.

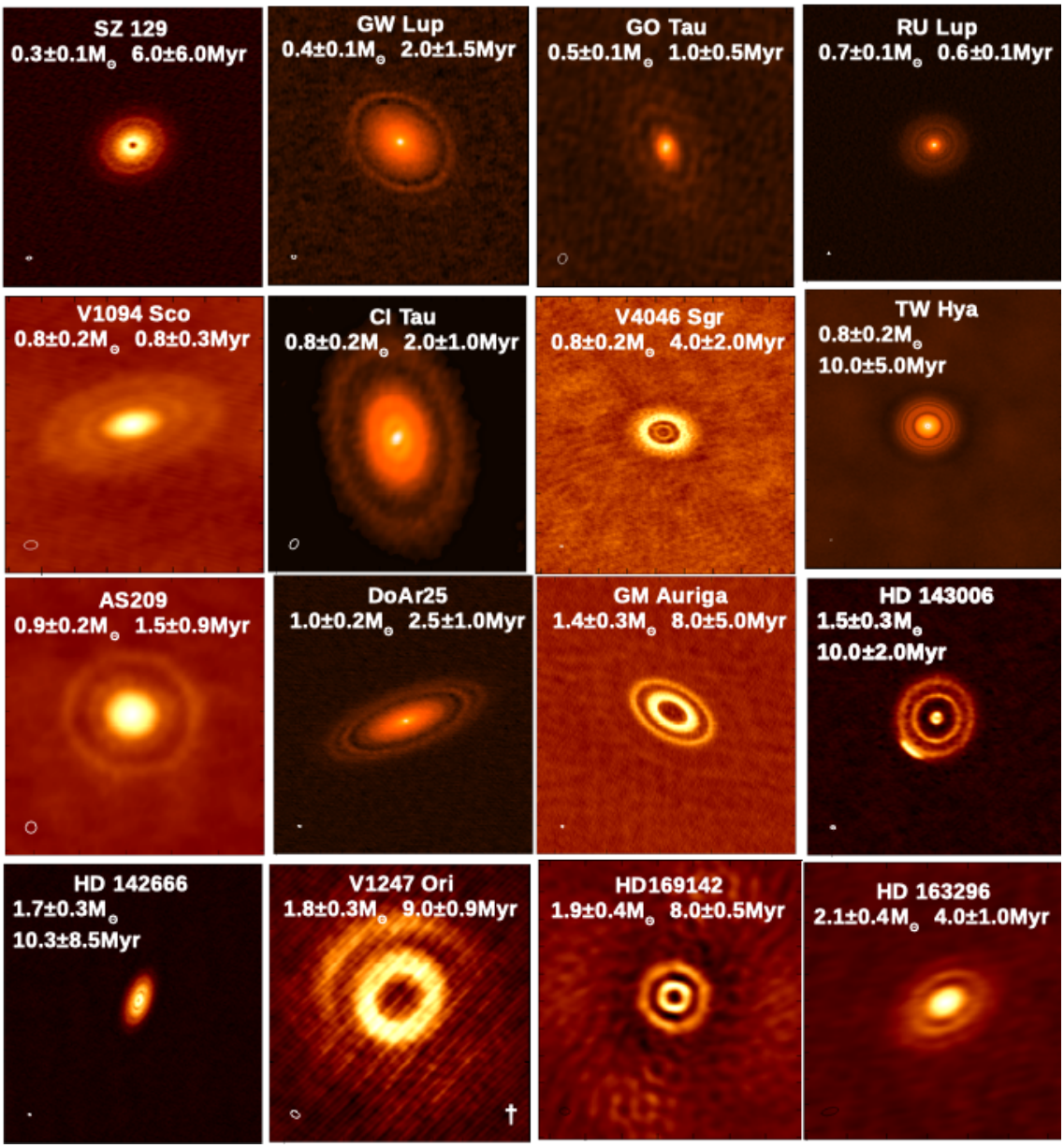

Figure 4.14: The Ring protoplanetary discs have been ordered according to stellar mass. SZ 129 has the lowest stellar mass of M_*=0.3M$_\odot$ whist HD 163296 has a stellar mass of M_*=2.1M$_\odot$. All images show a 500×500 au field–of–view. The discs with the † in the lower right show a 1000×1000 au field–of–view.

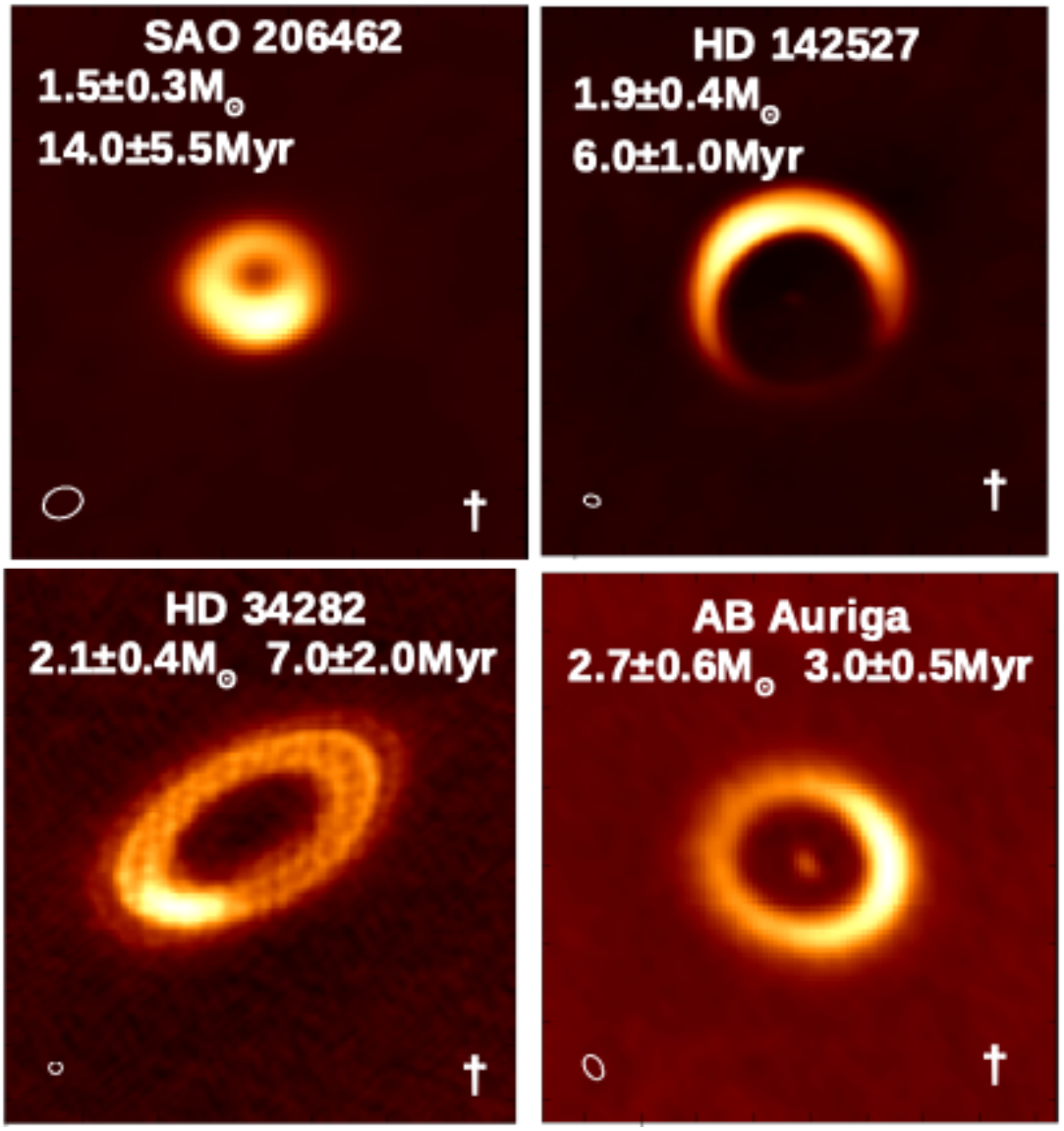

Figure 4.15: The Horseshoe protoplanetary discs have been ordered according to stellar mass. SAO206462 has the lowest stellar mass of M_*=1.5M$_\odot$ whilst AB Auriga has a stellar mass of M_*=2.7$_\odot$. These images of these discs, marked with the † in the lower right, show a 1000×1000 au field–of–view.

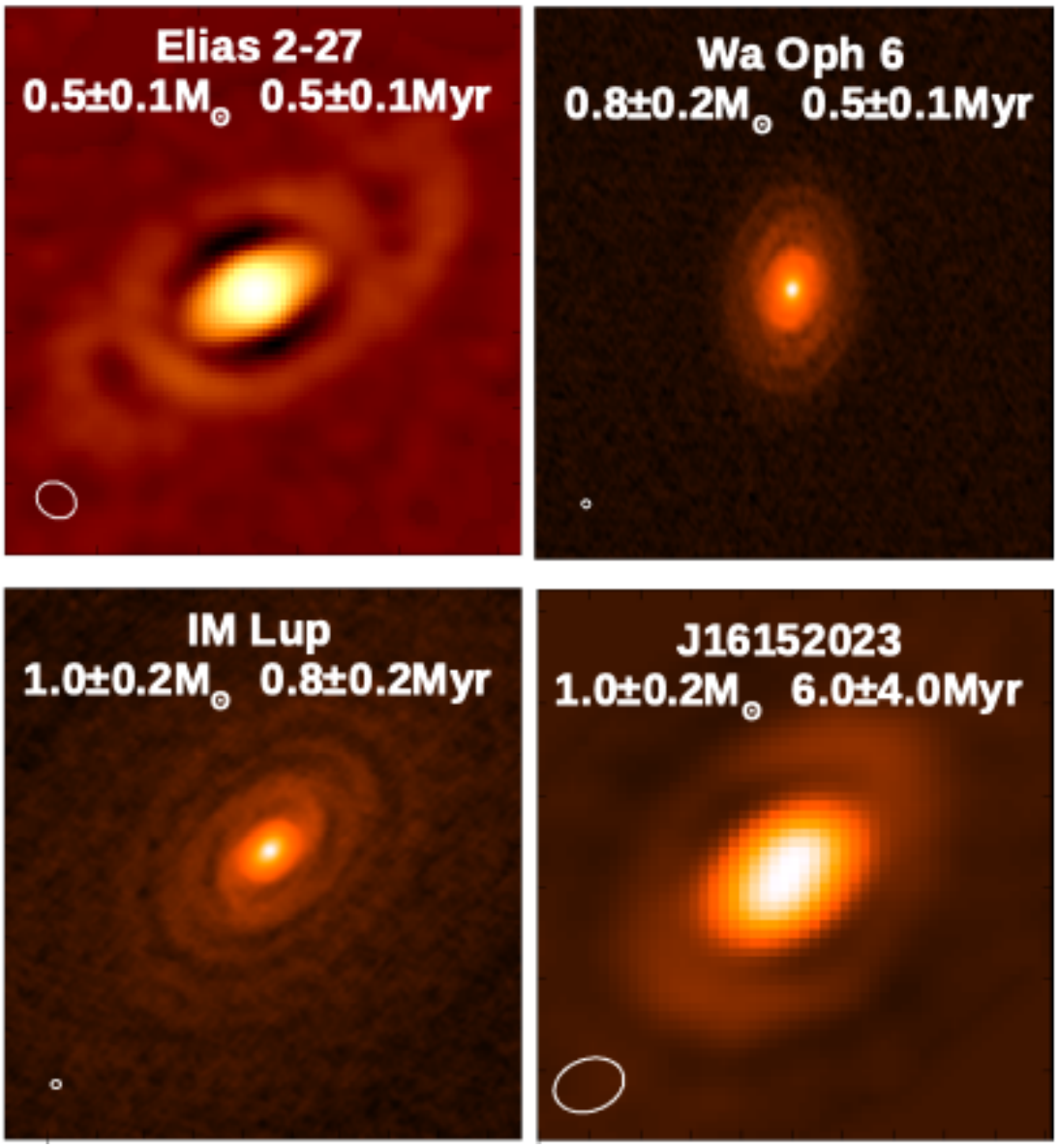

Figure 4.16: The Spiral protoplanetary discs have been ordered according to stellar mass. Elias 2–27 has the lowest stellar mass of M_*=0.5M$_\odot$ whilst J16152023 has a stellar mass of M_*=1.0$_\odot$. All images show a 500×500 au field–of–view.

the radius of the disc.

The slope relating the radius to the stellar mass of the Ring discs is equal to 6.3±20.0. The large error associated with this slope indicates that this may be a weak relationship. We calculate a correlation coefficient of 0.03 for this trend with a p–value of 0.92. This high p-value indicates that this slightly positive trend may not be statistically significant.

4.7 Discussion

4.7.1 Properties of Sample

The number of discs in each category can be seen in Figure 4.18. Of the 56 discs studied in this sample, Rim discs appear to be the most populous category in our sample featuring 32 discs. Sixteen discs have been classified as having rings. Horseshoe and Spiral discs are least populous, with four discs in each category.

Although the majority of our sample have been classified as a Rim disc, it should be noted that cavities are the easiest substructure to be detected with ALMA. As a result, the large number of Rim discs may be a selection effect due to extensive interest in them. This is further discussed in Section 4.7.2 below.

While Horseshoe shaped discs have been placed in their own category, they all feature a single ring of emission on the edge of a large cavity and could also be classified as Rim discs. This would increase the number of Rim discs to 36, more than 60% of our sample; intensifying the notion that the presence of a Rim seems to be a common feature in the current population of protoplanetary discs observed at mm-wavelengths.

We now investigate the properties of the host stars of each disc category.

Horseshoe: From Figure 4.1 we can see that Horseshoe shaped discs are most commonly found around intermediate–mass stars. These stars are all Herbig Ae/Be

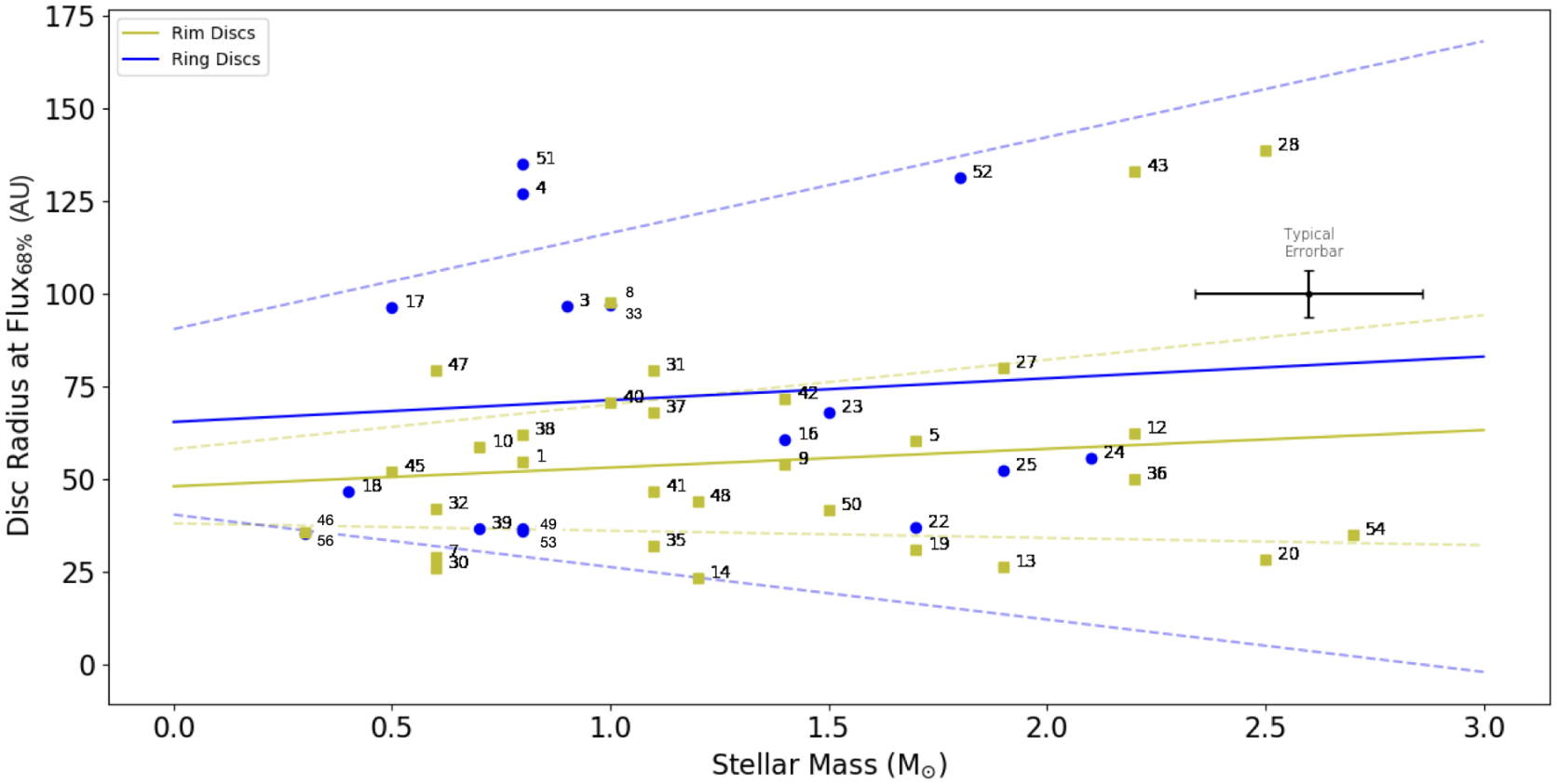

Figure 4.17: The radii of the protoplanetary discs containing 68 % of the total flux against the stellar mass. The yellow markers indicate the Rim discs while the blue indicate the Ring discs. The trendlines have been calculated using the linear regression package *linmix* by Kelly (2007) and are depicted in solid colour. The dashed lines represent the upper and lower bounds of the uncertainties on the trendlines for the Rim (yellow) and Ring (blue) discs.

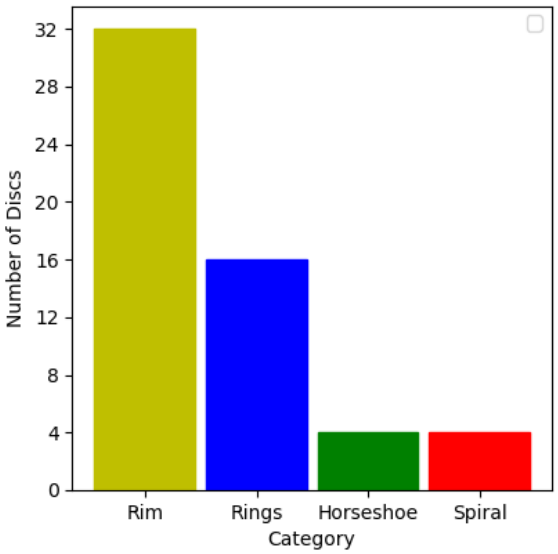

Figure 4.18: A total of 56 protoplanetary discs have been studied in our sample. Rim and Ringed protoplanetary discs are the most common discs that have been observed with ALMA. Horseshoe and Spiral discs are the least common types.

type stars, with their high effective temperatures (T_{eff} > 6000 K). The lack of Horseshoe shaped protoplanetary discs around low–mass stars may indicate that the formation mechanism responsible for forming a pile–up of dust grains on one side of the disc preferentially occurs in higher mass stars.

Spiral: Spiral discs surround just four host stars in our sample. All systems in this category are single star systems and are Class II T–Tauri type stars with stellar masses $\leq 1.0 M_{\odot}$. Due to the small number of both Horseshoe and Spiral discs, we cannot make any real conclusions about the characteristics of the host stars that these discs surround.

Rings: A ringed protoplanetary disc is more commonly found around low–mass stars compared to intermediate–mass stars, which can be seen in Figure 4.1. Our sample contains 43 discs surrounding low–mass stars, of which 14 have a ringed substructure. Two intermediate–mass stars (HD 169142 and HD 163296), are surrounded by a ringed disc, out of a possible 13 intermediate–mass stars. Therefore,

33% of the low–mass stars are surrounded by a ringed disc with a Poisson error of 9%. While only 15% of the intermediate–mass stars are surrounded by a ringed disc with an error of 11%.

This conclusion may, however, be affected by small number statistics as ALMA has observed more low-mass stars than intermediate-mass objects (see Section 4.7.2.2). Using n-root statistics, the number of low–mass stars surrounded by a ringed disc is 10–18, this is equivalent to ∼18–43% of the full sample of low–mass (43 objects). The number of intermediate–mass stars surrounded by a ringed disc is between 1–3 - or around 8–23% of the full sample of 13. The overlap between the range of discs featuring a rim of dust and a ring of emission indicate that the results reached above may be affected by small number statistics.

The low–mass stars which host a ringed protoplanetary disc have a wide range of luminosities and temperatures. GW Lup has a luminosity of 0.3±0.2 $L_{\odot}$ and a temperature of 3600±170 K, while HD 143006 has a much greater temperature and luminosity at 5600±260 K and 3.8±1.3 $L_{\odot}$. Therefore, ringed protoplanetary discs can form around low–mass stars with a range of stellar properties.

Rim: Thirty two discs in our sample have been classified as having a Rim; a single ring of dust surrounding a large cavity devoid of dust and/or gas. It is clear from Figure 4.1 that the hosts stars that are surrounded by a Rim disc cover both stellar temperature and luminosity quite uniformly. There are somewhat more Rim discs around low–mass stars than around intermediate–mass stars (24 low–mass stars and eight intermediate–mass stars). However, due to the nature of our classification scheme, all four of the high–mass Horseshoe discs could also be classified as Rim discs. Therefore, a single ring of emission on the edge of a large cavity appears to be a very common feature seen in protoplanetary discs regardless of temperature or luminosity.

There are numerous ways to form a rim of dust around a star and this may

explain why they are a frequent substructure seen in protoplanetary discs. A planet present in a disc would cause a pressure maximum to form. As dust radially migrates inwards from the outer regions of the disc it hits this pressure maximum. This would cause a pile up of dust grains to form in a ring around the orbit of the forming protoplanet (Paardekooper & Mellema 2006; Fouchet et al. 2007).

In order to detect if a rim has been formed due to a planetary companion, observations of CO isotopologues can be made. Gas gaps have previously been shown to have been carved out by a planetary or substellar companion (Bruderer et al. 2014; van der Marel et al. 2015, 2016a; Dong et al. 2017; Boehler et al. 2017, 2018). In recent work, Ubeira Gabellini et al. (2019) were able to show that depressions in both continuum and CO isotopologue ring maps could be caused by an embedded planet within the disc.

A rim can also form in the disc due to photoevaporation. UV or x-ray radiation from the central star can heat up the gas in the disc. This can cause the gas to dissociate and become unbound. The gas is accelerated away in the form of a thermally driven wind due to the pressure gradient in the disc. Previous models of photoevaporation have shown the formation of ring-shaped pressure maxima at ∼tens of au (Alexander et al. 2014; Ercolano & Pascucci 2017), with cavities interior to these maxima depleted, or void, of material.

4.7.2 Selection Effects and Limitations

4.7.2.1 Angular Resolution

We have shown that a rim of emission is a common substructure seen in the protoplanetary discs observed with ALMA. However, this may be due to a selection bias. Transition discs have explicitly been targeted by ALMA, both in individual projects as well as part of surveys (e.g. DSHARP (Andrews et al. 2018a)). This is because rim discs are easily detected, even at lower resolutions. More complex substructure,

such as spiral and horseshoes, may only be detected at higher resolutions.

The angular resolutions of the discs studied in this work are shown in Table 4.3. These discs were observed with a higher resolution than majority of the ALMA discs (see Table A.1 for the angular resolution of all the ALMA protoplanetary discs observed during Cycles 0–5).

Table 4.3: The angular resolutions of the protoplanetary discs featuring substructure studied in this work. The ALMA project code of the disc observations are also provided.

ID #	Name	Angular Resolution (Arcsec)	ALMA Project Code
1	AA Tau	0.19	2015.1.01017.S
2	AB Auriga	0.14	2012.1.00303.S
3	AS 209	0.15	2015.1.00486.S
4	CI Tau	0.07	2017.A.00014.S
5	CQ Tau	0.21	2013.1.00498.S
6	CS Cha	0.03	2017.1.00969.S
7	DM Tau	0.02	2017.1.01460.S
8	DoAr25	0.03	2016.1.00484.L
9	DoAr44	0.23	2012.1.00158.S
10	DS Tau	0.09	2016.1.01164.S
11	Elias 2–27	0.2	2013.1.00498.S
12	EM* SR 21A	0.23	2012.1.00158.S
13	EM* SR 24S	0.14	2013.1.00091.S
14	EM* SR 4	0.02	2016.1.00484.L
15	GG Tau	0.14	2013.1.00105.S
16	GM Auriga	0.02	2017.1.01151.S
17	GO Tau	0.10	2016.1.01164.S

Table 4.3: - continued.

ID #	Name	Angular Resolution (Arcsec)	ALMA Project Code
18	GW Lup	0.02	2016.1.00484.L
19	HD 100453	0.03	2017.1.01424.S
20	HD 100546	0.03	2015.1.00806.S
21	HD 142527	0.14	2012.1.00631.S
22	HD 142666	0.20	2013.1.00498.S.
23	HD 143006	0.40	2015.1.00964.S
24	HD 163296	0.17	2015.1.00847.S
25	HD 169142	0.13	2012.1.00799.S
26	HD 34282	0.14	2013.1.00658.S
27	HD 36112	0.03	2017.1.00492.S
28	HD 97048	0.03	2016.1.00826.S
29	IM Lup	0.39	2013.1.00226.S
30	IP Tau	0.09	2016.1.01164.S
31	LkCa15	0.17	2012.1.00870.S
32	J05052286+2531312	0.47	2016.1.01164.S
33	J16042165–2130284	0.16	2015.1.00888.S
34	J16152023–3255051	0.22	2011.0.00724.S
35	J16230923–2417047	0.13	2013.1.00157.S
36	MWC 480	0.11	2016.1.01164.S
37	PDS 70	0.08	2017.A.00006.S
38	PDS 99	0.24	2015.1.01301.S
39	RU Lup	0.02	2016.1.00484.L
40	RXJ1842.9–3532	0.14	2015.1.01083.S
41	RXJ1852.3–3700	0.14	2015.1.01083.S

Table 4.3: - continued.

ID #	Name	Angular Resolution (Arcsec)	ALMA Project Code
42	RY Lup	0.14	2017.1.00449.S
43	RY Tau	0.02	2017.1.01460.S
44	SAO 206462	0.35	2012.1.00870.S
45	SZ 111	0.28	2013.1.00220.S
46	SZ 129	0.02	2016.1.00484.L
47	SZ 91	0.13	2013.1.00663.S
48	T Cha	0.13	2012.1.00182.S
49	TW Hya	0.04	2017.1.00520.S
50	UX Tau	0.14	2013.1.00105.S
51	V1094 Sco	0.24	2016.1.01239.S
52	V1247 Ori	0.01	2015.1.00986.S
53	V4046 Sgr	0.54	2017.1.01167.S
54	V892 Tau	0.14	2013.1.00498.S
55	Wa Oph 6	0.03	2016.1.00484.L
56	WSB 60	0.10	2016.1.01042.S

We have plotted a histogram of the angular resolutions with which the protoplanetary discs were observed at. This is shown in Figure 4.19. From Figure 4.19 we can see that the majority of the ALMA observations of protoplanetary discs were not taken at a high enough resolution to resolve substructure.

We have looked at 794 protoplanetary discs; of them we have identified 56 that show substructure. As discussed in Section 4.2, we have omitted young, embedded discs as well as debris discs. The majority of our discs showing substructure (46) were observed with a resolution higher than 0.22". This limit is indicated by the

red dashed line on Figure 4.19. From the complete sample of ALMA discs looked at, 171 discs were observed with a resolution of 0.22" or better. Therefore ∼27% of the discs observed with ALMA with a resolution 0.22" or greater have resolvable substructure.

A resolution of 0.22" is still considered relatively moderate with ALMA. Studies explicitly targeting transition discs and discs with known substructure aim for resolutions of ≈0.1" or better. A total of 52 protoplanetary discs at a resolution of 0.1" or better have been observed with ALMA. This limit is shown as the green line on the histogram (Figure 4.19). Of these 52 discs, 22 have been shown to have substructure and have been classified here. This is approximately 42% of the discs.

Long et al. (2019) studied 32 protoplanetary discs with ALMA with a resolution of ≈0.12". They found that just under half of the discs showed dust gaps and rings. In agreement with the 42% we have found here for a similar resolution limit.

The DSHARP project, however, has found that all the discs they observe at a very high resolution of ≈0.035" feature substructure (Andrews et al. 2018a). For a resolution limit of $\lesssim$0.04", we find that the fraction of discs showing substructure increases to 60%. Therefore, in order to resolve substructure in the majority of the known disc population with ALMA, very high resolutions of ≈0.035" may be needed - much higher than the resolutions of the observations of protoplanetary discs observed by ALMA thus far.

4.7.2.2 ALMA Observational Biases

We have studied 56 protoplanetary discs that cover a wide parameter space. Both low and intermediate–mass stars have been looked at, with a wide range of ages, temperatures, and luminosities. A plot of the relation between the stellar masses of our sample, and their corresponding ages, has been made in order to determine if there are any observational biases in our sample (see Figure 4.20).

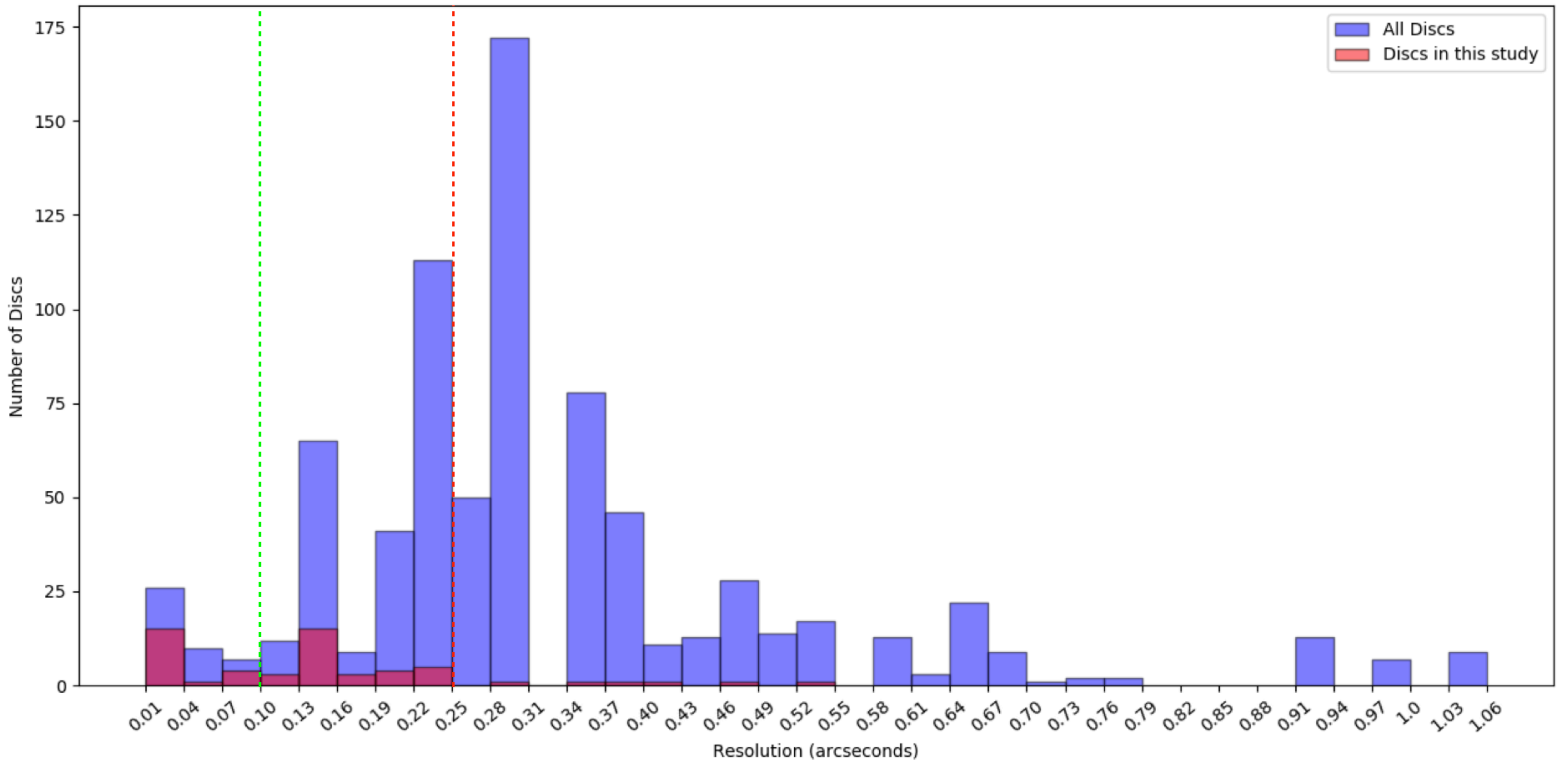

Figure 4.19: The resolutions of the entire sample of 794 protoplanetary discs, observed during Cycles 0–5, in the ALMA Archive. Details of the discs can be found in Table A.1. The discs have been binned with resolutions of 0.03 arcseconds. The red line indicates the resolution limit below which majority of the discs featuring substructure were observed at. The green line indicates a resolution limit of 0.1", below which is considered 'high resolution' with ALMA. We have highlighted, in pink, the discs identified as containing substructure and studied in this work.

There are a lack of old, low–mass stars that show protoplanetary substructure as well as significantly fewer old high mass stars. Although old, low–mass stars have been previously observed (Barenfeld et al. 2016), deep, high resolution observations have not been conducted with ALMA. This may indicate why there is a lack of old, low–mass stars in our sample.

We also see that there are significantly fewer young, intermediate and high–mass stars in our sample. The discs surrounding intermediate–mass stars have all gone by ∼10 Myr, whereas the low–mass discs last to ∼15-20Myr. This could be attributed to the fact that higher mass stars evolve on a much quicker timescale than low–mass stars, and thus the discs are dispersed on a shorter timescale. As well as this, higher mass stars may still be surrounded by an envelope, whilst actively accreting material, even as they evolve to the main-sequence phase (Beuther et al. 2007). Therefore, imaging a protoplanetary disc around a high–mass star may be problematic as the young disc may still be embedded.

Our sample contains more low–mass stars than intermediate–mass. However, it is known that low–mass stars are more common than intermediate and high mass stars, as would be expected from a standard Salpeter-like IMF (Salpeter 1955; Kroupa 2001; Chabrier 2003). Therefore, the finding that Ring discs are more common around low–mass stars may be a selection bias.

4.7.2.3 Comparison to Full ALMA Sample

A total of 794 protoplanetary discs were looked at in this work. Omitting young, embedded discs, as well as debris discs, we have identified 56 discs that show some kind of substructure, around 7% of all discs. This is in contrast to Long et al. (2019) and work by the DSHARP project (Andrews et al. 2018a), who find that at least 50% of the discs studied show substructure. As discussed in Section 4.7.2.1 above, this is due to the majority of ALMA observations being conducted at lower

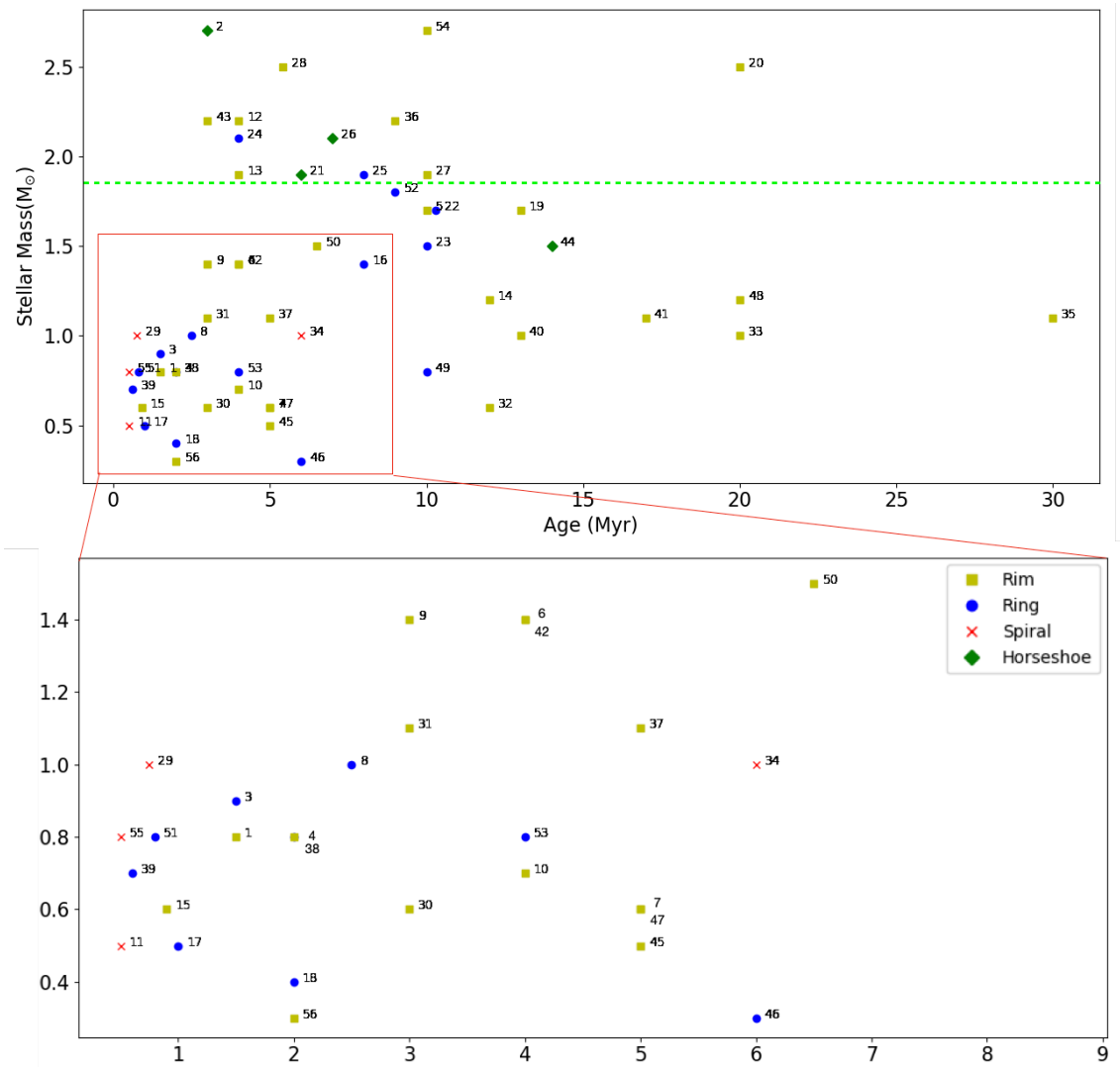

Figure 4.20: Stellar mass with age for our sample. The coloured markers indicate the category assigned to each protoplanetary disc in Section 4.3. The green dashed line indicates the limit between low–mass and intermediate–mass, as defined in Section 4.2.

resolutions than studied in these works.

The 794 protoplanetary discs studied here surround Class I, II, and III protostars. The protoplanetary disc surveys conducted by ALMA thus far, however, have focussed mainly on Class II discs from several star-forming regions. These include Chamaeleon I (Pascucci et al. 2016), IC 348 (Ruíz-Rodríguez et al. 2018), Lupus (Ansdell et al. 2016, 2018), NGC 2024 (van Terwisga et al. 2020), Ophiuchus (Cox et al. 2017; Cieza et al. 2019), the Orion Nebula Cluster (Eisner et al. 2018), σ Ori (Ansdell et al. 2017), Taurus (Akeson & Jensen 2014; Akeson et al. 2019; Long et al. 2018, 2019), and Upper Scorpius (Barenfeld et al. 2016). Although these surveys focussed on Class II protoplanetary discs, the star-forming regions have a range of ages. Therefore, the Class II discs in the ALMA archive are at different evolutionary stages. The sample of 56 discs studied here is representative of that. We have protostars from 11 different star-forming regions, with a range of ages (see Table A.2 in Appendix A.1). As well as this, there is a diverse range of calculated ages for the protostars; the youngest being Wa Oph 6 ($0.5 \pm 0.1 Myr$) and the oldest being J160230923 ($30.0 \pm 5.0 Myr$). Therefore, we have studied systems with a comparable range of Class II evolutionary states as that found in the ALMA Archive.

4.7.3 Substructure Dependence on Stellar Age

4.7.3.1 Rim Discs

The Rim discs, ordered by age, can be seen in Figure 4.8. The ages of the stars surrounded by a Rim protoplanetary disc varies quite widely. The youngest disc is a T–Tauri star with an age of 0.9 ± 0.2 Myr while J16230923 is the oldest disc with an age of 30.0±6.0 Myr. Therefore, a Rim is a long lasting structure of a protoplanetary disc. The intermediate–mass stars with Rims appear in the later stages of the evolutionary plot. However this may simply be an observational bias as there are very little observations of young intermediate–mass stars.

4.7.3.2 Ring Discs

The low–mass stars that feature protoplanetary rings have a wide range of ages, from 0.6 Myr for RU Lup to 10.3 Myr for HD 142666. The spread of ages imply that rings can form very early on in the evolution of the disc and are long lasting substructures or that they can form at a range of evolutionary stages.

Recent observations of HL Tau, Elias 2–24 and GY 91 revealed protoplanetary discs with multiple rings and gaps (ALMA Partnership et al. 2015; Dipierro et al. 2018; Sheehan & Eisner 2018). These young stellar objects all have ages less than 1 Myr. Therefore, planet formation is thought to begin very early on in the evolution of the disc. As the protoplanets grow in mass and size, they are able to carve gaps in the dust and gas of the protoplanetary disc forming rings. Mamajek (2009) showed that planet formation could end between 2-3 Myr as half of the protoplanetary discs in their sample disappeared by this time.

The majority of the low–mass discs in our sample have derived ages greater than 2 Myr (in part due to the removal of young, embedded discs from the sample), meaning that it is possible for their gaps and rings to have been formed by planets. In order to confirm this, similarly to rim discs, additional CO isotopologue observations could be carried out to determine the origin of the dust rings. However, the gas gaps in ring discs are harder to constrain, as discussed by Isella et al. (2016).

Other mechanisms, such as the accumulation and growth of materiel at various ice lines (Zhang et al. 2015) may be responsible for the ringed substructure. However, this method was recently put into question by Huang et al. (2018) and van der Marel et al. (2019) who showed that the gap radii in ringed protoplanetary discs do not correspond with common ice lines. The analysis conducted in this work cannot determine the precise origins of the protoplanetary rings seen.

4.7.3.3 Horseshoe Discs

Figure 4.10 shows the Horseshoe discs arranged according to age. There are a wide range of ages for the protoplanetary discs that feature a Horseshoe morphology. AB Auriga, the youngest star, has an age of 3.0±0.5 Myr, while the oldest disc, HD100546, is 20.0±4.0 Myr old. Therefore, the horseshoe-like morphology may be caused by a mechanism that occurs in the later evolutionary stage of a protoplanetary disc. However, due to our small sample and a lack of young intermediate stars observed with ALMA at a high resolution, we cannot make any definitive conclusions about this.

There appears to be no variation in the morphological structure of the discs as they get older. It can be seen that the radius of the disc is not correlated with the age of the star. The radii of the discs surrounding the intermediate–mass stars, AB Auriga, HD 142527, HD 34282, and SAO 206462 are 163±16 au, 186±27 au, 187±28 au and 120±62 au, respectively. The values were calculated in Section 4.5.1 above. However, our sample only features four protoplanetary discs with a horseshoe morphology, therefore, any conclusions may be due to small number statistics.

4.7.3.4 Spiral Discs

The T–Tauri stars featuring a spiral disc have young ages ($\sim$ 1.0 Myr when considering the lower age limit of J16152023). Figure 4.11 shows the spiral discs arranged according to age. The stars are relatively young, hence we can assume that spiral arms form very early on in the evolution of a protoplanetary disc. The lack of older, low–mass stars featuring a disc with a Spiral substructure may imply that the spiral arms are not long lasting; however due to the small sample of Spiral discs, we cannot make any definitive conclusions about this.

4.7.4 Comparisons to Scattered Light Observations

Observations of protoplanetary discs have previously been made at a number of different wavelengths, including optical, near–infrared and sub-mm. These different wavelengths probe different regions of the protoplanetary disc.

Observations at near-infrared wavelengths trace the smallest dust grains (typically μm–sized) in the inner most parts and surface of the protoplanetary disc. At these wavelengths the dust is optically thick. As the observing wavelength approaches mm/sub-mm, the dust in the midplane of the disc begins to become optically thin. The largest dust grains lie in the midplane of the disc and this is where the majority of the disc mass lies.

Substructures can be seen in protoplanetary discs in both millimetre and polarised scattered light observations. Garufi et al. (2018) studied the morphology of 58 protoplanetary discs in scattered light and classified them according to the following categories: Rim, Rings, Spirals, Faint, Giant, Inclined, and Small. Our sample has 36 protoplanetary discs in common with the sample studied by Garufi et al. (2018). Five discs have been classified as Spiral, five discs as Giant, five as Faint, six as Rim, eleven as Rings, three as Inclined, and one as Small.

We have discarded the Faint, Giant, Small and Inclined categories as they are not morphological structures and have reclassified these discs according to our classification. The scattered light observation of RU Lup, SZ111, CI Tau, MWC 480 and GW Lup were classified as Faint in Garufi et al. (2018), while HD 142666, T Cha and RY Lup were classified as Inclined, and CS Cha as Small. Since there are no clear substructures in the these discs, and they do not fit in any of our classification categories, we have discarded them from the common sample, leaving 28 discs for comparison.

Following the characteristics outlined in Section 4.3, three of the five discs classified as Giant by Garufi et al. (2018) have been classified as Spiral discs (AB Auriga,

HD 142527 and HD 100546). These three discs all surround intermediate–mass stars. The remaining two low–mass stars have been classified as Rim discs (GG Tau A and GM Auriga). The common sample and their classifications, including the newly reclassified Giant discs, can be found in Table 4.4.

Table 4.4: The discs studied in both this work at mm-wavelengths and by Garufi et al. (2018) in scattered light.

ID #	Name	Classification at sub–mm wavelengths	Classification in scattered light
2	AB Auriga	Horseshoe	Spiral
3	AS 209	Rings	Rings
5	CQ Tau	Rim	Spirals
9	DoAr44	Rim	Rim
12	EM*SR 21A	Rim	Rings
15	GG Tau	Rim	Rim
16	GM Auriga	Rings	Rim
19	HD 100453	Rim	Spirals
20	HD 100546	Rim	Spirals
21	HD 142527	Horseshoe	Spirals
23	HD 143006	Rings	Rings
24	HD 163296	Rings	Rings
25	HD 169142	Rings	Rings
26	HD 34282	Horseshoe	Spirals
27	HD 36112	Rim	Spirals
28	HD 97048	Rim	Rings
29	IM Lup	Spirals	Rings
31	LkCa15	Rim	Rim
33	J16042165–2130284	Rim	Rim

Table 4.4: - continued.

ID #	Name	Classification at sub–mm wavelengths	Classification in scattered light
34	J16152023–3255051	Spirals	Rings
37	PDS 70	Rim	Rim
41	RXJ1852.3–3700	Rim	Rings
44	SAO 206462	Horseshoe	Spirals
47	SZ 91	Rim	Rim
49	TW Hya	Rings	Rings
50	UX Tau	Rim	Rim
52	V1247 Ori	Rings	Spirals
53	V4046 Sgr	Rings	Rings

We compare the morphology seen in scattered light with the morphology seen in submillimetre for the 27 protoplanetary discs in Figure 4.21. The columns indicate the morphology assigned by Garufi et al. (2018) while the rows indicate the morphologies assigned in this work.

All of the discs showing a Horseshoe–shaped morphology in sub-mm continuum emission have a Spiral morphology in scattered light. The disc surrounding SAO 206462 was shown to have a mass of $\sim 0.002 M_{\odot}$ (Pérez et al. 2014), while the disc masses of AB Auriga, HD 142527, and HD 100546 have been shown to be $0.01 M_{\odot}$ (Tang et al. 2012), $0.1 M_{\odot}$ (Perez et al. 2015) and $\sim 0.03 M_{\odot}$ (Kama et al. 2016) respectively. The wide range of disc masses may indicate that disc mass plays little role in the type of morphology seen in discs in both sub-mm and scattered light.

This is supported when looking at the disc masses of systems with other morphologies. The disc surrounding HD 97048 features a Rim in sub-mm wavelengths

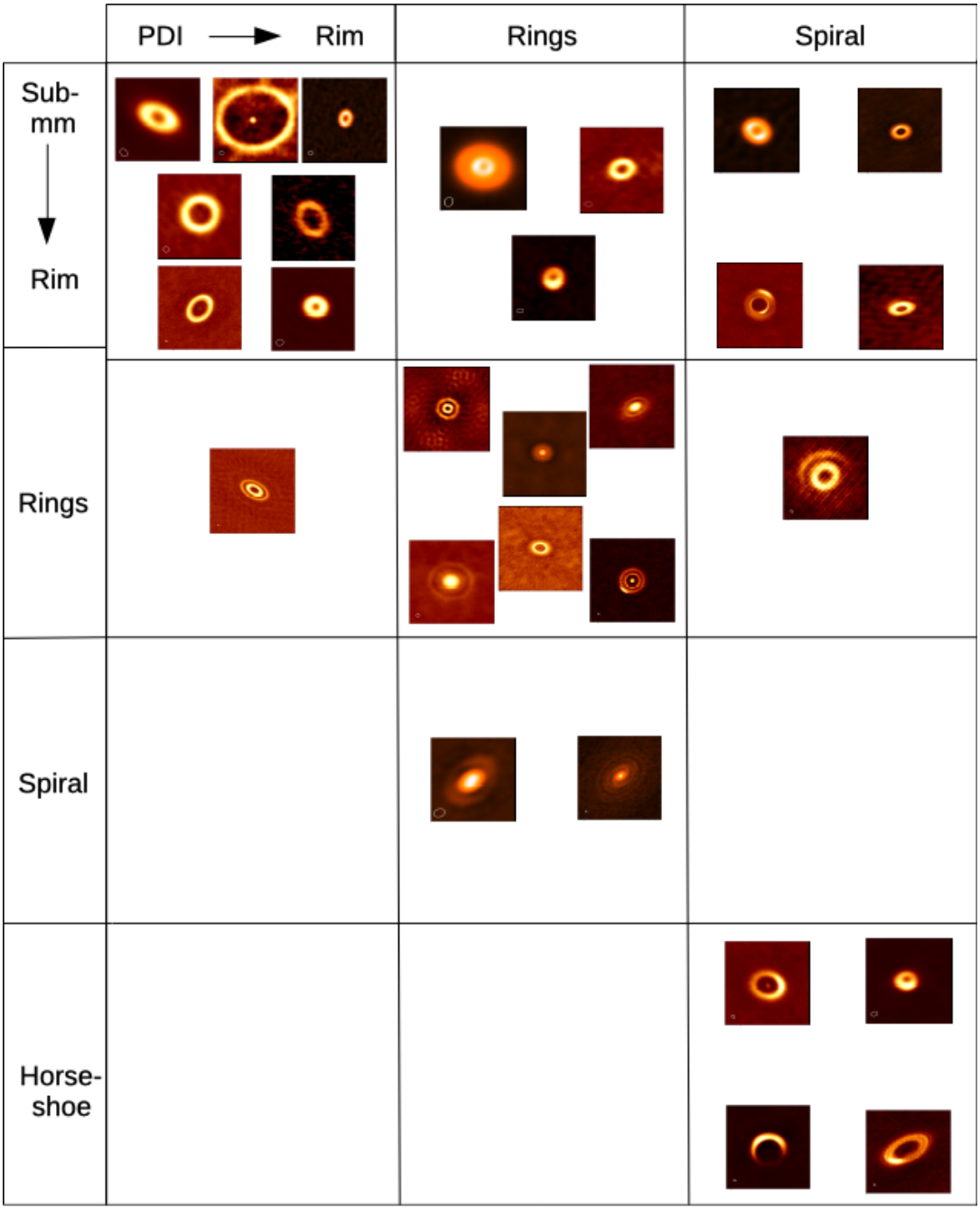

Figure 4.21: A comparison between the the morphology seen in protoplanetary discs at submillimetre continuum and near-IR polarised differential imaging. The columns show the morphology seen in scattered light while the rows show the morphology seen in submillimetre continuum.

and has a disc mass of $0.315_{\odot}$ (van der Marel et al. 2019). This disc, however, has been shown to have Rings in scattered light (Garufi et al. 2018). Similar to HD 97048, the disc surrounding EM*SR 21A features a Rim in sub-mm but Rings in scattered light. However, this disc has a much lower mass of $0.008_{\odot}$ (van der Marel et al. 2016a). The disc surrounding HD 100546 Rim in sub-mm but a Spiral in scattered light, has a mass of $0.040_{\odot}$ (van der Marel et al. 2019). The disc surrounding J161520233255051 has a comparable mass to that of the disc surrounding HD 100546 ($0.044_{\odot}$ (Andrews et al. 2011)). This disc, however, shows a Spiral substructure in sub-mm light, whereas it features Rings in scattered light. This supports our statement that disc mass may play little role in the type of morphology seen in both sub-mm and scattered light.

Spiral substructure seen in scattered light observations has previously been seen in a number of protoplanetary discs (Grady et al. 2001; Fukagawa et al. 2004; Casassus et al. 2012; Muto et al. 2012; Grady et al. 2013; Wagner et al. 2015; Akiyama et al. 2016; Ohta et al. 2016; Canovas et al. 2018). The sub-millimetre counterpart observations to these discs, however, show large cavities and axisymmetric substructure (Isella et al. 2013; van der Marel et al. 2013; Ansdell et al. 2016; Kraus et al. 2017; Tang et al. 2017; Cazzoletti et al. 2018; Dong et al. 2018a; Ohashi et al. 2018; Pineda et al. 2019). The millimetre observations shown here of IM Lup and J16152023 both feature a spiral like morphology, however rings were seen in scattered light observations rather than large cavities and axisymmetric substructures. This agrees with the results found by Avenhaus et al. (2018) and Huang et al. (2018) for these two discs.

The nine discs shown here with a spiral like morphology in scattered light were found to be relatively old (Garufi et al. 2018). The host stars had ages between $\approx$3 Myr to $\approx$12 Myr and are at the very late stage of their Pre-Main Sequence lifetime. Also, the lack of young stars featuring a Spiral disc led to the conclusion

that the formation of spiral arms in μm sized dust discs may only occur in the latter phases of their PMS lifetime. This contrasts with the results found in this work. The four Spiral discs in this work are at an early stage of their PMS lifetime and have ages $\leq 6Myr$. Therefore, the mechanism responsible for forming spiral arms in the sub-mm dust of a protoplanetary disc happens during the earliest stages of its evolution around low–mass stars. This discrepancy may suggest that there are different mechanisms forming the spiral arms seen in scattered light and those seen in the sub-mm.

In our common sample with Garufi et al. (2018), 14 discs have been classified as Rim discs in the sub-mm, ten of them being low–mass stars and four being intermediate–mass stars. Seven low–mass stars have been shown to have Rims in both sub-mm and scattered light. EM*SR 21A and HD 97048 are both intermediate–mass stars that show a Rim in sub-mm but have a ringed protoplanetary disc in scattered light. Both EM*SR 21A and HD 97048 have relatively young ages. Recent work by Muro-Arena et al. (2020) and van der Marel et al. (2020) have shown that the structure within these discs may be more complex and it may be possible for multiple rings to be present. Observations at a higher resolution would need to be conducted in order to confirm the structure within the disc.

All the discs in our sub-mm sample (56 discs) show some sort of cavity or gap. This is as expected since there are multiple mechanisms capable of forming a cavity. Garufi et al. (2018) found that 65% of the discs studied showed some sort of cavity in scattered light, indicating that they are a common occurrence in both sub-mm and scattered light.

The discs that showed a cavity in sub-mm and not scattered light were classified by Garufi et al. (2018) as either Faint or Inclined. The lack of a cavity may contribute to the faintness of the discs in scattered light, while the absence of a cavity in the Inclined discs may be an observational bias (Garufi et al. 2018). The high number

of discs that exhibit a cavity in both scattered light and sub-mm show that cavities are a common feature found in protoplanetary discs across a range of stellar types and evolutionary stages.

However, it should be noted that there may be a bias in both samples. The sample by Garufi et al. (2018) may contain many transition discs as they are bright due to their cavity wall. Likewise, the sample presented here may be biased towards transition discs as they are easiest to find at low resolution.

Eight discs classified as Rings in sub-mm have been studied in scattered light, six of which surround low–mass stars and two surrounding intermediate–mass stars. Rings in scattered light are seen in six of the protoplanetary discs as well as in the sub-mm. The two systems that do not show rings in scattered light are GM Auriga and V1247 Ori, both low–mass stars. The discs around these stars were shown to have a Rim and Spiral morphology respectively. The rings seen in protoplanetary discs in scattered light and in the sub-mm can form with similar mechanisms; such as the interaction of the disc with a companion (Pinilla et al. 2012a; de Juan Ovelar et al. 2013; Lin & Papaloizou 1979; Kley & Nelson 2012).

4.8 Summary

We have studied the morphology of the substructure seen in protoplanetary discs. We have classified all the discs with visible structure in the ALMA Archive Cycles 0–5. These 56 discs, observed in the sub-mm continuum, were placed into four categories: Rim, Ring, Horseshoe, and Spiral. By calculating the age of the host stars we are able to study the evolution of the substructures seen in protoplanetary discs over a range of ages. The sub-mm observations studied in this work were then compared to scattered light observations of protoplanetary discs studied by Garufi et al. (2018). The findings of this work are summarised as follows :

- We find that 27% of the discs observed with ALMA during Cycles 0–5 show substructure when observed with a moderate resolution of at least ∼0.22". Using a higher resolution of ∼0.1", 42% of the discs observed show clear substructure. The fraction of discs showing substructure increases to 60% when observed with a very high resolution of $\lesssim$0.04". Therefore, many of the discs observed with ALMA thus far may have substructure that remains unresolved due to the relatively low resolutions used.

- The protoplanetary discs studied here which show substructure surround Class II young stellar objects with a range of ages. This is representative of the full sample of discs observed by ALMA thus far, where the majority of the systems observed have been Class II YSOs. The discs studied here, however, were observed with much higher resolutions than the majority of the discs in the ALMA Archive. Therefore they are not representative of many discs which were observed at significantly lower resolutions.

- In our sample, the most populous substructure seen is a rim of sub-mm dust surrounding a large cavity. A rim of some sort is found for over half of the discs in our sample and they appear around stars with a range of ages, temperatures, and luminosities. This type of substructure, however, is the easiest to detect and have been explicitly targeted by ALMA. Nonetheless, it confirms that cavities and gaps are a popular substructure seen in protoplanetary discs.

- The second most populous substructure seen in our protoplanetary discs is a ringed disc. These discs are mostly found around young low–mass stars. As the majority of the discs observed with ALMA thus far were not observed using sufficiently high resolutions, a Ring disc may be the most popular substructure seen in protoplanetary discs.

- A distinctive horseshoe-shaped protoplanetary disc has only been seen in a

few systems. These systems contain relatively old intermediate–mass stars.

- A spiral substructure is rare in our observed protoplanetary discs. Our sample contains only four young, low–mass, spiral T–Tauri stars.
- The substructures seen in ALMA observations of protoplanetary discs mostly do not seem to follow an evolutionary sequence nor do they depend upon the mass of the star.
- All discs showing a horseshoe morphology in sub-mm continuum observations show a spiral-like morphology in scattered light.
- Low–mass stars that have been classified as Rim discs in the sub-mm have also been classified as Rim in scattered light. The occurrence of a single rim of emission around a large cavity seems to be a common substructure found in both scattered light and sub-mm continuum emission. This confirms the populous nature of a rim of material surrounding a cavity in protoplanetary discs.

Chapter 5

Modelling Protoplanetary Discs Observed with ALMA

5.1 Introduction

The substructures present in the protoplanetary discs surrounding young stellar objects can form in numerous ways. These formation mechanisms were outlined in Section 1.4. Simulations of protoplanetary discs need to be conducted in order to determine which theoretical model is responsible for the observed substructure. Several types of numerical methods and simulations may be utilised; including smooth particle hydrodynamics and radiative transfer codes.

In this chapter we model three protoplanetary discs previously studied with ALMA using smooth particle hydrodynamics. The discs surrounding Elias 2–27, 2MASS J16152023–3255051, and HD 36112, were chosen as these young stellar objects are of low, solar, and intermediate masses, respectively. Our aim is to form substructure within the disc before the gas has fully dissipated and a number of secondary objects (such as brown dwarfs and planets) are able to form.

We begin in Section 5.2 by outlining the numerical method used to produce

the simulations in this chapter. We follow by introducing each protostellar system, outlining the initial conditions used as well as the results of the simulations. We finish in Section 5.6 by comparing our SPH simulations with previous models of each protostellar system.

5.2 Numerical Method

To model the protoplanetary discs, the SPH code `SEREN` (Hubber et al. 2011) is used. The features of `SEREN` utilised in this work were first introduced in Chapter 3. The protoplanetary discs are represented by a large number of SPH particles. As the particles grow in density, they are replaced by a sink particle when ρ_{sink}=10^{-9} g cm^{-3} (Bate et al. 1995). This sink particle represents a bound object that interacts solely gravitationally and radiatively with the other particles. Particles within a radius of $R = 1$ AU of the sink particle are accreted onto it.

The heating and cooling of the gas particles in the disc are performed using an approximate radiative transfer method. This was first introduced by Stamatellos et al. (2007). The method obtains a cooling rate for the gas particles using the local opacity and estimating the column density through which the heating and cooling happens. This method includes effects from dust sublimation, ice melting, bound-free, free-free, and electron scattering interactions (see Section 3.2.1.6).

The simulations of the protoplanetary discs model the gas density population. For further analysis of the models, with regards to ALMA observations, we assume that dust grains trace the gas. We also assume the canonical dust-to-gas ratio of 100:1.

The SPH simulations for each stellar system were run with some common initial conditions. These are outlined below in Table 5.1. Unique stellar and disc parameters for Elias 2–27, J16152023, and HD36112 are outlined in Sections 5.3, 5.4, and 5.5, respectively.

The initial outer radii of the protoplanetary discs, R_{out}, are taken to be the outer radii of the discs measured using the ALMA observations. The radii are measured in `CASA` by fitting a 2D Gaussian to the disc and determining their extents. We compare our measured radii to literature values to confirm they are in agreement. A smoothing radius of R_0=0.5 AU is introduced for each protoplanetary disc. This is done to avoid the surface density $\Sigma \rightarrow \infty$ as $R \rightarrow 0$.

The surface density and temperature follow the profiles of $\Sigma \propto R^{-p}$ and $T \propto R^{-u}$, respectively. Following semi-analytical studies of cloud collapse (Lin & Pringle 1990; Tsukamoto et al. 2015), the surface density power index, p, is set to 1.5. A value of 0.6 is chosen for the temperature power index, u, following studies of pre-main sequence stars (Andrews et al. 2009). The temperature of the disc at a distance of 1 AU from the star, T_0, is taken to be 300 K.

The inner radius of each disc, R_{in}, is taken to be 1 AU; particles that drift within this radius are accreted onto the protostar. By choosing to truncate the disc at the accretion radius, any material that should exist just outside of this radius is accreted onto the sink. Interior to the accretion radius, the surface density of the model is set to decrease rather than drop to zero, and thus does not follow the power law introduced above. This creates an artificial peak close to the accretion radius in the surface density profiles of the models. Thus, the region interior to $\sim$15 AU in the disc models appear to feature the formation of a central concentration of material along with a cavity. Although this central gap is real in protostellar systems, in reality the surface density of the disc drops off much closer towards the central protostar ($\sim 10^{-2}$ AU). We therefore, conservatively assume anything within $\sim$15 AU is not real. As will be seen later in this Chapter, any substructure formed is located exterior to 10 AU, therefore the implementation of this accretion radius, and the subsequent formation of a central concentration of material, does not affect the disc further out and any results obtained in this work.

Table 5.1: The initial disc parameters for the SPH simulations conducted in this work.

Parameter	Value
N	5×10^5
R_{in}	1 AU
R_0	0.5 AU
T_0	300 K
T_∞	10 K
$\Sigma \propto R^{-p}$ where $p = 1.5$	
$T \propto R^{-u}$ where $u = 0.6$	

The contribution of heat to the disc from the background radiation field is included in the simulations and is given by $T_\infty = 10$ K. This is done as the ambient temperature in regions containing protoplanetary discs are ∼10–30K (Hayashi & Nakano 1965; Hayashi 1966; Tohline 1982; Larson 1985; Masunaga & Inutsuka 2000; Stamatellos et al. 2005a,b; Battersby et al. 2014).

We model the discs using N=5×10^5 SPH particles. These are placed in random locations between R_{in} and R_{out}. The high number of SPH particles ensures that any gravitational fragmentation in the disc can be resolved. Previous work by Stamatellos & Whitworth (2009b) have shown that N=1.5×10^5 SPH particles are sufficient to resolve fragment masses down to $0.25\mathrm{M}_{Jup}$. This number of SPH particles is also sufficient to resolve the vertical structure of the disc. The initial conditions for all the protoplanetary disc simulations are summarised in Table 5.1.

As our aim is to form spiral arms in the protoplanetary discs, we evolve the simulation for 30 kyr. Gravitational instabilities in protoplanetary discs develop on dynamical timescales, with a few rotations of the disc, and fragments can form within a few thousand years (Gammie 2001; Johnson & Gammie 2003; Rice et al. 2003,

2005). Thus an evolution time of 30 kyr allows sufficient time for any instabilities to arise.

Although we run each simulation for 30 kyr, the discs may fragment before this point. A sink particle is used to represent dense concentrations of SPH particles, where the density reaches ρ_{sink}=10^{-9} g cm^{-3} (Bate et al. 1995). The focus of this thesis is the creation and evolution of spiral arms in protoplanetary discs. However, the discs may fragment to form secondary objects (with the formation of a sink particle), or no substructure may be produced throughout the 30 kyr evolution. Thus the snapshots of the simulations run, shown below, may not show the full 30 kyr evolution studied as we are interested in the disc evolution before the disc fragments, or earlier if no substructure is formed.

5.3 Simulations of a Low–Mass Star

Elias 2–27 is a low–mass star (M_*=0.5-0.6$M_\odot$) (Luhman & Rieke 1999; Andrews et al. 2009) situated 118.5±13.1 pc away in the ρ Ophiuchus star forming region (Gaia Collaboration et al. 2018). Based on the analysis of its SED, this protostar has been classified as a Class II young stellar object (Andrews et al. 2009; Evans et al. 2009). It is, however, still surrounded by an envelope from which it accretes material (Natta et al. 2006), in contrast to many Class II YSOs.

The protoplanetary disc surrounding Elias 2–27 is also unusually massive (Meru et al. 2017; Hall et al. 2018). Previous estimates of the disc mass range from 0.04 to 0.1 $M_\odot$ (Andrews et al. 2009; Isella et al. 2009; Ricci et al. 2010). At radial distances of $>$ 10 AU, the emission is optically thin and traces the material down to the midplane of the disc (Pérez et al. 2016). Coupled with its remarkably large disc–to–star mass ratio, this object has been the subject of interest in many submillimetre studies.

ALMA observations conducted by Pérez et al. (2016) revealed two symmetric

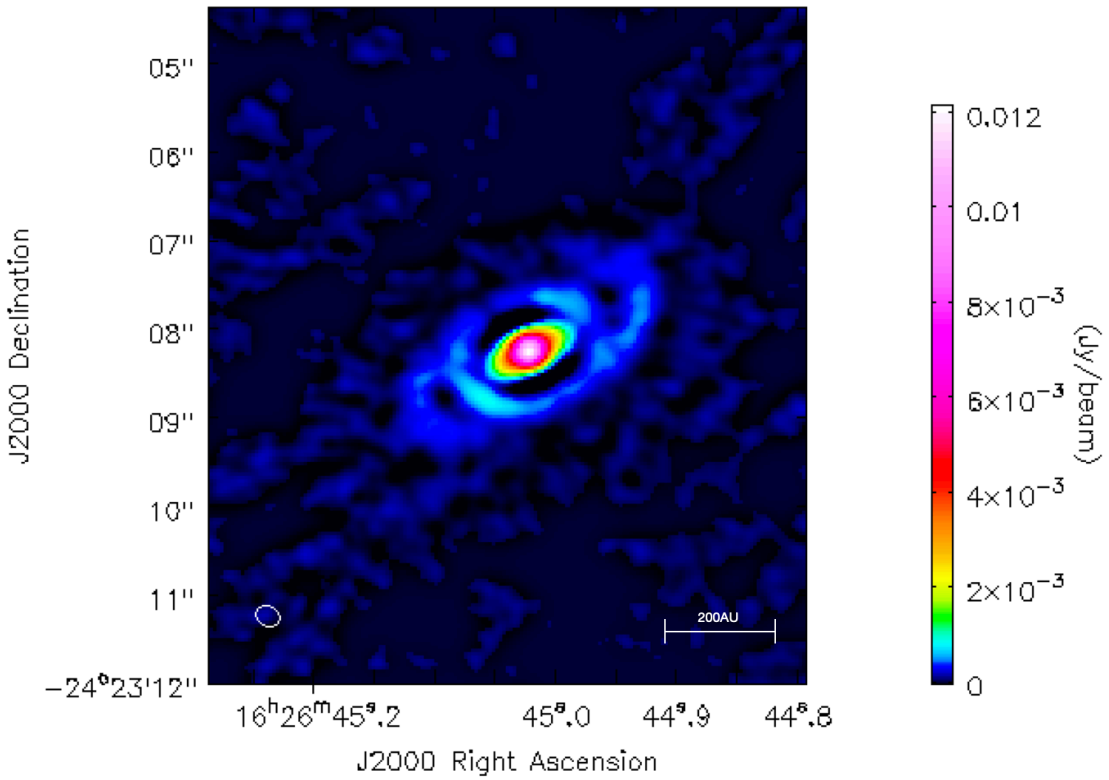

Figure 5.1: ALMA observation of Elias 2–27 after undergoing the process of unsharp masking. The observations were taken at 231 GHz (1.3 mm). The beam can be seen in the lower left corner and has a size of 0.24×0.20 arcsec. The position angle of the beam is -62°.

spiral arms at 1.3mm extending from an elliptical emission ring. This observation can be seen in Figure 5.1. The emission ring extends up–to 70 AU from the star, whilst the spiral arms were seen to extend from $R = 100 - 300$ AU.

The possibility that the spiral arms in Elias 2–27 are caused by gravitational instability was first introduced by Pérez et al. (2016). Previous work has shown that symmetric spiral arms could form in a protoplanetary disc if the accretion rate of the system is of the order 10^{-6} to $10^{-7} M_{\odot} yr^{-1}$ (Hall et al. 2016), and the disc–to–star mass ratio is at least ≈ 0.25 (Dong et al. 2015a) (e.g., Lodato & Rice (2005)). The accretion of rate of Elias 2–27 was previously measured to be $8 \times 10^{-8} M_{\odot} yr^{-1}$

Table 5.2: The initial disc parameters for the SPH simulations of Elias 2–27. Each run is identical, with the exception of the disc mass. The disc mass for each run (EL01-03) is given below.

Parameter	Value
M_*	0.5 $M_\odot$
T_*	3850 K
R_{out}	300 AU
M_{disc} ($M_\odot$)	
EL01	0.15
EL02	0.225
EL03	0.3

(Najita et al. 2015), indicating that it may have a high enough rate to form spiral arms.

Here, we attempt to recreate the spiral arms seen in Elias 2–27 by modelling a protoplanetary disc with the aim of causing it to become gravitationally unstable. We outline the initial conditions of the simulations in Section 5.3.1, followed by the outputs of the simulations in Section 5.3.2. We compare our findings to the literature models in Section 5.6.1.

5.3.1 Initial Conditions

We construct three protostellar systems with the same initial conditions but vary the disc masses in each case. The initial conditions for the protoplanetary disc were outlined in Section 5.2 in Table 5.1, and we summarise the parameters for the SPH simulations of Elias 2–27 in Table 5.2.

The stellar mass is set to M_* =0.5 $M_\odot$, whilst the effective temperature is taken to be T_* =3700 K. We utilise the stellar mass of Elias 2–27 derived in Section 4.4;

this value agrees with the derived mass of $M_* = 0.6_\odot$ from Andrews et al. (2009). The effective temperature of $T_* = 3700$ K was obtained from Isella et al. (2009). The metallicity of the protoplanetary disc is set to solar metallicity for all simulations. The outer radii of the discs were taken to be the outer radii of the spiral arms as detected by Pérez et al. (2016), $R = \sim 300$ AU. We confirm this by measuring the outer radius of the disc observation in `CASA`.

5.3.1.1 Initial Disc Mass Estimates

To determine an initial estimate for the disc mass, we calculate the mass of the material detected by the ALMA observation. Dust in protoplanetary discs do not absorb and re-emit all incident radiation perfectly. Therefore, dust is assumed to act like a modified blackbody (henceforth greybody). In order to model the dust in the disc, we model the emission using a greybody. To do this we assume a gas to dust ratio of 100:1 and model the flux using

$$F_\nu = \frac{\kappa_\nu B_\nu(T) M_{disc}}{D^2} \tag{5.1}$$

where D is the distance to the stellar object, M_{disc} is the mass of the disc, $B_\nu(T)$ is the blackbody intensity and κ_ν is the dust mass opacity coefficient (Hildebrand 1983).

We calculate the mass opacity coefficient, κ_ν using

$$\kappa_\nu = 0.1 \left\{ \frac{\nu}{\nu_{central}} \right\}^{\beta_{disc}} cm^2 g^{-1}\,, \tag{5.2}$$

where $\nu_{central} = 10^{12}$Hz. This follows the work of Beckwith et al. (1990). We assume a value for the opacity spectral index, β_{disc}, of ≈ 1. This is based upon previous determinations of the opacity spectral index from observations of protoplanetary discs (Beckwith & Sargent 1991; Andrews & Williams 2005).

Using `CASA`, an intensity of F_ν=175 mJy was measured for Elias 2–27. Assuming a dust temperature of 10 K and adopting the Gaia DR2 distance to Elias 2–27 (118 pc), we measure the disc mass from the ALMA observation to be M_{disc}=0.05M$_\odot$.

Simulations of protoplanetary discs are, however, run with disc masses around an order of magnitude greater than the masses observed (Andrews et al. 2013). This is due to the considerable uncertainties linked to inferred disc masses from observations. Assumptions that the gas–to–dust mass ratio is 100:1 may not be correct (Andrews & Williams 2005; Williams & Best 2014). As well as this, the value of κ_ν is a major uncertainty in the determination of protoplanetary disc masses. The opacity of a disc follows a power-law dependence on the frequency according to $\kappa_\nu \propto \nu^{\beta_{disc}}$ (see Section 1.2.2). The assumption that protoplanetary discs are optically thin is often made, including in this work. In reality, the optical depth may vary across different regions of a protoplanetary disc. This would imply that a constant value for β_{disc} could not be assumed for a protoplanetary disc. An optically thin disc consisting of dust with a similar composition to that of interstellar dust has been shown to have an opacity value of $\beta_{disc} \approx 2$ (Draine 2006).

Larger grains in the dust distribution would mean the disc remains optically thick, even up to wavelengths of 3 mm (Forgan & Rice 2013). This would further conceal hidden mass, and values for the opacity index would drop to less than one (Calvet et al. 2002; Testi et al. 2003). A value of $\beta_{disc} \approx 1$ has also previously been measured by studying the sub-mm SEDs of protoplanetary discs (Beckwith & Sargent 1991; Andrews & Williams 2005).

The composition of the dust grains may also affect the value of β_{disc}. Beckwith et al. (1990) showed that dust composed of spheroidal grains of silicate or graphite would have an opacity of $\beta \approx 2$ for sizes above 100 μm. However $\beta \leq 1$ for dust grains in a fractal arrangement beyond 1 mm. Therefore, choosing a constant value

for β_{disc} by assuming that the population of dust in a particular region consists of grains of similar size may be incorrect.

The uncertainty in the value of β_{disc} due to the reasons mentioned above may lead to major uncertainties in κ_ν and hence the determination of protoplanetary disc masses. Other assumptions, such as assuming the disc is optically thin, also lead to incorrect determinations of disc masses. Recent work by Dunham et al. (2014) and Evans et al. (2017) have shown that assuming the protoplanetary disc is isothermal and selecting an incorrect value for β_{disc} may result in disc mass underestimates by up to factors of 2-3 at millimetre wavelengths, or up to an order of magnitude at smaller wavelengths. Considering these limitations, we thus make an initial estimate for the disc mass of Elias 2–27 of M_{disc}=0.15 $M_\odot$. A high disc–to–star mass ratio is needed for gravitational instability, therefore we also model a protoplanetary disc with a large disc mass of M_{disc}=0.3 $M_\odot$. An 'intermediate' mass disc, M_{disc}=0.225 $M_\odot$, is also modelled.

5.3.2 SPH Simulations

We run three simulations, varying the disc mass in each. The runs have been titled EL01, EL02, and EL03; with disc masses being set to M_{disc}=[0.15, 0.225, 0.3]$M_\odot$, respectively. Initial conditions for the simulations are listed above in Table 5.2. Five snapshots from each SPH simulation are shown, corresponding to 1,2,4,6, and 10 kyr. Each 'field–of–view' has been scaled to 1000×1000 AU.

Snapshots from run EL01, showing the evolution of the disc surface density can be seen in Figure 5.2. The disc in this simulation has a mass of M_{disc}=0.15$M_\odot$, therefore a disc–to–star mass ratio of q= 0.3.

From Figure 5.2, we can see that the disc does not become gravitationally unstable throughout the evolution, and no substructure forms in the disc. The disc is initially uniform, with the surface density of the material increasing towards the

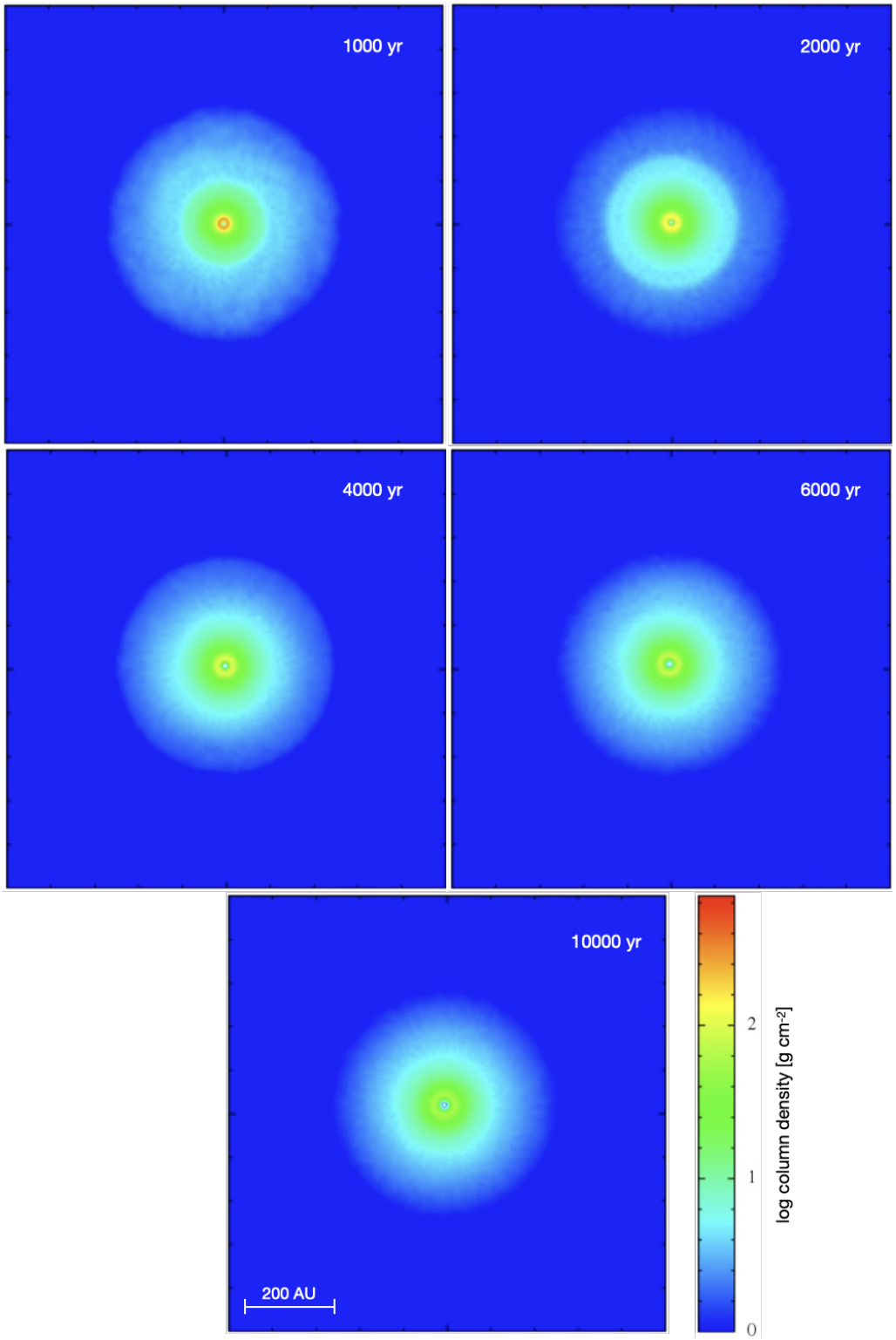

Figure 5.2: Disc evolution of Elias 2–27, with the run ID EL01. The disc has a mass of M_{disc}=0.15M$_{\odot}$ and initial parameters are listed in Table 5.2. The material migrates from the inner regions of the disc to the outer as the disc evolves. However, the disc does not become unstable.

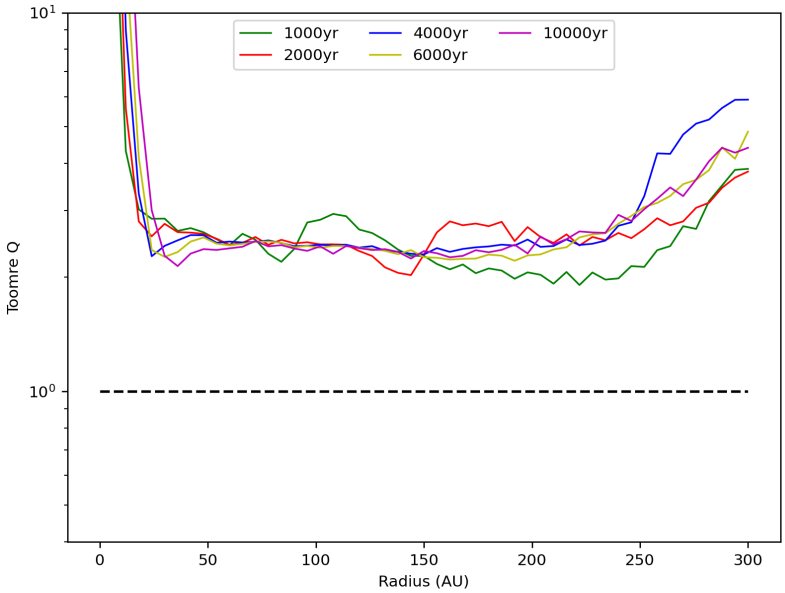

Figure 5.3: The azimuthally averaged Toomre parameter, Q, for the simulation run EL01. The Q value for different temporal snapshots is shown using different line colours. The black dotted line shows Q=1. Below this, the disc is gravitationally unstable.

centre of the disc. As the disc evolves, material expands from the inner regions as angular momentum is redistributed throughout the disc. Material can also accrete onto the central object.

We calculate the azimuthally averaged Toomre parameter, Q, for the simulation run, EL01.This is shown in Figure 5.3. The parameter Q, first introduced in Section 1.3.4.2, determines the stability of the disc, with a value of $Q < 1 - 1.5$ indicating a gravitationally unstable disc that may fragment.

From Figure 5.3, we can see that the protoplanetary disc is not unstable at any point throughout its evolution. This supports the results that we found no substructure formation in the disc.

In order to study the structure in the models, we convert the surface density snapshots to flux density snapshots using Equation 5.1 and the solid angle of the beam used in the original ALMA observations (see Chapter 6 for the beam sizes).

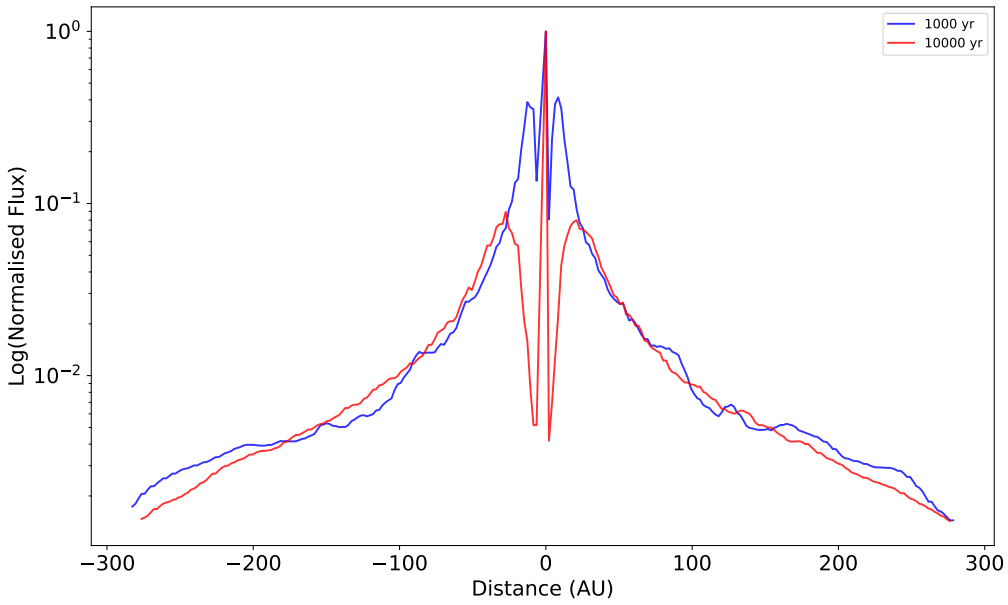

Figure 5.4: Spatial profile for the run EL01. The log normalised flux of the disc at 1ky is shown in blue, whilst the log normalised flux at 10 kyr is shown in red. The distance is taken from the centre of the disc.

As we are primarily concerned with the substructures formed in the models, and not the total value of the intensity, we normalise the flux to the peak flux.

We produce a spatial profile of the model shown in Figure 5.2. We do this by taking a cross–cut of the disc perpendicular to the x–axis (the y-direction). The cut is taken using the outer radius, R_{out}=300 AU as the width. We do not look at the disc parallel to the x–axis as the disc appears axisymmetric. Cross–cuts, both in the x- and y-directions are made from later simulations as some spiral arms do not extend much (see Section 5.5). Figure 5.4 shows the spatial profile of the simulation at 1 kyr and 10 kyr. The normalised flux of the central concentration of material is seen to drop between the two snapshots, however as discussed in Section 5.2, the inner ∼15 AU of the model should be considered not real. The disc also becomes more uniform and stable through the evolution.

The second simulation of the disc surrounding Elias 2–27, EL02, is shown in Figure 5.5. Snapshots of the column density can be seen as the disc evolves from 1 kyr to 10 kyr. The mass of this disc has been increased to M_{disc}=0.225M$_{\odot}$, therefore the disc–to–star mass ratio has increased to $q = 0.375$. The initial conditions are kept the same as the previous run (see Table 5.2).

Similar to EL01 where the disc mass was M_{disc}=0.15M$_{\odot}$, the disc in EL02 does not appear to become gravitationally unstable. The disc appears uniform with an increased surface density of material close to the centre of the disc.

The lack of substructure seen in the snapshots of run EL02, is also supported by the azimuthally averaged Toomre values. This is shown in Figure 5.6. The disc does not become unstable (with a value of $Q < 1 - 1.5$) throughout its evolution.

Material expands from the inner regions of the disc due to the redistribution of angular momentum. This is shown in Figure 5.7, where we see a drop in flux between the central concentrations of material between the two snapshots. The drop in flux after the peak should be considered not real as it us a numerical affect (see Section 5.2).

The third simulation of Elias 2–27, named EL03, has the same initial conditions listed in Table 5.2, with an increased disc mass of M$_{disc}$=0.3M$_{\odot}$. This increases the disc–to–star mass ratio to $q = 0.5$. This would be an unusually massive protoplanetary disc surrounding a Class II T–Tauri object. However, as discussed in Section 5.3.1.1, observations of protoplanetary discs may be heavily underestimating disc mass estimates. Snapshots of the column density from EL03 are shown in Figure 5.8.

The disc, again, fails to become gravitationally unstable. No substructure can be seen at any point in the disc evolution, regardless of its unusually high disc–to–star mass ratio. This is supported by Figure 5.9, where we plot the azimuthally averaged Toomre parameter. Although the disc is initially close to being unstable

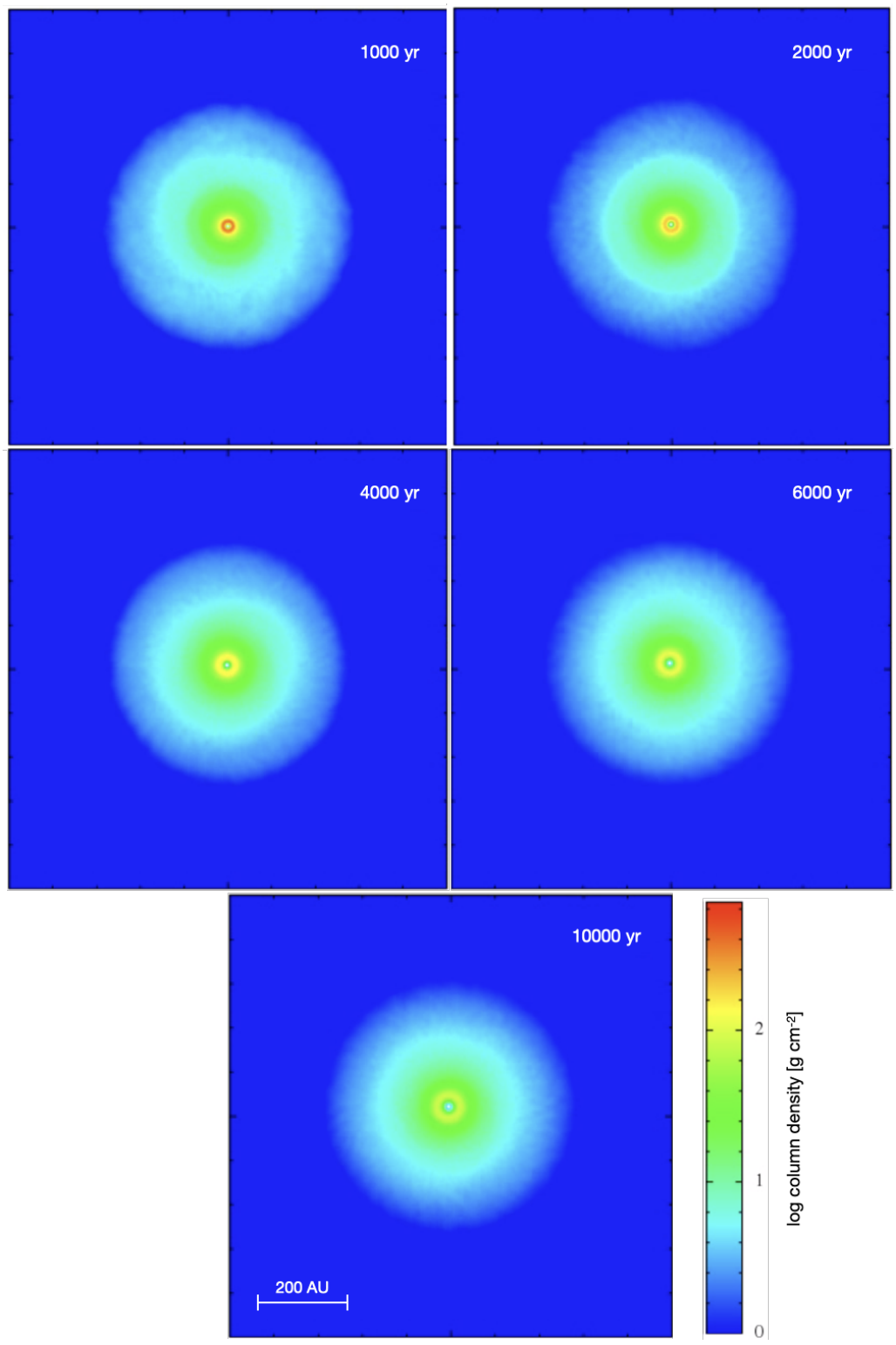

Figure 5.5: Disc evolution of Elias 2–27, with the run ID EL02. The disc has a mass of M_{disc}=0.225M$_{\odot}$. The disc does not become unstable.

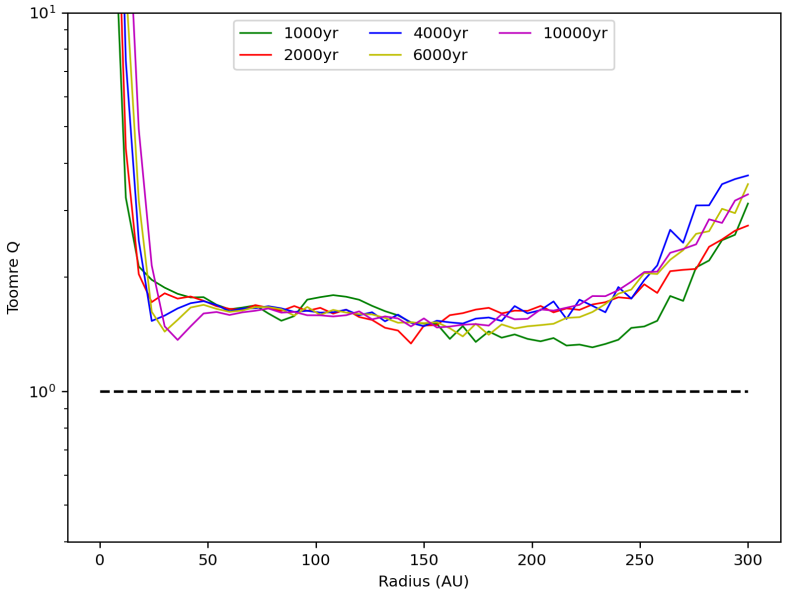

Figure 5.6: The azimuthally averaged Toomre parameter, Q, for the simulation run EL02. The Q value for different temporal snapshots are shown using different line colours. The black dotted line shows Q=1. Below this, the disc is gravitationally unstable.

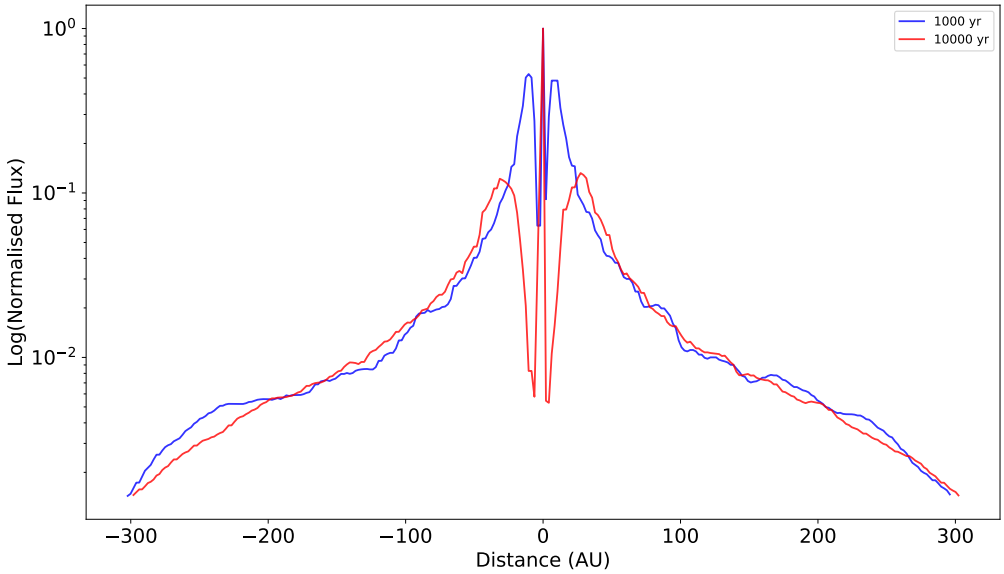

Figure 5.7: Spatial profile for the run EL02. The log normalised flux of the disc at 1 ky is shown in blue, whilst the log normalised flux at 10 kyr is shown in red. The distance is taken from the centre of the disc.

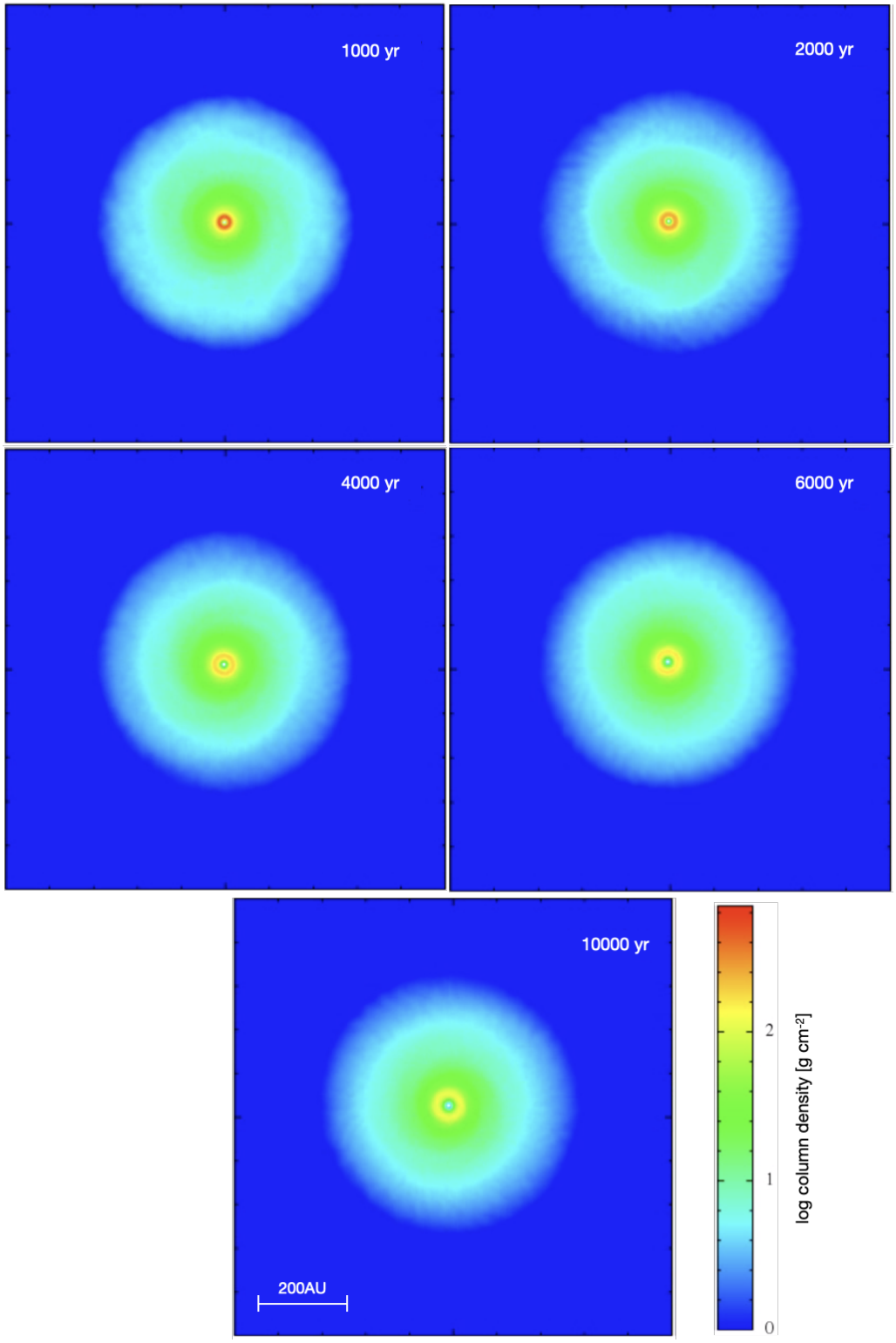

Figure 5.8: Disc evolution of Elias 2–27, with the run ID EL03. The disc has a mass of M_{disc}=0.3M$_{\odot}$. The material migrates from the inner regions of the disc to the outer as the disc evolves. However, the disc does not become unstable.

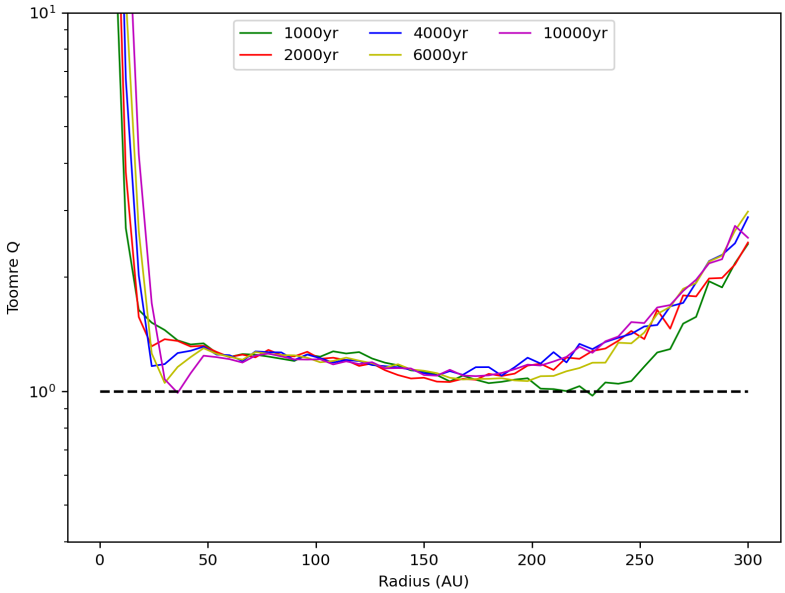

Figure 5.9: The azimuthally averaged Toomre parameter, Q, for the simulation run EL03. The Q value for different temporal snapshots are shown using different line colours. The black dotted line shows Q=1. Below this, the disc is gravitationally unstable.

(at 1000 yr), the Toomre parameter increases as the disc evolves and thus becomes more stable. This can be seen in Figure 5.10, where the normalised flux of the central concentration of dust grains decreases as the disc evolves.

All three simulations of Elias 2–27 failed to produce substructure in the protoplanetary discs. Although each protoplanetary disc has been modelled with a unusually high disc mass, each disc became more stable as it evolved. We further discuss the reasons why this may be the case in Section 5.6.1 below.

5.4 Simulations of a Solar–Mass Star

We now model the protoplanetary disc surrounding a solar–mass star in an attempt to form spiral arms in the disc. The young stellar object 2MASS J16152023–3255051 was studied in Chapter 4. After undergoing the process of unsharp masking (see

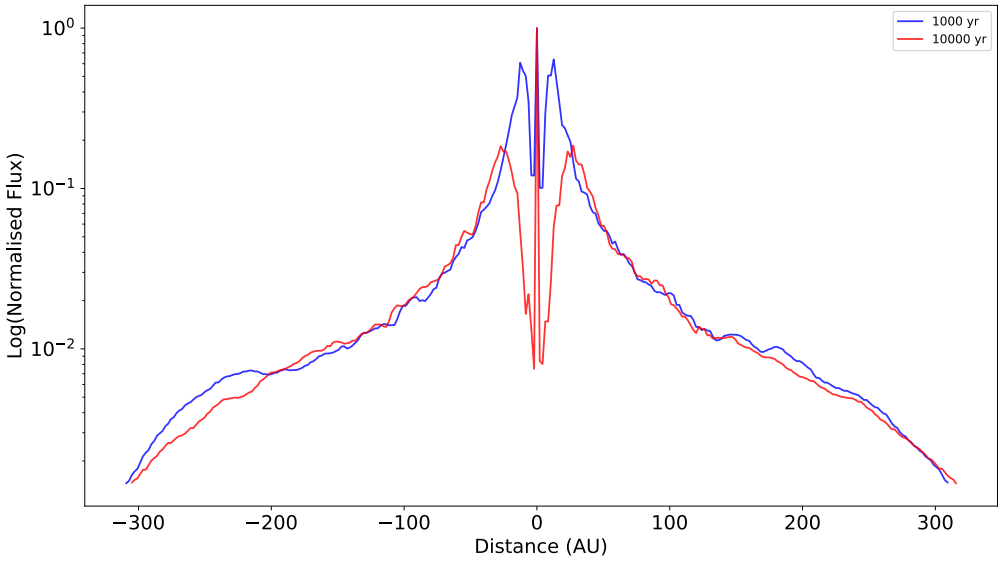

Figure 5.10: Spatial profile for the run EL03. The log normalised flux of the disc at 1 ky is shown in blue, whilst the log normalised flux at 10 kyr is shown in red. The distance is taken from the centre of the disc.

Section 4.3.1), tenuous spiral arms could be seen in the outer regions of the disc. Figure 5.11 shows the masked image of J16152023.

2MASS J16152023–3255051 is a solar–mass YSO (M_*=1.1M$_\odot$ (Andrews et al. 2011)) situated 157.7±0.9 pc away in the Lupus star forming region (Gaia Collaboration et al. 2018). The effective temperature of the star has been estimated to be $\sim$ 4400 K (Andrews et al. 2018b). Based on the analysis of its SED, this protostar has been classified as a Class II young stellar object (Merín et al. 2010; Wahhaj et al. 2010).

Similar to the disc surrounding Elias 2–27, the protoplanetary disc of J16152023 is also particularly massive. Previous submillimetre studies, assuming a gas-to-dust ratio of 100:1, have found a disc mass range from M_{disc} =0.13 to 0.47 M$_\odot$ (Andrews et al. 2011; van der Marel et al. 2015). Therefore, the disc–to–star mass ratio, q, lies in the range of 0.12 to 0.43.

Submillimetre observations by Andrews et al. (2011) determined a disc radius of

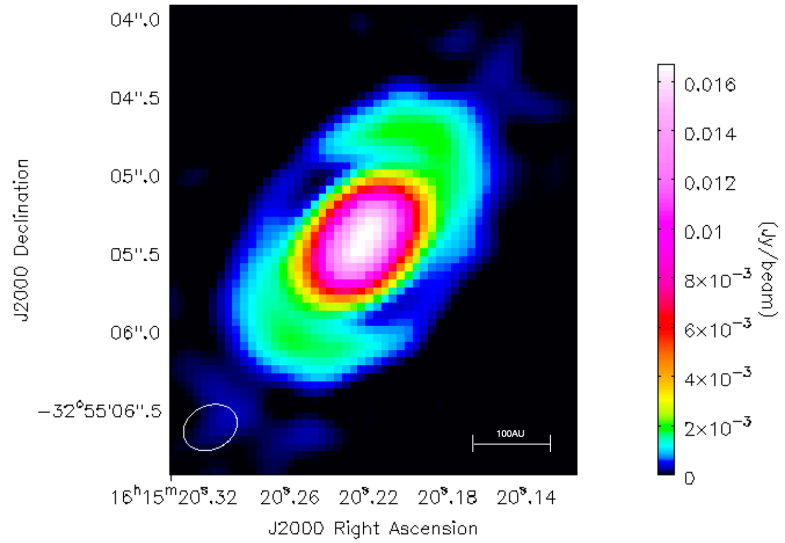

Figure 5.11: ALMA observation of J16152023 after undergoing the process of unsharp masking. The observation was taken at 688 GHz (0.4 mm). The beam can be seen in the lower left corner and has a size of 0.28×0.20 arcsec. The position angle of the beam is -79°.

∼120 AU. This was increased to 170 AU in recent analysis of ALMA observations by van der Marel et al. (2019). Analysis by both Andrews et al. (2011) and van der Marel et al. (2015) find a small cavity in the central regions of the disc with a radius of R =∼30 AU. A narrow radial dip has also been detected in the submillimetre dust disc ∼110 AU from the centre of the disc (van der Marel et al. 2015).

The disc surrounding J16152023 has not previously been extensively modelled. Nonetheless, we run SPH simulations of the disc surrounding J16152023 with the aim of determining if substructures can be formed via gravitational instability in the protoplanetary disc surrounding a solar–mass star. We outline the initial conditions of the simulations in Section 5.4.1, followed by the outputs of the simulations in Section 5.4.2. We compare our findings to previous work in the literature in Section 5.6.2.

Table 5.3: The initial disc parameters for the SPH simulations of J16152023. Each run is identical, with the exception of the disc mass. The disc mass for each run is given below.

Parameter	Value
M_*	1.0 $M_\odot$
T_*	4400 K
R_{out}	150 AU
M_{disc} ($M_\odot$)	
J01	0.25
J02	0.375
J03	0.5

5.4.1 Initial Conditions

We construct three protostellar systems with the same initial conditions but varying the disc mass. The initial conditions for the protoplanetary disc were outlined in Section 5.2, and we summarise the parameters for the SPH simulations of J16152023 in Table 5.3.

The stellar mass is set to M_* =1.0 $M_\odot$, whilst the effective temperature is taken to be T_* =4400 K. We utilise the stellar mass of J16152023 derived in Section 4.4; this value agrees with the derived mass of M_* =1.1 $M_\odot$ from Andrews et al. (2011). The effective temperature has been obtained from Andrews et al. (2018b). The metallicity of the disc is set to solar metallicity for all simulations. The outer radii of the discs were taken to be ∼150 AU. We measure this in `CASA` based on the ALMA observations used in Chapter 4.

To determine an initial estimate for the disc mass, we calculate the mass of the material detected by the ALMA observation. This was done following the method

outlined above for Elias 2–27 (see Section 5.3.1.1). Using `CASA`, a flux density of F_ν=686 mJy was measured for J16152023. Assuming a dust temperature of 10K and adopting the Gaia DR2 distance of 158 pc, we measure the disc mass from the ALMA observation to be M_{disc}=0.06 $M_\odot$.

As inferred disc masses from observations are, however, heavily underestimated for reasons outlined in Section 5.3.1.1, we make an initial estimate for the disc mass of J16152023 of M_{disc}=0.25 $M_\odot$. A high disc–to–star mass ratio is needed for gravitational instability, therefore we model a protoplanetary disc with a large disc mass of M_{disc}=0.50 $M_\odot$. An 'intermediate' mass disc, M_{disc}=0.375 $M_\odot$, is also modelled. The disc mass estimates made are inline with previous estimates from the literature (Andrews et al. 2011; van der Marel et al. 2015).

5.4.2 SPH Simulations

We run three simulations, varying the disc mass in each. The runs have been titled J01, J02, and J03; with disc masses being set to M_{disc}=[0.25, 0.375, 0.5] $M_\odot$, respectively. Initial conditions for the simulations are listed above in Table 5.3. Five snapshots from each SPH simulation are shown, with the timestamp of each snapshot in the top-right corner. Each 'field–of–view' has been scaled to 500×500 AU.

It should be noted that all structure discussed below should be considered physical. However, as outlined in Section 5.2, the dynamics of gas within 15 AU are not captured properly and any flux interior to this should be considered as not real.

Snapshots, from run J01, showing the evolution of the disc surface density can be seen in Figure 5.12. The disc in this simulation has a mass of M_{disc}=0.25 $M_\odot$. Thus the system has a disc–to–star mass ratio of $q = 0.25$.

From Figure 5.12, we can see that the disc does not become gravitationally unstable throughout the evolution and that no substructure can be seen. The disc is initially uniform with an increase in the surface density of material in the centre

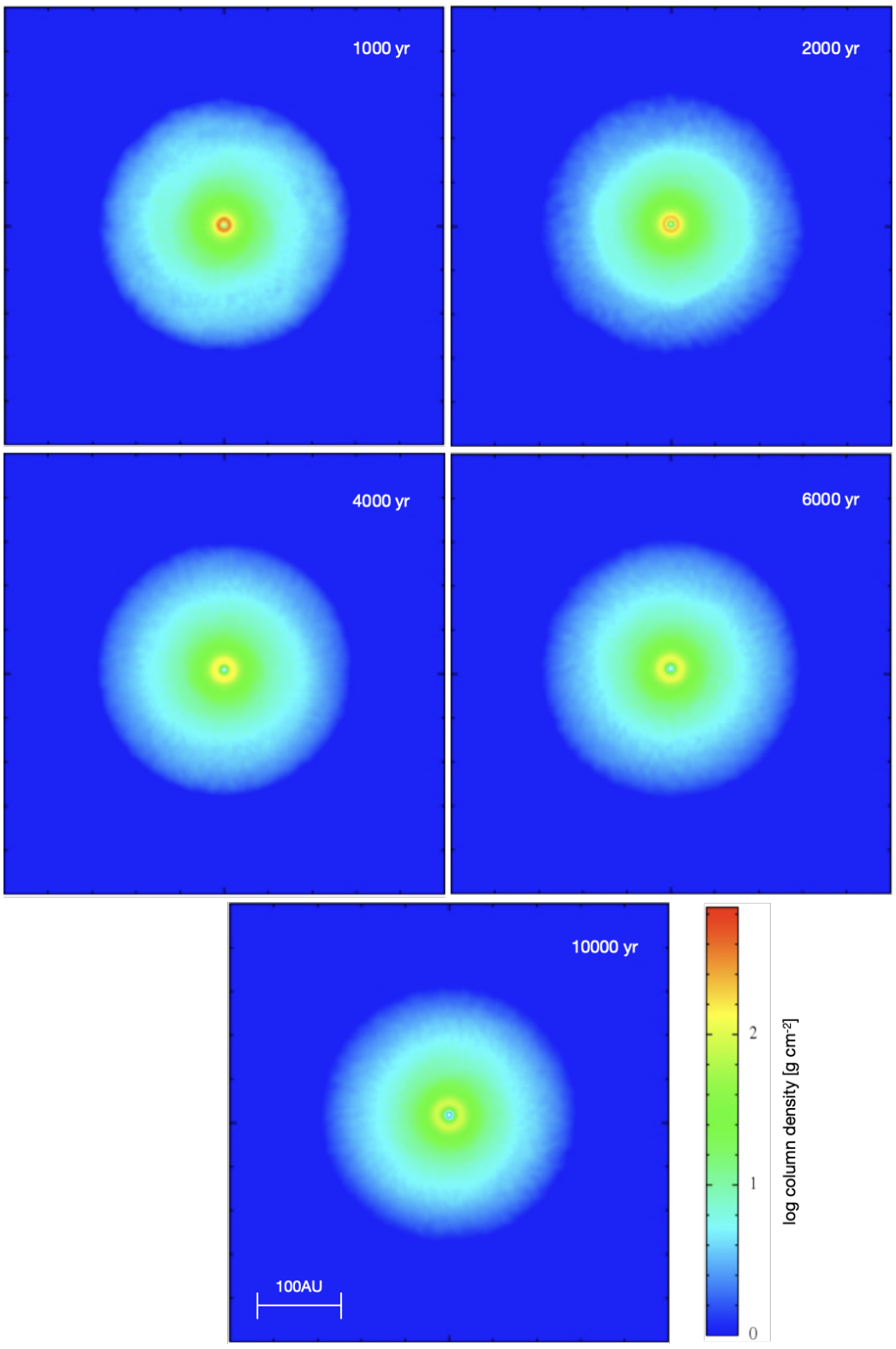

Figure 5.12: Disc evolution of J16152023, with the run ID J01. The disc has a mass of M_{disc}=0.25 $M_{\odot}$. The material migrates from the inner regions of the disc to the outer as the disc evolves. However, the disc does not become unstable.

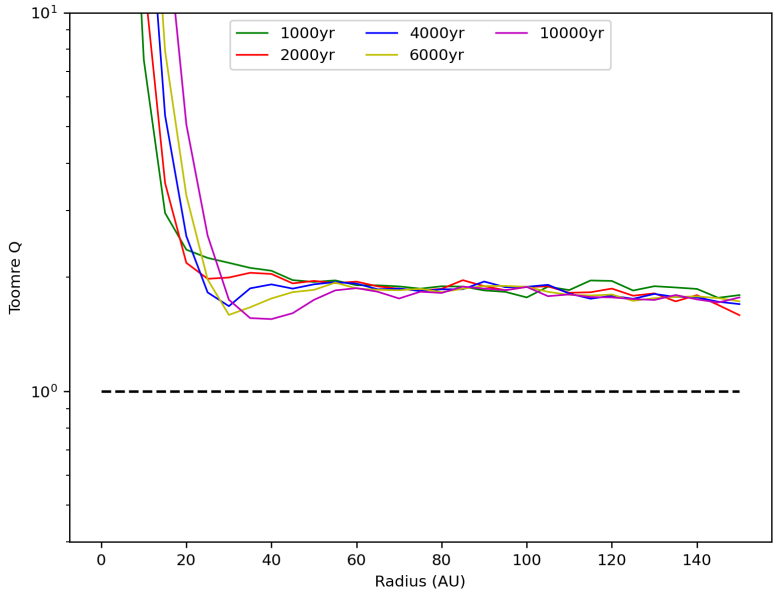

Figure 5.13: The azimuthally averaged Toomre parameter, Q, for the simulation run J01. The Q value for different temporal snapshots are shown using different line colours. The black dotted line shows Q=1. Below this, the disc is gravitationally unstable.

of the disc.

We confirm this by plotting the Toomre parameter as a function of the disc radius for the various temporal snapshots. This is shown in figure 5.13. The Q value does not reach 1 at any point during the evolution of the disc, and therefore, does not become gravitationally unstable.

As the disc evolves, material expands from the inner regions of the disc due to the redistribution of angular momentum. As angular momentum travels inwards, the gas in the inner regions of the disc is transported outwards in order to conserve angular momentum. As well as this, material accretes onto the central object. This can be seen in Figure 5.14 where we show the spatial profile of the simulation at 1 kyr and 10 kyr. The normalised flux of the central concentration of material is seen to drop between the two snapshots, and the disc becomes more uniform and stable through the evolution. It should, again, be noted that the drop interior to

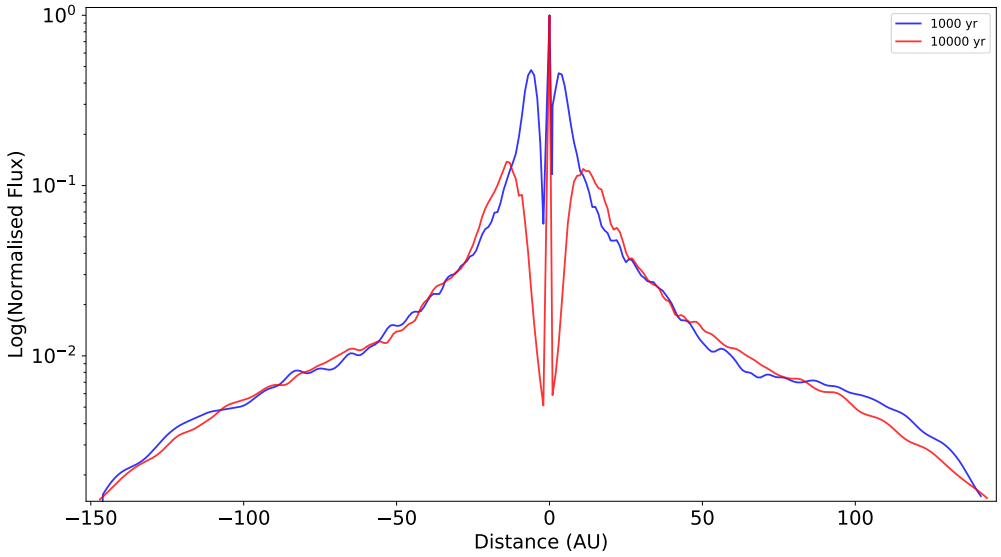

Figure 5.14: Spatial profile for the run J01. The log normalised flux of the disc at 1ky is shown in blue, whilst the log normalised flux at 10 kyr is shown in red. The distance is taken from the centre of the disc.

the peak should be considered as a numerical effect of invoking an accretion radius. As the disc appears to be axisymmetric, we only show the spatial profile taken perpendicular to the x–axis.

The second simulation of the disc surrounding J16152023, J02, is shown in Figure 5.15. Snapshots of the column density can be seen as the disc evolves from 1 kyr to 10 kyr. The mass of this disc has been increased to M_{disc}=0.375 $M_{\odot}$, therefore the disc–to–star mass ratio is $q = 0.375$. The initial conditions are kept the same as the first simulation run (see Table 5.3).

Similar to J01 where the disc mass was M_{disc}=0.25 $M_{\odot}$, the disc in J02 does not appear to become gravitationally unstable. At 2 kyr, tenuous spiral arms can be seen in the outer parts of the disc. However, these dissipate by 4 kyr. A concentration of material can be seen in the centre of the disc. A drop in flux in the central concentration of material can be seen in the spatial profile shown in Figure 5.16. This corresponds to the expansion of material as the angular momentum is redistributed

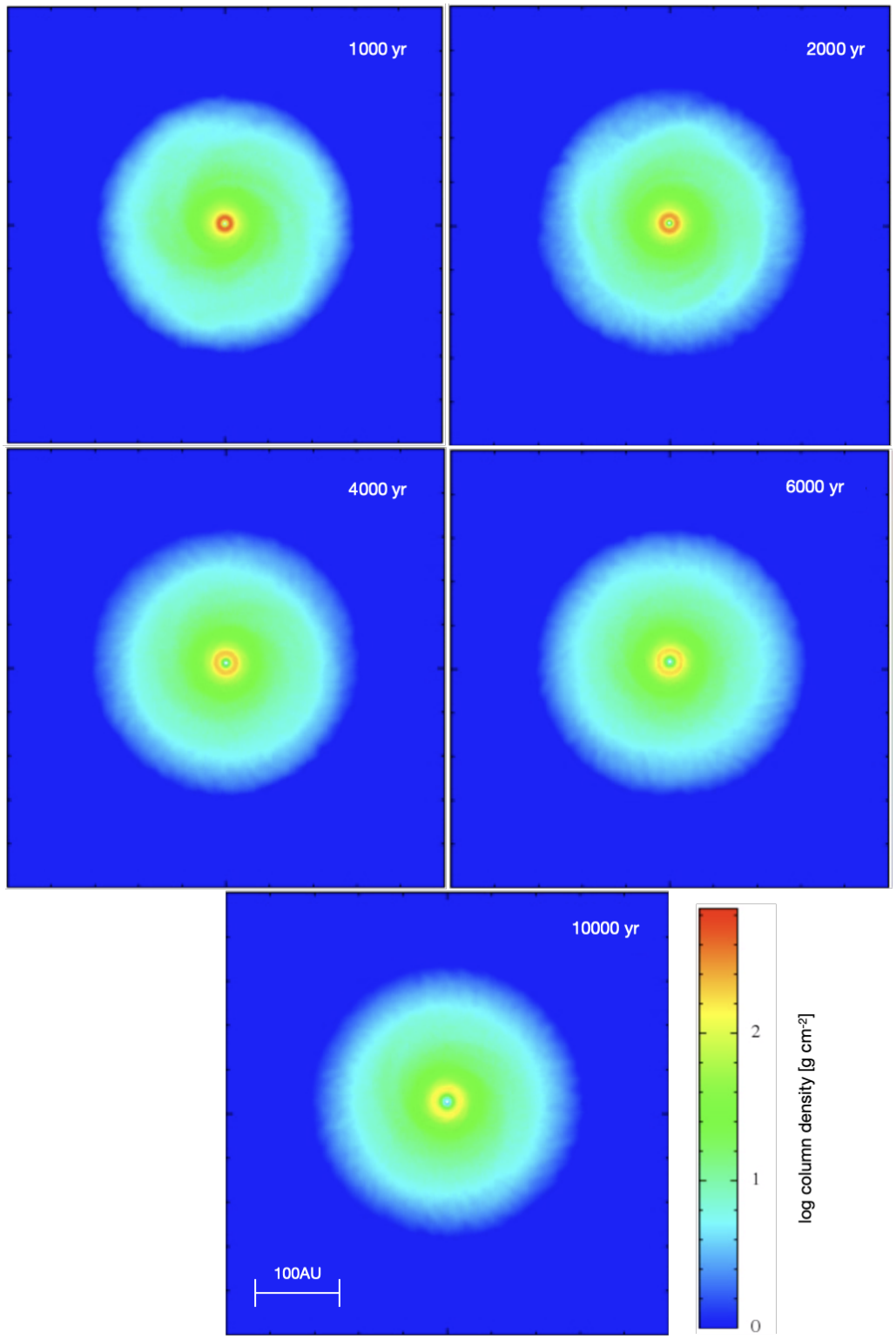

Figure 5.15: Disc evolution of J16152023, with the run ID J02. The disc has a mass of M_{disc}=0.375 $M_{\odot}$. The material migrates from the inner regions of the disc to the outer as the disc evolves. However, the disc does not become unstable.

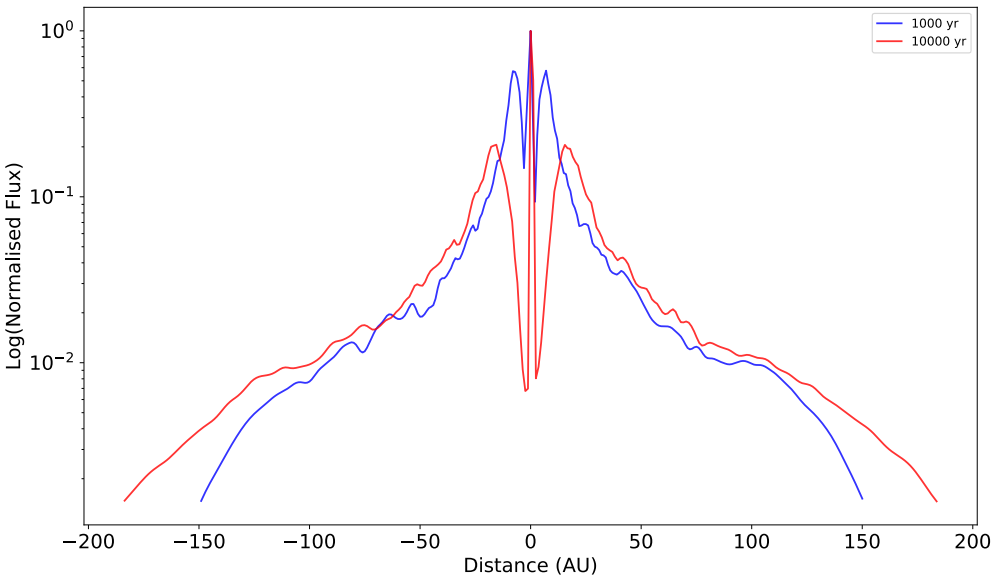

Figure 5.16: Spatial profile for the run J02 taken parallel to the x–axis. The log normalised flux of the disc at 1ky is shown in blue, whilst the log normalised flux at 10 kyr is shown in red. The distance is taken from the centre of the disc.

throughout the disc.

We confirm that the disc does not become gravitationally unstable by plotting the Toomre parameter as a function of radius. This is shown in Figure 5.17. Although the inner regions of the disc have Q values close to 1 at 6 kyr and 10 kyr, the disc is stable for the majority of its evolution.

A third simulation of J16152023 is run with increased disc mass of M_{disc}=0.5 $M_{\odot}$. This increases the disc–to–star mass ratio to $q = 0.5$ for the simulation titled J03. Snapshots of the column density of the simulation are shown in Figure 5.18. This simulation is allowed to run for longer as some substructure can be seen. Therefore, we show snapshots from 1 kyr to 17.5 kyr.

Tenuous spiral arms can be seen throughout the protoplanetary disc at 1 kyr. At 3 kyr, there appears to be a spiral arm in the outer regions of the disc, along with a gap in the material interior to this arm. Although the outer spiral arm dissipates slightly at 8 kyr, small arms seem to form in the central inner regions of the disc.

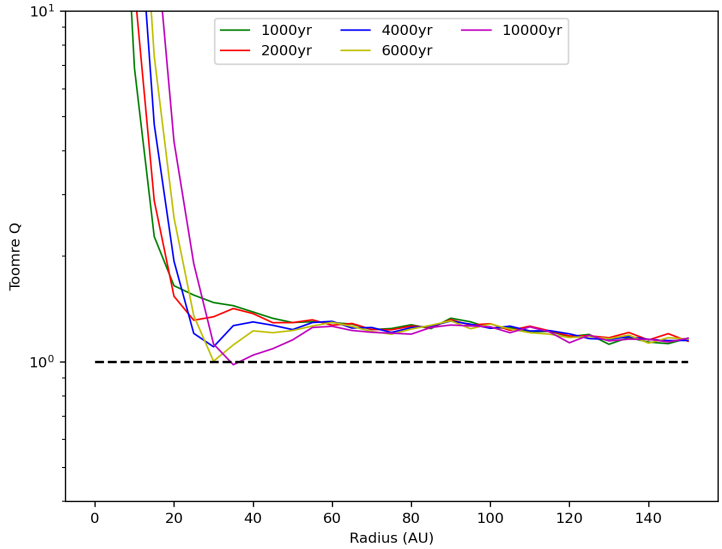

Figure 5.17: The azimuthally averaged Toomre parameter, Q, for the simulation run J02. The Q value for different temporal snapshots are shown using different line colours. The black dotted line shows Q=1. Below this, the disc is gravitationally unstable.

As the disc evolves to 15 kyrs these extend outward to the outer regions of the protoplanetary disc. The spirals remain both in the inner and outer regions of the disc at 17.5 kyr. The central spirals, however, appear weaker compared to earlier snapshots.

We plot the Toomre parameter as a function of disc radius for the various snapshots. This is shown in Figure 5.19. As we can see from Figure 5.19, the Toomre parameter is initially (1 kyr) very close to 1 throughout the disc radius. Therefore the disc is only marginally unstable. This can be seen in the snapshot at 1 kyr in Figure 5.18 where only tenuous spiral arms can be seen.

As the disc evolves, the Toomre parameter drops further under a value of 1. Thus showing that the disc is becoming increasingly unstable. This can, again, be seen in Figure 5.18 where spiral arms are seen to form in the later snapshots. The Toomre parameter stays close to a value of 1 and this may indicate why the spiral

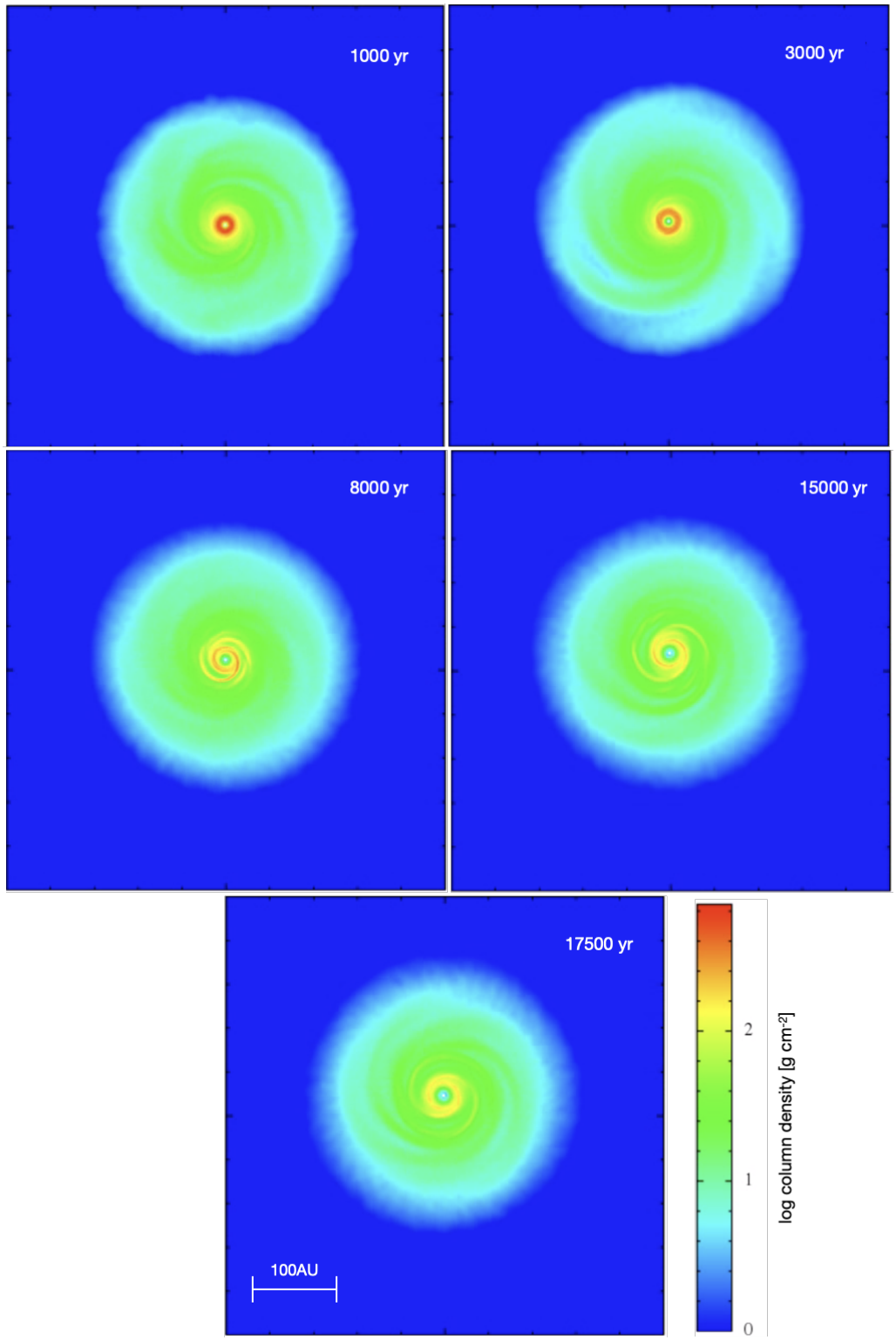

Figure 5.18: Disc evolution of J16152023, with the run ID J03. The disc has a mass of M_{disc}=0.5 $M_{\odot}$. The material migrates from the inner regions of the disc to the outer as the disc evolves. However, the disc does not become unstable.

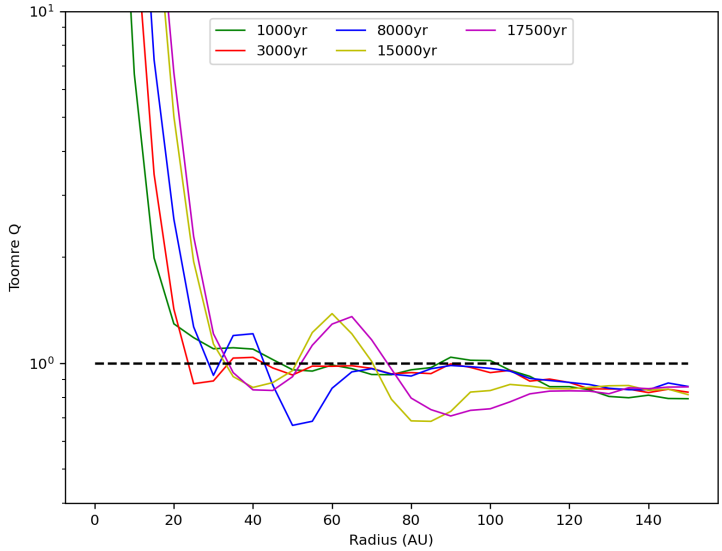

Figure 5.19: The azimuthally averaged Toomre parameter, Q, for the simulation run J03. The Q value for different temporal snapshots are shown using different line colours. The black dotted line shows Q=1. Below this, the disc is gravitationally unstable.

arms in the disc are quite tenuous.

To study the intensity and location of these spiral arms, we take cross–cuts of the disc parallel and perpendicular to the x–axis at all stages of the evolution shown. Figure 5.20 shows cross–cuts taken parallel to the x–axis. At 1 kyr, increases in the flux can be seen in the outer regions of the disc. These multiple increases, however, appear to be very minimal.

Across the evolution of the disc, the amount of material in the central peak decreases as the material expands to the outer regions of the disc. At 8 kyr, two additional peaks, at ∼40 AU and -40 AU from the centre of the disc. However, these become more prominent at at 15 kyr. These peaks can be attributed to the spiral arms seen in the centre of the protoplanetary disc in Figure 5.18.

These two spiral arms extend to the outer regions of the disc at 17.5 kyr, however their strength has very much decreased. This can be seen in Figure 5.20, where at

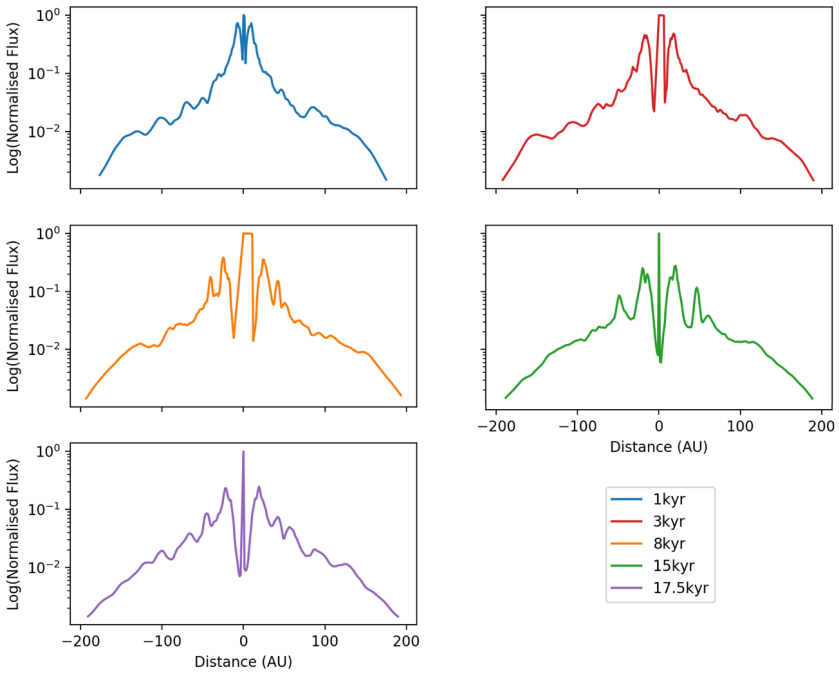

Figure 5.20: Spatial profiles for snapshots from the run J03 taken parallel to the x–axis. The distance is taken from the centre of the disc in each cross–cut.

17.5 kyr there appear to be multiple peaks in the outer regions of the disc. However, these are weaker than in the previous snapshot.

The cross–cuts taken perpendicular to the x–axis is shown in Figure 5.21. Contrary to the emission parallel to the x–axis, there does not appear to be any significant rises in the emission perpendicular to the x–axis at 1 kyr.

The increase in emission, and inferred spiral arm, seen at 15 kyr in Figure 5.20, does not appear to be prominent in the perpendicular cross–cuts. This peak is, however, detected at 17.5 kyr. If this emission was due to a ring of concentration, a peak would be detected both parallel and perpendicular to the x–axis at 15 kyr and 17.5 kyr.

The tenuous spiral arms seen in the outer regions of the protoplanetary disc in the SPH snapshots can also be seen in Figures 5.20 and 5.21. Parallel to the x–axis, at 17.5 kyr there is a slight peak of emission at ∼95 AU. This peak can be seen

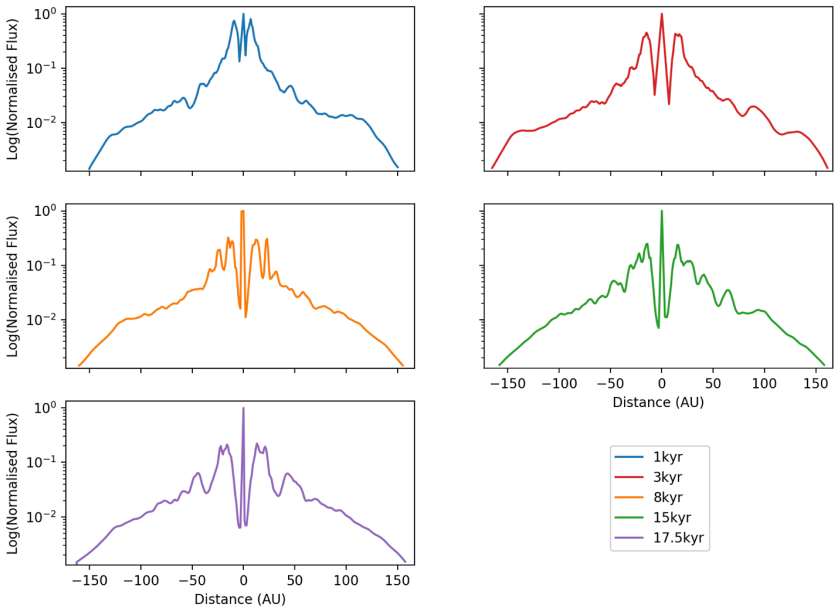

Figure 5.21: Spatial profiles for snapshots from the run J03 taken perpendicular to the x–axis. The distance is taken from the centre of the disc in each cross–cut.

perpendicular to the x–axis at 15 kyr.

Three SPH simulations of J6152023 have been run in this work. Tenuous spiral arms were only able to form in the last simulation, J03, where the disc–to–star mass ratio had a value of $q = 0.5$. We compare the location of the spiral arms produced here to the spirals seen in the ALMA observation in Section 5.6.2 below.

5.5 Simulations of an Intermediate–Mass Star

HD 36112 is an intermediate–mass star (M_*=1.4-2.0 $M_\odot$ (Isella et al. 2010; Shen et al. 2020)) situated 160.2±1.7 pc away (Gaia Collaboration et al. 2018), in the Taurus molecular cloud. It has previously been classified as a Herbig Ae star (Dong et al. 2018a), surrounded by a transitional disc (Isella et al. 2008, 2010; Mariñas et al. 2011; Grady et al. 2013)

The protoplanetary disc surrounding this young stellar object extends to

R_{disc} ∼100 AU (Dong et al. 2018a), and has a disc mass of ∼0.01 $M_{\odot}$ (Andrews et al. 2011). The inner regions of the disc (inwards of 40-50 AU) have been shown to be void of material (Isella et al. 2010; Andrews et al. 2011; Dong et al. 2018a), as well as being eccentric.

Near–Infrared scattered light observations conducted by Grady et al. (2013), revealed two small-scale spiral structures in the protoplanetary disc. These asymmetrically shadow the outer disc and are located at around 30–75 AU (Grady et al. 2013). The spiral arms were shown to extend from the submillimetre cavity, first detected by Isella et al. (2010). The spiral arms were later confirmed by Benisty et al. (2015); who also conducted near–infrared observations, albeit at a higher resolution.

Submillimetre observations were conducted with the Very Large Array (VLA) radio interferometer by Marino et al. (2015). A concentration of mm–sized dust grains (∼9 mm) were found to be incident upon dust emission observed in archival ALMA (∼0.8 mm) observations. The location of both the VLA and ALMA dust emission coincided with the spiral like features seen in scattered light (Grady et al. 2013).

Follow-up ALMA observations were conducted by Boehler et al. (2018) at ∼0.9 mm, the observations of which are shown below in Figure 5.22. Two clumps can be seen in the observation at 47 and 82 AU. One of the arc-like features seen in the near–infrared observations coincide with the inner edge of the dust clumps seen in the ALMA observation (Boehler et al. 2018). Reanalysis of the ALMA observation by Dong et al. (2018a) show that only one spiral arm seen in scattered light is seen at submillimetre wavelengths. This arm can faintly be seen at ∼72 AU. The detection of only one spiral arm could imply that the other does not trap material as effectively as the first arm.

The ALMA observations by Boehler et al. (2018) clearly show two dust clumps, as well as a rim of emission. Therefore, this disc was classified as a Rim disc in

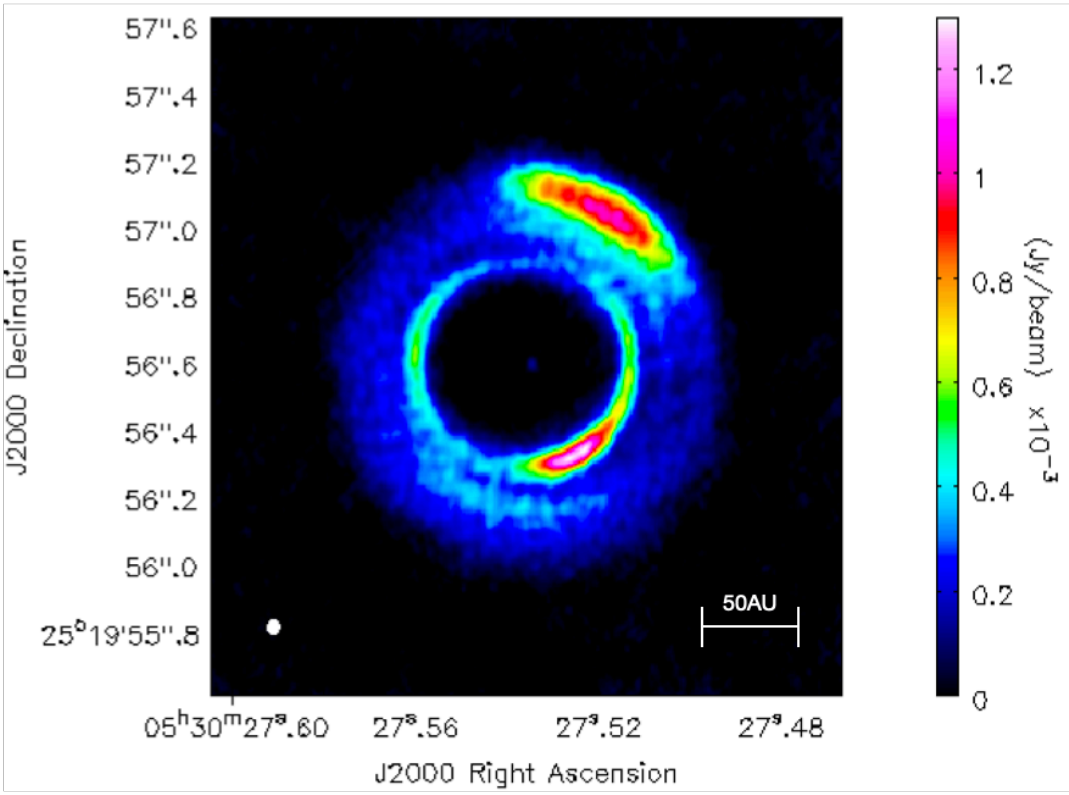

Figure 5.22: ALMA observation of HD 36112 taken at 340 GHz. The beam can be seen in the lower left corner and has a size of 0.04×0.03 arcsec. The position angle of the beam is -2.0°.

Chapter 4 as this is the most prominent structure seen (see Section 4.3 for caveat on classification categories). Dong et al. (2018a) show the dust clumps in the disc of HD 36112, the rim of emission, and the faint spiral arm at ∼72 AU. They also claim that the rim is actually comprised of 3 dust rings. However, this is not clearly apparent in the observations. A caveat of the analysis conducted in Chapter 4 is that a disc may fit into multiple categories; we place it in the Rim category as this is its most distinguishable feature. Nonetheless, the substructure in the disc of HD 36112 is incredibly complex.

Although the disc surrounding HD 36112 has been previously modelled, the majority of these studies aim to recreate the substructure using embedded planets (Dong et al. 2015a; Boehler et al. 2018; Baruteau et al. 2019; Calcino et al. 2020). However, there have been no confirmed detections of such a companion to date. Wagner et al. (2019) claim to detect a 2–5M_J companion at ∼95 AU from the central star. This separation, however, places the planet within the submillimetre continuum emission. A planet of this mass is expected to carve a deep, wide, gap in both the dust and gas disc. However, no such gap is seen in the high–resolution observations of Boehler et al. (2018).

Here we run SPH simulations of the disc surrounding HD 36112 with the aim of determining if substructure can be formed via gravitational instability. We outline the initial conditions of the simulations in Section 5.5.1, followed by the outputs of the simulations in Section 5.5.2. We compare our findings to the literature models in Section 5.6.3.

5.5.1 Initial Conditions

We construct three protostellar systems with the same initial conditions but vary the disc mass. The initial conditions for the protoplanetary disc were outlined in Section 5.2, and we summarise the parameters for the SPH simulations of HD 36112

Table 5.4: The initial disc parameters for the SPH simulations of HD 36112 . Each run is identical, with the exception of the disc mass. The disc mass for each run is given below.

Parameter	Value
M_*	1.9 $M_\odot$
T_*	7600 K
R_{out}	100 AU
M_{disc} ($M_\odot$)	
HD01	0.55
HD02	0.65
HD03	0.75

in Table 5.4.

The stellar mass is set to M_* =1.9 $M_\odot$, whilst the effective temperature is taken to be T_* =7600 K. We utilise the stellar mass of HD 36112 derived in Section 4.4; this value agrees with the derived mass range of M_* =1.4–2.0 $M_\odot$ from previous studies of this young stellar object (Isella et al. 2010; Shen et al. 2020). The effective temperature has been obtained from Andrews et al. (2018b). The metallicity of the disc is set to solar metallicity for all simulations.

The outer radii of the discs were taken to be R =100 AU. We measure this in `CASA` based on the ALMA observations used in Chapter 4. This value agrees with previous estimates by Isella et al. (2010) and Dong et al. (2018a). To determine an initial estimate for the disc mass, we calculate the mass of the material detected by the ALMA observation. This was done following the method outlined above for Elias 2–27 (see Section 5.3.1.1).

Using `CASA`, an intensity of F_ν=485 mJy was measured for HD 36112. Assuming a dust temperature of 10 K and adopting the Gaia DR2 distance of 160 pc, we

measure the disc mass from the ALMA observation to be M_{disc}=0.013M$_\odot$. This value is in agreement with previous disc mass estimates of 0.01M$_\odot$ by Andrews et al. (2011).

As inferred disc masses from observations are, however, heavily underestimated for reasons outlined in Section 5.3.1.1, we make an initial estimate for the disc mass of of M_{disc}=0.55M$_\odot$. A high disc–to–star mass ratio is needed for gravitational instability, therefore we model a protoplanetary disc with a large disc mass of M_{disc}=0.75M$_\odot$. An 'intermediate' mass disc, M_{disc}=0.65M$_\odot$, is also modelled.

5.5.2 SPH Simulations

We run three simulations, varying the disc mass in each. The runs have been titled HD01, HD02, and HD03; with disc masses being set to M$_{disc}$=[0.55, 0.65, 0.75]M$_\odot$, respectively. Initial conditions for the simulations are listed above in Table 5.4. Six snapshots from each SPH simulation are shown, with the timestamp of each snapshot in the top-right corner. Each 'field–of–view' has been scaled to 300×300 AU.

It should be noted that all structure discussed below should be considered physical, except any material interior to ∼15 AU.

5.5.2.1 HD01

Snapshots, from run HD01, showing the evolution of the disc surface density can be seen in Figure 5.23. The disc in this simulation has a mass of M_{disc}=0.55 M$_\odot$. Thus the system has a disc–to–star mass ratio of $q = 0.29$. This large disc–to–star mass ratio satisfies the global condition for instability outlined in Section 5.1.

From Figure 5.23 we can see that, similar to the simulations of Elias 2–27 and J16152023, there is a central concentration of material. As outlined in Section 5.2, any material interior to ∼15 AU is not real. As the disc evolves, material either extends to the outer regions of the disc or is accreted onto the central object.

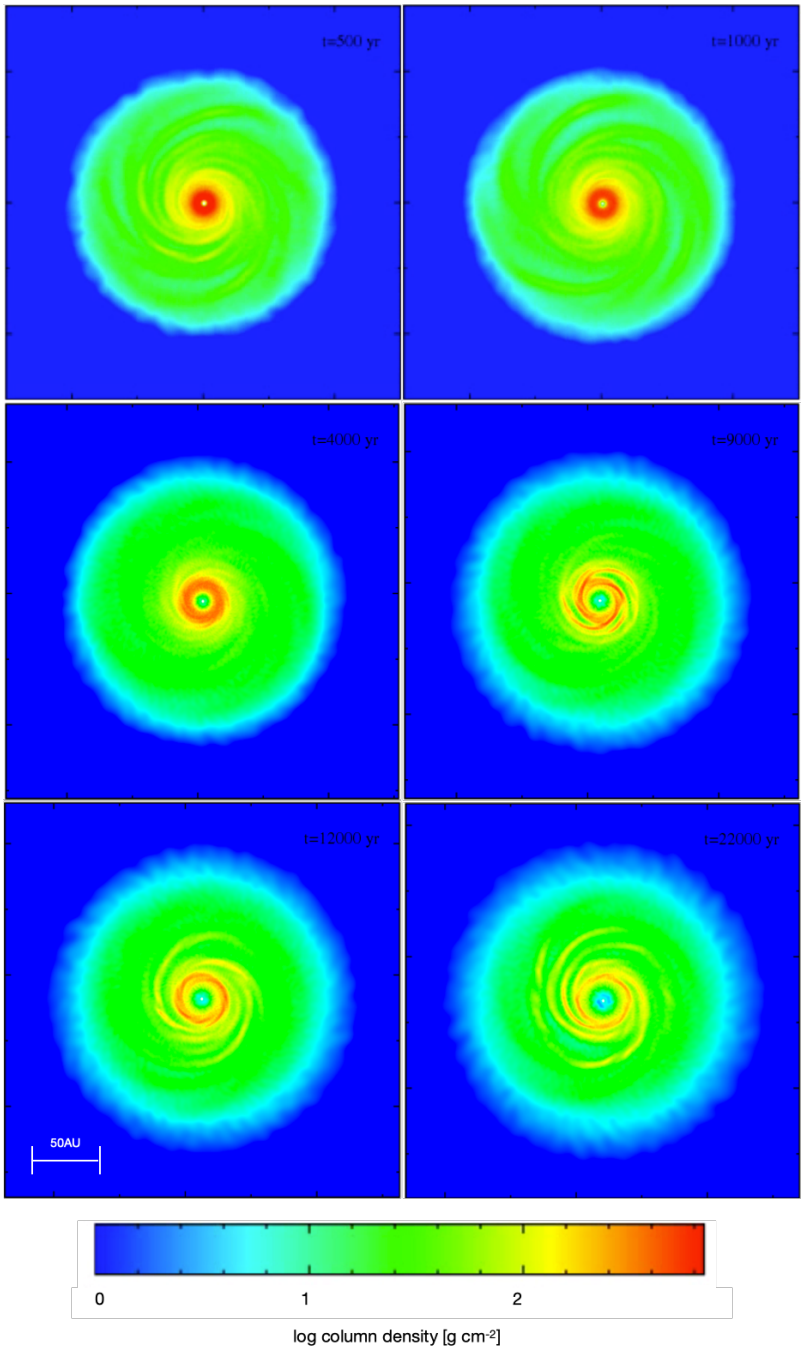

Figure 5.23: Disc evolution of HD 36112, with the run ID HD01. The disc has a mass of M_{disc}=0.55 $M_{\odot}$.

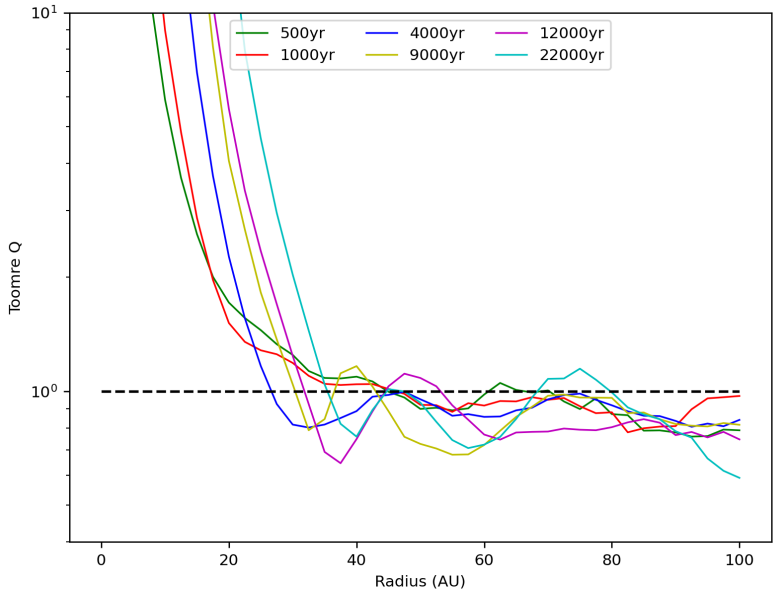

Figure 5.24: The azimuthally averaged Toomre parameter, Q, for the simulation run HD01. The Q value for different temporal snapshots are shown using different line colours. The black dotted line shows Q=1. Below this, the disc is gravitationally unstable.

Spiral arms can be seen throughout the simulation in both the inner and outer regions of the protoplanetary disc. The arms start at around the centre of the disc and extend to the outer regions in the majority of cases. Therefore, the arms cover a wide range of distances.

We confirm that spiral arms have been formed in the disc by looking at the Toomre parameter as a function of disc radius. This is shown in Figure 5.24. We can see that the disc is unstable past a radius of ∼35 AU. The disc at radii further out than that this is unstable throughout its evolution.

Looking at spatial plots of the protoplanetary disc allow us to study the spiral arm, with the peaks in the plot corresponding to the detection of a spiral arm. The spatial plots parallel and perpendicular to the x–axis are shown in Figures 5.25 and 5.26, respectively.

At 500 yr, faint spiral arms can be seen in the centre of the disc as well as in

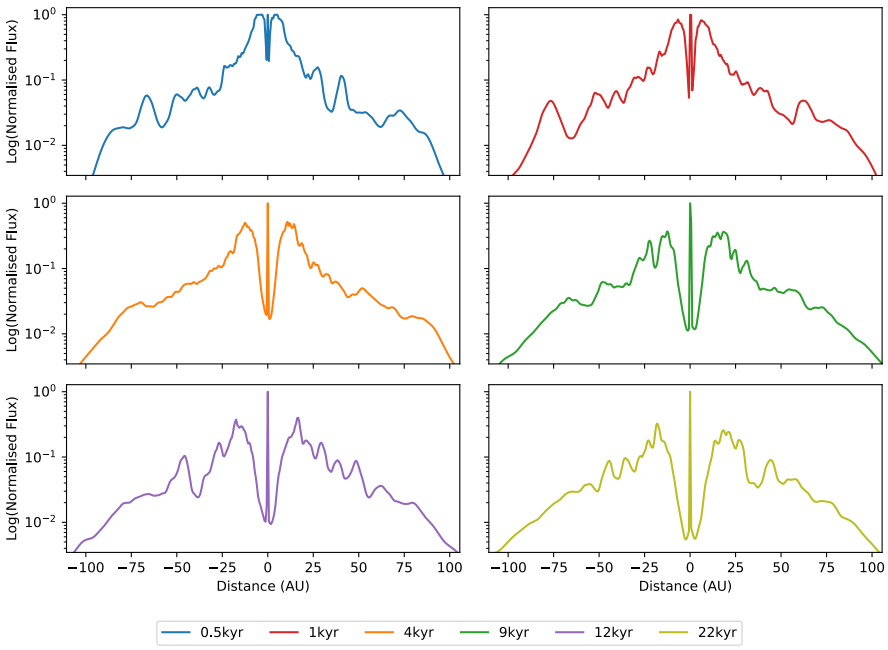

Figure 5.25: Spatial profiles for snapshots from the run HD01 taken perpendicular to the x–axis. The distance is taken from the centre of the disc in each cross–cut.

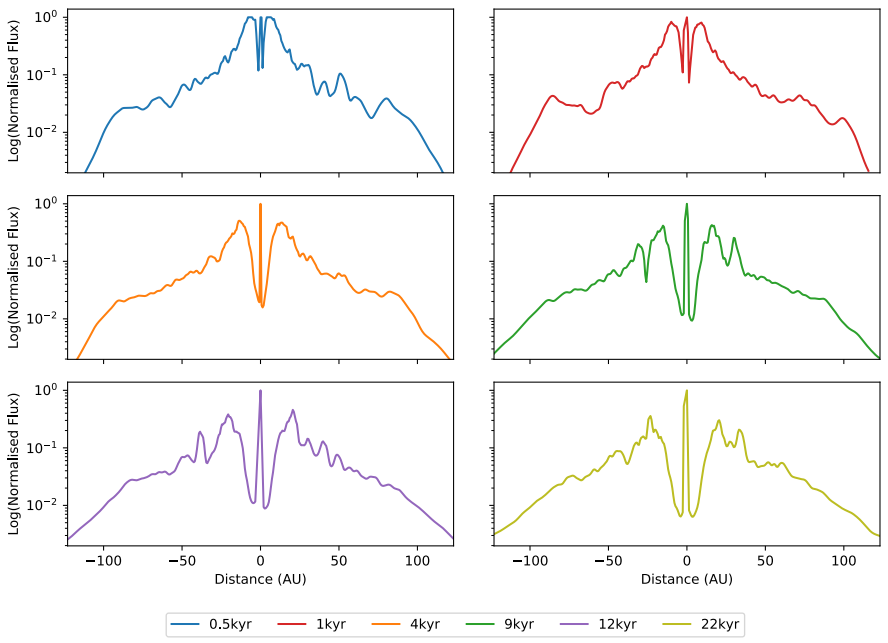

Figure 5.26: Spatial profiles for snapshots from the run HD01 taken parallel to the x–axis. The distance is taken from the centre of the disc in each cross–cut.

the outer regions. Perpendicular to the disc, in Figure 5.25, the spiral arms are first detected at ∼40 AU. This agrees with 5.24, where we find Q <1 (and hence unstable disc) past ∼35 AU. These arms extend to the outer regions of the disc and are detected at ∼-70 AU. They are, however, tenuous and have a reduced magnitude, which can be seen in Figure 5.25. Parallel to the x–axis at 500 yr, an inner arm can be seen at 50 AU, which extends to ∼80 AU. These can be seen as peaks in Figure 5.26.

The ends of the spiral arms extending to the outer regions of the protoplanetary disc are last detected at 1 kyr. The arms previously seen at -75 AU(perpendicular to x–axis) and 80 AU (parallel to the x–axis), now appear to be at -75 AU and 100 AU, respectively. It should be noted that the peak at -75 AU is broader than first detected at 500 yr. This is is due to material expanding from the inner regions of the disc, to the outer regions, thus making the peak and spiral arm broader. The inner regions of the spiral arms seen perpendicular to the x–axis at 40 AU, can now be seen at 60 AU. It has, however, been reduced in magnitude. There are no prominent peaks seen parallel to the x–axis at 1 kyr in Figure 5.26.

The protoplanetary disc appears to be relatively substructure-free at 4 kyr and no prominent spiral arms can be seen in the inner nor outer regions of the disc. Similarly, no peaks, broad or sharp, can be seen on the spatial profiles of the disc taken perpendicular and parallel to the x–axis (see Figures 5.25 and 5.26).

The inner region of the disc becomes gravitationally unstable at 9 kyr and spiral arms can be seen. Perpendicular to the x–axis, sharp peaks can be seen at -25 AU and 30 AU. The peaks due to these spiral arms can be more prominently seen in Figure 5.26, parallel to the x–axis, at -30 AU and 30 AU. The instability of the disc at this radius can also be seen in Figure 5.24, where we see $Q < 1$ between 25–35 AU at 9 kyr.

The spiral arms in the inner region then begin to extend to the middle regions

of the protoplanetary disc at 12 kyr. They do, however, appear to be much fainter compared to the spiral arms seen at 9 kyr. The axisymmetric spiral arms seen at 9 kyr at -30 AU and 30 AU have now extended and appear in Figures 5.25 at -45 AU and 45 AU. They also appear parallel to the x–axis in Figure 5.26 at ∼40 AU, however, these peaks are much fainter.

The last snapshot of the simulation, at 22 kyr, show the spiral arms extending to near the outer regions of the protoplanetary disc. They do not, however, appear to be broad arms, but rather narrow, short, spiral arms. The arms are located at ∼-45 AU and 45 AU perpendicular to the x–axis and are the same arms previously seen at 12 kyr. Parallel to the x–axis, the spiral arm at -45 AU is not detected. The arm at 45 AU can be seen in Figure 5.26. The inner region of the disc has many additional spiral arms. However, these are too faint to show up predominantly on the spatial plots. Instead, these are visible as small peaks interior to ∼50 AU.

5.5.2.2 HD02

The second simulation of the disc surrounding HD 36112, HD02, is shown in Figure 5.27. Snapshots of the column density can be seen as the disc evolves from 100 yr to 1800 yr. The mass of this disc has been increased to M_{disc}=0.65 $M_{\odot}$, whilst the initial conditions are kept the same (see Table 5.4). The disc still satisfies the global condition for instability as $q = 0.34$.

From Figure 5.27 we can see that spiral arms form throughout the entire evolution of the protoplanetary disc. Narrow, high intensity, spiral arms form in the inner regions of the disc, and extend to broad spiral arms in the outer parts of the disc. The spiral arms can be seen throughout the entire evolution within the inner regions of the disc, however, their extension to the outer regions of the disc only appear after 1 kyr.

Figure 5.28 shows the Toomre parameter for each snapshot as a function of

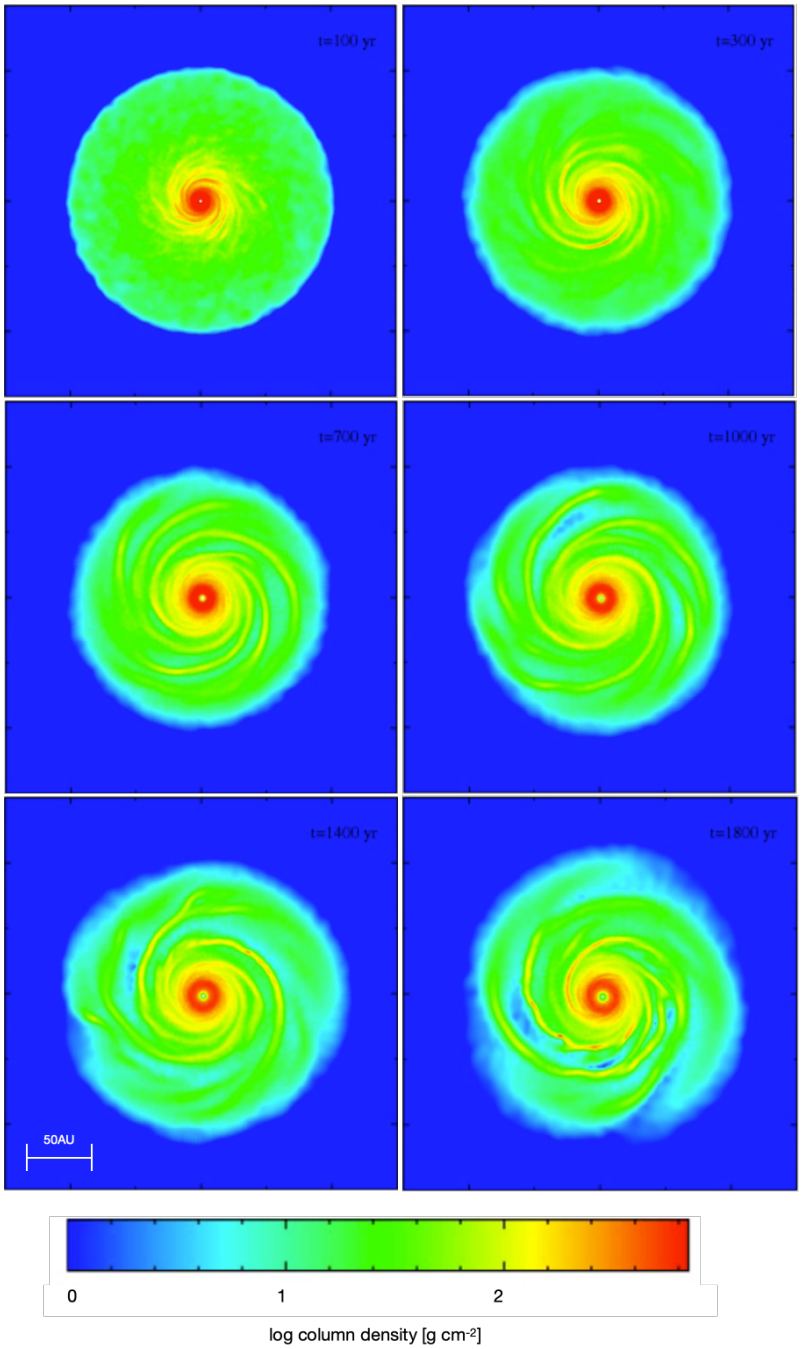

Figure 5.27: Disc evolution of HD 36112 , with the run ID HD02. The disc has a mass of M_{disc}=0.65 $M_{\odot}$.

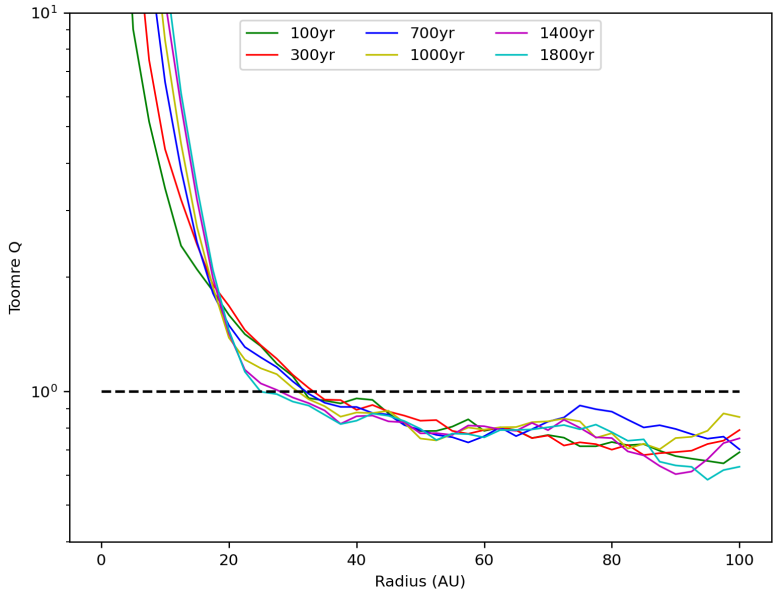

Figure 5.28: The azimuthally averaged Toomre parameter, Q, for the simulation run HD02. The Q value for different temporal snapshots are shown using different line colours. The black dotted line shows Q=1. Below this, the disc is gravitationally unstable.

radius. We can see that the disc has a Q value less than 1 at radii $R >\sim 25$ AU at all evolutionary snapshots. Therefore the disc is gravitationally unstable and explains the appearance of the spiral arms seen in the SPH snapshots.

Simulation run HD02 has an increased mass of $0.1 M_{\odot}$ compared to run HD01. The increase in mass has resulted in the disc becoming even more unstable. This is apparent by comparing the Toomre plot from run HD01 (see Figure 5.24) to run HD02 (see Figure 5.28). The Q values in the lower mass disc, at all snapshots, are $\sim$1 throughout the majority of the disc radii (past a radii of $R >$35 AU). At some radii, however, the Toomre parameter is greater than 1, indicating a locally stable region of the disc. In contrast to this, run HD02 has a Toomre value less than 1 across all disc radii (past a radii of $R >$35 AU), at all snapshots. Therefore, the disc in run HD02 is unstable compared to the disc modelled in run HD01.

To study the intensity and location of the spiral arms, we take cross–cuts of the

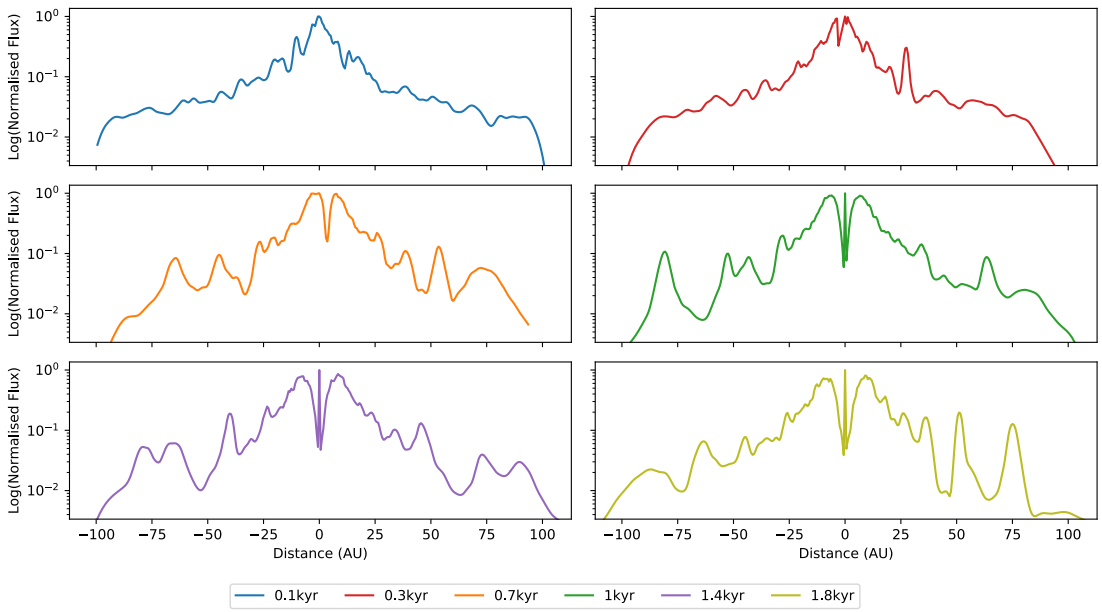

Figure 5.29: Spatial profiles for snapshots from the run HD02 taken perpendicular to the x–axis. The distance is taken from the centre of the disc in each cross–cut.

disc parallel and perpendicular to the x–axis at all stages of the evolution shown. Figures 5.29 and 5.30 shows cross–cuts taken perpendicular and parallel to the x–axis respectively.

At 100 yr, the disc appears to be stable, however, tenuous spiral arms can be seen within the inner regions of the disc. This is evident in the spatial profiles taken perpendicular to the x–axis, where we see small peaks throughout the profile, with no predominant peaks. There does, however, appear to be peaks parallel to the x–axis at -40 AU and 50 AU. These can be seen in Figure 5.30.

Although the inner spirals move outward by 300 yr, they do not yet extend to form broad spiral arms in the outer regions of the disc. A sharp peak can be seen in the perpendicular spatial plot, at 300 yr, at 30 AU (see Figure 5.29). The faint peaks caused by the narrow spiral arms in the inner regions of the disc can be seen inwards of ∼-60 AU. More predominant peaks can be seen in the parallel spatial plot; with spiral arms being seen at -40, -45 and -60 AU. Small peaks can be seen

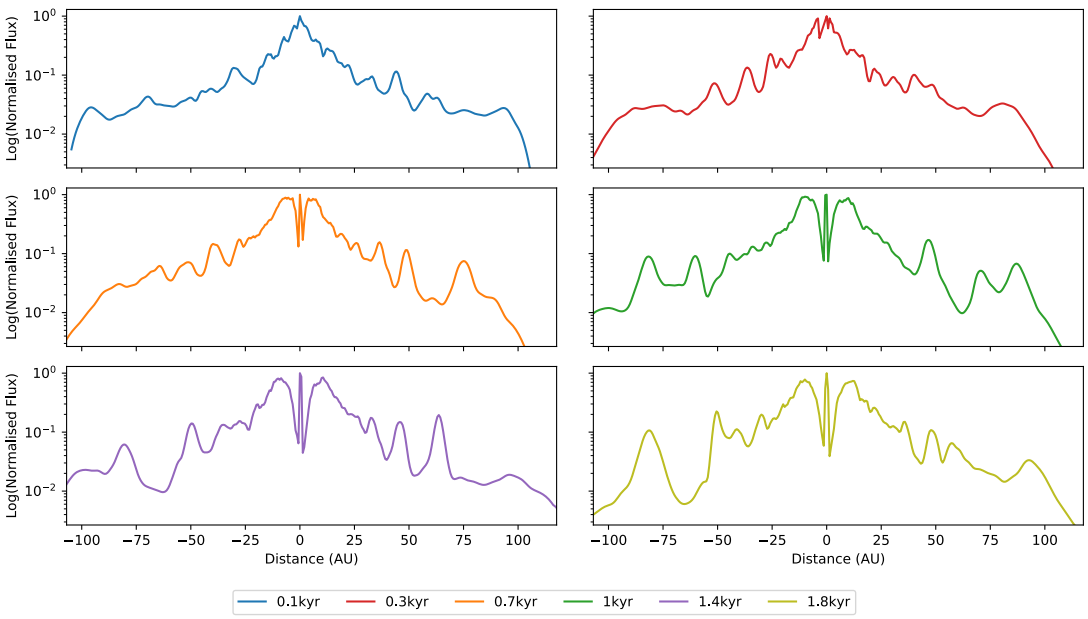

Figure 5.30: Spatial profiles for snapshots from the run HD02 taken parallel to the x–axis. The distance is taken from the centre of the disc in each cross–cut.

across the centre of the disc, however, these are faint. Therefore, we cannot make any conclusions about the axisymmetric nature of the spiral arms at 300 yr.

At 700 yr, the spiral arms have extended to the outer regions of the protoplanetary disc, and the broad, tenuous nature of the arms can be seen. Looking at the spatial plot perpendicular to the x–axis in Figure 5.29, there appear to be four peaks located at -60, -40, 40 and 55 AU. By looking at Figure 5.27, the peaks at -60 AU and 40 AU appear to be due to the same spiral arm. The peak due to the spiral arm at -40 AU is detected parallel to the x–axis at 70 AU, this can be seen in Figure 5.30. The peak detected parallel to the x–axis at -40 AU is due to the spiral arm detected at -40 AU in the perpendicular spatial plot.

At 1000 yr, the narrow inner spiral arms have now extended to the outer regions of the protoplanetary disc and have begun to form wide–spread spiral arms. There also appears to be a gap forming in the top regions of the snapshot. Symmetrical peaks can be seen in the perpendicular spatial plot of the simulation at 1000 yr;

visible at -30 AU and 30 AU. The spiral arm causing the peak at 30 AU extends to the outer regions of the disc and forms a broad spiral arm at -80 AU. This can be seen at the top of the snapshot, where a gap appears to be forming, and is clearly visible in Figure 5.29. A peak can be seen at 60 AU as well as a double peak centred at -50 AU. This is due to one narrow spiral arm extending to two, which can be seen in Figure 5.27. Parallel to the x–axis, peaks can be seen in a number of locations in Figure 5.30. A spiral arm is visible at -80 AU as well as 80 AU. These extend from the spiral arms seen at 60 AU and -50 AU in the perpendicular spatial plots, respectively. A sharp peak can also be seen at 45 AU; caused by the narrow spiral arm seen at -30 AU and 60 AU in the perpendicular spatial plots.

The disc evolves to become more unstable at 1400 yr and spiral arms are clearly visible both in the inner and outer regions. A gap can also be seen in Figure 5.27. The narrow spiral arm located at the top of the disc, appears to be comprised of two narrow arms. These are visible on the perpendicular spatial plot, Figure 5.29, at -80 AU and -65 AU. This narrow, arm is also visible at 40 AU. A sharp peak can also be seen at $\sim$-45 AU. This is due to a spiral arm which extends and splits into two spiral arms at 80 AU. The spiral arms causing these peaks are also visible parallel to the x–axis in Figure 5.30. Peaks are seen at -50 AU and 60 AU which correspond to the double pronged spiral arms seen perpendicular to the x–axis and -80 AU and 80 AU, respectively.

Clear gaps and spiral arms are seen in the last snapshot of the simulation at 1800 yr. Broad spiral arms can bee seen in the outer regions which are extensions of the narrow arms seen in the inner regions of the disc. A broad arm is detected at $\sim$-80 AU both perpendicular and parallel to the x–axis in Figures 5.29 and 5.30, respectively. A narrow arm is seen at -60 AU perpendicular to the x–axis and extends to 80 AU. The spiral arms causing these peaks can also be seen parallel to the x–axis at $\sim$50 AU. The spiral arm corresponding to the peak seen at $\sim$50 AU

perpendicular to the x–axis can also be seen at ∼-90 AU parallel to the x–axis.

5.5.2.3 HD03

The final simulation of the disc surrounding HD03, is shown in Figure 5.31. Snapshots of the column density can be seen as the disc evolves from 60 yr to 700 yr. The mass of this disc has been increased to M_{disc}=0.75 $M_{\odot}$, whilst the initial conditions are kept the same (see Table 5.4). The disc still satisfies the global condition for instability ($q > 0.25$ Dong et al. (2015b)) as $q = 0.39$.

Spiral arms can be seen forming in the protoplanetary disc from 200 yr; this is evident in Figure 5.31. Narrow, high intensity, spiral arms form in the inner regions of the disc and extend to form broader spiral arms in the outer parts. The outer spiral arms in the disc of HD03, however, are less prominent than the broad spiral arms seen in run HD02.

We plot the Toomre parameter as a function of disc radius for the various evolutionary snapshots of run HD03. This is shown in Figure 5.32. As can be seen from the plot, the disc is gravitationally unstable at every snapshot at radii greater than ∼30 AU. Therefore, the spiral arms seen in the SPH snapshots of run HD03 are due to the disc becoming gravitationally unstable.

To study the intensity and location of these spiral arms, we take cross–cuts of the disc parallel and perpendicular to the x–axis at all stages of the evolution shown. Figures 5.33 and 5.34 show cross–cuts taken perpendicular and parallel to the x–axis respectively.

At 60 yr the protoplanetary disc appears relatively smooth, although tenuous spiral arms can be seen in the inner most regions of the disc. Material from this region has also begun to redistribute to outer parts of the disc. This can be seen in Figures 5.33 and 5.34, where there are many peaks throughout the discs extent as the intensity varies.

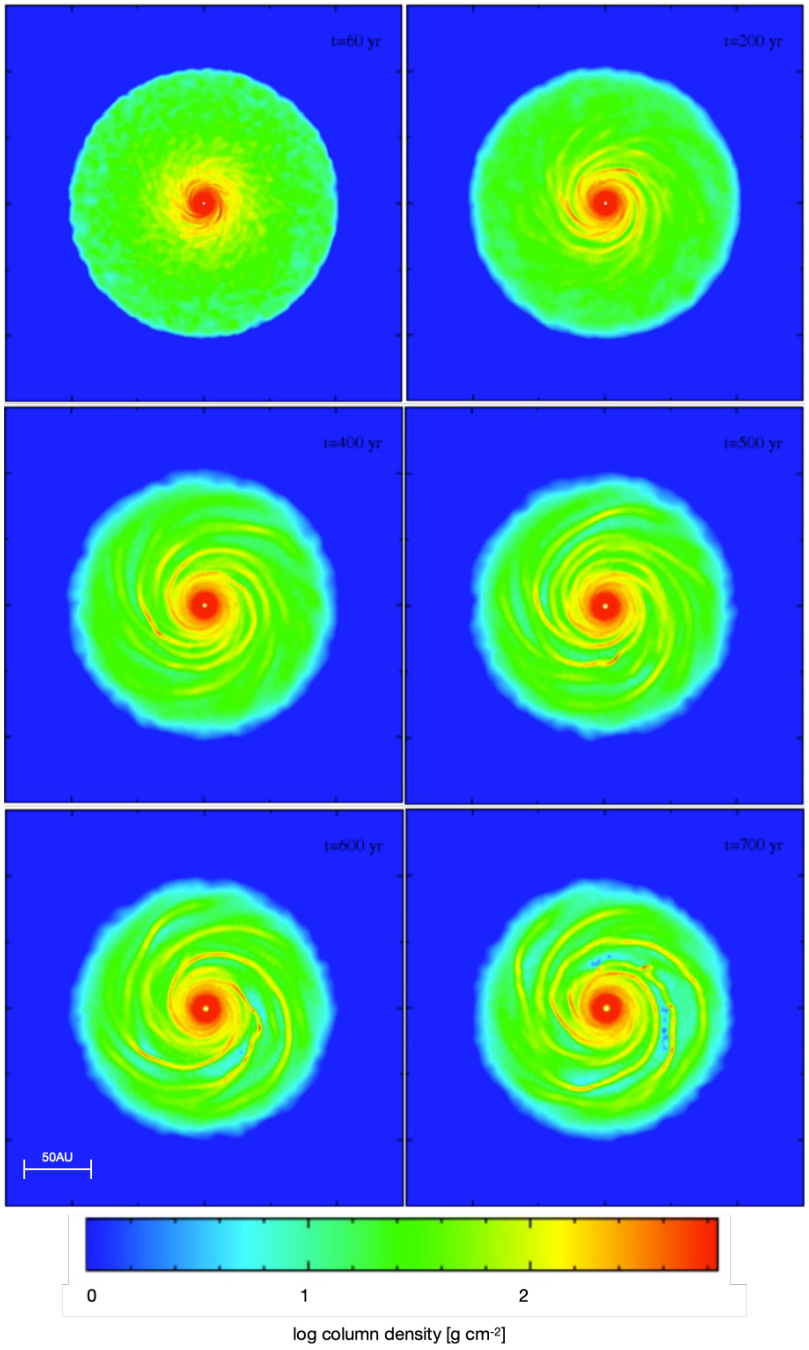

Figure 5.31: Disc evolution of HD 36112, with the run ID HD03. The disc has a mass of M_{disc}=0.75 $M_{\odot}$.

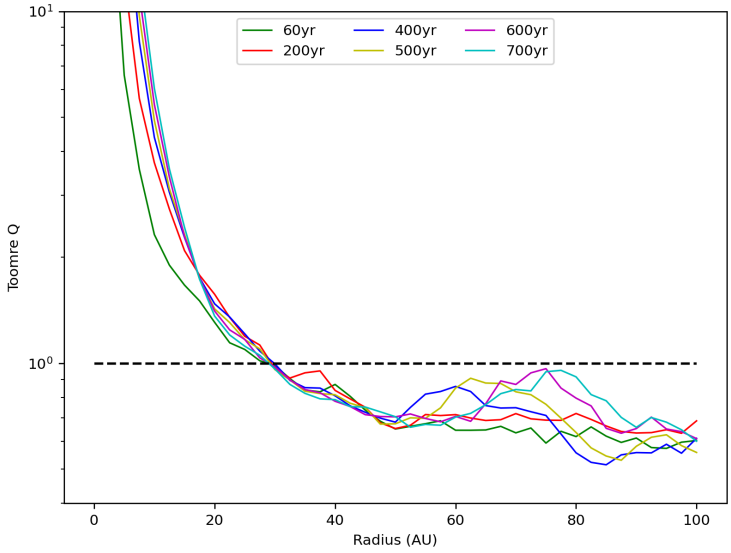

Figure 5.32: The azimuthally averaged Toomre parameter, Q, for the simulation run HD03. The Q value for different temporal snapshots are shown using different line colours. The black dotted line shows Q=1. Below this, the disc is gravitationally unstable.

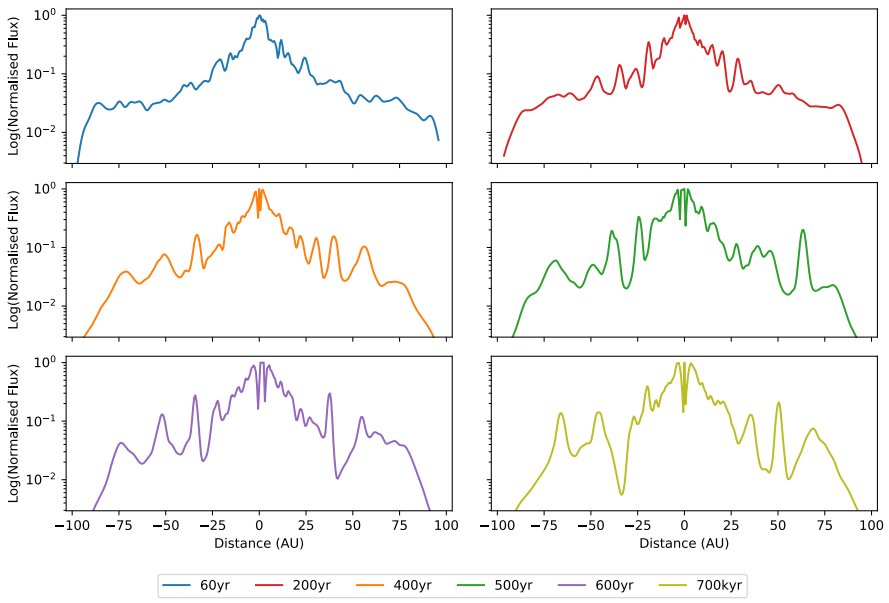

Figure 5.33: Spatial profiles for snapshots from the run HD03 taken perpendicular to the x–axis. The distance is taken from the centre of the disc in each cross–cut.

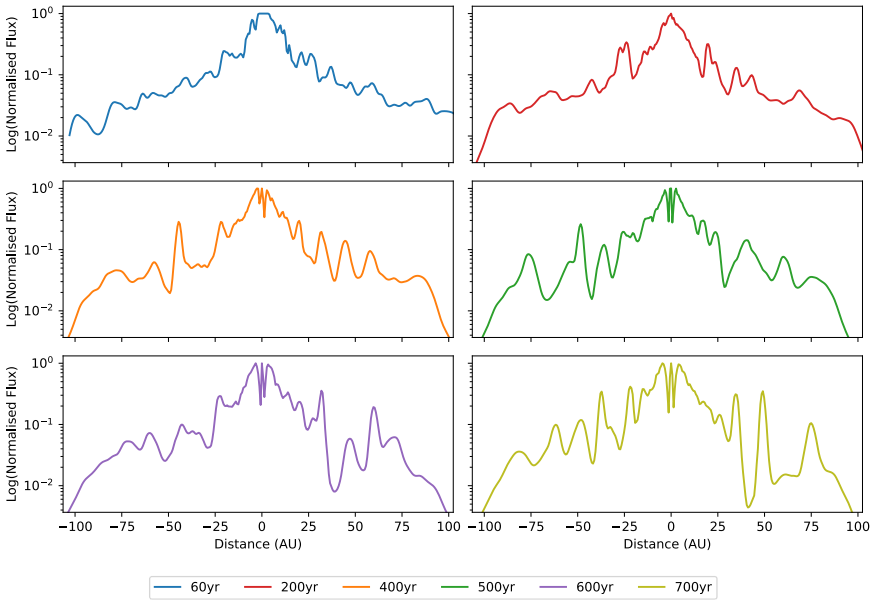

Figure 5.34: Spatial profiles for snapshots from the run HD03 taken parallel to the x–axis. The distance is taken from the centre of the disc in each cross–cut.

After 200 yr, narrow, high intensity spiral arms can be seen extending to the mid-regions of the disc. Perpendicular to the x–axis, Figure 5.33 shows that the peaks are localised interior to -50 AU and 50 AU. Prominent peaks are located at -35 AU and -20 AU. We also find peaks at ∼30 AU and ∼20 AU. Therefore the spiral arms within the inner regions appear to be somewhat symmetrical. Parallel to the x–axis, we again see that the spiral arms are located in the inner regions of the disc as the majority of the peaks in Figure 5.34 are located interior to -50 AU and 50 AU. Double peaks are detected at ∼-25 AU and 30 AU. The spiral arms coinciding with these peaks are the arms detected at -35 AU and -20 AU perpendicular to the x–axis. A sharp peak is also detected at 20 AU parallel to the x–axis and extends to form the spiral arm seen at ∼30 AU perpendicular to the x–axis.

The narrow spiral arms extend to the outer regions of the disc as it evolves to 400 yr. This can be seen in Figures 5.33 and 5.34 where the peaks are no longer localised interior to -50 AU and 50 AU. Perpendicular to the x–axis, we find peaks

at ∼-50 AU, as well as at 60 AU. The spiral arm causing the peak located at 60 AU can also be seen parallel to the x–axis at ∼40 AU. A sharp peak is also seen parallel to the x–axis at -40 AU. The spiral arm causing this peak cannot be distinguished perpendicular to the x–axis as it is interior to ∼30 AU. The peak at ∼60 AU parallel to the x–axis can be seen as a sharp peak at ∼40 AU perpendicular to the x–axis.

Although the spiral arms have extended to the outer regions of the disc at 500 yr, they are not broad. This contrasts to run HD01, where faint, broad arms could be seen at 500 yr. Parallel to the x–axis, a narrow peak is seen at -50 AU. The spiral arm causing this peak extends to -70 AU, which can be seen in the perpendicular spatial plot (Figure 5.33). This arm also causes the peak seen at 25 AU. The spiral arms causing the peaks perpendicular to the x–axis at -35 AU and -25 AU also cause peaks to appear at 60 AU and 40 AU parallel to the x–axis, respectively. The peak seen at 65 AU perpendicular to the x–axis coincides with the spiral arm seen at ∼20 AU parallel to the x–axis.

At 600 yr, no broad spiral arms can be seen in the outer regions of the plot, however, narrow arms in the inner regions of the disc can be seen to be extending outwards. Perpendicular to the x–axis, we see peaks on the spatial plot (shown in Figure 5.33) at ∼-55 AU and -35 AU. The spiral arms causing these peaks also produce peaks parallel to the x–axis at -40 AU and -20 AU, respectively. The latter spiral also extends parallel to the x–axis up to a distance of ∼60 AU.

Gaps can be seen in the mid-regions of the protoplanetary disc at 700 yr. A gap in the disc is visible in Figure 5.33, perpendicular to the x–axis, at -30 AU, where the magnitude steeply decreases. Parallel to the x–axis, a steep decrease in magnitude at ∼40 AU can be attributed to the gap visible in Figure 5.31 at 700 yr.

A spiral arm is seen to extend from 25 AU anti-clockwise around the protoplanetary disc in Figure 5.31. The peak from this arm can be seen in Figure 5.33. As the arm extends around the disc, peaks are measured parallel, perpendicular, and

parallel to the x–axis at -30 AU, -50 AU, and 75 AU, respectively. The sharp peak seen perpendicular to the x–axis at ∼-65 AU corresponds to the spiral arm, which is also seen parallel to the x–axis at -50 AU. Lastly, a prominent peak can be seen parallel to the x–axis at 50 AU. The arm responsible for this peak, however, is only seen tenuously perpendicular to the x–axis at ∼70 AU.

5.6 Discussion

We use the SPH code `SEREN` in order to model the protoplanetary disc around three young stellar objects. The features utilised here in `SEREN` were first outlined in Section 3.2.1. Section 3.2.2 also provided the results of the tests run on `SEREN`. We also discussed that `SEREN` provides similar results with other well-established hydrodynamic codes (Fletcher et al. 2019).

As we are interested in the formation of spiral arms, we expect their formation when the Toomre parameter of the disc reaches $Q \lesssim 1$; as is predicted by theory. The SPH simulations of the disc surrounding Elias 2-27 failed to produce spiral arms. This is evident in the snapshots shown in Figures 5.2, 5.5, and 5.8. We have plotted the Toomre parameter as a function of disc radius for each of these discs in Figures 5.3, 5.6, and 5.9, respectively. In each of these plots, we find that the Toomre value does not come close to 1 at any point in the disc's evolution. Thus justifying the stability of the disc and showing that SEREN produced what expected from theoretical studies regarding the disc stability.

We also model the disc surrounding HD 36112, and find spiral arms forming in all models run (see Figures 5.23, 5.27, 5.31). We find that the Toomre parameter for these discs at the various evolutionary snapshots are all less than 1 (see Figures 5.24, 5.28, 5.32), thus verifying that the code reproduces what is expected from theory.

5.6.1 Elias 2–27

The aim of our SPH simulations were to recreate the spiral substructure seen in the disc of Elias 2–27 (Pérez et al. 2016). To do this, the disc would need to become gravitationally unstable without fragmenting to produce secondary objects. We run three simulations of the disc surrounding Elias 2–27, increasing the disc mass in each case. Although each disc is modelled with an unusually high disc mass, none of the discs became gravitationally unstable. Each disc became more uniform as it evolved.

The stability of a protoplanetary disc is governed by the Toomre parameter, Q, first introduced in Section 1.3.4.2,

$$Q = \frac{c_s K}{\pi G \Sigma} \tag{5.3}$$

where c_s is the sound speed of the disc gas, K is the epicyclic frequency, and Σ is the surface density (Toomre 1964). Discs with $Q \sim 1$ will be unstable to non-axisymmetric perturbations and may form spiral structures. Although the discs modelled here had unusually high masses, and therefore surface densities, they are comparable with previous disc models of Elias 2–27 that were able to gravitationally fragment (Meru et al. 2017; Forgan et al. 2018). Therefore, it is likely that another disc parameter is responsible for the stability of the discs modelled here.

Meru et al. (2017) ran hydrodynamic and radiative transfer models of Elias 2–27 to determine the origin of the spiral structure seen in the disc. Elias 2–27 was modelled using a stellar mass of M_* =0.5 $M_\odot$, and was surrounded by a disc of mass M_{disc} =0.24 $M_\odot$. This gives a disc–to–star mass ratio of $q = 0.48$, similar to the mass ratio of $q = 0.5$ used here in EL03. They, however, were able to reproduce the grand design spiral arms seen in the disc. Although they use the same prescription for cooling as us and a shallower power law index of 0.45 for their temperature

profile (an index of 0.6 is used here), they initially begin their simulations with a colder disc than ours (∼145 K at 1 AU compared to 300 K at 1 AU used here). This lower initial temperature enables the disc to become gravitationally unstable. The initial temperature at 1 AU invoked this work is not overestimation as previous works which have been able to form spiral arms (see discussion regarding Forgan et al. (2018) below) have used initial disc temperatures of ∼700 K at 1 AU.

It should be noted, however, that Meru et al. (2017) were also able to reproduce the spiral arms by inserting a companion into the disc of Elias 2–27. Previous simulations by Zhu et al. (2015) and Dong et al. (2015a) were able to show that planet-companion disc interactions (PDIs) alone are capable of opening a gap and inducing temperature contrasts similar to what is seen in Elias 2–27 (Pérez et al. 2016). A protoplanet of mass, $M_p > 10 - 13$ M_{Jup} located at $\approx 300 - 700$ AU from the central object was able to induce spiral arms in the disc, thus indicating that Elias 2–27 may either be gravitationally unstable or has already undergone fragmentation to form secondary objects in the disc.

These results were confirmed by Forgan et al. (2018) who run similar SPH simulations to Meru et al. (2017). Spiral arms were shown to be induced in the disc via both gravitational instability and with an embedded planet. Forgan et al. (2018), however, were able to show that the spiral arms produced by gravitational instability are symmetric, whilst those produced by a companion are asymmetric. Symmetric spiral arms are two arms which appear symmetrical about the disc centre (see Figure 5.1 for the symmetrical spiral arms of Elias 2-27). The conclusions reached by Forgan et al. (2018) highlight the need to utilise synthetic observations in order to assess the validity of numerical simulations and make direct comparisons to observations (c.f. (Haworth et al. 2018)). We explore this further in Chapter 6.

The formation of spiral arms due to gravitational instability in the disc of Elias 2–27 has also been shown by Hall et al. (2018). Using SPH simulations, coupled with

radiative transfer techniques, simulations of protoplanetary discs varying the disc metallicity, disc–to–star mass ratio and irradiation temperature were conducted. The disc–to–star mass ratios investigated by Hall et al. (2018) are the same as those investigated in this work. Hall et al. (2018) vary the disc metallicity between solar metallicity and 0.25× solar metallicity. The ambient temperature is varied between 5 K and 10 K.

All SPH simulations run by Hall et al. (2018) show some sort of spiral substructure in the disc before synthetic observations are made. The SPH simulations presented here may fail to produce spiral substructure as they differ from Hall et al. (2018) with regards to the disc metallicity and irradiation temperature.

Prominent spiral arms were seen to form in the SPH discs of Hall et al. (2018) when an irradiation temperature of T_{∞} =5 K was used. We, however, use irradiation temperature of T_{∞} =10 K. This is done as ambient temperature in regions containing protoplanetary discs are ∼10–30K (Hayashi & Nakano 1965; Hayashi 1966; Tohline 1982; Larson 1985; Masunaga & Inutsuka 2000; Stamatellos et al. 2005a,b; Battersby et al. 2014). We do not explore temperatures below 10 K as it is highly unlikely that these low temperatures will be present in regions containing systems such as Elias 2–27.

Hall et al. (2018) use metallicity as a proxy for the opacity, and assume that the relationship between these parameters is 1:1 (Semenov et al. 2003). Prominent spiral arms in the SPH simulations only form with a metallicity of 0.25× solar metallicity (i.e. when the opacity is four times lower than the canonical value). Here we follow the commonly used opacity of κ_{ν}=2.3 cm^{2}g^{-1} (Beckwith et al. 1990) and assume a gas-to-dust ratio of 100:1, consistent with the interstellar medium (Bohlin et al. 1978). Since the absolute values for opacity and dust-to-gas ratio for protoplanetary discs are poorly constrained (as discussed in Section 5.3.1.1), determining the opacity of the disc surrounding Elias 2-27 may be difficult. And

hence the exact parameter space needed to form spiral arms in the disc surrounding Elias 2–27 may be problematic.

Although there have been multiple studies attempting to recreate the spiral arms seen in the disc surrounding Elias 2-27, not all of them have been successful - including in this work. Furthermore, each successful study has explored different regions of the parameter space (e.g. different temperature profiles, surface density profiles, irradiative temperatures, disc masses etc.) in order to recreate the symmetric spiral arms (Meru et al. 2017; Forgan et al. 2018; Hall et al. 2018). Therefore, our inability to produce spiral arms in the disc of Elias 2-27 may be due to the incredibly narrow region of parameter space (Hall et al. 2018) that does lead to the formation of spiral arms. Alternative mechanisms for the formation of the arms, such as external perturbations, may need to be explored.

5.6.2 J16152023

The aim of our SPH simulations was to recreate the spiral substructure seen in the disc of J16152023. These substructures were observed in the dust continuum using ALMA observations and were first introduced in Chapter 4. The spiral arms previously detected are tenuous and only clearly visible after undergoing an unsharp masking process (see Section 4.3.1). Nonetheless, the simulations run here enable us to determine if spiral structures due to gravitational instability can form around solar–mass young stellar objects.

We run three simulations of the disc surrounding J16152023, increasing the disc mass in each case. Although each disc satisfies the global condition for instability, it is only the system with a disc–to–star mass ratio of $q = 0.5$ that becomes gravitationally unstable and forms spiral arms. The disc of J16152023 has not been studied as extensively as that of Elias 2–27; there is also a lack of previous literature on the disc being modelled. Therefore, we compare the simulations run here to the

previous ALMA observations.

The first simulation, J01, was run with a disc mass of M_{disc}=0.25 $M_{\odot}$. However, no spiral arms formed during the evolution of the disc. The simulations were stopped at 10 kyr once the disc became stable and uniform. Tenuous spirals arms could be seen in the second simulation, J02, when the disc mass was increased to M_{disc}=0.375 $M_{\odot}$. However, these dissipated by 8 kyr, and the disc evolved to become stable and uniform. This agrees with the work of Hall et al. (2019), who were able to show that spiral arms may only last for a few thousand years.

Previous studies have shown that symmetric spiral arms could form in a protoplanetary disc if the accretion rate of the system is of the order 10^{-6} to $10^{-7}M_{\odot}yr^{-1}$ (Hall et al. 2016) and the disc–to–star mass ratio is at least $\approx$ 0.25 (Dong et al. 2015a). Manara et al. (2014) measure the accretion rate of J16152023 as $3\times10^{-9}M_{\odot}yr^{-1}$, two orders of magnitude below the required level. The accretion rate of gravitationally unstable discs have, however, been shown to be highly episodic (Vorobyov & Basu 2015). Therefore, the formation of spiral arms in the disc of J16152023 may be possible. Spiral arms were able to form in the disc once the disc mass reached M_{disc}=0.5 $M_{\odot}$. Although this is a high disc mass, it agrees with previous disc mass estimates of 0.13 to 0.47 $M_{\odot}$ (Andrews et al. 2011; van der Marel et al. 2015).

Spiral arms could be seen in the outer regions of the disc as well as within the central regions. We detect a prominent spiral arm at ∼40AU from the centre of the disc. These cannot be seen in the central regions of the ALMA observation of J16152023 (see Figure 5.11). The outer spiral arms were detected at a distance of 95 AU from the centre of the disc. This aligns with the spiral arms detected in the ALMA observation ∼100 AU from the centre of the disc. Therefore, we have been able to produce a spiral arm situated at a comparable distance from the star as that seen in the original ALMA observation of J16152023.

5.6.3 HD 36112

The aim of the SPH simulations of HD 36112 was to determine if substructures can be formed in the protoplanetary disc via gravitational instability. Three simulations were run, increasing the disc mass for each subsequent run, and stopped once the disc became stable, or fragmented to form secondary objects. Spiral arms were able to form in all simulations run: HD01, HD02, and HD03. However, the nature and location of these arms varied between each run.

The first simulation of HD 36112, named HD01, consisted of a protoplanetary disc with disc mass M_{disc}=0.55 $M_{\odot}$. Although prominent, broad spiral arms are not visible in the disc at any point in its evolution, we do find narrow, high intensity arms forming towards the mid-centre and inner regions of the protoplanetary disc. The narrow spiral arms appear to be somewhat symmetrical about the centre of the disc. We also find that they exist within two regions; between ∼70–80 AU and between 25–50 AU. We detect spiral arms within regions that agree with the position of the dust clumps observed by Boehler et al. (2018) at 47 AU and 82 AU. Spiral arms can also be seen within the region where an arm could be seen in the ALMA observation (Dong et al. 2018a). The intensity of the modelled arms, however, are particularly low compared with the overall disc emission. This can be seen in Figures 5.25 and 5.26. Therefore, it is unclear whether these arms would be resolvable after undergoing simulated ALMA observations. This will be further explored in Chapter 6.

Broad-scale spiral arms could be seen in the second simulation of HD 36112, HD02. The protoplanetary disc was modelled using a disc mass of M_{disc}=0.65$M_{\odot}$. Spirals within the inner regions of the disc formed early on in the evolution at 300 yr; broader spiral arms were only visible at 1000 yr. Similar to run HD01, we see spiral arms forming predominantly within two regions of the protoplanetary disc; between 30-50 AU and between 60–80 AU. These can be seen in Figures 5.29 and 5.30. The

majority of the spiral arms appear to be symmetrical about the centre of the disc. This is expected for spiral arms forming via gravitational instability (Forgan et al. 2018). Regions of the spiral arms are detected within the same location of the dust clumps, and spiral arm, observed by Boehler et al. (2018) and Dong et al. (2018a). Cavities can also be seen in the simulations at 1400 yr and 1800 yr at ∼80 AU and 50 AU. Although the cavity at 80 AU was detected in the ALMA observations, a cavity at ∼40–50 AU has previously been detected by Isella et al. (2010).

We increase the disc mass of HD 36112 for the final simulation, HD03, to M_{disc}=0.75 $M_{\odot}$. The disc evolves much more quickly with this increase in mass, therefore we only show snapshots of the first ∼1000 yrs as the disc fragmented and formed secondary objects after this point (see Section 5.2). In contrast to the previous run, HD02, we do not see broad spiral arms forming in the outer regions of the protoplanetary disc. Sharp, high intensity peaks are seen in the inner regions, as well as extending to the outer regions of the disc. The sharp, high intensity spiral arms are seen to exist between ∼20–50 AU. This was shown in the spatial profiles of HD03 in Figures 5.33 and 5.34. As the narrow spiral arms extend to the outer regions of the disc, they are seen to lie at an outer radius of ∼60–75 AU. The radial extent of the inner spiral arms agree with the location of the dust inner region clumps observed by Boehler et al. (2018), however, the outer region dust clump was observed at 82 AU.

Smooth particle hydrodynamic and radiative transfer simulations of the disc surrounding HD 36112 were conducted by Dong et al. (2015a). They find that a disc–to–star mass ratio of at least q=0.25 is needed to produce the spiral arms seen at near-infrared wavelengths. As well as this, a requirement that the spirals exist on relatively compact scales of R<100 AU is also discussed. The results of the simulations run here, HD01, HD02, and HD03 agree with these findings as disc–to–star mass ratios of q =0.29, 0.34, and 0.39 were used, respectively. As well as this,

the spiral arms detected all had locations of less than R =100 AU.

The majority of the spiral arms formed in the simulations run here were symmetrical. Hall et al. (2016) showed that symmetric spiral arms could form in a protoplanetary disc if the accretion rate of the system is of the order 10^{-6} to $10^{-7}\mathrm{M}_{\odot}\mathrm{yr}^{-1}$. The accretion rate of HD 36112 has previously been measured at $\sim 10^{-8}\mathrm{M}_{\odot}\mathrm{yr}^{-1}$ (Eisner et al. 2009; Boehler et al. 2018). Although this is an order of magnitude smaller than the limits imposed by Hall et al. (2016), the stellar mass accretion rate of gravitationally unstable disc can be highly episodic (Vorobyov & Basu 2015). Therefore, it may be possible for spiral arms to form in the protoplanetary disc surround HD 36112.

Although the spiral arms produced in this chapter are of a relatively high intensity, they are particularly narrow. Therefore, it is unclear if they would be resolvable using ALMA observations. This scenario is further explored in Chapter 6 where we run synthetic ALMA observations of the protoplanetary disc simulations of HD 36112.

Chapter 6

Comparison Between Theory and Data

6.1 Introduction

Theoretical models of protoplanetary discs are often compared to actual data in order to interpret observations. However, this may prove problematic as the emission detected in observations may not be truly representative of the actual emission from the source. Interferometric observations suffer from many limitations which affect the fidelity of the final image.

6.1.1 Limitations of Interferometric Observations

As previously discussed in Chapter 2, each antenna pair in an interferometer does not measure the sky brightness distribution, but rather, the Fourier Transform of this (van Cittert 1934; Zernike 1938). Each antenna pair will measure a point on the (u, v) plane, the coordinate space used in radio interferometry (see Figure 2.1). Observations aim to fill this (u, v) plane in order to fully sample the intensity distribution of observational target. However this cannot be achieved as the instrument is

comprised of individual antennas, thus forming fixed baseline pairs. Therefore, the (u, v) plane will be sampled at discrete points rather than filled completely. This can introduce artefacts in the final images which may be mistaken for real emission.

In order to overcome a sparsely filled (u, v) plane, interferometers use a technique called *Aperture Synthesis*. An object should ideally be observed for a number of hours. As the Earth rotates, the orientation of the interferometric array with respect to the target changes, hence increasing the coverage of the (u, v) plane (Ryle & Hewish 1960). Each antenna in the ALMA array can also be moved (See Section 2.2.1.1). Changing the configuration of the interferometer allows previously unsampled areas of the (u, v) plane to be filled. Although aperture synthesis allows for the maximum sampling of the (u, v) plane, a truly complete sampling can never be achieved.

Processing interferometric data is also filled with many complications, as discussed in Section 2.2.3. The fidelity of the image can be affected by the phase stability of the atmosphere, pointing errors, and changes in atmospheric opacity. Although self-calibration can improve the images, artefacts may remain in the image and be mistaken for real emission.

Therefore, in order to determine if theoretical protoplanetary disc models are scientifically robust, synthetic observations need to be conducted. This will determine the observability of the simulated emission and allow appropriate modifications to the models to be made.

6.1.2 Simalma

Smooth particle hydrodynamic simulations of three protoplanetary discs were run in Chapter 5 to determine if any substructure could be formed in the disc due to gravitational instability. Spiral arms, as well as a central concentration of material, were only able to form in the models of the disc surrounding HD 36112. In order

to assess if the previously run models match the actual ALMA observations of the disc, we produce synthetic observations using *simalma*.

The `CASA` task *simalma* allows users to produce synthetic ALMA observations. These can then be imaged and analysed. Simulations can be run utilising all three observational components of ALMA: the 12–m array, 7–m compact array, and total power arrays. Synthetic observations allow observers to determine if their object of interest will be resolvable with ALMA. It also allows theorists to ascertain if their astrophysical models agree with observations.

Two `CASA` processes are internally called when utilising the *simalma* task: *simobserve* and *simanalyze*. Synthetic observations can be made by running these two processes individually, or by utilising the *simalma* package.

The first step in generating a synthetic ALMA observation is to obtain a model image or component list. This is a representation of the sky brightness distribution that needs to be synthetically observed. The user may start with an existing FITS image representing an observation of a target. The spatial axes and flux may then be scaled to simulate what would be observed for a similar target at a different distance. Alternatively, a user may supply a component list using the `CASA` component list tool (*cl*). This allows the user to specify a set of point sources, Gaussians, or discs.

The task *simobserve* is used to generate model visibilities of the synthetic observations. This creates the (u,v) data that the interferometer would measure had it observed the specified input sky brightness distribution. The header of the model brightness distribution can be modified to best represent the desired synthetic observation. Input parameters allow the observer to scale the flux densities, specify the central coordinates of the target, set the angular scale of each pixel and define the frequency of the synthetic observations as well as the channel width.

Model visibilities are then generated based upon the inputted telescope and antenna configuration, as well as the length of time of the observation. In order to

create realistic synthetic observations, noise can be added to the visibilities. *Simobserve* utilises atmospheric models to simulate real observing conditions. The routines of Pardo (2019) model the transmission of cm/mm/sub–mm wavelength radiation through the Earth's atmosphere. Lastly, the precipitable water vapour level can be input in order to recreate the observing conditions at the time of the observation.

The *simanalyze* task is then used to image the model visibilities. These are then Fourier-Transformed and 'cleaned' using the input parameters. The weighting on visibility sampling points, uv-tapering, and primary beam corrections are required, whilst the user manually cleans the data. This produces a fully-cleaned simulated ALMA observation which can be used for further analysis.

6.2 Synthetic Observations of HD 36112

Three smooth particle hydrodynamic simulations of the disc surround the 1.9 $M_{\odot}$ YSO HD 36112 were run in Chapter 5. In each subsequent model, the disc mass was increased, with the aim of forming substructure in the disc via gravitational instabilities. Narrow, high intensity spiral arms could be seen in all three simulations, whilst broad-scale spiral arms in the outer regions of the disc could be seen in simulations HD02 and HD03. Here we run synthetic ALMA observations of the HD 36112 models in order to determine if the spiral substructure seen are resolvable with ALMA.

6.2.1 Observational Parameters

To make a coherent comparison between the simulated observations and actual observations, we use the observing parameters of the ALMA observations when running *simalma*. The simulated observations are run at the same frequency of the original observations as well as the same channel width. In order to get the same

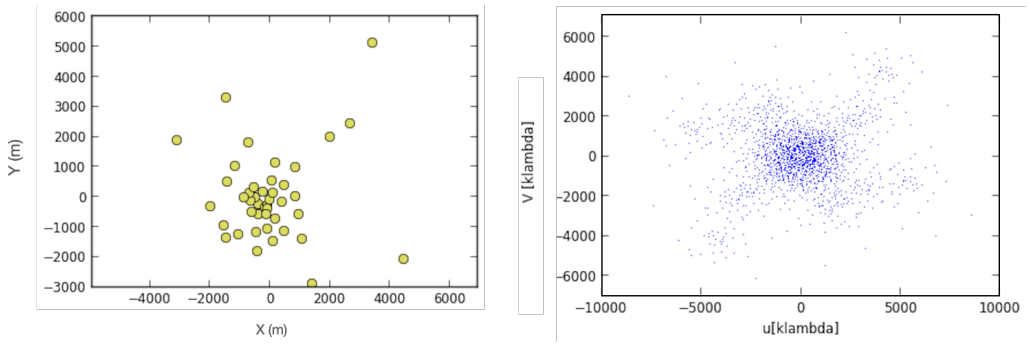

Figure 6.1: Left: Antenna configuration, C43-8, of the synthetic observation of HD 36112. Right: (u, v) coverage of the synthetic observation. The (u, v) space is measured in unit wavelengths.

level of emission and to resolve to the same scales, we use the ALMA configuration used in the original observation and keep the same integration and observing time. The antenna configuration and (u, v) coverage of the observations are shown in Figure 6.1.

In order to ensure that the simulated observing conditions are comparable with the real–time observing conditions, we ensure that the precipitable water vapour is at the same level as when the object was observed. The `CASA` package *clean* is used to clean the simulated observations and this is performed manually. We use the same weighting and robust parameters when cleaning the data as was used in the original observations.

We outline the observing conditions and simulated observation parameters in Table 6.1. We include the ALMA project code of the original observation and reference to the observation publication.

6.2.2 HD01

The protoplanetary disc modelled in simulation run HD01 had a disc mass of M_{disc}=0.55 $M_{\odot}$. Narrow, high intensity spiral arms could be seen in the inner

Table 6.1: Observational parameters used in the synthetic observations of HD 36112. These are the same parameters used in the original ALMA observations (project code given below).

Observational Property	Value
Configuration	C43-8
Frequency (GHz)	340
Channel Width (GHz)	1.78
Integration Time (s)	7510
Total Observing Time (min)	125
PWV (mm)	0.675
Robust Parameter	0.5
Weighting	Briggs
Right Ascension	$05^h30^m27.5^s$
Declination	$+25°19'56.6''$
Project Code	2017.1.00492.S
Publication	Boehler et al. (2018)

regions of the disc as well as in the outer regions in later evolutionary snapshots. The simulated observation of HD01 is shown in Figure 6.2. All synthetic observations have a field–of–view of 300×300 AU to allow for comparison between the spatial extent of the synthetic observations and the models. We do not perform the unsharp masking process (see Section 4.3.1 on our synthetic observations as the original observations were conducted without this filtering.

The disc of HD 36112 was modelled using a radius of R_{disc}=100 AU. At 500 yr we can see from Figure 6.2, that the outer, diffuse material in the disc model is not observable with ALMA. This may either be due to the flux level being too low to observe, or some of the smooth structure being resolved out. The disc, at this evolutionary time-step, has a radius of R_{disc} ∼35 AU. We calculate this radius in `CASA` using the same method outlined in Section 5.2.

At the last time-step in the disc evolution (at 22000 yr), the outer disc material can be seen; however the material appears diffuse and the disc has a radius of R_{disc} ∼60 AU, still smaller than the original model. The increase in the disc radius between 500 yr and 22000 yr may be due to the surface brightness increasing in the outer regions of the disc at later evolutionary steps. This may occur as some material is transported to the outer regions of the disc alongside the formation of the spiral arms.

A concentration of material can be seen to be forming in the disc at 4000 yr, as well as the opening of a cavity. The inner edge of this rim is located at R ∼7 AU. The apparent cavity increases in size as the disc evolves and by 22000 yr, the inner edge of the rim can be seen at R ∼12 AU.

A faint spiral arm can be seen in the top right of the protoplanetary disc at R ∼25 AU at 12000 yr, however it is tenuous. It increases in magnitude by 22000yr and can be seen in the bottom right at the same radius. The small radius of this spiral arm indicates that it is part of the inner region spiral arms seen in the HD01 SPH

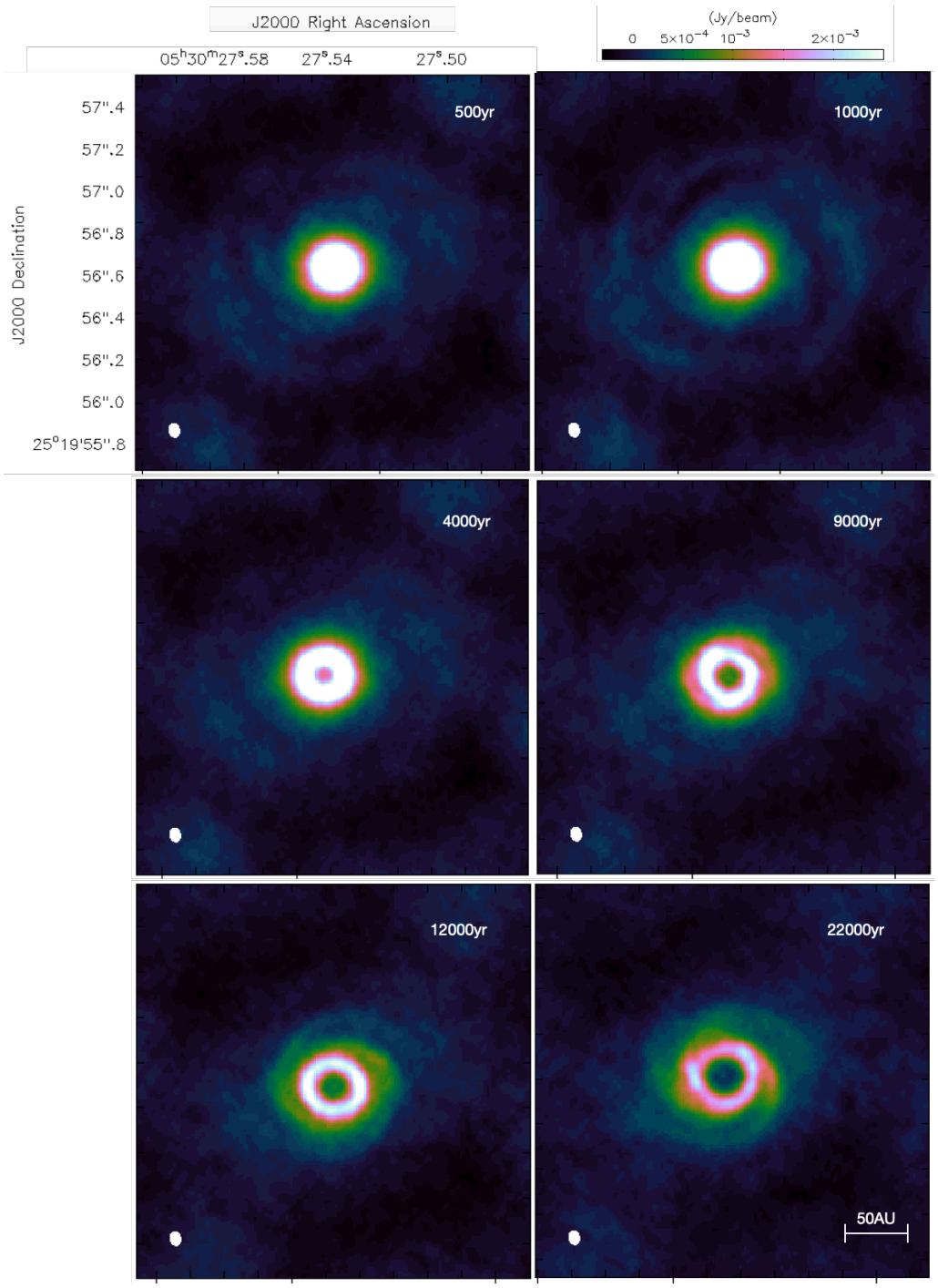

Figure 6.2: Synthetic observation of the protoplanetary disc surrounding HD 36112. Snapshots from the model HD01 were used to generate these observations using *simalma*. All observations have a field–of–view of 300×300 AU. The beam of the synthetic observation can be seen in the bottom right corner and has a size of 0.04×0.03 arcsec.

disc model interior to R =50 AU. The outer region narrow arms in the disc models between 25–50 AU and 70–80 AU are too tenuous to be resolved in the synthetic observations. Contrary to the spiral arms seen in the protoplanetary disc model HD01 (see Figure 5.2), the spiral arms seen here do not appear to be axisymmetric.

6.2.3 HD02

The protoplanetary disc modelled in simulation run HD02 had a disc mass of M_{disc}=0.65 $M_{\odot}$. Narrow, high intensity spiral arms could be seen in the inner regions of the disc and extended to the outer regions in later evolutionary snapshots. As well as this, broad-scale spiral arms could be seen in the outer regions of the disc from 1000 yr. These became more prominent as the disc evolved. The simulated observation of HD02 is shown in Figure 6.3.

Similar to the synthetic observations of HD01, the outer regions of the disc model are not resolvable using the observational parameters used in *simalma*. The disc radius is measured as R_{disc} ∼35 AU at 100 yr, this however, increases to R_{disc} ∼80 AU by 1800 yr; a much larger increase in radius compared to run HD01. The increase of disc radii between the first and last evolutionary timestep may be due to material moving to the outer regions of the disc as spiral arms form. This would increase the surface brightness in the outer regions of the disc, thus making it detectable in the synthetic ALMA observations. The increase in disc mass between runs HD01 and HD02 causes the disc to evolve much more rapidly. Thus, material is transported to the outer regions of the disc much more rapidly, increasing the surface brightness and the observability of fainter structure.

A ring of concentrated material can be seen to be forming at 1000 yr. The inner gap of which, however, is not clear as the model was stopped by 1800 yr. We do, however, state that the inner regions of the disc (within ∼5 AU) are to be considered not real. Therefore, the cavity seen here, forming after 1000 yr, are an artificial effect

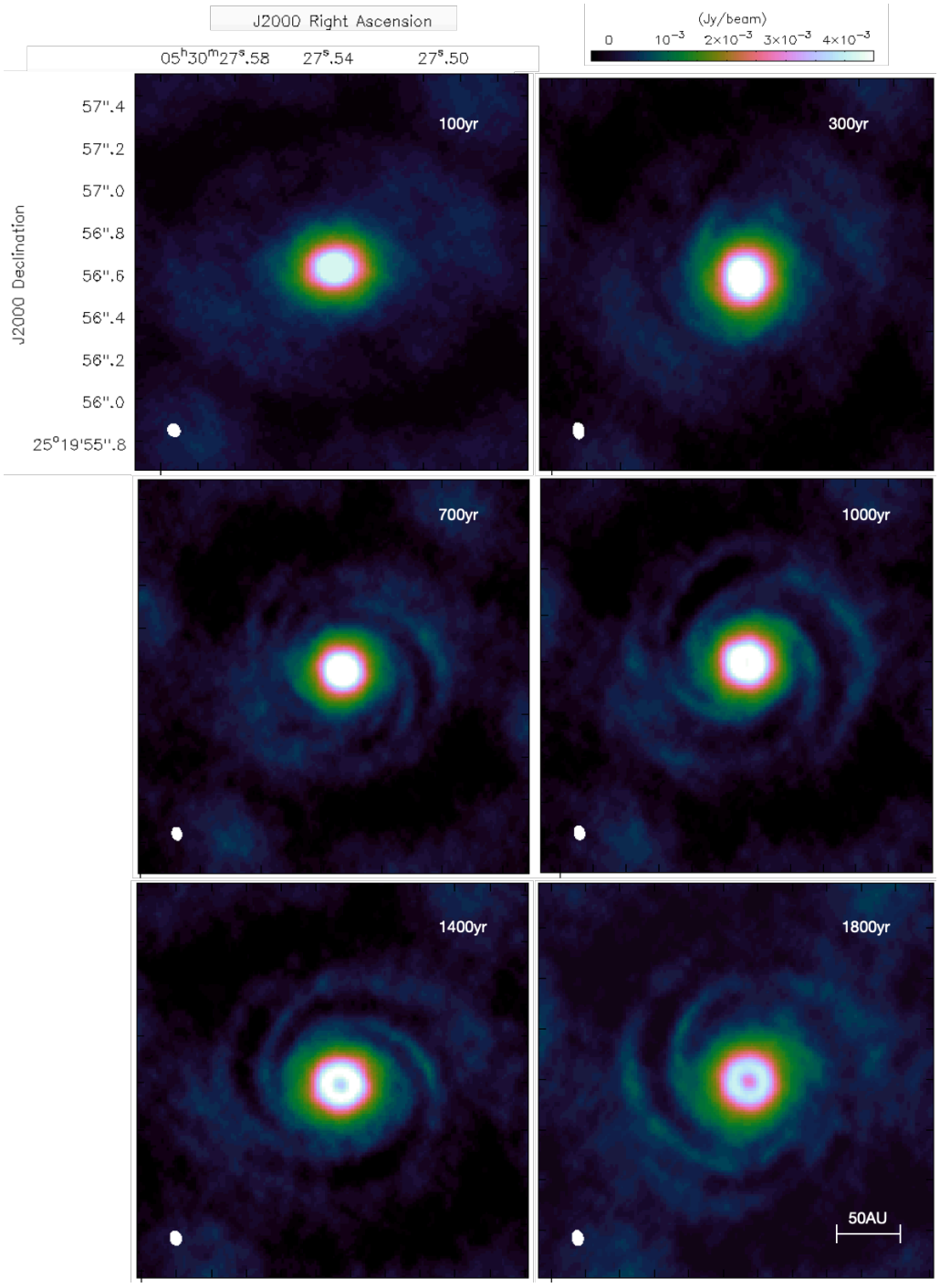

Figure 6.3: Synthetic observation of the protoplanetary disc surrounding HD 36112. Snapshots from the model HD02 were used to generate these observations using *simalma*. All observations have a field–of–view of 300×300 AU. The beam of the synthetic observation can be seen in the bottom right corner and has a size of 0.04×0.03 arcsec.

of the disc models.

Spiral arms can be seen to form in the disc at 700 yr, and become more prominent in the outer regions of the disc at 1000 yr. A spiral arm can be seen at $R \sim$70 AU on the right side of the protoplanetary disc. A spiral arm can also be seen to begin on the left of the centre of the disc at $R \sim$55 AU. As this arm progresses, however, to the outer regions of the disc, its intensity decreases and the arm is difficult to disentangle from the ambient disc material. We do not see any prominent spiral arms with an inner edge at a radius $R \lessapprox$50 AU, which were seen in the protoplanetary disc model of HD02.

The spiral arms at 1000 yr can also be seen at 1400 yr and 1800 yr. Approximately symmetric spiral arms can be seen at 1400 yr at $R \sim$50 AU. A tenuous arm in the outer region of the disc can also be seen at $R \sim$65 AU. The symmetrical nature of the arms cannot be seen at 1800 yr, however we find spiral arms at the same radial distance. The location of the spiral arms seen in the simulated observations agree with the spiral arms detected in the models of HD02 at a radius of 50 AU$< R <$80 AU.

6.2.4 HD03

The protoplanetary disc modelled in simulation run HD03 had a disc mass of M_{disc}=0.75 $M_{\odot}$. Narrow, high intensity spiral arms could be seen in the inner regions of the disc. These extended to the outer regions in later evolutionary snapshots where they evolve to form tenuous broad–scale spiral arms. However, these spiral arms are not as prominent as the broad-scale spiral arms seen in model HD02. The simulated ALMA observations of HD03 are shown in Figure 6.4.

The diffuse material in the outer regions of the protoplanetary disc models have again not been observable in the simulated ALMA observations. At 60 yr, only material interior to $\sim$35 AU is observable and is visible in Figure 6.4. This could be

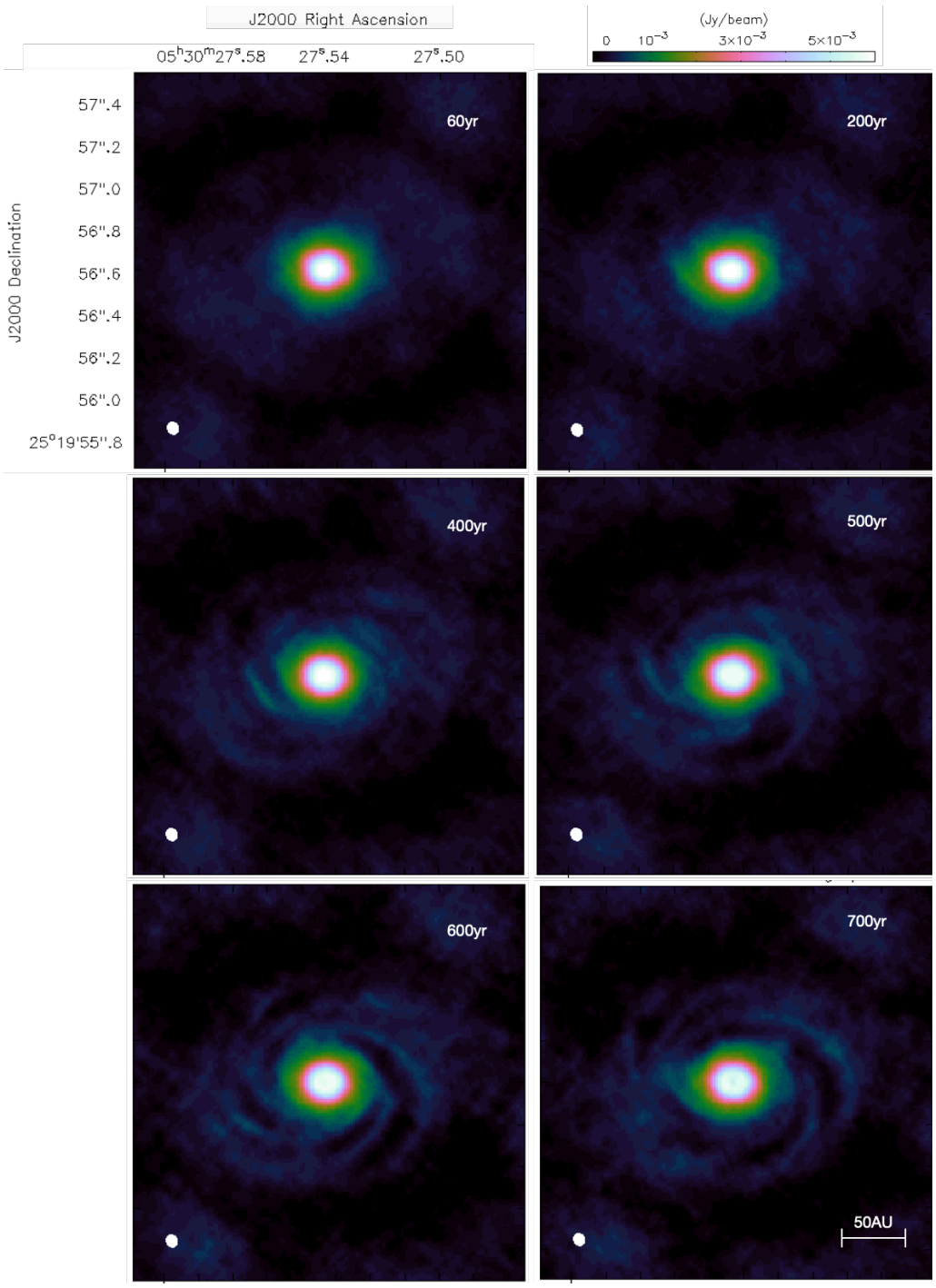

Figure 6.4: Synthetic observation of the protoplanetary disc surrounding HD 36112. Snapshots from the model HD03 were used to generate these observations using *simalma*. All observations have a field–of–view of 300×300 AU. The beam of the synthetic observation can be seen in the bottom right corner and has a size of 0.04×0.03 arcsec.

due to the low surface density of the disc. The radius of the disc, however, increases by 700 yr to ∼85 AU. This is due to the formation of spiral arms, which transfers some material to the outer regions of the disc, hence increasing the disc surface density. As well as this, the increase in disc mass between runs HD02 and HD03 has led to a larger outer disc radius being observable at a much earlier disc evolutionary stage

The narrow, high intensity spiral arms seen in the disc model HD03 at 500 yr are resolvable with ALMA. They are, however, tenuous and the outer edge of the arms are difficult to distinguish from the diffuse disc material. The inner edge of the spiral arms extend from the centre of the disc up to a radius of R ∼70 AU at 500 yr. As the disc evolves, the intensity of the arms increase in magnitude and become more prominent in the simulated observations. At 700 yr, a spiral arm can be seen to extend from the centre of the disc at R ∼50 AU and progresses to a radius of R ∼70 AU. The location of the inner edge of these spiral arms coincide with the spiral arms seen in the disc models at R ∼40–50 AU and R ∼60–75 AU.

The inner regions of the spiral arms seen at R ∼20–50 AU in the disc models are not, however, resolvable with ALMA. Instead, the material appears to be smoothed out in the central regions of the protoplanetary disc. This is even more apparent in the simulated snapshots at 500 yr in Figure 6.4. This could be attributed to the resolution of the synthetic observations not being high enough in order to separate the thin, narrow arms from the rest of the disc material.

6.3 Discussion

Synthetic ALMA observations of HD 36112 were run in order to determine if the substructures seen in the protoplanetary disc models are resolvable with ALMA. Here we compare the synthetic observations to the actual ALMA observations to

assess if the mechanism of gravitational instability can produce any of the substructure seen in the protoplanetary disc of HD 36112; particularly the large cavity (Isella et al. 2010; Andrews et al. 2011; Dong et al. 2018a) and the partial spiral arm (Dong et al. 2018b). Synthetic observations of three models were run, HD01, HD02, and HD03; the snapshots of these models can be seen in Chapter 5.

The synthetic observations of the protoplanetary disc surrounding HD 36112 do not completely match with actual ALMA observations in all three disc models. Two concentrations of dust grains could be seen in the disc at radii of 47 AU and 82 AU (see Figure 5.22) (Boehler et al. 2018), along with a cavity inwards of 40–50 AU (Isella et al. 2010; Andrews et al. 2011; Dong et al. 2018a). A decrease in material can be seen in the synthetic observations of two disc models (HD01 and HD02), as well as broad spiral arms (HD02 and HD03). The location of the substructure seen in the synthetic observations somewhat agree with the ALMA observations, however the intensity does not. Here we discuss each run in more detail and make comparisons to the actual ALMA data.

6.3.1 Outer Radius

The protoplanetary disc surrounding HD 36112 extends up to a radius of R_{disc} ∼100 AU (Dong et al. 2018a). The synthetic ALMA observations of all three disc models, HD01, HD02, and HD03, failed to match the radial extent of the disc.

The material in the outer regions of the disc model HD01 were observed up to a radius of R_{disc} ∼60 AU. Exterior to this radius, the disc material is too diffuse to be observed with ALMA. Increasing the disc mass allows more material to extend outward as the angular momentum in the disc redistributes. We see this in the model HD02, which has an increased disc mass compared to run HD01. This disc can be observed up to an outer radius of R_{disc} ∼80 AU. Similarly, increasing the disc mass further in run HD03 results in a observable disc radius of R_{disc} ∼85 AU.

Submillimetre observations of the disc surrounding HD 36112 find a disc mass of $0.01 M_{\odot}$ (Andrews et al. 2011). Similarly, we find a disc mass of M_{disc}=0.013$M_{\odot}$ based upon the ALMA observation used in Chapter 4. Here we have used increased disc masses of M_{disc}=[0.55, 0.65, 0.75]$M_{\odot}$ for runs HD01, HD02, and HD03, respectively (see Section 5.3.1.1 for reasoning). Increasing the disc mass further, in order to observe the outer regions of the disc, seem unrealistic. The upper limit disc mass modelled here, of 0.75$M_{\odot}$, results in a disc–to–star mass ratio of 0.40 (with M_{*} =1.9 $M_{\odot}$).

Previous protostellar systems have been modelled with greater disc–to–star mass ratios (e.g. Elias 2–27 by Hall et al. (2018)). However, these systems are relatively young compared to HD 36112. A stellar age of 10.0±5.0 Myr was estimated in this work (see Section 4.4), which agrees with the age of 3.5±2.0 Myr calculated by Meeus et al. (2012). Therefore, it is unlikely that this disc is surrounded by a parent molecular cloud, which could provide additional disc material, thus making it sufficiently massive to develop gravitational instabilities.

In order to increase the material in the outer disc, thus making it observable, the surface density profile may be altered. Gravitational instabilities in the disc surrounding HD 36112 have not been extensively modelled. Dong et al. (2015a) were able to model the spiral arms seen in scattered light. They use the same surface density power law adopted here ($\Sigma \propto R^{-3/2}$), however, a decreased outer disc radius of R_{outer} = 60 AU. Altering the surface density profile may result in a distribution of material that is observable with ALMA.

Alternatively, the disc radii used in the models run here may be considered as a lower limit to the radial extent of the disc. Estimates of the outer radii were made using previous continuum observations of the protoplanetary discs. However, dust grains undergo radial migration. Therefore, it is feasible that the gas disc may be significantly larger than that of the dust disc (Pérez et al. 2012). Theoretical

models of protoplanetary discs may need to be run with disc radii larger than what is currently seen in continuum observations in order to accurately model the radial extent of the disc.

6.3.2 Cavity

One of the key features of the submillimetre disc surrounding HD 36112 is the cavity inwards of 40-50 AU (Isella et al. 2010; Andrews et al. 2011; Dong et al. 2018a). A decrease in material could be seen in synthetic observations of two protoplanetary discs models studied here: HD01 and HD02. However, the cavities produced here are not real as the decrease in surface density seen in the disc models which produce these effects are within ∼15 AU. A decrease interior to ∼15 AU due to computational reasons (see Section 5.2). We expect this to extend up to radii of ∼20 AU in the synthetic observations of HD 36112. Therefore, the drop of emission interior to this in the synthetic observations can be considered as an artificial effect of the modelling.

Nonetheless, we compare the cavities seen in each disc models with the cavities observed in the synthetic observations. This may give some insight into how real cavities, with physical origins, in disc models may need to be treated when undergoing synthetic observations in order to replicate actual data.

A reduction in the disc material was seen inwards of 8 AU at 22000 yr in the disc model HD01. However, some of the disc material is resolved out with ALMA as we see the inner edge of the cavity at R ∼12 AU in the synthetic observations. This is significantly smaller than the cavity of 40–50 AU seen in the actual submillimetre observations (Isella et al. 2010; Andrews et al. 2011; Dong et al. 2018a).

A similar result is seen in the synthetic observations of HD02. A reduction in the disc material is seen inwards of R ∼5 AU in SPH disc models. Whereas a cavity is seen in the synthetic observations at R ∼7 AU. The extent of the cavity increases between the disc model and synthetic observations. Therefore, we can assume that

some of the material is being resolved out as the disc is synthetically observed. The cavity, again, is significantly smaller than that seen in the actual submillimetre observations.

Various processes, first outlined in Section 1.4.1, may result in the opening of a disc cavity. These are continuous processes that may take place over a large proportion of the disc lifetime. Here we evolve the disc for 30 kyr; ending the simulation early if the disc gravitationally fragments, or reaches a stage at which it is clear that no substructures will develop. This is but a fraction of the maximum disc lifetime (Mamajek 2009). Therefore, in order to recreate here the extent of the cavity seen in HD 36112, the disc models may need to be evolved for a longer period of time. This would, however, put constraints on other disc parameters which may affect the stability of the disc over longer evolutions.

Observations of protoplanetary discs have shown that the inner cavities may not be completely void of material (Francis & van der Marel 2020). Rather, observations are unable to completely resolve all the material present. A shallower surface density profile may redistribute more material from the inner regions to the outer. The decrease in material in the inner regions may result in some of this material resolving out once synthetic observations are made; thus giving the appearance of a cavity. Observations of HD 36112 would need to be conducted in order to determine if the cavity is completely void of material or if there is some emission that remains unresolved.

6.3.3 HD01

The disc model HD01 was run using a disc mass of $M_{disc} = 0.55$ $M_{\odot}$. Broad spiral arms could be seen in the outer disc at ∼70–80 AU, as well as narrow arms at ∼40 AU. As the disc evolved, the outer arms dissipated, whilst the inner arms extended to ∼45–50 AU. The synthetic observations fail to resolve both the inner

and outer region spiral arms seen in the disc model. A short spiral arm can, however, be seen to extend from the inner regions of the synthetic observation at 22 kyr (see Figure 6.2). This arm is located at a radial extent of $R \sim 24$ AU. The narrow spiral arms located interior to ∼30 AU may be responsible for this detection. The narrow arms extending to ∼45–50 AU, as well as the broad arms, formed in the model, are too tenuous to be resolved in the synthetic observations.

This short spiral arm detected at $R \sim 24$ AU in the synthetic observations does not compare with the clump located at $R \sim 47$ AU in the actual ALMA observations. As well as this, the central ring of material appears to dominate the disc in the synthetic observations. Whereas, the dust clump in the actual observations dominate the disc emission. The outer spiral arm seen in the ALMA observations ($R \sim 87$ AU) have not been detected due to the outer disc not being resolved in the synthetic observations.

Although the cavity seen in the synthetic observations of HD01 is the largest of the three simulations, and thus closer to the actual observations, there are a lack of spiral arms seen in the disc. Altering the surface density profile of the model may increase the density of material in the outer disc. Thus forming more prominent spiral arms at outer radii. These may then be resolvable with the synthetic observations.

6.3.4 HD02

Increasing the disc mass of HD02 to $M_{disc} = 0.65$ $M_\odot$ resulted in more prominent spiral arms forming in the disc model. At the earlier stages of the disc evolution, narrow spiral arms were seen to extend from R ∼30–50 AU. After 1000 yr, widespread spiral arms were seen to extend from R ∼60–80 AU. The location of these arms match with the locations of the arms detected in the ALMA observations.

The synthetic observations of HD02 are able to resolve some of the emission seen

in the disc models. The outer spiral arms seen after 1000 yr can be seen in Figure 6.3 at $R \sim 70$ AU. The arms are tenuous and are significantly less intense than the material seen in the inner disc. Spiral arms can also be seen to extend to ∼55 AU. Although these arms coincide with the outer arms seen in the disc models, they are narrow and are difficult to distinguish from the background material. Whereas the spiral arms seen in the disc model are broad and widespread.

The inner regions of the protoplanetary disc ($R \lessapprox 40$ AU) in model HD02 have not been resolved in the synthetic ALMA observations. The disc model was able to produce spiral arms extending to $R \sim 45$ AU, which agree with the location of the clumps seen in the ALMA observations. However, the unresolved substructure in the synthetic observations mean these are not visible.

The outer edge of the spiral arm in the synthetic observations of HD02 at 1800 yr can be seen at $R \sim 75$ AU. This matches with the spiral arm seen at $R = 72$ AU in the ALMA observation (Dong et al. 2018b). These arms may extend further as the disc evolves, however the simulation was ended as the disc underwent gravitational fragmentation. These arms are thin and difficult to distinguish from the background material.

6.3.5 HD03

Increasing the disc mass to $M_{disc} = 0.65$ $M_\odot$ in HD03 allows the spiral arms in the disc model to be resolved more prominently. Spiral arms in the early stages of the disc evolution could be seen in the disc model inwards of $R \sim 50$ AU. These were narrow spiral arms, however, their radial extent agreed with the dust clump located at 47 AU in the ALMA observations (Boehler et al. 2018). As the disc evolved, these spiral arms extended to radii of ∼60–75 AU. The radial extent of these arms are somewhat smaller than the inner edge of the dust clump located at 82 AU by Boehler et al. (2018).

The inner regions of the protoplanetary disc model (inwards of $R \sim 40$ AU) have not been resolved in the synthetic ALMA observations. The emission appears to have been smoothed over. Spiral arms can be seen in the outer regions of the disc observations from 600 yr. These extend up to a radius of ∼75 AU by 700 yr. These arms appear to be narrow, and are comparable to the arms seen in the disc model in both location and intensity.

A spiral arm is seen to extend from the disc at 700 yr from $R \sim 50$ AU in the synthetic observations. Although this agrees with the location of the dust clump seen at 47 AU, the spiral arm is tenuous and only just distinguishable from the background material. This contrasts to the ALMA observation where the dust clump is a prominent feature of the disc.

Similar to the synthetic observations of HD02, we find a spiral arm extending to $R \sim$75 AU in the synthetic observations. This agrees with the spiral arm seen in the ALMA observations (Dong et al. 2018a).

The synthetic observations of the disc model HD03 appear to have very similar structure to those of HD02 regardless of a disc mass difference of $0.1\mathrm{M}_{\odot}$. However, the increase in disc mass caused the disc to evolve much more quickly. As a result, the simulation is stopped at 0.7 kyr, after which point gravitational fragmentation occurred. Although the increase in disc mass has resulted in more prominent spiral arms forming, HD03 lacks a cavity, previously seen in HD01 and HD02. As well as this, the rapid evolution of the disc means it would be incredibly unlikely to catch gravitational instabilities, and thus spiral arms, forming during disc observations.

6.4 Summary

We have run synthetic ALMA observations of the protoplanetary disc models produced, in Chapter 5, using the `CASA` package *simalma*. These model simulate the disc surrounding HD 36112, with the aim of developing gravitational instabilities in

the disc. Three disc models were run - HD01, HD02, and HD03, with disc masses of M_{disc}=[0.55, 0.65, 0.75]$M_{\odot}$, respectively. The synthetic observations were run with the same observational parameters as the original observations. This allowed us to determine if the substructures seen in the disc models are resolvable with ALMA and comparable to those seen in the original observations. The findings of this chapter are summarised as follows:

- The outer material in the disc models of HD 36112 can not be fully observed in the synthetic ALMA observations. The material is too diffuse in the disc models and, thus, the radial extent of all three synthetically observed discs is less than the radius seen in the actual ALMA observations.

  The radial extent of the synthetically observed disc does, however, increase as the mass of the disc increases. Therefore, the surface density profile of the disc may be altered in order to resolve the emission in the outer regions of the disc. Alternatively, the models could be rerun using larger outer disc radii.

- The cavity seen inwards of 40-50 AU in the actual ALMA observations have not been resolved in the synthetic observations. The cavity size decreases as we increase the disc mass of the models. However, this could be due to the increase in the evolutionary timescale, and thus stoppage, of the disc simulations.

  The extent of the cavity increases between the disc models and the synthetic observations as some material is resolved out. Therefore, observations of protoplanetary discs with cavities may be overestimating their true radial extent. Synthetic observations of protoplanetary disc models are needed in order to determine if the substructure modelled accurately depicts the observed substructure.

- A disc mass greater than M_{disc} =0.55$M_{\odot}$ is needed in order to produce spiral arms in the disc surrounding HD 36112. The radial extent of these spiral arms

only somewhat agree with location of the dust clumps seen in the ALMA observations. We have, however, been able to recreate the spiral arm seen at 72 AU in the ALMA observations. This has not been done in previous modelling of the disc around HD 36112. Therefore, overall, we have not been able to accurately recreate all components of the substructure seen in the ALMA observations of HD 36112 using gravitational instabilities.

Assuming a shallower surface density profile for the disc may result in denser outer regions. This could enhance the intensity of the spiral arms as well as increase the size of the cavity seen in the synthetic observations. This may produce substructure similar to that seen in the ALMA observations using gravitational instabilities.

Chapter 7

Discussion

In this chapter we discuss the main findings of our work, and its implications with regards to current knowledge in the field of planet formation. We begin by discussing the work conducted in Chapter 4 regarding the substructures observed by ALMA in protoplanetary discs thus far. We then discuss the simulations run in Chapter 5, and the type of substructures that were able to form. Lastly we discuss the synthetic observations conducted in Chapter 6, and what the results mean for the current ALMA disc population.

7.1 The Detectability of Substructures

We have studied the morphology of substructure seen in protoplanetary discs surrounding young stars. We have looked at 794 protoplanetary discs observed with ALMA, of which 56 showed resolvable substructure. These were organised into four categories based upon the observed dust morphology: Rim, Ring, Horseshoe, and Spiral.

A Rim of emission surrounding a large cavity was seen in the majority of our sample (32 discs). However, this could be an observational bias as these types of substructures have been explicitly targeted in some ALMA surveys (e.g. the

DSHARP survey (Andrews et al. 2018a)). Moreover, they are the easiest substructure to detect, even at lower resolutions. Nonetheless, we find them to be a common substructure in both young and old systems, as well as around intermediate and low-mass stars.

A histogram was previously plotted in Chapter 4 showing the spatial resolutions of the entire sample of protoplanetary discs studied here. This histogram is again shown in Figure 7.1. The dashed lines now indicate resolution limits of 0.10" and 0.04", with Table 7.1 outlining the number of discs showing substructure for each resolution limit.

We find that ∼42% of protoplanetary discs show resolvable substructure when observed with a resolution of <0.10". This agrees with the work conducted by Long et al. (2019), where just under half the discs studied showed substructure when observed with a resolution of ≈0.12". The amount of discs showing substructure when observed at 'ultra–high' resolutions of <0.04" increases to 60%. This somewhat agrees with the DSHARP project who find that all discs show substructure when observed at a resolution of ≈0.035" (Andrews et al. 2018a). Therefore, increasing the resolution of the observations dramatically increases the total number of discs within which substructure can be seen.

7.2 Resolution Effects

Out of 794 protoplanetary discs initially studied here, only 52 protostellar systems were observed with a resolution <0.10", the approximate resolution required to observe substructure in just under half of the discs. This corresponds to ∼7% of the total disc sample. Furthermore, only 27 protoplanetary discs have been observed by ALMA using an 'ultra–high' resolution limit of <0.04". Therefore, only ≈3% of the 794 discs studied here have been observed at the resolution limit where we have shown that 60% of protoplanetary discs show substructure.

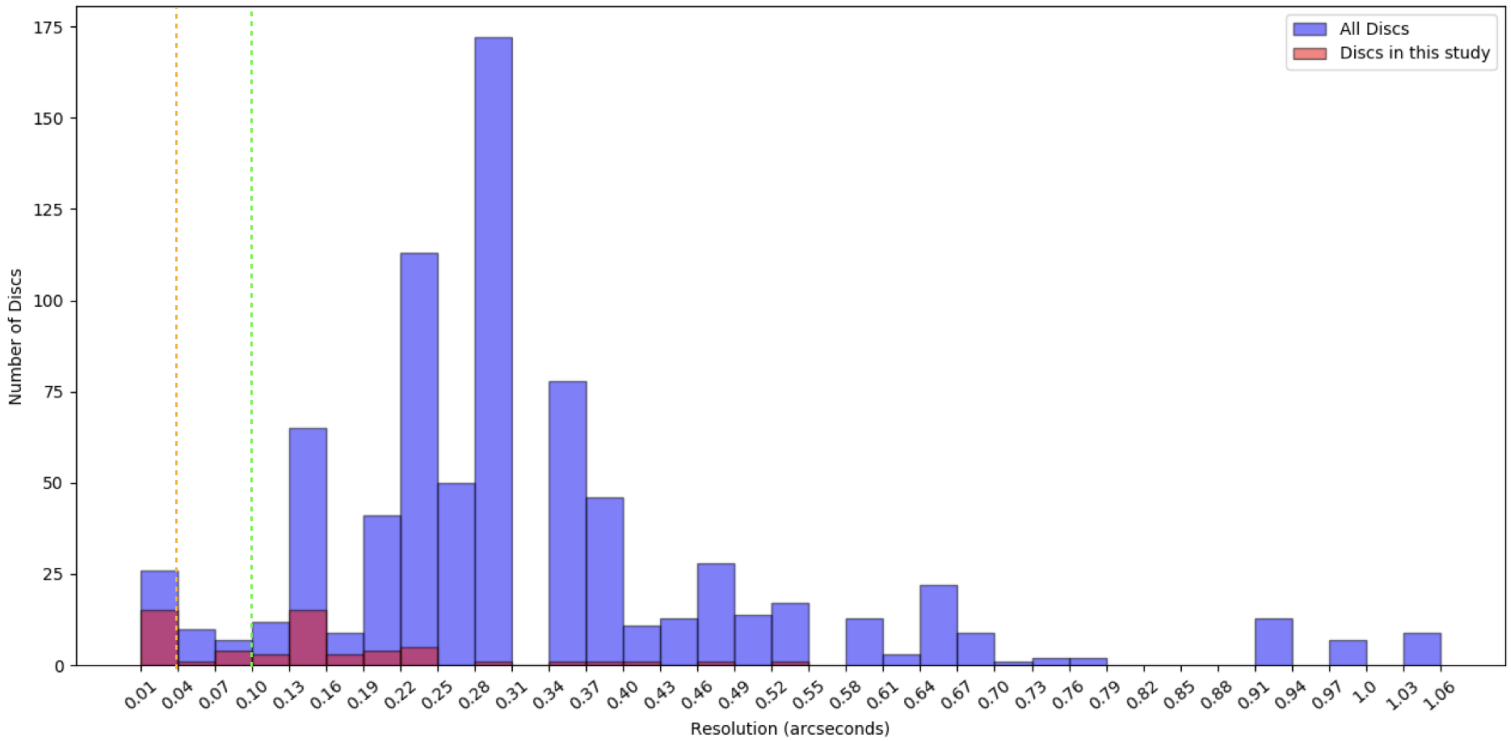

Figure 7.1: The resolutions of the entire sample of 794 protoplanetary discs, observed during Cycles 0–5, in the ALMA Archive. Details of the discs can be found in Table A.1 in Appendix A. We have highlighted, in pink, the discs identified as containing substructure and studied in this work. The discs have been binned with resolutions of 0.03 arcseconds. The green line indicates a resolution limit of 0.1", below which is considered 'high resolution' with ALMA. The orange line indicates a resolution limit of 0.04", below which is considered 'ultra–high' resolution with ALMA.

Table 7.1: The number of discs studied in this work using different resolution limits. The percentages in brackets refer to the fraction of discs with substructure within each resolution bin.

Complete ALMA Sample	
Number of discs	794
With observable substructure	56 (7%)
Discs observed with a resolution <0.10”	
Number of discs	52
With observable substructure	22 (42%)
Discs observed with a resolution <0.04”	
Number of discs	27
With observable substructure	16 (60)%

Resolvable substructure was only seen in 56 protoplanetary discs. This corresponds to 7% of the discs currently in the ALMA Archive. If all 794 protoplanetary discs were to be re-observed using resolutions of 0.04” or greater, we would expect that the fraction of discs showing substructure would increase to ≈60%; a much greater proportion of discs than we see currently. Unless these ‘ultra–high’ resolutions have been used to observe the protoplanetary discs, the true structure of the discs cannot be confirmed.

Re-observing protoplanetary discs, with known substructure, using higher resolution observations in order to determine the true nature of the emission has recently been conducted by Francis & van der Marel (2020). The authors were able to show that the cavities of transition discs are often not void of dust. Therefore, there may be unresolved dust rings (or additional structure) in some of the discs classified as being Rim discs in both this work and in the literature. Furthermore, the most populous substructure seen in discs may be protoplanetary rings, and not Rim discs as

found in this work; but this remains in question until higher resolution observations of discs can be made.

Unresolved substructure in previously observed discs has also been found by Facchini et al. (2020). The Class II T–Tauri object, LkCa15, was recently re-observed with ALMA. In previous works, and here, it has been classified as a rim surrounding a cavity. These observations were made using a moderate ALMA resolution of 0.17". However, observations with an increased resolution of ∼0.04" allowed multiple dust rings to be resolved in a location previously thought to be a void of material.

The need for 'ultra–high' resolution observations, and not simply high resolutions of ∼0.1", has also been demonstrated by Jennings et al. (2021). The authors reanalyse the discs imaged as part of the DSHARP survey. The aim of the work is to resolve higher resolution substructure that may not have been resolvable using the `CASA` *CLEAN* package. The 20 DSHARP objects are reanalysed using the resolution enhancing code Frankenstein (`Frank`). This code fits the visibilities of the original observations to a baseline 4.1 times longer than allowed by the *CLEAN* package. The enhanced discs show additional substructures inwards of 30 AU in multiple discs. As well as this, previously imaged gaps are shown to be deeper, wider, and more structured; with dust rings appearing narrower and brighter.

Furthermore, we have excluded young, embedded, as well as debris discs, from our sample. The DSHARP project look at 20 discs at 'ultra–high' resolutions, 12 of which we have studied here. Their sample includes young and old systems, within which substructure can be seen in all cases. Therefore, using a less biased sample may increase the fraction of discs showing substructure here to greater than 60%; thus confirming the ubiquitous nature of substructure within protoplanetary discs.

These recent studies highlight the need to re-observe protoplanetary discs under 'ultra–high' resolution conditions in order to confirm the substructure therein. Furthermore, as we have shown that the majority of ALMA observations have been

made at relatively low resolutions, it can be assumed that our knowledge of the substructures that exist the current disc population is heavily incomplete.

7.3 Modelling Substructures in Protoplanetary Discs

We have run smooth particle hydrodynamic simulations of the protoplanetary discs surrounding three young stellar objects: Elias 2–27, J16152023, and HD36112. Although the aim was to produce substructure in the disc via gravitational instabilities, substructure was only able to form in our simulations of the disc surrounding the intermediate–mass star, HD 36112.

The initial conditions for the simulations run here were the same for all three protostars, with four exceptions. Stellar temperature values for each protostar were taken from literature, with the stellar masses, disc masses, and outer radii being measured in Chapter 4. Although the disc–to–star mass ratios were comparable for each protostar, substructure could only form in the disc surrounding HD 36112. Broad-scale spiral arms could be seen to extend to the outer disc for the simulations of J16152023; these formed when the disc mass had a value of $M_{disc} = 0.5 M_{\odot}$. However, the spiral arms were relatively short-lived and the disc became more stable as it evolved. No previous models have been run for J16152023, therefore we cannot compare the results we have found here to published models.

The initial parameters for Elias 2–27 utilised here differ from the literature parameters which were able to form spiral arms in the disc. A power law index of 0.6 for the temperature profile was used in this work, whereas indices of 0.45 and 0.75 have been used previously (Meru et al. 2017; Forgan et al. 2011). Previous values for the power law index of the surface density profile range from 0.75 to 1 (Forgan et al. 2011; Meru et al. 2017; Hall et al. 2018), whereas a steeper power

index of 1.5 was used here. We use an irradiation temperature of $T_\infty = 10$ K based upon the ambient temperature of regions containing protoplanetary discs (Hayashi & Nakano 1965; Hayashi 1966; Tohline 1982; Larson 1985; Masunaga & Inutsuka 2000; Stamatellos et al. 2005a,b; Battersby et al. 2014). Previous works however have used a lower irradiation temperature of $T_\infty = 5$ K. The parameters used here to initialise the simulations have not resulted in the formation of spiral arms in the disc.

7.4 Substructure Formation using Gravitational Instabilities

The ability of a disc to become gravitationally unstable depends upon the Toomre parameter; this was first outlined in Section 1.3.4.2. One factor that affects the stability of the disc is the thermal support. This is dictated by the temperature of the disc, where we have used a power law of $T \propto R^{-u}$ (where $u = 0.6$) in this work. However, this profile may have resulted in the discs being too warm, and therefore, unable to gravitationally fragment. Additional simulations could be explored using alternative power law indices which may result in instabilities forming in the disc.

The stability of a disc is also dependant upon the surface density, Σ. The simulations for the stars modelled here have disc–to–star mass ratios within the range 0.3–0.6. The outer radii of the discs, however, vary between the simulations. These are set to 300 AU, 150 AU, and 100 AU, for the discs surrounding Elias 2–27, J16152023, and HD 36112, respectively. Therefore, the surface density of the discs increase for the simulations as we increase the mass of the star. This could explain why the disc surrounding Elias 2–27 did not develop instabilities, J16152023 developed slight instabilities, whilst spiral arms were seen to form in HD 36112.

We find that in order to form substructure in the discs of Elias 2–27, J161252023,

and HD 36112 using a gravitationally unstable disc, the required disc masses for given radii are significantly higher than what we see in the ALMA observations. This was up to an order of magnitude larger in the case of HD 36112. Although disc mass estimates based upon observations are thought to be underestimates (Andrews et al. 2013), it is unlikely that we are still underestimating disc masses in the models run here as we are using unusually large disc–to–star mass ratios of up to 0.5.

Similarly, the estimates for the outer radii were made using previous continuum observations of each protoplanetary disc. As dust grains are thought to undergo radial migration, it is likely that the gas disc surrounding each protostar is significantly larger than estimated here (Pérez et al. 2012). Adopting these upper limits for the outer disc radii would result in smaller surface densities, thus making it more difficult for instabilities to form in the disc. Therefore, spiral arms in discs with large outer radii may need to form with an alternative mechanism to that of gravitational instabilities.

The unusually high disc masses used in the models here, coupled with what may be underestimates for the disc radii, imply that we may not be sampling the full parameter space in order to form substructure via gravitational instabilities. Alternatively, there may be another mechanism responsible for forming the substructure seen in the discs modelled here.

7.5 Modelling the Disc of HD 36112

Various substructures have previously been seen in the disc of HD 36112 at submillimetre wavelengths (Boehler et al. 2018). The inner edge of two dust clumps are located at 47 and 82 AU (Boehler et al. 2018), with a faint spiral arm being detected at 72 AU. In all the simulations run here, spiral arms were able to form in the disc. Multiple arms could be seen throughout the disc evolution, both in the inner regions and the outer regions of the discs. The narrow arms in the inner regions were of high

intensity. These reduced in magnitude, as well as broadening, as they expanded to the outer regions of the disc. As the disc mass increased between simulations, more material was able to expand to the outer regions of the disc, enabling the formation of broad spiral arms. The increase in mass, however, caused the disc to evolve at a much quicker timescale. This resulted in the third disc model, HD03, being stopped rather early as it began to gravitationally fragment.

A central cavity has previously been imaged in the disc of HD 36112 inwards of 40–50 AU (Isella et al. 2010; Andrews et al. 2011; Dong et al. 2018a). A central concentration of material is seen to form in run HD01 at 4000 yr; with a reduction of material inwards of this. As the system evolves, material accretes onto the central object as well as expand to outer regions of the disc. This results in the radius of the central concentration to increase to $\sim$12 AU. This reduction of material is significantly smaller than the cavity seen in the submillimetre observations. This could be due to the rapid evolution, and subsequent fragmentation, of the disc.

The spiral arms that form in the disc of HD 36112 (and briefly in run J03 for J16152023) evolve rapidly. The disc surrounding J16152023 developed spiral arms within 3000 yr. Although their presence could be seen at 17500 yr, they were tenuous and difficult to discern from the rest of the disc material. Similarly, the broad spiral arms in the disc surrounding HD 36112 were able to form within 2000 yr. After this point, fragmentation occurred, rapidly breaking apart the spiral arms. Therefore, the spiral arms formed in the simulations run here are rapidly evolving substructure. This would make it incredibly difficult to observe in protoplanetary discs, and may explain the low population of such substructures in the ALMA Archive.

Similar to the models of Elias 2–27 and J16152023, we find that the disc masses needed to form the substructure within the disc of HD 36122 are significantly larger than currently observed. We measure a disc mass of M_{disc}=0.013M$_{\odot}$ from the ALMA observations. However, substructure could only be formed once the disc

mass reached M_{disc}=0.55M$_{\odot}$. This is over an order of magnitude greater than what is detected by ALMA.

Furthermore, we find that spiral arms can only form in protoplanetary discs once the disc mass for a given radius is high enough. The disc of HD 36112 had the highest surface density of all three modelled protostar. However, given that disc radii are often underestimated in submillimetre observations (Pérez et al. 2012), the parameters needed to form spiral arms in protoplanetary disc models differ significantly from those seen in observations; not just in the modelled disc masses, but also in disc radii as well.

This mismatch between the models and the data imply that we are missing some aspect of physics when modelling the spiral arms seen in protoplanetary discs using gravitational instabilities. The parameters used here, based upon the observations have not been able to fully recreate the observed substructure. Alternatively, another mechanism may be responsible for the spiral arms seen in the ALMA observations.

7.6 Synthetic Observations of the Disc Around HD 36112

Synthetic observations of the disc models of HD 36112 were conducted in order to compare the substructure seen in the models with the actual ALMA observations. This allows us to determine if gravitational instabilities in the disc are a possible formation mechanism for the substructures seen in the dust continuum. Performing synthetic observations also allow us to test the robustness of the models after undergoing synthetic observations. The original ALMA observation can be seen in Figure 7.2. We also include a snapshot from the synthetic observations run of the disc model HD02. This snapshot most resembles the ALMA observation.

The synthetic observations of the disc models resulted in some emission being

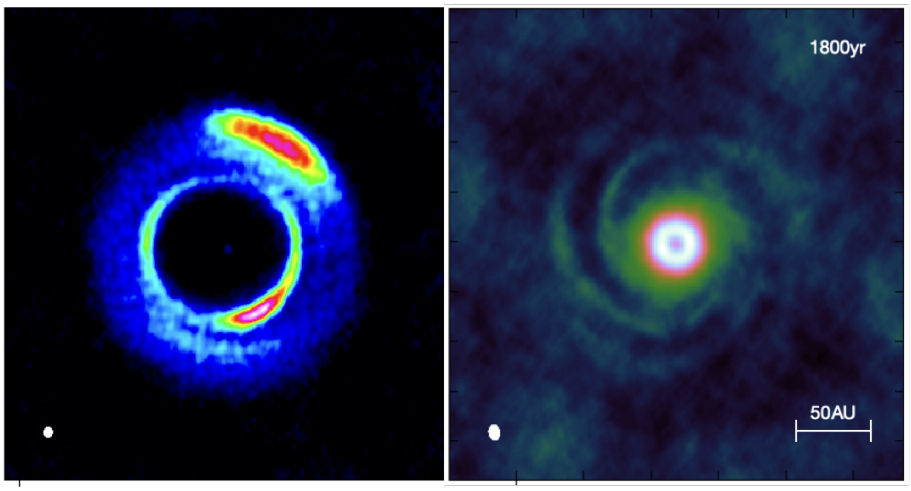

Figure 7.2: The ALMA observation of HD 36112 alongside a synthetic observation of one of the disc models run here. The ALMA observation (left) was taken at 340 GHz. The synthetic observation (right) shows the disc of HD 36112 from the model HD02 at 1800 yr. The scale bar in the bottom right represents 50 AU for both the ALMA and synthetic observations.

resolved out. The inner cavity seen in the disc models and synthetic observations were to be considered not real. We do, however, note that the extent of the cavity increases between the SPH simulations and the synthetic observations. This agrees with Francis & van der Marel (2020) who find that the inner cavities seen in discs may not be completely void of material. This does, however, imply that many protoplanetary discs have unresolved dust emission, as well as substructure. Knowledge of this unknown structure could affect the type of conditions needed in order to recreate the true structure of the disc. Therefore, it may not be possible to fully recreate the structure of a protoplanetary disc without fully resolved observations.

We use the observed dust disc radius from the ALMA observations as an initial parameter in the models. This follows previous work modelling protoplanetary discs (Dong et al. 2015a; Hall et al. 2018). We find, however, that the outer dust disc radii of the models are truncated after undergoing synthetic observations. Therefore,

using the observed dust disc radii may not be a suitable initial parameter when modelling protoplanetary discs as it could lead to an underestimation of the disc radii after undergoing synthetic observations.

Pérez et al. (2012) find that the gas disc may be significantly larger than the dust disc. Therefore, in order to accurately recreate the observed features in a protoplanetary disc, spectroscopic observations need to be made in order to determine the true extent of the gas disc - the radius of which can be used to model the disc. This may then result in the synthetic observations resolving the disc radii to the same extent seen in the ALMA continuum observations.

We have not been able to recreate the dust clumps first observed by Boehler et al. (2018). Furthermore, the spiral arms seen in the synthetic observations are considerably less intense than the rest of the disc material. The location of the spiral arms seen in models HD02 and HD03 do, however, coincide with the location of the inner dust clump. As well as this, spiral arms are seen to extend to $\sim$75 AU in both HD02 and HD03. This is the location of the spiral arms seen in scattered light (Grady et al. 2013; Benisty et al. 2015), and faintly detected by ALMA (Dong et al. 2018a) (see Figure 7.2).

We have not been able to recreate the dust clumps seen in the disc of HD 36112 using gravitational instabilities. We have however, been able to recreate the spiral arms seen in the submillimetre dust continuum emission. This type of substructure has not previously been seen in disc models of HD 36112 performed previously (Dong et al. 2015a; Boehler et al. 2018; Baruteau et al. 2019; Calcino et al. 2020).

7.7 The Complex Structure of HD 36112

The disc surrounding HD 36112 is complex, featuring a central cavity, dust clumps, faint rings, and spiral arms. We have shown that spiral arms are able to form in the disc via gravitational instabilities, however, dust clumps cannot. No previous

models have been able to form spiral arms. Therefore, it may not be possible to form the substructure in this disc using gravitational instabilities alone.

As outlined in Section 1.4, spiral arms can form in protoplanetary discs via gravitational instabilities as well as due to the presence of massive planets. The substructure in the disc of HD 36112 has previously been modelled using giant planets in a number of different orbits (Baruteau et al. 2019; Calcino et al. 2020). The simulations by Baruteau et al. (2019) are able to recreate the dust clumps as well as the cavity, by placing two giant planets in the disc. These planets are located interior and exterior to the spiral arms seen in scattered light.

Calcino et al. (2020) are able to form the spiral morphology seen in scattered light, in addition to the inner disc clump, by placing a giant planet inside the cavity. They are, however, unsuccessful in recreating the outer disc clump seen in the ALMA observations as well as the spiral arm. Only through the models run here, using gravitationally unstable discs, have faint spiral arms been seen in disc models of HD 36112 at millimetre wavelengths.

Although previous models have been performed using planets, there have however, been no confirmed detections of companions within the disc of HD 36112. Wagner et al. (2019) claim the detection of a giant planet at $\sim$100 AU. However, no deep, wide, gaps have been imaged in the gas emission of the disc (Boehler et al. 2018), an indicator of the presence of a giant planet. Similarly, the location of the claimed giant planet disagrees with the location of the modelled planet needed to produce the substructure (Baruteau et al. 2019).

Thus, the complex nature, and multiple substructures, seen in the disc of HD 36112 may not be due to simply one formation mechanism. A combination of embedded planets as well as gravitational instabilities may be needed to reproduce the cavity, dust rings, spiral arms, and dust clumps seen in the disc of HD 36112.

7.8 Linking Theory and Data

The synthetic observations produced here of the protoplanetary disc surrounding HD 36112 do not completely agree with the disc models as not all of the emission has been observable. Similar to work conducted by Dipierro et al. (2014, 2015), the inner region spiral arms seen in the disc models became entangled in the synthetic observations. This resulted in either a rim of material forming or multiple spiral arms combing to form a single arm. Furthermore, different substructures were seen in the synthetic observations compared to the disc models (a central rim of material). This demonstrates the importance of comparing real ALMA observations of protoplanetary discs to synthetic observations; rather than direct comparisons to disc models.

We have focused on the formation of substructure formed via gravitational instabilities in the protoplanetary disc. We find that substructure can only be formed in protoplanetary discs using disc masses much greater than currently seen in submillimetre observations. Therefore, either we are significantly underestimating disc masses when making observations, or an alternative mechanism is responsible for the spiral arms seen in the ALMA observations. Disc masses can be underestimated in observations due to the unknown disc opacity, as well as assuming the canonical gas–to–dust ratio of 100:1. Embedded planets could be an alternative mechanism for forming spiral arms in protoplanetary discs.

When substructure were able to form in the disc models, we find that the surface density of the disc needs to be sufficiently large. This resulted in spiral arms only forming in the discs surrounding HD 36112. Although the disc–to–star mass ratio was comparable for all simulations, the disc radius of HD 36112 was initially set to 100 AU. This resulted in a larger surface density compared to the modelled discs of Elias 2–27 and J16152023 where the disc radii were set to 300 AU and 150 AU,

respectively.

This finding agrees with the work of Hall et al. (2019), who were able to show that discs with high disc–to–star mass ratios ($\gtrsim 0.25$) could only form spiral arms if the radius of the disc was $R \lesssim 100$ AU. Thus, it is unlikely that gravitational instabilities can cause the spiral arms that are seen in discs such as Elias 2–27 and J16152023 where the disc radii are much larger.

The high surface density of the disc around HD 36112 may indicate that the spiral arms seen in the ALMA observations have formed due to gravitational instabilities in the disc, whereas,the low surface densities of Elias 2–27 and J16152023 may indicate that the spiral arms have formed via a different mechanism.

Furthermore, although we have not been able to form the clumps in the disc of HD 36112, we have been able to form the spiral arms seen in submillimetre wavelengths, a feature that has never successfully been modelled. This highlights the need to use multiple mechanisms for the formation of substructure in protoplanetary discs. Gravitational instabilities may be responsible for the formation of the spiral arms, whilst planets may be responsible for the dust clumps (Boehler et al. 2018; Calcino et al. 2020). Thus the nature of protoplanetary discs is more complex than previously thought.

7.9 Implications for Substructure Formation Mechanisms

The findings of the work conducted here have various implications for the current observations of protoplanetary discs, as well as the mechanisms that lead to the formation of substructure within the discs.

Observations of protoplanetary discs in both near–infrared scattered light and submillimetre wavelengths show that spiral features can be present in up to 20% of

discs (Dong et al. 2018b; Andrews et al. 2018a; Huang et al. 2018; Kurtovic et al. 2018; Cieza et al. 2019). This is a significant population of protoplanetary discs, thus indicating the importance of studying their formation mechanisms. In Chapter 4, we were able to show that only four out of 56 discs showed a spiral substructure; approximately 7%. Including the observation of HD 36112, where a faint arm could be seen in the disc, increases this to ≈9%. Nonetheless, this is significantly smaller than 20% of discs, as found by the authors above.

In Chapter 5, the spiral arms formed in the simulations of the gravitationally unstable disc around HD 36112 evolved quickly and dissipated on a dynamical timescale - around a few thousand years. This makes it incredibly difficult to image this substructure when it is present in protoplanetary discs, and may explain their rare occurrence.

Furthermore, Hall et al. (2019) were able to show that 'ultra–high' resolution observations ($< 0.04''$) are needed in order to resolve spiral arms caused by gravitationally unstable discs. Only ∼3% of the protoplanetary discs initially studied in Chapter 4 were observed at a resolution of $0.04''$ or greater. Therefore, if spiral arms formed via gravitational instabilities in discs are a common substructure, their detection may not be possible due to the 'low' resolution observations of the current disc population.

As well as this, the moderate resolution synthetic observations of HD 36112 produce substructure not seen in the disc models. The inner region spiral arms in models HD01 and HD02 smeared during the synthetic observations and appeared as a rim of material. This agrees with the work of Dipierro et al. (2014, 2015) who showed that multiple spiral arms may smear into one, or two, arms.

Therefore, many of the discs that we have previously classified as Rims, in Chapter 4, may be unresolved Spiral discs. Using 'ultra–high' resolution observations to observe the Rim discs may result in their reclassification to the Spiral category; with

the population of Spiral discs increasing to a number more consistent with recent findings (Dong et al. 2018b; Andrews et al. 2018a; Huang et al. 2018; Kurtovic et al. 2018; Cieza et al. 2019).

Unless 'ultra–high' resolution observations are used, the substructure seen in protoplanetary discs, even at sub-arcsecond resolutions, may not be the true substructure in the disc. Modelling the formation mechanisms of substructure is, therefore, more complicated than previously anticipated. If only ∼3% of protoplanetary discs have fully-resolved substructure, then these discs may need to be the benchmark from which substructure formation mechanisms need to be based. Modelling the formation of substructures such as rims of emission, may be futile as these features may be the result of relatively poor observing conditions.

Furthermore, we have been able to show that the disc masses seen in ALMA observations are significantly smaller than those required to produce the spiral arms seen in protoplanetary discs. This discrepancy between the disc models and data indicate that we are either missing some aspect of physics in our models or alternative mechanisms are responsible for the substructure seen.

The need for alternative mechanisms is also highlighted by the fact that we have been able to recreate the spiral arms seen in the disc of HD 36112, but not the dust clumps. Although the clumps have previously been seen in the simulations by Baruteau et al. (2019) and Calcino et al. (2020), the spiral arms were not produced. Thus, the formation of substructure in protoplanetary discs may be more complex than previously thought, and multiple mechanisms may be responsible for the observed morphology.

Embedded planets have previously been shown to form substructure within protoplanetary discs (Zhu et al. 2015; Dong et al. 2015b). This mechanism may be responsible for the formation of spiral arms seen in Elias 2–27 and J16152023 where the surface densities were too low to form spiral arms via gravitational instabilities.

The embedded planets, however, must have formed via a mechanism other than the gravitational fragmentation of the discs. The only other currently accepted formation mechanism of planets besides gravitational instabilities, is the core accretion method.

This method, however, has limitations. The ages of Elias 2–27 and J16152023 were shown to be 0.5±0.1 Myr and 6±4 Myr, respectively, in Chapter 4. Therefore these are still relatively young systems. The core accretion method of planet formation occurs on timescales larger than the average lifetime of the disc (Haisch et al. 2001; Cieza et al. 2007). Therefore, if the spiral arms in the discs of Elias 2–27 and J16152023 are forming via embedded planets, either the core accretion method of planet formation is more efficient than previously thought, or the planets are forming via a different, unknown mechanism.

Chapter 8

Conclusions

In this thesis we have studied the dust substructure seen in protoplanetary discs observed with the Atacama Large Millimetre/submillimetre Array. This is done in order to study the different morphologies seen in discs, as well as attempting to model the structure using smooth particle hydrodynamics.

We began by identifying the different substructure morphologies seen in protoplanetary discs. These were classified, and trends relating to the host protostar were then investigated. This was followed by the numerical modelling of three protoplanetary systems with the aim of forming substructure due to gravitational instabilities in the discs. The models were then synthetically observed in order to allow for comparison to the actual ALMA observations. This tests the robustness of the protoplanetary disc models.

Here I summarise the results from each of these works, and conclude the thesis by exploring possible future ventures.

8.1 Substructure Seen In Protoplanetary Discs

In Chapter 4 we studied the different substructures seen in the dust morphology of protoplanetary discs observed with ALMA. These were categorised, and trends

were then found relating to the different properties of the host protostar. We also compared the substructure seen in the submillimetre dust continuum to those seen in scattered light observations.

We began by obtaining observations of 794 protoplanetary discs from the ALMA Archive. The continuum product files for each object were studied and any discs that were spatially resolved, and featured clear substructure, were chosen. We excluded both debris discs and young, embedded discs from the sample, leaving 56 protoplanetary discs for further study. Thus, only 7% of the current ALMA disc population show resolvable substructure.

The substructure in each disc was then classified according to the morphology seen in the submillimetre continuum observations. Each disc was placed into one of four categories - Rim, Rings, Spiral, and Horseshoe - depending upon the most prominent feature seen. We acknowledged that some discs may fit into multiple classifications, but use the most prominent feature in the analysis conducted here.

Individual stellar ages and masses were then calculated for the protostellar systems. We used the stellar evolutionary models and isochronal tracks of Siess et al. (2000) and Baraffe et al. (2015) in order to calculate these values. The ages are then compared to the estimated star forming region each star belongs to in order to confirm the accuracy of the results.

We then order the discs in each category according to their stellar age and mass. To study the extent of the discs as the systems get older, and more massive, we calculated the radii of each disc that contains 68% of the total flux. This was done as each ALMA observation were taken with different resolutions and sensitivities. We found no clear evolutionary sequence in the substructure of the disc as the systems become older. We also found no trend between the substructure seen in the discs and the mass of the host star.

We found that a rim of emission is the most populous substructure seen in

ALMA observations of protoplanetary discs, with 32 out of 56 discs showing a rim. A ringed substructure was the next most populous, with spirals and horseshoes only existing around a very small sample of stars. Although the high occurrence of rim discs may be a selection effect, we confirm the ubiquitousness of cavities and gaps in protoplanetary discs. This is also supported by the result that a rim of material can be seen around stars with a range of ages and stellar masses. We find that horseshoes only appear around relatively old, intermediate–mass, systems; whilst spirals can be seen in young, low–mass, T–Tauri stars.

We compared the substructures seen in submillimetre observations to those seen by Garufi et al. (2018) in scattered light. We found that all discs showing a horseshoe morphology in submillimetre observations showed a spiral morphology in scattered light. Therefore the mechanism responsible for their formation may be the same. We again confirmed the ubiquitous nature of rims and cavities in protoplanetary discs by finding that all the discs featuring a rim at submillimetre wavelengths show a rim in scattered light.

We investigated the various selection effects of the ALMA observations and the limitations on the work conducted here. We find that ∼42% of discs observed with ALMA at a high resolution of $\lessapprox$0.1" show resolvable substructure. This is inline with Long et al. (2019), who find less than half of discs show substructure when observed at the same resolution limit. Increasing the resolution limit to $\lessapprox$0.04" increases the fraction of discs showing substructure to 60%. This somewhat agrees with Andrews et al. (2018a) who find that all discs show substructure when observed with an 'ultra–high' resolution of ≈0.035".

We have found that only ≈3% of the 794 discs studied here have been observed at 'ultra–high' resolutions where we have shown that 60% of protoplanetary discs show substructure. Thus, if all 794 protoplanetary discs studied here were to be re-observed at 'ultra–high' resolutions of ≈0.04", we can assume that the fraction

of discs showing substructure could increase to as high as 60%.

8.2 Modelling Gravitationally Unstable Discs

In Chapter 5 we ran smooth particle hydrodynamic simulations of the protoplanetary discs in three stellar systems. Our aim was to form substructure in the disc by allowing gravitational instabilities to form. The models were then compared to the literature in order to determine the robustness of the parameters utilised here.

The discs surrounding three protostars: Elias 2–27, J16152023, and HD 36112 were modelled. These were classified as Spiral, Spiral, and Rim discs in Chapter 4, respectively. We used the self-gravitating SPH code `SEREN` to model the discs. We modelled three discs for each protostar, increasing the disc mass in each subsequent run. The initial radii and disc masses were taken from the ALMA observations, first shown in Chapter 4. Each disc was evolved for 30 kyr, and stopped early only in the cases of fragmentation, or clear stabilisation.

We found that no spiral arms form in the disc models of Elias 2–27. Although we have used unusually high disc–to–star mass ratios to model the discs, each disc became more stable as it evolved. The simulations run here differ from models in the literature with regards to several parameters: the power law indices for the surface density, and temperature profiles, irradiation temperature, and disc metallicity (Meru et al. 2017; Hall et al. 2018). This disc may not have developed instabilities due to the surface density of the disc being too low, or alternatively, the disc being too hot.

Brief spiral arms arms could be seen in the outer disc of J16152023 as we reached the upper limits of the disc–to–star mass ratios modelled. These arms, however, rapidly dissipated. This agrees with the results of Hall et al. (2019) who show that spiral arms formed due to gravitational instabilities dissipate over $\sim 10^4$ years.

Both narrow and broad-scale spiral arms could be seen in the disc models of

HD 36112. As the disc mass increased, spiral arms were able to form much more quickly. This, however, meant that they evolved and dissipated at a much faster rate. The spiral arms formed in the disc models run here match with the location of the dust clumps seen in the actual ALMA observations. The extent of the arms also agree with the extent of the faint arm first detected by Dong et al. (2018a). We did, however, find that the intensity of the spiral arms are much smaller than the rest of the disc material.

Our inability to form substructure within the discs of Elias 2–27 and J16152023 may indicate that gravitational instabilities are not the cause of the observed morphologies. The radii of these discs are much larger than that of HD 36112; resulting in smaller surface densities which may not be able to trigger gravitational instabilities. This result agrees with the work conducted by Hall et al. (2019), who show that spiral arms formed by gravitational instabilities can only form in discs with radii < 100 AU. This, however, implies that alternative mechanisms are responsible for forming the spiral arms seen in the discs of Elias 2–27 and J16152023.

The disc masses, however, required to form spiral arms in the disc around HD 36112 are much greater than what is seen in observations, assuming a dust temperature, opacity, and dust-to-gas ratio. These masses can be up to an order of magnitude larger than what is observed. Therefore, there is a discrepancy between the disc masses needed to form substructure in the disc models and those measured from disc observations. This could be due to two possible reasons; either we are missing a fundamental aspect of physics when modelling spiral arms in protoplanetary discs due to gravitational instabilities, or the spiral arms are forming via a different mechanism, such as embedded planets.

8.3 Synthetically Observed Protoplanetary Discs

Synthetic observations of the disc models of HD 36112 were run in order to make comparisons to the actual ALMA observations. This also allowed us to test the robustness of our models, and determine if the physics behind them are responsible for the substructure seen in the disc of HD 36112. The synthetic observations of the disc were made under the same observing conditions as the original ALMA observations. This was done to allow for a realistic comparison to be made.

We found that the radial extent of the disc is not observable with the synthetic ALMA observations. This is due to the outer regions of the disc being too diffuse. Models using a shallower surface density profile power index could be run. This would increase the density of material in the outer regions of the disc, which may lead to it being observable with ALMA.

When modelling the protoplanetary discs, we find that an inner cavity is formed due to numerical effects. These cavities also appear in our synthetic observations, and are thus, also not real. Nonetheless we looked at the extent of the cavity between the the disc model and synthetic observations to determine how real cavities should be treated in the future when modelling discs. We found we found that their radii increase between the models and synthetic observations. Therefore, current observations of protoplanetary discs may be overestimating the true size of cavities as the process of observing them increases their apparent size.

We found that our simulations required a disc mass greater than M_{disc} =0.55M$_{\odot}$ in order to produce observable spiral arms in the disc of HD 36112. This disc mass is much greater than the disc mass measured in the actual ALMA observations (M_{disc} =0.013M$_{\odot}$). Therefore, we are either missing some mass in protoplanetary disc observations, or the substructure seen in the protoplanetary discs modelled here have been formed via some alternative mechanism.

Although the extent of the spiral arms coincided with the locations of the dust clumps seen in submillimetre observations, their intensity do not match. Furthermore, we found that the spiral arms seen in the synthetic observation match with the faint arms seen in the ALMA observations. A feature that has not been produced in previous modelling attempts of the disc surrounding HD 36112 at submillimetre wavelengths.

8.4 Implications for Substructure Formation Mechanisms

We have found that the majority of protoplanetary disc observations conducted with ALMA thus far have been made at resolutions insufficient to resolve substructure. Only 5% of the 794 discs initially studied here were made at high resolutions of $\lesssim$0.1". This decreases to 3% for resolutions of $\lesssim$0.04" - the limit below which we found 60% of discs show resolvable substructure. Therefore, the current knowledge of the substructure present in protoplanetary discs remains heavily incomplete.

The most commonly seen substructure in protoplanetary discs, i.e. a rim of material, may in fact be an observational effect. The process of running synthetic observations of our disc models smear multiple spiral arms. The synthetic observations thus show artificial rims. Therefore, 'ultra–high' resolution observations of the 794 protoplanetary discs studied here may increase the population of discs within which substructure can be seen. Furthermore, these higher resolution observations may resolve known substructure into further components.

Modelling the formation of substructure within protoplanetary discs should, therefore, be performed on the ALMA discs observed using 'ultra–high' resolutions. We found that comparisons between synthetic observations of disc models and the actual data are essential instead of comparisons between the SPH models and the

data.

Our disc models are able to recreate the spiral arm seen in the disc of HD 36112 at submillimetre wavelengths. This has not previously been done before in any other disc model. We have not, however, been able to recreate the clumps seen in the ALMA observation. Thus the formation of substructure in protoplanetary discs is more complex than previously thought. Multiple mechanisms may be required in order to form all components of the substructure seen in protoplanetary discs.

We have found that the disc surface densities required to form substructure in protoplanetary discs are much higher than is observed. Therefore, we are either missing a substantial fraction of the disc mass in observations, or an alternative mechanism is responsible for the observed substructure. Embedded planets are thought to also excite spiral arms in protoplanetary discs.

If planets are responsible for observed spiral arms, however, they must have formed via some mechanism other than the gravitational fragmentation of discs. Currently, the only other planet formation mechanism is the core accretion model. The timescale of this method, however, is much longer than current estimates for the lifetime of discs. Therefore, the planets do not form fast enough to be already pre–existing in the discs within which we observe spiral arms.

Planet formation via core accretion, therefore, may be more efficient than previously thought. Alternatively, the embedded planets in the disc may have formed via a mechanism other than core accretion or gravitational fragmentation of the disc. Another explanation for the discrepancy between our models and the data is that the substructures present in the protoplanetary discs may have formed by some unknown mechanism other than gravitational instabilities and embedded planets.

8.5 Main Conclusions of this Thesis

Below we summarise the main conclusions of this thesis.

- We find that a rim of material is the most common substructure seen in protoplanetary discs observed with ALMA. Concentric rings of emission are the next most common, with spiral arms, and horseshoe–like concentrations of material, only forming in a small number of discs. A rim of emission being the most populous substructure may be a selection effect due to them being the easiest substructure to detect, with many ALMA projects explicitly targeting these types of discs.

- We have looked at 794 protoplanetary discs in this work, of which 56 show resolvable substructure, only 7% of the disc sample. We find that 42% of protoplanetary discs show resolvable substructure when observed with high resolutions of $\lessapprox$0.1". This increases to 60% when 'ultra–high' resolution observations of $\lessapprox$0.04" are used. As only 3% of protoplanetary discs studied here have been observed with 'ultra–high' resolution observations, we can assume that the majority of protoplanetary discs in the ALMA Archive have unresolved substructure. Furthermore, re-observing the 794 protoplanetary discs studied here using 'ultra–high' observations may lead to the fraction of discs showing substructure to increase from 7% to up to 60%.

- We have been able to recreate the spiral arm seen in the dust continuum emission of the disc around HD 36112. This has not been achieved in previous modelling of this protostar. We have not been able to recreate the dust clumps seen in the ALMA observations. This has previously been modelled using embedded planets. Thus, we conclude that a number of mechanisms, including embedded planets and gravitational instabilities, may be responsible for the complex substructure seen in the protoplanetary disc around HD 36112.

- We find that synthetically observing disc models result in not all of the emission being observable. The outer disc radii appear to be truncated in the synthetic

observations due to the diffuseness of the material at the same radii in the disc models. An artificial cavity can be seen in the inner regions of the models, however we do find that the radius of this apparent cavity increases between the models and the synthetic observations. Therefore, we may be overestimating the extent of cavities seen in current disc populations due to some material being resolved away during observations.

- We also find that spiral arms present in the disc models can merge and appear as a rim of material in the synthetic observations. This is consistent with previous findings in the literature. Thus we confirm that the populous nature of a rim of emission seen in the current disc population may be an observational effect. Further, 'ultra–high' resolution observations may resolve these rims of emission into constituent components. As a result, the modelling of the formation of substructure in protoplanetary discs should only be performed using discs that have been observed at 'ultra–high' resolutions in order to ensure the intrinsic substructure is being modelled and not an artificial effect of interferometric observations.

- We find that the surface densities required to form substructure within protoplanetary discs via gravitational instabilities are much higher than currently observed. The disc masses required in the models can be up to an order of magnitude greater than measured from observations. Therefore, we are either missing a substantial fraction of mass when making observations of protoplanetary discs, or we are missing a key aspect of physics when modelling the substructure within protoplanetary discs formed via gravitational instabilities. Alternatively, another mechanism, such as embedded planets, may be responsible for the spiral substructure we currently seen in protoplanetary discs.

- A great deal of the foregoing discrepancies between our models and the ALMA data can be summarised in terms of the surface density of the discs. This has been seen in different circumstances as either needing higher mass or smaller radius discs - both of which lead to higher surface density. Another possible solution to these discrepancies is that the physics emulated in our SPH simulations is missing some astrophysical reality that can only be successfully reproduced by boosting the disc surface density. Possibilities in this class could include magnetic fields, the viscosity of the disc, incorrect dust–to–gas ratios, or some dust–gas micro–physics that triggers gravitational collapse more efficiently than we capture in our models. Further work will be needed to differentiate between these possibilities.

8.6 Future Work

There are various ways in which this work can be furthered. Firstly, our classification scheme was only applied to Class II young stellar objects. We discard young, embedded protostars from our sample, as well as debris discs. Although systems of vastly different ages cannot be compared directly, we can apply our classification scheme to both the oldest and youngest discs within which substructure can be seen. This would allow us to determine the most prevalent substructure at different evolutionary stages, as well as confirm the ubiquitous nature of substructure in protoplanetary discs.

We have found in this work that the majority of protoplanetary discs in the ALMA Archive have been observed using resolutions insufficiently high enough to resolve all of the substructure in the disc. Moving forward, proposals could be submitted with the aim of beginning to re-observe discs with known substructure. The observations would need to be run using 'ultra–high' resolutions in order to fully resolve the substructure. The outcomes of the observations may affect the current

theoretical disc models of known discs as new substructure may be found.

Here we have run models of the disc surrounding HD 36112 with the aim of producing substructure using a gravitationally unstable disc. Although we have been able to reproduce the spiral arm seen in the ALMA observations, we have been unable to produce the other complex features. Similarly, previous models of this object have failed to reproduce the observed spiral arm at submillimetre. Therefore, theoretical modelling of the disc surrounding HD 36112 could be repeated using multiple mechanisms to form the substructure in the disc. A gravitationally unstable disc would enable the formation of the observed spiral arm, whilst the inclusion of giant planets may aid to produce the complex substructure seen in the protoplanetary disc.

Finally, we have synthetically observed our disc models using the observing conditions under which the original observations were made. In order to further this work, we could conduct further synthetic observations of our disc models using a range of observing conditions. This would allow us to explore the extent of which disc models can be affected by undergoing synthetic observations. It would also allow us to determine the full spectrum of substructure that may simply be observational effects rather than actual structure produced in disc models.

Bibliography

Adachi, I., Hayashi, C., & Nakazawa, K. 1976, Progress of Theoretical Physics, 56, 1756

Agra-Amboage, V., Dougados, C., Cabrit, S., Garcia, P. J. V., & Ferruit, P. 2009, *Astron. Astrophys.*, 493, 1029

Akeson, R. L. & Jensen, E. L. N. 2014, *Astrophys. J.*, 784, 62

Akeson, R. L., Jensen, E. L. N., Carpenter, J., et al. 2019, *Astrophys. J.*, 872, 158

Akiyama, E., Hashimoto, J., Liu, H. B., et al. 2016, *Astron. J.*, 152, 222

Alcala, J. M., Covino, E., Franchini, M., et al. 1993, *Astron. Astrophys.*, 272, 225

Alcalá, J. M., Manara, C. F., Natta, A., et al. 2017, *Astron. Astrophys.*, 600, A20

Alexander, R., Pascucci, I., Andrews, S., Armitage, P., & Cieza, L. 2014, in Protostars and Planets VI, ed. H. Beuther, R. S. Klessen, C. P. Dullemond, & T. Henning, 475

ALMA Partnership, Brogan, C. L., Pérez, L. M., et al. 2015, *Astrophys. J. Letters*, 808, L3

Andre, P. 1994, in The Cold Universe, Proceedings of the 28th Rencontre de Moriond, ed. T. Montmerle, C. Lada, I. Mirabel, & J. Tran Thanh Van (Editions Frontieres)

Andre, P., Ward-Thompson, D., & Barsony, M. 1993, *Astrophys. J.*, 406, 122

Andrews, S. M. 2020, Annual Review of Astronomy and Astrophysics, 58, 483528

Andrews, S. M., Huang, J., Pérez, L. M., et al. 2018a, *Astrophys. J. Letters*, 869, L41

Andrews, S. M., Rosenfeld, K. A., Kraus, A. L., & Wilner, D. J. 2013, *Astrophys. J.*, 771, 129

Andrews, S. M., Terrell, M., Tripathi, A., et al. 2018b, *Astrophys. J.*, 865, 157

Andrews, S. M. & Williams, J. P. 2005, *Astrophys. J.*, 631, 1134

Andrews, S. M., Wilner, D. J., Espaillat, C., et al. 2011, *Astrophys. J.*, 732, 42

Andrews, S. M., Wilner, D. J., Hughes, A. M., Qi, C., & Dullemond, C. P. 2009, *Astrophys. J.*, 700, 1502

Ansdell, M., Williams, J. P., Manara, C. F., et al. 2017, *Astron. J.*, 153, 240

Ansdell, M., Williams, J. P., Trapman, L., et al. 2018, *Astrophys. J.*, 859, 21

Ansdell, M., Williams, J. P., van der Marel, N., et al. 2016, *Astrophys. J.*, 828, 46

Armitage, P. J. 2011, *Ann. Rev. Astron, Astrophys.*, 49, 195

Ataiee, S., Pinilla, P., Zsom, A., et al. 2013, *Astron. Astrophys.*, 553, L3

Avenhaus, H., Quanz, S. P., Garufi, A., et al. 2018, *Astrophys. J.*, 863, 44

Bachiller, R. 1996, *Ann. Rev. Astron, Astrophys.*, 34

Bai, X.-N. & Stone, J. M. 2010, *Astrophys. J.*, 722, 1437

Bai, X.-N. & Stone, J. M. 2014, *Astrophys. J.*, 796, 31

Baines, M. J., Williams, I. P., & Asebiomo, A. S. 1965, *Mon. Not. Roy. Astron. Soc.*, 130, 63

Baraffe, I., Homeier, D., Allard, F., & Chabrier, G. 2015, *Astron. Astrophys.*, 577, A42

Barenfeld, S. A., Carpenter, J. M., Ricci, L., & Isella, A. 2016, *Astrophys. J.*, 827, 142

Barsony, M. 1994, in Astronomical Society of the Pacific Conference Series, Vol. 65, Clouds, Cores, and Low Mass Stars, ed. D. P. Clemens & R. Barvainis, 197

Baruteau, C., Barraza, M., Pérez, S., et al. 2019, *Mon. Not. Roy. Astron. Soc.*, 486, 304

Baruteau, C., Crida, A., Paardekooper, S. J., et al. 2014, in Protostars and Planets VI, ed. H. Beuther, R. S. Klessen, C. P. Dullemond, & T. Henning, 667

Bate, M. R., Bonnell, I. A., & Price, N. M. 1995, *Mon. Not. Roy. Astron. Soc.*, 277, 362

Battersby, C., Ginsburg, A., Bally, J., et al. 2014, *Astrophys. J.*, 787, 113

Baudry, A., Marchet, F. B., Kurlandcyk, H., & Rossi, S. 2006, The Messenger, 125, 37

Beckwith, S. V. W. & Sargent, A. I. 1991, *Astrophys. J.*, 381, 250

Beckwith, S. V. W., Sargent, A. I., Chini, R. S., & Guesten, R. 1990, *Astron. J.*, 99, 924

Beichman, C. A., Myers, P. C., Emerson, J. P., et al. 1986, *Astrophys. J.*, 307, 337

Beitz, E., Guttler, C., Meisner, T., & Wurm, G. 2011, *Astrophys. J.*, 736, 34

Bell, C. P. M., Mamajek, E. E., & Naylor, T. 2015, *Mon. Not. Roy. Astron. Soc.*, 454, 593

Bell, K. R. & Lin, D. N. C. 1994, *Astrophys. J.*, 427, 987

Benisty, M., Juhasz, A., Boccaletti, A., et al. 2015, *Astron. Astrophys.*, 578, L6

Benz, W. 1990, in Numerical Modelling of Nonlinear Stellar Pulsations Problems and Prospects, ed. J. R. Buchler, 269

Bergin, E. A. & Tafalla, M. 2007, *Ann. Rev. Astron, Astrophys.*, 45, 339

Berrilli, F., Corciulo, G., Ingrosso, G., et al. 1992, *Astrophys. J.*, 398, 254

Bertout, C., Siess, L., & Cabrit, S. 2007, *Astron. Astrophys.*, 473, L21

Béthune, W., Lesur, G., & Ferreira, J. 2016, *Astron. Astrophys.*, 589, A87

Beuther, H., Churchwell, E. B., McKee, C. F., & Tan, J. C. 2007, in Protostars and Planets V, ed. B. Reipurth, D. Jewitt, & K. Keil, 165

Birnstiel, T., Dullemond, C. P., & Brauer, F. 2009, *Astron. Astrophys.*, 503, L5

Birnstiel, T., Dullemond, C. P., & Brauer, F. 2010, *Astron. Astrophys.*, 513, A79

Birnstiel, T., Dullemond, C. P., & Pinilla, P. 2013, *Astron. Astrophys.*, 550, L8

Birnstiel, T., Ormel, C. W., & Dullemond, C. P. 2011, *Astron. Astrophys.*, 525, A11

Blanco, A., Rizzo, F., & Fonti, S. 1991, Infrared Physics, 31, 167

Blum, J. 2018, *Space Sci. Rev.*, 214, 52

Blum, J. & Munch, M. 1993, *Icarus*, 106, 151

Blum, J. & Wurm, G. 2008, *Ann. Rev. Astron, Astrophys.*, 46, 21

Bodenheimer, P. 1995, *Ann. Rev. Astron, Astrophys.*, 33, 199

Boehler, Y., Ricci, L., Weaver, E., et al. 2018, *Astrophys. J.*, 853, 162

Boehler, Y., Weaver, E., Isella, A., et al. 2017, *Astrophys. J.*, 840, 60

Bohlin, R. C., Savage, B. D., & Drake, J. F. 1978, *Astrophys. J.*, 224, 132

Boley, A. C. 2009, *Astrophys. J. Letters*, 695, L53

Boss, A. P. 1997, Science, 276, 1836

Boss, A. P. 2011, *Astrophys. J.*, 731, 74

Boss, A. P. 2012, *Mon. Not. Roy. Astron. Soc.*, 419, 1930

Boss, A. P. & Bodenheimer, P. 1979, *Astrophys. J.*, 234, 289

Bouwman, J., de Koter, A., Dominik, C., & Waters, L. B. F. M. 2003, *Astron. Astrophys.*, 401, 577

Brauer, F., Dullemond, C. P., & Henning, T. 2008, *Astron. Astrophys.*, 480, 859

Brisset, J., Heißelmann, D., Kothe, S., Weidling, R., & Blum, J. 2016, *Astron. Astrophys.*, 593, A3

Brisset, J., Heißelmann, D., Kothe, S., Weidling, R., & Blum, J. 2017, *Astron. Astrophys.*, 603, A66

Brown, J. M., Blake, G. A., Qi, C., et al. 2009, *Astrophys. J.*, 704, 496

Bruderer, S., van der Marel, N., van Dishoeck, E. F., & van Kempen, T. A. 2014, *Astron. Astrophys.*, 562, A26

Bryden, G., Beichman, C. A., Carpenter, J. M., et al. 2009, *Astrophys. J.*, 705, 1226

Buchhave, L. A., Latham, D. W., Johansen, A., et al. 2012, *Nature*, 486, 375

Bukhari Syed, M., Blum, J., Wahlberg Jansson, K., & Johansen, A. 2017, *Astrophys. J.*, 834, 145

Burke, B. & Graham-Smith, F. 1997, An Introduction to Radio Astronomy (Cambridge University Press), 50–58

Caballero, J. A. & Solano, E. 2008, *Astron. Astrophys.*, 485, 931

Calcino, J., Christiaens, V., Price, D. J., et al. 2020, *Mon. Not. Roy. Astron. Soc.*, 498, 639

Calvet, N., D'Alessio, P., Hartmann, L., et al. 2002, *Astrophys. J.*, 568, 1008

Cameron, A. G. W., Kopal, Z., & Sonett, C. P. 1978, Moon and Planets, 18, 3

Canovas, H., Montesinos, B., Schreiber, M. R., et al. 2018, *Astron. Astrophys.*, 610, A13

Casassus, S., Perez M., S., Jordán, A., et al. 2012, *Astrophys. J. Letters*, 754, L31

Casassus, S., van der Plas, G. M., Perez, S., et al. 2013, *Nature*, 493, 191

Casassus, S., Wright, C. M., Marino, S., et al. 2015, *Astrophys. J.*, 812, 126

Cazzoletti, P., van Dishoeck, E. F., Pinilla, P., et al. 2018, *Astron. Astrophys.*, 619, A161

Chabrier, G. 2003, *Astrophys. J. Letters*, 586, L133

Chokshi, A., Tielens, A. G. G. M., & Hollenbach, D. 1993, *Astrophys. J.*, 407, 806

Cieza, L., Padgett, D. L., Stapelfeldt, K. R., et al. 2007, *Astrophys. J.*, 667, 308

Cieza, L. A., Ruíz-Rodríguez, D., Hales, A., et al. 2019, *Mon. Not. Roy. Astron. Soc.*, 482, 698

Clark, B. G. 1980, *Astron. Astrophys.*, 89, 377

Clark, B. G. 1989, in Astronomical Society of the Pacific Conference Series, Vol. 6, Synthesis Imaging in Radio Astronomy, ed. R. A. Perley, F. R. Schwab, & A. H. Bridle, 1–9

Cox, E. G., Harris, R. J., Looney, L. W., et al. 2017, *Astrophys. J.*, 851, 83

Cuzzi, J. N. & Hogan, R. C. 2003, *Icarus*, 164, 127

Cuzzi, J. N. & Zahnle, K. J. 2004, *Astrophys. J.*, 614, 490

Da Rio, N., Robberto, M., Soderblom, D. R., et al. 2010, *Astrophys. J.*, 722, 1092

de Juan Ovelar, M., Min, M., Dominik, C., et al. 2013, *Astron. Astrophys.*, 560, A111

Deckers, J. & Teiser, J. 2013, *Astrophys. J.*, 769, 151

Dehnen, W. & Aly, H. 2012, *Mon. Not. Roy. Astron. Soc.*, 425, 1068

Di Folco, E., Dutrey, A., Le Bouquin, J. B., et al. 2014, *Astron. Astrophys.*, 565, L2

Dipierro, G., Laibe, G., Price, D. J., & Lodato, G. 2016, *Mon. Not. Roy. Astron. Soc.*, 459, L1

Dipierro, G., Lodato, G., Testi, L., & de Gregorio Monsalvo, I. 2014, *Mon. Not. Roy. Astron. Soc.*, 444, 1919

Dipierro, G., Pinilla, P., Lodato, G., & Testi, L. 2015, *Mon. Not. Roy. Astron. Soc.*, 451, 974

Dipierro, G., Ricci, L., Pérez, L., et al. 2018, *Mon. Not. Roy. Astron. Soc.*, 475, 5296

Dittrich, K., Klahr, H., & Johansen, A. 2013, *Astrophys. J.*, 763, 117

Dodson-Robinson, S. E. & Salyk, C. 2011, *Astrophys. J.*, 738, 131

Dominik, C. & Dullemond, C. P. 2008, *Astron. Astrophys.*, 491, 663

Dominik, C. & Tielens, A. G. G. M. 1997, *Astrophys. J.*, 480, 647

Dong, R., Hall, C., Rice, K., & Chiang, E. 2015a, *Astrophys. J. Letters*, 812, L32

Dong, R., Liu, S.-y., Eisner, J., et al. 2018a, *Astrophys. J.*, 860, 124

Dong, R., Najita, J. R., & Brittain, S. 2018b, *Astrophys. J.*, 862, 103

Dong, R., van der Marel, N., Hashimoto, J., et al. 2017, *Astrophys. J.*, 836, 201

Dong, R., Zhu, Z., & Whitney, B. 2015b, *Astrophys. J.*, 809, 93

Doyle, L. R., Carter, J. A., Fabrycky, D. C., et al. 2011, Science, 333, 1602

Draine, B. T. 2003, *Ann. Rev. Astron, Astrophys.*, 41, 241

Draine, B. T. 2006, *Astrophys. J.*, 636, 1114

Dubrulle, B., Morfill, G., & Sterzik, M. 1995, *Icarus*, 114, 237

Dullemond, C. P. & Dominik, C. 2005, *Astron. Astrophys.*, 434, 971

Dullemond, C. P. & Dominik, C. 2008, *Astron. Astrophys.*, 487, 205

Dullemond, C. P., Dominik, C., & Natta, A. 2001, *Astrophys. J.*, 560, 957

Dullemond, C. P., Hollenbach, D., Kamp, I., & D'Alessio, P. 2007, Protostars and Planets V, 555

Dunham, M. M., Vorobyov, E. I., & Arce, H. G. 2014, *Mon. Not. Roy. Astron. Soc.*, 444, 887

Durisen, R. H., Boss, A. P., Mayer, L., et al. 2007, in Protostars and Planets V, ed. B. Reipurth, D. Jewitt, & K. Keil, 607

Dutrey, A., Di Folco, E., Beck, T., & Guilloteau, S. 2016, *Astron. Astrophys. Rev.*, 24, 5

Duvert, G., Guilloteau, S., Ménard, F., Simon, M., & Dutrey, A. 2000, *Astron. Astrophys.*, 355, 165

Eisner, J. A., Arce, H. G., Ballering, N. P., et al. 2018, *Astrophys. J.*, 860, 77

Eisner, J. A., Graham, J. R., Akeson, R. L., & Najita, J. 2009, *Astrophys. J.*, 692, 309

Eisner, J. A., Hillenbrand, L. A., Carpenter, J. M., & Wolf, S. 2005, *Astrophys. J.*, 635, 396

Ercolano, B. & Pascucci, I. 2017, Royal Society Open Science, 4, 170114

ESA. 1997, in ESA Special Publication, Vol. 1200, ESA Special Publication

ESO. 2015, How Does ALMA Work? (ESO)

Evans, Neal J., I., Dunham, M. M., Jørgensen, J. K., et al. 2009, *Astrophys. J. Supple.*, 181, 321

Evans, M. G., Ilee, J. D., Hartquist, T. W., et al. 2017, *Mon. Not. Roy. Astron. Soc.*, 470, 1828

Facchini, S., Benisty, M., Bae, J., et al. 2020, *Astron. Astrophys.*, 639, A121

Fairlamb, J. R., Oudmaijer, R. D., Mendigutía, I., Ilee, J. D., & van den Ancker, M. E. 2015, *Mon. Not. Roy. Astron. Soc.*, 453, 976

Fedele, D., Carney, M., Hogerheijde, M. R., et al. 2017, *Astron. Astrophys.*, 600, A72

Fedele, D., Tazzari, M., Booth, R., et al. 2018, *Astron. Astrophys.*, 610, A24

Fletcher, M., Nayakshin, S., Stamatellos, D., et al. 2019, *Mon. Not. Roy. Astron. Soc.*, 486, 4398

Forgan, D. & Rice, K. 2013, *Mon. Not. Roy. Astron. Soc.*, 433, 1796

Forgan, D., Rice, K., Cossins, P., & Lodato, G. 2011, *Mon. Not. Roy. Astron. Soc.*, 410, 994

Forgan, D. H., Ilee, J. D., & Meru, F. 2018, *Astrophys. J. Letters*, 860, L5

Fouchet, L., Maddison, S. T., Gonzalez, J. F., & Murray, J. R. 2007, *Astron. Astrophys.*, 474, 1037

Francis, L. & van der Marel, N. 2020, *Astrophys. J.*, 892, 111

Fukagawa, M., Hayashi, M., Tamura, M., et al. 2004, *Astrophys. J. Letters*, 605, L53

Fukagawa, M., Tamura, M., Itoh, Y., et al. 2006, *Astrophys. J. Letters*, 636, L153

Gaia Collaboration, Brown, A. G. A., Vallenari, A., et al. 2018, *Astron. Astrophys.*, 616, A1

Gaia Collaboration, Brown, A. G. A., Vallenari, A., et al. 2016, *Astron. Astrophys.*, 595, A2

Gammie, C. F. 2001, *Astrophys. J.*, 553, 174

Garufi, A., Benisty, M., Pinilla, P., et al. 2018, *Astron. Astrophys.*, 620, A94

Garufi, A., Podio, L., Bacciotti, F., et al. 2019, *Astron. Astrophys.*, 628, A68

Gingold, R. A. & Monaghan, J. J. 1977, *Mon. Not. Roy. Astron. Soc.*, 181, 375

Goldreich, P. & Tremaine, S. 1980, *Astrophys. J.*, 241, 425

Goldreich, P. & Ward, W. R. 1973, *Astrophys. J.*, 183, 1051

Gonzalez, J. F., Laibe, G., & Maddison, S. T. 2017, *Mon. Not. Roy. Astron. Soc.*, 467, 1984

Grady, C. A., Muto, T., Hashimoto, J., et al. 2013, *Astrophys. J.*, 762, 48

Grady, C. A., Polomski, E. F., Henning, T., et al. 2001, *Astron. J.*, 122, 3396

Greenberg, R., Wacker, J. F., Hartmann, W. K., & Chapman, C. R. 1978, *Icarus*, 35, 1

Greene, T. P., Wilking, B. A., Andre, P., Young, E. T., & Lada, C. J. 1994, *Astrophys. J.*, 434, 614

Grosso, N., Bouvier, J., Montmerle, T., et al. 2007, *Astron. Astrophys.*, 475, 607

Guenther, E. W., Esposito, M., Mundt, R., et al. 2007, *Astron. Astrophys.*, 467, 1147

Gundlach, B., Blum, J., Keller, H. U., & Skorov, Y. V. 2015, *Astron. Astrophys.*, 583, A12

Güttler, C., Blum, J., Zsom, A., Ormel, C. W., & Dullemond, C. P. 2010, *Astron. Astrophys.*, 513, A56

Guzmán, V. V., Huang, J., Andrews, S. M., et al. 2018, *Astrophys. J. Letters*, 869, L48

Haisch, Karl E., J., Lada, E. A., & Lada, C. J. 2001, *Astrophys. J. Letters*, 553, L153

Hall, C., Dong, R., Rice, K., et al. 2019, The Astrophysical Journal, 871, 228

Hall, C., Forgan, D., Rice, K., et al. 2016, *Mon. Not. Roy. Astron. Soc.*, 458, 306

Hall, C., Rice, K., Dipierro, G., et al. 2018, *Mon. Not. Roy. Astron. Soc.*, 477, 1004

Hardy, A., Caceres, C., Schreiber, M. R., et al. 2015, *Astron. Astrophys.*, 583, A66

Hartmann, L., Calvet, N., Gullbring, E., & D'Alessio, P. 1998, *Astrophys. J.*, 495, 385

Haworth, T. J., Glover, S. C. O., Koepferl, C. M., Bisbas, T. G., & Dale, J. E. 2018, *New Astronomy Reviews*, 82, 1

Hayashi, C. 1966, *Ann. Rev. Astron, Astrophys.*, 4, 171

Hayashi, C. & Nakano, T. 1965, Progress of Theoretical Physics, 34, 754

Hayashi, C., Nakazawa, K., & Nakagawa, Y. 1985, in Protostars and Planets II, ed. D. C. Black & M. S. Matthews, 1100–1153

Heißelmann, D., Blum, J., & Fraser, H. J. 2007, in Proc. 58th Int. Astronautical Congress 2007 (Paris: Int. Astronautical Federation), 2102

Herbig, G. H. 1960, *Astrophys. J. Supple.*, 4, 337

Herbig, G. H. 1962, Advances in Astronomy and Astrophysics, 1, 47

Hernquist, L. & Katz, N. 1989, *Astrophys. J. Supple.*, 70, 419

Hildebrand, R. H. 1983, *Quarterly Journal of the Royal Astronomical Society*, 24, 267

Hillenbrand, L. A., Strom, S. E., Vrba, F. J., & Keene, J. 1992, *Astrophys. J.*, 397, 613

Högbom, J. A. 1974, *Astron. Astrophys. Suppl.*, 15, 417

Hollenbach, D., Johnstone, D., Lizano, S., & Shu, F. 1994, *Astrophys. J.*, 428, 654

Hopkins, P. F. 2015, *Mon. Not. Roy. Astron. Soc.*, 450, 53

Huang, J., Andrews, S. M., Dullemond, C. P., et al. 2018, *Astrophys. J. Letters*, 869, L42

Hubber, D. A., Batty, C. P., McLeod, A., & Whitworth, A. P. 2011, *Astron. Astrophys.*, 529, A27

Hughes, A. M., Wilner, D. J., Qi, C., & Hogerheijde, M. R. 2008, *Astrophys. J.*, 678, 1119

Isella, A., Carpenter, J. M., & Sargent, A. I. 2009, *Astrophys. J.*, 701, 260

Isella, A., Guidi, G., Testi, L., et al. 2016, *Phys. Rev. L*, 117, 251101

Isella, A., Huang, J., Andrews, S. M., et al. 2018, *Astrophys. J. Letters*, 869, L49

Isella, A., Natta, A., Wilner, D., Carpenter, J. M., & Testi, L. 2010, *Astrophys. J.*, 725, 1735

Isella, A., Pérez, L. M., Carpenter, J. M., et al. 2013, *Astrophys. J.*, 775, 30

Isella, A., Tatulli, E., Natta, A., & Testi, L. 2008, *Astron. Astrophys.*, 483, L13

Isella, A., Testi, L., & Natta, A. 2006, *Astron. Astrophys.*, 451, 951

Jaeger, S. 2008, in Astronomical Society of the Pacific Conference Series, Vol. 394, Astronomical Data Analysis Software and Systems XVII, ed. R. W. Argyle, P. S. Bunclark, & J. R. Lewis, 623

Jager, C., Mutschke, H., & Henning, T. 1998, *Astron. Astrophys.*, 332, 291

James, D. J., Melo, C., Santos, N. C., & Bouvier, J. 2006, *Astron. Astrophys.*, 446, 971

Jennings, J., Booth, R. A., Tazzari, M., Clarke, C. J., & Rosotti, G. P. 2021, arXiv e-prints, arXiv:2103.02392

Johansen, A. & Youdin, A. 2007, *Astrophys. J.*, 662, 627

Johansen, A., Youdin, A., & Klahr, H. 2009, *Astrophys. J.*, 697, 1269

Johnson, B. M. & Gammie, C. F. 2003, *Astrophys. J.*, 597, 131

Johnson, J. A., Fischer, D. A., Marcy, G. W., et al. 2007, *Astrophys. J.*, 665, 785

Jørgensen, B. R. & Lindegren, L. 2005, *Astron. Astrophys.*, 436, 127

Joy, A. H. 1945, *Astrophys. J.*, 102, 168

Kama, M., Bruderer, S., van Dishoeck, E. F., et al. 2016, *Astron. Astrophys.*, 592, A83

Kelly, B. C. 2007, *Astrophys. J.*, 665, 1489

Kenyon, S. J., Gómez, M., & Whitney, B. A. 2008, Low Mass Star Formation in the Taurus-Auriga Clouds, ed. B. Reipurth, Vol. 4, 405

Kenyon, S. J. & Hartmann, L. 1987, *Astrophys. J.*, 323, 714

Kenyon, S. J. & Hartmann, L. W. 1990, *Astrophys. J.*, 349, 197

Kley, W. & Dirksen, G. 2006, *Astron. Astrophys.*, 447, 369

Kley, W. & Nelson, R. P. 2012, *Ann. Rev. Astron, Astrophys.*, 50, 211

Koike, C., Hasegawa, H., & Manabe, A. 1980, *Astrophys. Space Sci.*, 67, 495

Kothe, S. 2016, PhD thesis

Kothe, S., Blum, J., Weidling, R., & Güttler, C. 2013, *Icarus*, 225, 75

Kratter, K. & Lodato, G. 2016, *Ann. Rev. Astron, Astrophys.*, 54, 271

Kraus, A. L. & Hillenbrand, L. A. 2009, *Astrophys. J.*, 704, 531

Kraus, S., Ireland, M. J., Sitko, M. L., et al. 2013, *Astrophys. J.*, 768, 80

Kraus, S., Kreplin, A., Fukugawa, M., et al. 2017, *Astrophys. J. Letters*, 848, L11

Krijt, S., Ormel, C. W., Dominik, C., & Tielens, A. G. G. M. 2015, *Astron. Astrophys.*, 574, A83

Kroupa, P. 2001, *Mon. Not. Roy. Astron. Soc.*, 322, 231

Kudo, T., Hashimoto, J., Muto, T., et al. 2018, *Astrophys. J. Letters*, 868, L5

Kuiper, G. P. 1951, Proceedings of the National Academy of Science, 37, 1

Kurtovic, N. T., Pérez, L. M., Benisty, M., et al. 2018, *Astrophys. J. Letters*, 869, L44

Kusaka, T., Nakano, T., & Hayashi, C. 1970, Progress of Theoretical Physics, 44, 1580

Lada, C. J. 1985, *Ann. Rev. Astron, Astrophys.*, 23, 267

Lada, C. J. 1987, in IAU Symposium, Vol. 115, Star Forming Regions, ed. M. Peimbert & J. Jugaku, 1–17

Landeck, W. 2016, *Bachelor Thesis, Technische Universität Braunschweig, Germany*

Langlois, M., Pohl, A., Lagrange, A. M., et al. 2018, *Astron. Astrophys.*, 614, A88

Larson, R. B. 1985, *Mon. Not. Roy. Astron. Soc.*, 214, 379

Laughlin, G. & Rozyczka, M. 1996, *Astrophys. J.*, 456, 279

Lin, D. N. C. & Papaloizou, J. 1979, *Mon. Not. Roy. Astron. Soc.*, 188, 191

Lin, D. N. C. & Papaloizou, J. 1986, *Astrophys. J.*, 309, 846

Lin, D. N. C. & Pringle, J. E. 1990, *Astrophys. J.*, 358, 515

Lissauer, J. J. 1993, *Ann. Rev. Astron, Astrophys.*, 31, 129

Lodato, G. & Rice, W. K. M. 2005, *Mon. Not. Roy. Astron. Soc.*, 358, 1489

Long, F., Herczeg, G. J., Harsono, D., et al. 2019, *Astrophys. J.*, 882, 49

Long, F., Pinilla, P., Herczeg, G. J., et al. 2018, *Astrophys. J.*, 869, 17

Lucy, L. B. 1977, *Astron. J.*, 82, 1013

Luhman, K. L. 2007, *Astrophys. J. Supple.*, 173, 104

Luhman, K. L. & Rieke, G. H. 1999, *Astrophys. J.*, 525, 440

Lynden-Bell, D. & Pringle, J. E. 1974, *Mon. Not. Roy. Astron. Soc.*, 168, 603

Macías, E., Espaillat, C. C., Ribas, Á., et al. 2018, *Astrophys. J.*, 865, 37

Malfait, K., Waelkens, C., Waters, L. B. F. M., et al. 1998, *Astron. Astrophys.*, 332, L25

Mamajek, E. E. 2009, in American Institute of Physics Conference Series, Vol. 1158, Exoplanets and Disks: Their Formation and Diversity, ed. T. Usuda, M. Tamura, & M. Ishii, 3–10

Mamajek, E. E. & Bell, C. P. M. 2014, *Mon. Not. Roy. Astron. Soc.*, 445, 2169

Manara, C. F., Testi, L., Natta, A., et al. 2014, *Astron. Astrophys.*, 568, A18

Manoj, P., Bhatt, H. C., Maheswar, G., & Muneer, S. 2006, *Astrophys. J.*, 653, 657

Mariñas, N., Telesco, C. M., Fisher, R. S., & Packham, C. 2011, *Astrophys. J.*, 737, 57

Marino, S., Casassus, S., Perez, S., et al. 2015, *Astrophys. J.*, 813, 76

Markiewicz, W. J., Mizuno, H., & Voelk, H. J. 1991, *Astron. Astrophys.*, 242, 286

Masset, F. 2000, *Astron. Astrophys. Suppl.*, 141, 165

Masunaga, H. & Inutsuka, S.-i. 2000, *Astrophys. J.*, 531, 350

Matzner, C. D. & Levin, Y. 2005, *Astrophys. J.*, 628, 817

Mayer, L., Quinn, T., Wadsley, J., & Stadel, J. 2004, *Astrophys. J.*, 609, 1045

McKee, C. F. & Ostriker, J. P. 1977, *Astrophys. J.*, 218, 148

Meeus, G., Montesinos, B., Mendigutía, I., et al. 2012, *Astron. Astrophys.*, 544, A78

Mendigutía, I., Fairlamb, J., Montesinos, B., et al. 2014, *Astrophys. J.*, 790, 21

Mennella, V., Brucato, J. R., Colangeli, L., et al. 1998, *Astrophys. J.*, 496, 1058

Mennella, V., Colangeli, L., Bussoletti, E., et al. 1995, *Planetary and Space Science*, 43, 1217

Merín, B., Brown, J. M., Oliveira, I., et al. 2010, *Astrophys. J.*, 718, 1200

Meru, F., Juhász, A., Ilee, J. D., et al. 2017, *Astrophys. J. Letters*, 839, L24

Metchev, S. A., Hillenbrand, L. A., & Meyer, M. R. 2004, *Astrophys. J.*, 600, 435

Mizuno, H., Markiewicz, W. J., & Voelk, H. J. 1988, *Astron. Astrophys.*, 195, 183

Monaghan, J. J. 1997, Journal of Computational Physics, 136, 298

Monaghan, J. J. & Gingold, R. A. 1983, Journal of Computational Physics, 52, 374

Monaghan, J. J. & Lattanzio, J. C. 1985, *Astron. Astrophys.*, 149, 135

Monnier, J. D., Berger, J. P., Millan-Gabet, R., et al. 2006, *Astrophys. J.*, 647, 444

Morris, J. P. & Monaghan, J. J. 1997, Journal of Computational Physics, 136, 41

Mulders, G. D., Pascucci, I., & Apai, D. 2015, *Astrophys. J.*, 798, 112

Muro-Arena, G. A., Ginski, C., Dominik, C., et al. 2020, *Astron. Astrophys.*, 636, L4

Musiolik, G., Teiser, J., Jankowski, T., & Wurm, G. 2016a, *Astrophys. J.*, 818, 16

Musiolik, G., Teiser, J., Jankowski, T., & Wurm, G. 2016b, *Astrophys. J.*, 827, 63

Muto, T., Grady, C. A., Hashimoto, J., et al. 2012, *Astrophys. J. Letters*, 748, L22

Najita, J. R., Andrews, S. M., & Muzerolle, J. 2015, *Mon. Not. Roy. Astron. Soc.*, 450, 3559

Nakagawa, Y., Sekiya, M., & Hayashi, C. 1986, *Icarus*, 67, 375

Natta, A., Prusti, T., Neri, R., et al. 2001, *Astron. Astrophys.*, 371, 186

Natta, A., Testi, L., Calvet, N., et al. 2007, in Protostars and Planets V, ed. B. Reipurth, D. Jewitt, & K. Keil, 767

Natta, A., Testi, L., & Randich, S. 2006, *Astron. Astrophys.*, 452, 245

Ohashi, S., Kataoka, A., Nagai, H., et al. 2018, *Astrophys. J.*, 864, 81

Ohta, Y., Fukagawa, M., Sitko, M. L., et al. 2016, *Pub. Astron. Soc. Japan*, 68, 53

Ormel, C. W. & Cuzzi, J. N. 2007, *Astron. Astrophys.*, 466, 413

Osorio, M., D'Alessio, P., Muzerolle, J., Calvet, N., & Hartmann, L. 2003, *Astrophys. J.*, 586, 1148

Paardekooper, S. J. & Mellema, G. 2006, *Astron. Astrophys.*, 453, 1129

Paraskov, G. B., Wurm, G., & Krauss, O. 2007, *Icarus*, 191, 779

Pardo, J. R. 2019, in ALMA Development Workshop, 36

Pascucci, I., Testi, L., Herczeg, G. J., et al. 2016, *Astrophys. J.*, 831, 125

Pérez, L. M., Benisty, M., Andrews, S. M., et al. 2018, *Astrophys. J. Letters*, 869, L50

Pérez, L. M., Carpenter, J. M., Andrews, S. M., et al. 2016, Science, 353, 1519

Pérez, L. M., Carpenter, J. M., Chandler, C. J., et al. 2012, *Astrophys. J. Letters*, 760, L17

Pérez, L. M., Isella, A., Carpenter, J. M., & Chandler, C. J. 2014, *Astrophys. J. Letters*, 783, L13

Pérez, S., Casassus, S., Baruteau, C., et al. 2019, *Astron. J.*, 158, 15

Perez, S., Casassus, S., Ménard, F., et al. 2015, *Astrophys. J.*, 798, 85

Piétu, V., Dutrey, A., & Guilloteau, S. 2007, *Astron. Astrophys.*, 467, 163

Pineda, J. E., Szulágyi, J., Quanz, S. P., et al. 2019, *Astrophys. J.*, 871, 48

Pinilla, P., Benisty, M., & Birnstiel, T. 2012a, *Astron. Astrophys.*, 545, A81

Pinilla, P., Birnstiel, T., Benisty, M., et al. 2013, *Astron. Astrophys.*, 554, A95

Pinilla, P., Birnstiel, T., Ricci, L., et al. 2012b, *Astron. Astrophys.*, 538, A114

Pinilla, P., Pérez, L. M., Andrews, S., et al. 2017a, *Astrophys. J.*, 839, 99

Pinilla, P., Pohl, A., Stammler, S. M., & Birnstiel, T. 2017b, *Astrophys. J.*, 845, 68

Pinilla, P., Tazzari, M., Pascucci, I., et al. 2018, *Astrophys. J.*, 859, 32

Pohl, A., Pinilla, P., Benisty, M., et al. 2015, *Mon. Not. Roy. Astron. Soc.*, 453, 1768

Pollack, J. B., Hubickyj, O., Bodenheimer, P., et al. 1996, *Icarus*, 124, 62

Pontoppidan, K., van Dishoeck, E., Dartois, E., & Thi, W.-F. 2005, Highlights of Astronomy, 13, 479

Preibisch, T. & Mamajek, E. 2008, The Nearest OB Association: Scorpius-Centaurus (Sco OB2), ed. B. Reipurth, Vol. 5, 235

Price, D. J. 2007, *Pub. Astron. Soc. Australia*, 24, 159

Price, D. J. 2012, *Mon. Not. Roy. Astron. Soc.*, 420, L33

Price, D. J. & Monaghan, J. J. 2004, *Mon. Not. Roy. Astron. Soc.*, 348, 139

Price, D. J. & Monaghan, J. J. 2007, *Mon. Not. Roy. Astron. Soc.*, 374, 1347

Price, D. J., Wurster, J., Tricco, T. S., et al. 2018, *Pub. Astron. Soc. Australia*, 35, e031

Pudritz, R. E. & Norman, C. A. 1983, *Astrophys. J.*, 274, 677

Pudritz, R. E. & Norman, C. A. 1986, *Astrophys. J.*, 301, 571

Pudritz, R. E., Wilson, C. D., Carlstrom, J. E., et al. 1996, *Astrophys. J. Letters*, 470, L123

Recoquillon, C., Baudry, A., Begueret, J.-B., Gauffre, S., & Montignac, G. 2005, *ALMA Memo No. 532*

Remijan, A., Biggs, A., Cortes, P., et al. 2020, *ALMA Doc 8.3*, 1

Ricci, L., Testi, L., Natta, A., & Brooks, K. J. 2010, *Astron. Astrophys.*, 521, A66

Rice, W. K. M., Armitage, P. J., Bate, M. R., & Bonnell, I. A. 2003, *Mon. Not. Roy. Astron. Soc.*, 339, 1025

Rice, W. K. M., Armitage, P. J., Mamatsashvili, G. R., Lodato, G., & Clarke, C. J. 2011, *Mon. Not. Roy. Astron. Soc.*, 418, 1356

Rice, W. K. M., Lodato, G., & Armitage, P. J. 2005, *Mon. Not. Roy. Astron. Soc.*, 364, L56

Rice, W. K. M., Lodato, G., Pringle, J. E., Armitage, P. J., & Bonnell, I. A. 2004, *Mon. Not. Roy. Astron. Soc.*, 355, 543

Rice, W. K. M., Lodato, G., Pringle, J. E., Armitage, P. J., & Bonnell, I. A. 2006, *Mon. Not. Roy. Astron. Soc.*, 372, L9

Rodríguez, L. F., Loinard, L., D'Alessio, P., Wilner, D. J., & Ho, P. T. P. 2005, *Astrophys. J. Letters*, 621, L133

Rohlfs, K. & Wilson, T. 2000, Tools of Radio Astronomy (Springer), 168–173

Ros, K. & Johansen, A. 2013, in AAS/Division for Planetary Sciences Meeting Abstracts, Vol. 45, AAS/Division for Planetary Sciences Meeting Abstracts #45, 510.03

Ros, K., Johansen, A., Riipinen, I., & Schlesinger, D. 2019, *Astron. Astrophys.*, 629, A65

Rosotti, G. P., Juhasz, A., Booth, R. A., & Clarke, C. J. 2016, *Mon. Not. Roy. Astron. Soc.*, 459, 2790

Ruden, S. P. 1995, *Astrophys. Space Sci.*, 223, 57

Ruíz-Rodríguez, D., Cieza, L. A., Williams, J. P., et al. 2018, *Mon. Not. Roy. Astron. Soc.*, 478, 3674

Ryle, M. & Hewish, A. 1960, *Mon. Not. Roy. Astron. Soc.*, 120, 220

Safronov, V. S. & Zvjagina, E. V. 1969, *Icarus*, 10, 109

Saito, E. & Sirono, S.-i. 2011, *Astrophys. J.*, 728, 20

Salpeter, E. E. 1955, *Astrophys. J.*, 121, 161

Schneider, P. C., France, K., Günther, H. M., et al. 2015, *Astron. Astrophys.*, 584, A51

Schräpler, R. & Blum, J. 2011, *Astrophys. J.*, 734, 108

Schräpler, R., Blum, J., Krijt, S., & Raabe, J.-H. 2018, *Astrophys. J.*, 853, 74

Schräpler, R., Blum, J., Seizinger, A., & Kley, W. 2012, *Astrophys. J.*, 758, 35

Schwab, F. R. 1984, *Astron. J.*, 89, 1076

Seizinger, A., Krijt, S., & Kley, W. 2013, *Astron. Astrophys.*, 560, A45

Semenov, D., Henning, T., Helling, C., Ilgner, M., & Sedlmayr, E. 2003, *Astron. Astrophys.*, 410, 611

Shakura, N. I. & Sunyaev, R. A. 1973, *Astron. Astrophys.*, 500, 33

Sheehan, P. D. & Eisner, J. A. 2018, *Astrophys. J.*, 857, 18

Shen, B.-T., Tang, Y.-W., & Koch, P. M. 2020, *Astrophys. J.*, 904, 125

Siess, L., Dufour, E., & Forestini, M. 2000, *Astron. Astrophys.*, 358, 593

Simon, J. B. & Armitage, P. J. 2014, *Astrophys. J.*, 784, 15

Simon, T., Ayres, T. R., Redfield, S., & Linsky, J. L. 2002, *Astrophys. J.*, 579, 800

Snell, R. L., Loren, R. B., & Plambeck, R. L. 1980, *Astrophys. J.*, 239, L17

Sod, G. A. 1978, Journal of Computational Physics, 27, 1

Springel, V. 2005, *Mon. Not. Roy. Astron. Soc.*, 364, 1105

Springel, V. & Hernquist, L. 2002, *Mon. Not. Roy. Astron. Soc.*, 333, 649

Stamatellos, D. & Whitworth, A. P. 2009a, *Mon. Not. Roy. Astron. Soc.*, 392, 413

Stamatellos, D. & Whitworth, A. P. 2009b, *Mon. Not. Roy. Astron. Soc.*, 400, 1563

Stamatellos, D., Whitworth, A. P., Bisbas, T., & Goodwin, S. 2007, *Astron. Astrophys.*, 475, 37

Stamatellos, D., Whitworth, A. P., Boyd, D. F. A., & Goodwin, S. P. 2005a, *Astron. Astrophys.*, 439, 159

Stamatellos, D., Whitworth, A. P., & Goodwin, S. P. 2005b, Astronomische Nachrichten, 326, 882

Stammler, S. M., Birnstiel, T., Panić, O., Dullemond, C. P., & Dominik, C. 2017, *Astron. Astrophys.*, 600, A140

Stepinski, T. F. & Valageas, P. 1996, *Astron. Astrophys.*, 309, 301

Stevenson, D. J. & Lunine, J. I. 1988, *Icarus*, 75, 146

Stoehr, F., Murphy, E., Lacy, M., et al. 2020, ALMA Doc 8.15, 1

Suriano, S. S., Li, Z.-Y., Krasnopolsky, R., & Shang, H. 2017a, *Mon. Not. Roy. Astron. Soc.*, 468, 3850

Suriano, S. S., Li, Z.-Y., Krasnopolsky, R., & Shang, H. 2017b, *Mon. Not. Roy. Astron. Soc.*, 468, 3850

Takahashi, S. Z. & Inutsuka, S.-i. 2016, *Astron. J.*, 152, 184

Tang, Y.-W., Guilloteau, S., Dutrey, A., et al. 2017, *Astrophys. J.*, 840, 32

Tang, Y. W., Guilloteau, S., Piétu, V., et al. 2012, *Astron. Astrophys.*, 547, A84

Tanii, R., Itoh, Y., Kudo, T., et al. 2012, *Pub. Astron. Soc. Japan*, 64, 124

Teiser, J., Küpper, M., & Wurm, G. 2011, *Icarus*, 215, 596

Teiser, J. & Wurm, G. 2009a, *Astron. Astrophys.*, 505, 351

Teiser, J. & Wurm, G. 2009b, *Mon. Not. Roy. Astron. Soc.*, 393, 1584

Testi, L., Birnstiel, T., Ricci, L., et al. 2014, in Protostars and Planets VI, ed. H. Beuther, R. Klessen, C. Dullemond, & T. Hennings (Univeristy of Arizona Press), 339–361

Testi, L., Natta, A., Shepherd, D. S., & Wilner, D. J. 2003, *Astron. Astrophys.*, 403, 323

Thompson, R. A. 1989, in Astronomical Society of the Pacific Conference Series, Vol. 6, Synthesis Imaging in Radio Astronomy, ed. R. A. Perley, F. R. Schwab, & A. H. Bridle, 11–34

Tohline, J. E. 1982, *Fundamentals of Cosmic Physic*, 8, 1

Tomley, L., Steiman-Cameron, T. Y., & Cassen, P. 1994, *Astrophys. J.*, 422, 850

Toomre, A. 1964, *Astrophys. J.*, 139, 1217

Tripathi, A., Andrews, S. M., Birnstiel, T., & Wilner, D. J. 2017, *Astrophys. J.*, 845, 44

Tsukagoshi, T., Momose, M., Kitamura, Y., et al. 2019, *Astrophys. J.*, 871, 5

Tsukamoto, Y., Takahashi, S. Z., Machida, M. N., & Inutsuka, S. 2015, *Mon. Not. Roy. Astron. Soc.*, 446, 1175

Tuthill, P. G., Monnier, J. D., & Danchi, W. C. 2001, *Nature*, 409, 1012

Ubeira Gabellini, M. G., Miotello, A., Facchini, S., et al. 2019, *Mon. Not. Roy. Astron. Soc.*, 486, 4638

Uribe, A. L., Klahr, H., Flock, M., & Henning, T. 2011, *Astrophys. J.*, 736, 85

van Cittert, P. H. 1934, *Physica*, 1, 201

van den Ancker, M. E., The, P. S., Tjin A Djie, H. R. E., et al. 1997, *Astron. Astrophys.*, 324, L33

van der Marel, N., Birnstiel, T., Garufi, A., et al. 2020, arXiv e-prints

van der Marel, N., Dong, R., di Francesco, J., Williams, J. P., & Tobin, J. 2019, *Astrophys. J.*, 872, 112

van der Marel, N., van Dishoeck, E. F., Bruderer, S., et al. 2016a, *Astron. Astrophys.*, 585, A58

van der Marel, N., van Dishoeck, E. F., Bruderer, S., et al. 2013, Science, 340, 1199

van der Marel, N., van Dishoeck, E. F., Bruderer, S., Pérez, L., & Isella, A. 2015, *Astron. Astrophys.*, 579, A106

van der Marel, N., van Dishoeck, E. F., Bruderer, S., et al. 2016b, in Young Stars & Planets Near the Sun, ed. J. H. Kastner, B. Stelzer, & S. A. Metchev, Vol. 314, 139–142

van der Plas, G., Ménard, F., Canovas, H., et al. 2017, *Astron. Astrophys.*, 607, A55

van Leeuwen, F. 2007, *Astron. Astrophys.*, 474, 653

van Terwisga, S. E., van Dishoeck, E. F., Ansdell, M., et al. 2018, *Astron. Astrophys.*, 616, A88

van Terwisga, S. E., van Dishoeck, E. F., Mann, R. K., et al. 2020, *Astron. Astrophys.*, 640, A27

Voelk, H. J., Jones, F. C., Morfill, G. E., & Roeser, S. 1980, *Astron. Astrophys.*, 85, 316

Vorobyov, E. I. & Basu, S. 2015, *Astrophys. J.*, 805, 115

Wagner, K., Apai, D., Kasper, M., et al. 2016, Science, 353, 673

Wagner, K., Apai, D., Kasper, M., & Robberto, M. 2015, *Astrophys. J. Letters*, 813, L2

Wagner, K., Dong, R., Sheehan, P., et al. 2018, *Astrophys. J.*, 854, 130

Wagner, K., Stone, J. M., Spalding, E., et al. 2019, *Astrophys. J.*, 882, 20

Wahhaj, Z., Cieza, L., Koerner, D. W., et al. 2010, *Astrophys. J.*, 724, 835

Walker, C. K., Lada, C. J., Young, E. T., & Margulis, M. 1988, *Astrophys. J.*, 332, 335

Ward-Thompson, D., Scott, P. F., Hills, R. E., & Andre, P. 1994, *Mon. Not. Roy. Astron. Soc.*, 268, 276

Weidenschilling, S. 1977, *Mon. Not. Roy. Astron. Soc.*, 180, 57

Weidenschilling, S. J. 1980, *Icarus*, 44, 172

Weidenschilling, S. J. & Cuzzi, J. N. 1993, in Protostars and Planets III, ed. E. H. Levy & J. I. Lunine, 1031

Weidling, R. & Blum, J. 2015, *Icarus*, 253, 31

Weidling, R., Güttler, C., & Blum, J. 2012, *Icarus*, 218, 688

Weidling, R., Güttler, C., Blum, J., & Brauer, F. 2009, *Astrophys. J.*, 696, 2036

Weintraub, D. A., Sandell, G., & Duncan, W. D. 1989, *Astrophys. J. Letters*, 340, L69

Whipple, F. L. 1972, in From Plasma to Planet, ed. A. Elvius, 211

White, R. J., Ghez, A. M., Reid, I. N., & Schultz, G. 1999, *Astrophys. J.*, 520, 811

Whitworth, A. P. & Stamatellos, D. 2006, *Astron. Astrophys.*, 458, 817

Whizin, A. D., Blum, J., & Colwell, J. E. 2017, *Astrophys. J.*, 836, 94

Wilking, B. A., Gagné, M., & Allen, L. E. 2008, Star Formation in the ρ Ophiuchi Molecular Cloud, ed. B. Reipurth, Vol. 5, 351

Wilking, B. A., Lada, C. J., & Young, E. T. 1989, *Astrophys. J.*, 340, 823

Williams, J. P. & Best, W. M. J. 2014, *Astrophys. J.*, 788, 59

Windmark, F., Birnstiel, T., Guttler, C., et al. 2012, *Astron. Astrophys.*, 540, A73

Windmark, F., Birnstiel, T., Ormel, C. W., & Dullemond, C. P. 2012, *Astron. Astrophys.*, 544, L16

Wolszczan, A. & Frail, D. A. 1992, *Nature*, 355, 145

Wright, E. L. 1987, *Astrophys. J.*, 320, 818

Wurm, G., Paraskov, G., & Krauss, O. 2005, *Phys. Rev. E*, 71, 021304

Wurm, G., Paraskov, G., & Krauss, O. 2005, *Icarus*, 178, 253

Yang, C. C., Johansen, A., & Carrera, D. 2017, *Astron. Astrophys.*, 606, A80

Youdin, A. N. & Goodman, J. 2005, *Astrophys. J.*, 620, 459

Youdin, A. N. & Shu, F. H. 2002, *Astrophys. J.*, 580, 494

Zernike, F. 1938, *Physica*, 5, 785

Zhang, K., Blake, G. A., & Bergin, E. A. 2015, *Astrophys. J. Letters*, 806, L7

Zhu, Z., Dong, R., Stone, J. M., & Rafikov, R. R. 2015, *Astrophys. J.*, 813, 88

Zhu, Z., Nelson, R. P., Dong, R., Espaillat, C., & Hartmann, L. 2012, *Astrophys. J.*, 755, 6

Zhu, Z., Nelson, R. P., Hartmann, L., Espaillat, C., & Calvet, N. 2011, *Astrophys. J.*, 729, 47

Zhu, Z., Stone, J. M., Rafikov, R. R., & Bai, X.-n. 2014, *Astrophys. J.*, 785, 122

Zinnecker, H. & Yorke, H. W. 2007, *Ann. Rev. Astron, Astrophys.*, 45, 481

Zsom, A., Ormel, C. W., Dullemond, C. P., & Henning, T. 2011, *Astron. Astrophys.*, 534, A73

Zsom, A., Ormel, C. W., Güttler, C., Blum, J., & Dullemond, C. P. 2010, *Astron. Astrophys.*, 513, A57

Zubko, V., Dwek, E., & Arendt, R. G. 2004, *Astrophys. J. Supple.*, 152, 211

Appendix A

Protoplanetary Disc Taxonomy with ALMA

A.1 Complete list of Discs

The ALMA archive has been searched for protoplanetary discs that feature substructure in the millimetre dust continuum. Only discs observed during Cycles 0–5 were looked at. Table A.1 lists the complete sample of discs looked at in this work.

Table A.1: The complete sample of the ALMA observations we have looked at in our search for protoplanetary discs with substructure. Observations were taken during Cycles 0–5 and the ALMA project code are given. We have listed major star forming regions only; explanations of the initials can be found in the table notes. All distances have been obtained from Gaia DR2 (Gaia Collaboration et al. 2018), unless otherwise stated.

ID #	Name[†]	Distance (pc)	SFR[††]	Res. (")	Project Code
1	* q01 Eri	17± 1	-	0.42	2015.1.00307.S
2	* tau Cet	4± 1	-	0.99	2013.1.00588.S
3	LSPM J0343+1958	21± 1	-	0.54	2015.1.00783.S

Table A.1: - continued.

ID #	Name†	Distance (pc)	SFR††	Res. (")	Project Code
4	Wolf 219	19± 1	-	0.54	2015.1.00783.S
5	LP 413-40	182± 3	-	0.54	2015.1.00783.S
6	HZ 10	34± 1	-	0.54	2015.1.00783.S
7	J04215810+2826300	631± 60	-	0.14	2013.1.00498.S
8	UCAC2 40978291	1404± 105	-	0.64	2012.1.00350.S
9	[XCR2012] TrES J043145+285909	484± 9	-	0.64	2012.1.00350.S
10	J05382310-0236269	1247± 113	-	0.24	2015.1.00089.S
11	[HHM2007] 852	908± 210	-	0.24	2015.1.00089.S
12	HD 38858	15± 1	-	0.63	2015.1.00307.S
13	HD 44627	50± 1	-	0.15	2015.1.01210.S
14	V* Z CMa	233± 48	-	0.05	2016.1.00110.S
15	HD 54341	101± 1	-	0.52	2015.1.00716.S
16	HD 61005	36± 1	-	0.45	2015.1.00633.S
17	HD 305539	3106± 289	-	0.02	2015.1.01323.S
18	HD 98922	691± 16	-	0.68	2015.1.01600.S
19	HD 107146	27± 1	-	0.35	2016.1.00104.S
20	* 61 Vir	9± 1	-	0.63	2013.1.00359.S
21	LAWD 50	60± 1	-	0.69	2015.1.00783.S
22	V* QS Vir	50± 1	-	0.69	2015.1.00783.S
23	PG 1350-090	20± 1	-	0.69	2015.1.00783.S
24	SDSS J135523.91+085645.4	642± 71	-	0.66	2016.1.01055.S
25	EC 14012-1446	60± 1	-	0.69	2015.1.00783.S
26	SDSS J141134.70+102839.7	753± 395	-	0.66	2016.1.01055.S
27	V* GK Vir	475± 28	-	0.66	2016.1.01055.S
28	LBQS 1437-0053	519± 32	-	0.66	2016.1.01055.S
29	HD 131488	155± 2	-	0.52	2015.1.01243.S
30	* g Lup	17± 1	-	0.48	2015.1.00307.S
31	J15430227-3444059	18519± 89163	-	0.28	2013.1.00220.S

Table A.1: - continued.

ID #	Name†	Distance (pc)	SFR††	Res. (")	Project Code
32	V* NN Ser	522± 27	-	0.99	2016.1.01055.S
33	THA 15-8	2304± 287	-	0.28	2013.1.00220.S
34	THA 15-9	2257± 204	-	0.28	2013.1.00220.S
35	IRAS 15563-4146	5988± 3980	-	0.28	2013.1.00220.S
36	J16070863-3947219	4762± 658	-	0.28	2013.1.00220.S
37	HD 164249	50± 1	-	0.20	2013.1.01147.S
38	HD 319139	72± 1	-	0.54	2011.0.00084.S
39	HD 169142	114± 1	-	0.13	2012.1.00799S
40	HD 172555	28± 1	-	0.20	2013.1.01147.S
41	HD 181327	48± 1	-	0.13	2013.1.00025.S
42	HD 202628	24± 1	-	0.64	2016.1.00515.S
43	HD 207129	16± 1	-	0.49	2015.1.00307.S
44	NGC 7293	201± 3	-	0.24	2015.1.00762.S
45	* kap And	50± 1	-	0.14	2015.1.01210.S
46	V* RW Aur	65± 15.5*	-	0.15	2015.1.01506.S
47	* bet Leo	11± 0.1*	-	0.48	2015.1.00676.S
48	EM* AS 220	237± 24.2*	-	0.51	2015.1.01600.S
49	* alf PsA	8± 0.1*	-	0.38	2011.0.00191.S
50	J18191220-2047297	1900*	-	0.03	2015.1.00480.S
51	GAL 035.03+00.35	3490*	-	0.38	2011.0.00275.S
52	MSX5C G023.0126-00.4177	4590*	-	0.15	2015.1.00615.S
53	IRAS 13481-6124	3600*	-	0.03	2016.1.01504.S
54	J15354856-2958551	-	-	0.28	2013.1.00395.S
55	WRAY 16-23	900*	-	0.66	2016.1.01055.S
56	Parsamian 21	400*	-	0.14	2015.1.01067.S
57	hd97048	185± 1	-	0.03	2016.1.00826.S
58	HD 142527	157± 1	-	0.14	2012.1.00631.S
59	J18572247-3734427	2309± 288	-	0.26	2015.1.01058.S
60	J18593428-3721410	1575± 201	-	0.26	2015.1.01058.S
61	HD 14082B	40± 1	βP	0.21	2013.1.01147.S

Table A.1: - continued.

ID #	Name†	Distance (pc)	SFR††	Res. (")	Project Code
62	HD 15115	49± 1	βP	0.45	2015.1.00633.S
63	BD+30 397	41± 1	βP	0.21	2013.1.01147.S
64	* 51 Eri	30± 1	βP	0.15	2016.1.00358.S
65	* bet Pic	20± 1	βP	0.49	2011.0.00087.S
66	* eta Tel	47± 1	βP	0.15	2013.1.01147.S
67	V* PZ Tel	47± 1	βP	0.17	2015.1.01210.S
68	WRAY 15-1880	154± 1	CA	0.14	2015.1.01083.S
69	J18521730-3700119	146± 1	CA	0.14	2015.1.01083.S
70	J18563974-3707205	159± 5	CA	0.26	2015.1.01058.S
71	J18564024-3655203	149± 3	CA	0.26	2015.1.01058.S
72	W J1858509-370631	155± 8	CA	0.26	2015.1.01058.S
73	J19002906-3656036	155± 9	CA	0.64	2011.0.00733.S
74	J19005804-3645048	153± 1	CA	0.60	2011.0.00733.S
75	J19005974-3647109	144± 6	CA	0.26	2015.1.01058.S
76	J19011149-3645337	154± 5	CA	0.26	2015.1.01058.S
77	V* V667 CrA	156± 3	CA	0.26	2015.1.01058.S
78	J19011893-3658282	149± 5	CA	0.26	2015.1.01058.S
79	J19012901-3701484	153± 2	CA	0.64	2011.0.00733.S
80	HD 176386	159± 2	CA	0.26	2015.1.01058.S
81	V* TY CrA	136± 3	CA	0.26	2015.1.01058.S
82	J19015374-3700339	147± 6	CA	0.26	2015.1.01058.S
83	V* DG CrA	157± 5	CA	0.26	2015.1.01058.S
84	J19021201-3703093	159± 4	CA	0.26	2015.1.01058.S
85	J19021667-3645493	155± 3	CA	0.26	2015.1.01058.S
86	SSTgbs J1902330-365821	139± 4	CA	0.26	2015.1.01058.S
87	ISO-CrA 177	282± 39	CA	0.26	2015.1.01058.S
88	VSST 10	164± 8	CA	0.26	2015.1.01058.S
89	J19032429-3715076	148± 35	CA	0.26	2015.1.01058.S
90	J19032547-3655051	154± 4	CA	0.26	2015.1.01058.S
91	V* V721 CrA	155± 2	CA	0.24	2015.1.01301.S

Table A.1: - continued.

ID #	Name†	Distance (pc)	SFR††	Res. (")	Project Code
92	J18570785-3654041	148**	CA	0.26	2015.1.01058.S
93	[QZM2013] MM3	148**	CA	0.38	2011.0.00275.S
94	[WGL92] iras 10	148**	CA	0.26	2015.1.01058.S
95	[LEM2005b] CrA 444b	148**	CA	0.26	2015.1.01058.S
96	V* S CrA	148**	CA	0.26	2015.1.01058.S
97	HH 730A	148**	CA	0.26	2015.1.01058.S
98	J19013232-3658030	148**	CA	0.26	2015.1.01058.S
99	J19013385-3657448	148**	CA	0.26	2015.1.01058.S
100	MHO 2008	148**	CA	0.26	2015.1.01058.S
101	J19014041-3651422	148**	CA	0.26	2015.1.01058.S
102	J19015180-3710478	148**	CA	0.26	2015.1.01058.S
103	AX 1858.4-3700	148**	CA	0.26	2015.1.01058.S
104	J19015173-3655143	148**	CA	0.26	2015.1.01058.S
105	J19015112-3654122	148**	CA	0.26	2015.1.01058.S
106	[SHK2011b] 9	148**	CA	0.26	2015.1.01058.S
107	V* T CrA	148**	CA	0.26	2015.1.01058.S
108	J19020410-3657013	148**	CA	0.26	2015.1.01058.S
109	J19020682-3658411	148**	CA	0.26	2015.1.01058.S
110	J19021464-3700328	148**	CA	0.26	2015.1.01058.S
111	J19022708-3658132	148**	CA	0.26	2015.1.01058.S
112	J19031185-3709020	148**	CA	0.60	2011.0.00733.S
113	J19041725-3659030	148**	CA	0.26	2015.1.01058.S
114	V* DX Cha	108± 1	Ch	0.20	2013.1.00592.S
115	IRAS 12535-7623	160± 11	Ch	0.21	2013.1.00708.S
116	SZ 49	195± 2	Ch	0.21	2013.1.00708.S
117	SZ 50	147± 13	Ch	0.21	2013.1.00708.S
118	V* SX Cha	196**	Ch	0.35	2013.1.00437.S
119	SZ 4	196**	Ch	0.35	2013.1.00437.S
120	CHXR 9C	196**	Ch	0.37	2013.1.01075.S
121	HH 48	196**	Ch	0.28	2016.1.00460.S

Table A.1: - continued.

ID	Name[†]	Distance	SFR[††]	Res.	Project
#		(pc)		(")	Code
122	Hn 4	196**	Ch	0.37	2013.1.01075.S
123	CHXR 15	196**	Ch	0.37	2013.1.01075.S
124	J11062942-7724586	196**	Ch	0.35	2013.1.00437.S
125	[CCE98] 2-21	196**	Ch	0.35	2013.1.00437.S
126	HH 927	196**	Ch	0.37	2013.1.01075.S
127	V* VV Cha	196**	Ch	0.35	2013.1.00437.S
128	V* HK Cha	196**	Ch	0.35	2013.1.00437.S
129	Glass H	196**	Ch	0.37	2013.1.01075.S
130	V* VW Cha	196**	Ch	0.35	2013.1.00437.S
131	ESO-HA 562	196**	Ch	0.35	2013.1.00437.S
132	V* HP Cha	196**	Ch	0.02	2017.1.01460.S
133	J11082570-7716396	196***	Ch	0.35	2013.1.00437.S
134	V* HU Cha	196**	Ch	0.35	2013.1.00437.S
135	V* HX Cha	196**	Ch	0.35	2013.1.00437.S
136	V* WX Cha	196**	Ch	0.35	2013.1.00437.S
137	OTS 44	196**	Ch	0.61	2015.1.00243.S
138	Glass Q	196**	Ch	0.35	2013.1.00437.S
139	ESO-HA 569	196**	Ch	0.35	2013.1.00437.S
140	CHX 18	196**	Ch	0.37	2013.1.01075.S
141	J11160287-7624533	196**	Ch	0.35	2013.1.00437.S
142	J11175211-7629392	196**	Ch	0.37	2013.1.00437.S
143	CHXR 68	196**	Ch	0.37	2013.1.01075.S
144	IRAS F11171-7919	209**	Ch	0.37	2013.1.00437.S
145	J12534285-7715114	209**	Ch	0.21	2013.1.00708.S
146	J12580676-7709094	209**	Ch	0.21	2013.1.00708.S
147	SSTc2d J130529.0-774140	209**	Ch	0.21	2013.1.00708.S
148	V* BK Cha	209**	Ch	0.21	2013.1.00708.S
149	SZ 62	209**	Ch	0.21	2013.1.00708.S
150	J10533978-7712338	192± 4	Ch	0.35	2013.1.00437.S
151	J10561638-7630530	196± 4	Ch	0.37	2013.1.00437.S

Table A.1: - continued.

ID	Name[†]	Distance	SFR[††]	Res.	Project
#		(pc)		(")	Code
152	V* SY Cha	183± 1	Ch	0.35	2013.1.00437.S
153	J10580597-7711501	187± 4	Ch	0.35	2013.1.00437.S
154	V* SZ Cha	190± 1	Ch	0.35	2013.1.00437.S
155	V* TW Cha	185± 1	Ch	0.35	2013.1.00437.S
156	Hen 3-545	187± 1	Ch	0.35	2013.1.00437.S
157	Ass Cha T 1-6	192± 2	Ch	0.37	2013.1.00437.S
158	V* CS Cha	176± 1	Ch	0.03	2017.1.00969.S
159	Hn 1	195± 6	Ch	0.35	2013.1.00437.S
160	Ass Cha T 1-8	182± 2	Ch	0.35	2013.1.00437.S
161	CHSM 1715	192± 3	Ch	0.37	2013.1.00437.S
162	V* CT Cha	192± 1	Ch	0.35	2013.1.00437.S
163	BYB 18	193± 3	Ch	0.37	2013.1.00437.S
164	SZ 13	194± 3	Ch	0.35	2013.1.00437.S
165	J11062554-7633418	209± 5	Ch	0.37	2013.1.00437.S
166	CHXR 73	191± 6	Ch	0.37	2013.1.01075.S
167	CHSM 7869	187± 7	Ch	0.37	2013.1.00437.S
168	ISO-ChaI 79	205± 22	Ch	0.35	2013.1.00437.S
169	Hn 5	195± 2	Ch	0.35	2013.1.00437.S
170	V* UX Cha	185± 1	Ch	0.35	2013.1.00437.S
171	V* UY Cha	190± 2	Ch	0.35	2013.1.00437.S
172	J11065939-7530559	196± 4	Ch	0.37	2013.1.00437.S
173	V* UZ Cha	196± 1	Ch	0.35	2013.1.00437.S
174	CHSM 9484	199± 4	Ch	0.35	2013.1.00437.S
175	[CCE98] 1-46	173± 7	Ch	0.35	2013.1.00437.S
176	[NC98] Cha HA 9	199± 12	Ch	0.35	2013.1.00437.S
177	V* DI Cha	191± 1	Ch	0.35	2013.1.00437.S
178	CHXR 76	189± 3	Ch	0.42	2012.1.00350.S
179	Ass Cha T 1-15	195± 2	Ch	0.35	2013.1.00437.S
180	J11074656-7615174	194± 7	Ch	0.37	2013.1.00437.S
181	SZ 23	184± 2	Ch	0.35	2013.1.00437.S

Table A.1: - continued.

ID #	Name†	Distance (pc)	SFR††	Res. (")	Project Code
182	Ass Cha T 1-16	163± 8	Ch	0.35	2013.1.00437.S
183	V* HM Cha	187± 12	Ch	0.35	2013.1.00437.S
184	CHXR 30A	253± 26	Ch	0.35	2013.1.00437.S
185	ISO-ChaI 138	186± 7	Ch	0.35	2013.1.00437.S
186	ISO-ChaI 143	193± 5	Ch	0.35	2013.1.00437.S
187	ISO-ChaI 147	200± 8	Ch	0.35	2013.1.00437.S
188	V* HQ Cha	179± 4	Ch	0.35	2013.1.00437.S
189	Ass Cha T 1-20	188± 2	Ch	0.35	2013.1.00437.S
190	SZ 28	193± 3	Ch	0.35	2013.1.00437.S
191	V* PU Car	188± 1	Ch	0.35	2013.1.00437.S
192	V* VY Cha	186± 2	Ch	0.35	2013.1.00437.S
193	V* HS Cha	195± 4	Ch	0.35	2013.1.00437.S
194	NAME Sz 30A	197± 5	Ch	0.37	2013.1.01075.S
195	V* HV Cha	203± 8	Ch	0.35	2013.1.00437.S
196	V* VZ Cha	192± 1	Ch	0.35	2013.1.00437.S
197	HJM C 7-1	188± 6	Ch	0.35	2013.1.00437.S
198	HJM C 1-24	195± 3	Ch	0.35	2013.1.00437.S
199	BYB 43	193± 5	Ch	0.35	2013.1.00437.S
200	HD 97300	193± 1	Ch	0.37	2013.1.01075.S
201	ISO-ChaI 220	186± 16	Ch	0.35	2013.1.00437.S
202	ISO-ChaI 217	240± 13	Ch	0.35	2013.1.00437.S
203	Ass Cha T 1-23	202± 6	Ch	0.35	2013.1.00437.S
204	V* WW Cha	192± 1	Ch	0.35	2013.1.00437.S
205	V* FN Cha	195± 1	Ch	0.35	2013.1.00437.S
206	HJM C 1-4	201± 3	Ch	0.35	2013.1.00437.S
207	J11100785-7727480	200± 13	Ch	0.35	2013.1.00437.S
208	V* WY Cha	180± 9	Ch	0.35	2013.1.00437.S
209	HJM C 1-8	195± 2	Ch	0.35	2013.1.00437.S
210	ISO-ChaI 252	204± 12	Ch	0.35	2013.1.00437.S
211	Ass Cha T 1-27	185± 1	Ch	0.35	2013.1.00437.S

Table A.1: - continued.

ID #	Name†	Distance (pc)	SFR††	Res. (")	Project Code
212	V* IK Cha	196± 11	Ch	0.35	2013.1.00437.S
213	V* WZ Cha	195± 1	Ch	0.35	2013.1.00437.S
214	HJM C 2-5	140± 14	Ch	0.35	2013.1.00437.S
215	V* XX Cha	191± 1	Ch	0.35	2013.1.00437.S
216	CHX 18N	193± 1	Ch	0.35	2013.1.00437.S
217	V* IM Cha	185± 4	Ch	0.37	2013.1.00437.S
218	SZ 40	193± 2	Ch	0.35	2013.1.00437.S
219	SZ 41	194± 1	Ch	0.35	2013.1.00437.S
220	V* CV Cha	193± 1	Ch	0.35	2013.1.00437.S
221	V* CW Cha	196± 2	Ch	0.35	2013.1.00437.S
222	Ass Cha T 2-54	202± 17	Ch	0.42	2012.1.00350.S
223	HJM E 2-9	191± 2	Ch	0.35	2013.1.00437.S
224	Hn 18	190± 2	Ch	0.35	2013.1.00437.S
225	Hn 21W	189± 3	Ch	0.37	2013.1.00437.S
226	Hn 21	189± 3	Ch	0.37	2013.1.01075.S
227	BYB 53	194± 7	Ch	0.37	2013.1.01075.S
228	Ass Cha T 1-32	188± 1	Ch	0.35	2013.1.00437.S
229	J11241186-7630425	185± 2	Ch	0.37	2013.1.00437.S
230	[FLG2003] eps Cha 17	181± 18	Ch	0.37	2013.1.00437.S
231	V* T Cha	110± 1	Ch	0.13	2012.2.00182.S
232	V* DK Cha	244± 22	Ch	0.21	2013.1.00708.S
233	NAME Sz 46N	196± 2	Ch	0.21	2013.1.00708.S
234	J13005927-7714027	220± 10	Ch	0.21	2013.1.00708.S
235	SZ 51	199± 1	Ch	0.21	2013.1.00708.S
236	V* CM Cha	194± 1	Ch	0.21	2013.1.00708.S
237	J13022287-7734494	205± 4	Ch	0.21	2013.1.00708.S
238	SZ 52	204± 3	Ch	0.21	2013.1.00708.S
239	Hn 22	199± 1	Ch	0.21	2013.1.00708.S
240	Hn 24	197± 1	Ch	0.21	2013.1.00708.S
241	Hn 25	197± 3	Ch	0.21	2013.1.00708.S

Table A.1: - continued.

ID	Name[†]	Distance	SFR[††]	Res.	Project
#		(pc)		(")	Code
242	SZ 53	197± 2	Ch	0.21	2013.1.00708.S
243	Hen 3-854	197± 1	Ch	0.21	2013.1.00708.S
244	J13052169-7738102	202± 5	Ch	0.21	2013.1.00708.S
245	SZ 56	191± 2	Ch	0.21	2013.1.00708.S
246	SZ 58	186± 2	Ch	0.21	2013.1.00708.S
247	J13071806-7740529	199± 5	Ch	0.21	2013.1.00708.S
248	Hn 26	198± 3	Ch	0.21	2013.1.00708.S
249	V* BM Cha	202± 2	Ch	0.21	2013.1.00708.S
250	J13082714-7743232	205± 6	Ch	0.21	2013.1.00708.S
251	SZ 63	202± 1	Ch	0.21	2013.1.00708.S
252	Cl* Trumpler 14 VBF 125	3000**	CN	0.02	2015.1.01323.S
253	[SBM2003] J104405.4-592940	3000**	CN	0.02	2015.1.01323.S
254	[GG2014] 230	3000**	CN	0.02	2015.1.01323.S
255	HD 21997	70± 1	Co	0.98	2011.0.00780.S
256	HD 100453	104± 1	DC	0.03	2017.1.01424.S
257	HD 100546	110± 1	DC	0.03	2015.1.00806.S
258	V* EH Cha	99± 1	ηC	0.42	2012.1.00350.S
259	V* EI Cha	100± 1	ηC	0.52	2012.1.00350.S
260	V* ET Cha	92± 3	ηC	0.40	2011.0.00133.S
261	NAME IC 2162 IR Cluster	200000**	Ge	0.08	2015.1.00500.S
262	V* V471 Tau	48± 1	Hy	0.54	2015.1.00783.S
263	HG 7-85	42± 1	Hy	0.54	2015.1.00783.S
264	EGGR 29	50± 1	Hy	0.54	2015.1.00783.S
265	V* GW Ori	402± 11	λO	0.10	2017.1.00286.S
266	HD 121191	132± 1	LCC	0.50	2015.1.01243.S
267	HD 121617	117± 1	LCC	0.50	2015.1.01243.S
268	CD-40 8434	113± 1	LCC	0.05	2017.A.00006.S
269	SZ 66	157± 2	Lu	0.28	2013.1.00220.S
270	J15445789-3423392	153± 3	Lu	0.28	2013.1.00220.S
271	V* HW Lup	155± 2	Lu	0.28	2013.1.00220.S

Table A.1: - continued.

ID #	Name†	Distance (pc)	SFR††	Res. (")	Project Code
272	V* GW Lup	156± 1	Lu	0.02	2016.1.00484.L
273	V* HM Lup	156± 1	Lu	0.28	2013.1.00220.S
274	CD-35 10525	152± 1	Lu	0.14	2013.1.00374.S
275	[L2013] J155140.32-214610.6	142± 2	Lu	0.28	2013.1.00395.S
276	J15521088-2125372	168± 8	Lu	0.28	2013.1.00395.S
277	[L2013] J155301.32-211413.7	146± 3	Lu	0.28	2013.1.00395.S
278	NAME THA 15-10A	160± 2	Lu	0.28	2013.1.00220.S
279	THA 15-12	158± 1	Lu	0.39	2013.1.00226.S
280	V* RU Lup	160± 2	Lu	0.02	2016.1.00484.L
281	SZ 84	153± 2	Lu	0.28	2013.1.00220.S
282	WRAY 15-1400	162± 1	Lu	0.03	2016.1.00484.L
283	J15592523-4235066	147± 2	Lu	0.28	2013.1.00220.S
284	V* RY Lup	159± 2	Lu	0.14	2017.1.00449.S
285	J16000060-4221567	161± 2	Lu	0.28	2013.1.00220.S
286	J16000236-4222145	164± 2	Lu	0.28	2013.1.00220.S
287	J16002612-4153553	164± 3	Lu	0.60	2011.0.00733.S
288	SZ 130	160± 1	Lu	0.28	2013.1.00220.S
289	V* MY Lup	157± 1	Lu	0.60	2011.0.00733.S
290	SZ 131	160± 1	Lu	0.28	2013.1.00220.S
291	V* MZ Lup	191± 4	Lu	0.39	2012.1.00350.S
292	V* NO Lup	134± 1	Lu	0.39	2012.1.00350.S
293	HD 143675	139± 1	Lu	0.54	2015.1.01243.S
294	SZ 133	153± 13	Lu	0.28	2013.1.00220.S
295	V* HO Lup A	158± 1	Lu	0.28	2013.1.00220.S
296	J16070854-3914075	176± 13	Lu	0.28	2013.1.00220.S
297	THA 15-21	160± 1	Lu	0.28	2013.1.00220.S
298	THA 15-20	159± 2	Lu	0.13	2013.1.00663.S
299	J16073773-3921388	174± 5	Lu	0.28	2013.1.00220.S
300	SZ 95	158± 2	Lu	0.60	2011.0.00733.S
301	J16080017-3902595	160± 3	Lu	0.28	2013.1.00220.S

Table A.1: - continued.

ID #	Name†	Distance (pc)	SFR††	Res. (")	Project Code
302	SZ 96	157± 1	Lu	0.60	2011.0.00733.S
303	J16081497-3857145	146± 19	Lu	0.28	2013.1.00220.S
304	V* V1279 Sco	156± 1	Lu	0.28	2013.1.00220.S
305	THA 15-24	158± 2	Lu	0.28	2013.1.00220.S
306	THA 15-25	159± 2	Lu	0.28	2013.1.00220.S
307	THA 15-26	137± 3	Lu	0.28	2013.1.00220.S
308	THA 15-30	165± 2	Lu	0.28	2013.1.00220.S
309	IRAS 16051-3820	156± 1	Lu	0.28	2013.1.00220.S
310	V* V856 Sco	161± 2	Lu	0.47	2015.1.01600.S
311	V* V856 Sco	161± 2	Lu	0.28	2013.1.00220.S
312	SZ 107	152± 3	Lu	0.60	2011.0.00733.S
313	V* V1192 Sco	151± 14	Lu	0.28	2013.1.00220.S
314	V* V1193 Sco	160± 1	Lu	0.28	2013.1.00220.S
315	J16085373-3914367	134± 44	Lu	0.28	2013.1.00220.S
316	THA 15-33	158± 1	Lu	0.28	2013.1.00220.S
317	SZ 112	160± 2	Lu	0.60	2011.0.00733.S
318	J16085529-3848481	158± 3	Lu	0.28	2013.1.00220.S
319	THA 15-34	163± 2	Lu	0.28	2013.1.00220.S
320	J16090141-3925119	164± 2	Lu	0.60	2011.0.00733.S
321	THA 15-35	162± 1	Lu	0.28	2013.1.00220.S
322	SZ 115	158± 2	Lu	0.28	2013.1.00220.S
323	THA 15-37	159± 1	Lu	0.28	2013.1.00220.S
324	SZ 118	164± 1	Lu	0.28	2013.1.00220.S
325	SONYC Lup3-29	193± 7	Lu	0.28	2013.1.00220.S
326	J16101307-3846165	145± 5	Lu	0.28	2013.1.00220.S
327	J16101984-3836065	159± 3	Lu	0.28	2013.1.00220.S
328	J16102955-3922144	163± 2	Lu	0.60	2011.0.00733.S
329	J16104536-3854547	5435± 3072	Lu	0.28	2013.1.00220.S
330	NAME THA 15-42B	1497± 323	Lu	0.28	2013.1.00220.S
331	J16114865-3817580	1812± 263	Lu	0.28	2013.1.00220.S

Table A.1: - continued.

ID #	Name†	Distance (pc)	SFR††	Res. (")	Project Code
332	J16115979-3823383	165± 3	Lu	0.28	2013.1.00220.S
333	J16120445-3809589	4630± 14168	Lu	0.28	2013.1.00220.S
334	J16124373-3815031	160± 1	Lu	0.28	2013.1.00220.S
335	J16134410-3736462	160± 2	Lu	0.28	2013.1.00220.S
336	HD 145880	126± 1	Lu	0.54	2015.1.01243.S
337	WRAY 15-1443	158± 1	Lu	0.22	2011.0.00724.S
338	V1094 Sco	154± 1	Lu	0.17	2016.1.01239.S
339	CPD-36 6759	136± 1	Lu	0.35	2012.1.00870.S
340	NAME Lupus I	144**	Lu	0.28	2013.1.00220.S
341	J15450634-3417378	144**	Lu	0.28	2013.1.00220.S
342	[MHR2017] L1S2 9	144**	Lu	0.28	2013.1.00220.S
343	[DB2002b] G339.17+16.08	144**	Lu	0.28	2013.1.00220.S
344	DCld 339.0+15.0	144**	Lu	0.28	2013.1.00220.S
345	RX J1548.1-3515	144**	Lu	0.28	2013.1.00220.S
346	IRAS 15567-4141	144**	Lu	0.28	2013.1.00220.S
347	J16011549-4152351	144**	Lu	0.28	2013.1.00220.S
348	J16070384-3911113	144**	Lu	0.28	2013.1.00220.S
349	J16075475-3915446	144**	Lu	0.28	2013.1.00220.S
350	[G2006] 16	144**	Lu	0.28	2013.1.00220.S
351	J16080618-3912225	144**	Lu	0.28	2013.1.00220.S
352	[GMM2009] Lupus III 33	197**	Lu 3	0.28	2013.1.00220.S
353	THA 15-27	197**	Lu 3	0.60	2011.0.00733.S
354	[MJS2008] 52	197**	Lu 3	0.28	2013.1.00220.S
355	J16083156-3847292	197**	Lu 3	0.60	2011.0.00733.S
356	[G2006] 72	197**	Lu 3	0.28	2013.1.00220.S
357	[SC95] ZET 14	197**	Lu 3	0.28	2013.1.00220.S
358	J16085834-3907491	197**	Lu 3	0.28	2013.1.00220.S
359	J16091644-3904438	197**	Lu 3	0.28	2013.1.00220.S
360	[BPB2012] Lup3 C3	197**	Lu 3	0.28	2013.1.00220.S

Table A.1: - continued.

ID #	Name†	Distance (pc)	SFR††	Res. (")	Project Code
361	J16092032-3904015	197**	Lu 3	0.28	2013.1.00220.S
362	J16092317-3904074	197**	Lu 3	0.28	2013.1.00220.S
363	J16092697-3836269	197**	Lu 3	0.28	2013.1.00220.S
364	[MJS2008] 94	197**	Lu 3	0.28	2013.1.00220.S
365	[BPB2012] Lup3 C5	197**	Lu 3	0.28	2013.1.00220.S
366	J16095399-3923275	197**	Lu 3	0.60	2011.0.00733.S
367	J16095628-3859518	197**	Lu 3	0.28	2013.1.00220.S
368	J16102741-3902299	197**	Lu 3	0.28	2013.1.00220.S
369	J16121120-3832197	197**	Lu 3	0.28	2013.1.00220.S
370	J16122269-3713276	197**	Lu 3	0.28	2013.1.00220.S
371	WRAY 16-203	422± 96***	Lu	0.37	2012.1.00857.S
372	J16164198-3650456	38462± 178994***	Lu	0.77	2015.1.00791.S
373	J16232807-4015368	19231± 37721***	Lu	0.77	2015.1.00791.S
374	V* V1003 Oph	117± 1	Op	0.52	2011.0.00531.S
375	Hen 3-1258	124± 1	Op	0.03	2016.1.00484.L
376	EM* AS 209	121± 1	Op	0.15	2015.1.00486.S
377	Haro 1-16	146± 1	Op	0.23	2012.1.00158.S
378	J16230923-2417047	161± 1	Op	0.13	2013.1.00157.S
379	EM* SR 21A	138± 1	Op	0.23	2012.1.00158.S
380	[LMW2000] VLA 1623A	133**	Op	0.16	2015.1.00084.S
381	ROXs 12B	133**	Op	0.15	2015.1.00773.S
382	ROXs 12B	133**	Op	0.66	2016.1.01018.S
383	DoAr 26	133**	Op	0.30	2015.1.00637.S
384	EM* SR 24B	133**	Op	0.20	2013.1.00498.S
385	BKLT J162736-243020	133**	Op	0.13	2013.1.00100.S
386	[JJK2008] SMM J162740-24431	133**	Op	0.10	2016.1.01042.S
387	WLY 2-55	133**	Op	0.39	2012.1.00350.S

Table A.1: - continued.

ID #	Name†	Distance (pc)	SFR††	Res. (")	Project Code
388	GBS-VLA J163115.25-243313.8	133**	Op	0.49	2016.1.01018.S
389	J16313124-2426281	133**	Op	0.18	2016.1.00771.S
390	WSB 71	133**	Op	0.30	2015.1.00637.S
391	IRAS 16285-2355	133**	Op	0.02	2015.1.01512.S
392	NAME IRAS 16293-2422B	133**	Op	0.20	2013.1.00393.S
393	EM* SR 24S	114± 5	Op	0.14	2013.1.00091.S
394	V* V1366 Ori	312± 5	Or	0.14	2013.1.00658.S
395	HD 36112	160± 2	Or	0.29	2015.1.01600.S
396	V* V2377 Ori	912± 262	Or	0.43	2011.0.00028.S
397	[HHM2007] 81	376± 37	Or	0.24	2015.1.00089.S
398	J05375486-0241092	393± 19	Or	0.24	2015.1.00089.S
399	[BZR99] S Ori 35	415± 58	Or	0.24	2015.1.00089.S
400	[BZR99] S Ori 12	374± 29	Or	0.24	2015.1.00089.S
401	Haro 5-7	236± 22	Or	0.24	2015.1.00089.S
402	J05380097-0226079	349± 7	Or	0.24	2015.1.00089.S
403	J05380552-0235571	354± 58	Or	0.24	2015.1.00089.S
404	V* V1247 Ori	398± 10	Or	0.01	2015.1.00986.S
405	Kiso A-0976 316	397± 10	Or	0.24	2015.1.00089.S
406	Kiso A-0904 67	425± 8	Or	0.24	2015.1.00089.S
407	HD 294268	374± 7	Or	0.24	2015.1.00089.S
408	Kiso A-0976 326	392± 11	Or	0.24	2015.1.00089.S
409	J05382119-0254110	344± 16	Or	0.24	2015.1.00089.S
410	[W96] rJ053820-0234	343± 19	Or	0.24	2015.1.00089.S
411	V* V2725 Ori	378± 16	Or	0.24	2015.1.00089.S
412	V* V505 Ori	397± 6	Or	0.24	2015.1.00089.S
413	V* V2728 Ori	339± 41	Or	0.24	2015.1.00089.S
414	[BNM2013] 93.03 227	353± 18	Or	0.24	2015.1.00089.S
415	Haro 5-9	415± 6	Or	0.24	2015.1.00089.S
416	V* TX Ori	572± 85	Or	0.24	2015.1.00089.S

Table A.1: - continued.

ID #	Name†	Distance (pc)	SFR††	Res. (")	Project Code
417	[BNM2013] 93.03 29	402± 15	Or	0.24	2015.1.00089.S
418	[W96] rJ053833-0236	385± 32	Or	0.24	2015.1.00089.S
419	J05383902-0245321	428± 15	Or	0.24	2015.1.00089.S
420	J05384053-0233275	372± 14	Or	0.24	2015.1.00089.S
421	[BNM2013] 92.01 24	388± 12	Or	0.24	2015.1.00089.S
422	J05384386-0237068	385± 13	Or	0.24	2015.1.00089.S
423	V* V595 Ori A	212± 11	Or	0.24	2015.1.00089.S
424	Mayrit 89175	395± 20	Or	0.24	2015.1.00089.S
425	J05384818-0244007	428± 33	Or	0.24	2015.1.00089.S
426	** CAB 27B	502± 17	Or	0.24	2015.1.00089.S
427	[BHM2009] SigOri-MAD-34	404± 8	Or	0.24	2015.1.00089.S
428	[W96] pJ053847-0234	395± 14	Or	0.24	2015.1.00089.S
429	[BZR99] S Ori 15	364± 28	Or	0.24	2015.1.00089.S
430	J05384755-0227120	381± 15	Or	0.24	2015.1.00089.S
431	J05385060-0242429	399± 22	Or	0.24	2015.1.00089.S
432	J05384970-0234526	419± 20	Or	0.24	2015.1.00089.S
433	V* V2737 Ori	412± 52	Or	0.24	2015.1.00089.S
434	V* RU Ori	405± 5	Or	0.24	2015.1.00089.S
435	J05385831-0216101	399± 7	Or	0.24	2015.1.00089.S
436	ESO-HA 1693	371± 12	Or	0.24	2015.1.00089.S
437	J05390297-0241272	410± 14	Or	0.24	2015.1.00089.S
438	J05390193-0235029	336± 23	Or	0.24	2015.1.00089.S
439	Mayrit 458140	450± 33	Or	0.24	2015.1.00089.S
440	J05390387-0220081	347± 18	Or	0.24	2015.1.00089.S
441	[BZR99] S Ori 7	332± 20	Or	0.24	2015.1.00089.S
442	J05390878-0231115	335± 15	Or	0.24	2015.1.00089.S
443	[BZR99] S Ori 30	339± 57	Or	0.24	2015.1.00089.S
444	Haro 5-20	411± 7	Or	0.24	2015.1.00089.S
445	[BNM2013] 90.02 146	381± 15	Or	0.24	2015.1.00089.S
446	Haro 5-21	402± 9	Or	0.24	2015.1.00089.S

Table A.1: - continued.

ID	Name[†]	Distance	SFR[††]	Res.	Project
#		(pc)		(")	Code
447	V* BG Ori	384± 7	Or	0.24	2015.1.00089.S
448	J05392633-0228376	370± 19	Or	0.24	2015.1.00089.S
449	J05392935-0227209	387± 10	Or	0.24	2015.1.00089.S
450	Haro 5-25	392± 5	Or	0.24	2015.1.00089.S
451	V* RW Ori	383± 20	Or	0.24	2015.1.00089.S
452	V* V603 Ori	368± 16	Or	0.24	2015.1.00089.S
453	Haro 5-27	395± 5	Or	0.24	2015.1.00089.S
454	V* RV Ori	398± 4	Or	0.24	2015.1.00089.S
455	J05394318-0232433	363± 13	Or	0.24	2015.1.00089.S
456	[BZR99] S Ori 10	413± 37	Or	0.24	2015.1.00089.S
457	Haro 5-32	388± 10	Or	0.24	2015.1.00089.S
458	Haro 5-30	401± 17	Or	0.24	2015.1.00089.S
459	Haro 5-34	407± 5	Or	0.24	2015.1.00089.S
460	Mayrit 1045094	435± 74	Or	0.24	2015.1.00089.S
461	J05395421-0227326	382± 21	Or	0.24	2015.1.00089.S
462	V* V605 Ori B	397± 15	Or	0.24	2015.1.00089.S
463	Haro 5-36	373± 12	Or	0.24	2015.1.00089.S
464	Mayrit 1196092	635± 212	Or	0.24	2015.1.00089.S
465	J05400525-0230522	354± 28	Or	0.24	2015.1.00089.S
466	V* V608 Ori	403± 6	Or	0.24	2015.1.00089.S
467	J05400933-0225067	380± 21	Or	0.24	2015.1.00089.S
468	Haro 5-38	416± 6	Or	0.24	2015.1.00089.S
469	[DRS2009] 2091	450*	Or	0.43	2011.0.00028.S
470	* tet01 Ori F	450*	Or	0.43	2011.0.00028.S
471	[FRM2016] 426	450*	Or	0.07	2017.1.01478.S
472	[KPM2006] 139	450*	Or	0.43	2011.0.00028.S
473	ESO-HA 1656	440**	Ori	0.24	2015.1.00089.S
474	J05381189-0245568	440**	Ori	0.24	2015.1.00089.S
475	J05381319-0226088	440**	Ori	0.24	2015.1.00089.S
476	J05381778-0240500	440**	Ori	0.24	2015.1.00089.S

Table A.1: - continued.

ID #	Name†	Distance (pc)	SFR††	Res. (")	Project Code
477	V* V2726 Ori	440**	Ori	0.24	2015.1.00089.S
478	2XMM J053826.4-023428	440**	Ori	0.24	2015.1.00089.S
479	Mayrit 803197	440**	Ori	0.24	2015.1.00089.S
480	Haro 5-11	440**	Ori	0.24	2015.1.00089.S
481	[W96] rJ053831-0235	440**	Ori	0.24	2015.1.00089.S
482	J05383976-0232203	440**	Ori	0.24	2015.1.00089.S
483	[BZR99] S Ori 74	440**	Ori	0.24	2015.1.00089.S
484	[BHM2009] SigOri-MAD-2	440**	Ori	0.24	2015.1.00089.S
485	J05385911-0247133	440**	Ori	0.24	2015.1.00089.S
486	GSC2 S02003215312	440**	Ori	0.24	2015.1.00089.S
487	J05391427-0221458	440**	Ori	0.24	2015.1.00089.S
488	[HHM2007] 1242	440**	Ori	0.24	2015.1.00089.S
489	J05395804-0237402	440**	Ori	0.24	2015.1.00089.S
490	IRAS 03292+3039	300**	Pe	0.15	2015.1.01053.S
491	J17112317-2724315	130**	PN	0.03	2016.1.01186.S
492	HD 98363	139± 1	SC	0.67	2015.1.01243.S
493	HD 131835	134± 4	SC	0.30	2013.1.01166.S
494	CPD-36 6759	136± 1	SC	0.26	2012.1.00870.S
495	HD 139614	135± 1	SC	0.54	2015.1.01600.S
496	HD 141569	111± 1	SC	0.53	2015.1.01600.S
497	HD 95086	86± 1	SC	0.91	2013.1.00773.S
498	CD-40 8434	113± 1	SC	0.08	2017.A.00006.S
499	SH 2-68 N	193**	Se	0.51	2015.1.01478.S
500	[B96] Serpens 2	193**	Se	0.13	2015.1.00354.S
501	J18295766+0113045	193**	Se	0.51	2015.1.01478.S
502	SSTc2d J182959.5+011159	193**	Se	0.51	2015.1.01478.S
503	[ETC2005] 19	193**	Se	0.51	2015.1.01478.S
504	IRAS 04158+2805	90± 5	Ta	0.06	2016.1.00460.S
505	HD 32297	133± 1	Ta	0.46	2015.1.00633.S
506	IRAS 04113+2758	140***	Ta	0.47	2011.0.00150.S

Table A.1: - continued.

ID #	Name†	Distance (pc)	SFR††	Res. (")	Project Code
507	IP Tau	131± 1	Ta	0.09	2016.1.01164.S
508	MHO 2	133± 4	Ta	0.14	2013.1.00498.S
509	J04141188+2811535	131± 3	Ta	0.25	2012.1.00743.S
510	V* FM Tau	132± 1	Ta	0.13	2013.1.00426.S
511	[BCG93] 1	136± 2	Ta	0.42	2011.0.00259.S
512	V* FP Tau	128± 1	Ta	0.23	2012.1.00743.S
513	V* CX Tau	128± 1	Ta	0.13	2013.1.00426.S
514	V* FO Tau	157± 9	Ta	0.14	2013.1.00105.S
515	J04161210+2756385	137± 2	Ta	0.23	2012.1.00743.S
516	V* CY Tau	129± 1	Ta	0.14	2013.1.00498.S
517	J04181710+2828419	124± 5	Ta	0.23	2012.1.00743.S
518	J04182147+1658470	181± 1	Ta	0.64	2012.1.00350.S
519	V* V892 Tau	117± 2	Ta	0.14	2013.1.00498.S
520	J04190110+2819420	119± 2	Ta	0.23	2012.1.00743.S
521	WK81 1	132± 1	Ta	0.64	2012.1.00350.S
522	J04202555+2700355	170± 5	Ta	0.23	2012.1.00743.S
523	J04213459+2701388	167± 4	Ta	0.23	2012.1.00743.S
524	IRAS 04187+1927	149± 2	Ta	0.92	2013.1.00105.S
525	V* DE Tau	127± 1	Ta	0.13	2013.1.00426.S
526	J04230607+2801194	134± 2	Ta	0.25	2012.1.00743.S
527	IRAS 04200+2759	139± 3	Ta	0.06	2016.1.00460.S
528	[XCR2012] TrES J042423+265008	155± 2	Ta	0.64	2012.1.00350.S
529	[BLH2002] KPNO-Tau 3	156± 6	Ta	0.25	2012.1.00743.S
530	J04263055+2443558	119± 10	Ta	0.92	2013.1.00105.S
531	CoKu FV Tau c	140± 3	Ta	0.47	2011.0.00150.S
532	V* DG Tau	121± 2	Ta	0.02	2015.1.01268.S
533	J04295950+2433078	131± 3	Ta	0.14	2013.1.00105.S
534	V* ZZ Tau	134± 5	Ta	0.92	2013.1.00105.S
535	V* HK Tau	133± 2	Ta	0.47	2011.0.00150.S

Table A.1: - continued.

ID #	Name†	Distance (pc)	SFR††	Res. (")	Project Code
536	V* V710 Tau B	145± 1	Ta	0.14	2013.1.00105.S
537	Haro 6-13	130± 3	Ta	0.11	2016.1.01042.S
538	J04321606+1812464	145± 2	Ta	0.14	2013.1.00105.S
539	J04322210+1827426	142± 2	Ta	0.23	2012.1.00743.S
540	J04322415+2251083	155± 3	Ta	0.92	2013.1.00105.S
541	V* FZ Tau	130± 1	Ta	0.13	2013.1.00426.S
542	JH 112	165± 2	Ta	0.47	2011.0.00150.S
543	J04324938+2253082	165± 7	Ta	0.92	2013.1.00105.S
544	V* V1321 Tau	147± 1	Ta	0.64	2012.1.00350.S
545	V* V807 Tau	113± 8	Ta	0.14	2013.1.00105.S
546	J04330945+2246487	149± 9	Ta	0.92	2013.1.00105.S
547	IRAS 04303+2240	148± 6	Ta	0.92	2013.1.00105.S
548	V* GK Tau	129± 1	Ta	0.47	2011.0.00150.S
549	V* IS Tau	133± 5	Ta	0.14	2013.1.00105.S
550	V* HN Tau	137± 3	Ta	0.47	2011.0.00150.S
551	V* DL Tau	159± 1	Ta	0.20	2015.1.01207.S
552	J04334465+2615005	173± 6	Ta	0.24	2012.1.00743.S
553	V* DM Tau	145± 1	Ta	0.02	2017.1.01460.S
554	V* CI Tau	159± 1	Ta	0.07	2017.A.00014.S
555	V* AA Tau	137± 2	Ta	0.19	2015.1.01017.S
556	V* HO Tau	161± 1	Ta	0.47	2011.0.00150.S
557	V* DN Tau	128± 1	Ta	0.26	2015.1.01207.S
558	J04361030+2159364	118± 8	Ta	0.92	2013.1.00105.S
559	J04362151+2351165	115± 2	Ta	0.92	2013.1.00105.S
560	HD 283759	163± 2	Ta	0.64	2012.1.00350.S
561	ITG 3	145± 15	Ta	0.25	2012.1.00743.S
562	V* GM Tau	138± 3	Ta	0.25	2012.1.00743.S
563	V* DO Tau	139± 1	Ta	0.23	2015.1.01207.S
564	J04385859+2336351	127± 2	Ta	0.24	2012.1.00743.S
565	J04390163+2336029	128± 1	Ta	0.24	2012.1.00743.S

Table A.1: - continued.

ID #	Name†	Distance (pc)	SFR††	Res. (")	Project Code
566	J04390396+2544264	144± 4	Ta	0.25	2012.1.00743.S
567	EM* LkCa 15	159± 1	Ta	0.17	2012.1.00870.S
568	V* VY Tau	152± 3	Ta	0.14	2013.1.00105.S
569	J04393364+2359212	127± 2	Ta	0.24	2012.1.00743.S
570	IRAS F04366+2555	137± 2	Ta	0.24	2012.1.00743.S
571	J04400067+2358211	121± 2	Ta	0.24	2012.1.00743.S
572	J04403979+2519061	152± 11	Ta	0.64	2012.1.00350.S
573	NAME JH 223B	141± 3	Ta	0.14	2013.1.00105.S
574	ITG 33A	141± 4	Ta	0.14	2013.1.00105.S
575	ITG 34	157± 6	Ta	0.14	2013.1.00105.S
576	J04414489+2301513	120± 5	Ta	0.14	2013.1.00105.S
577	J04414825+2534304	136± 4	Ta	0.25	2012.1.00743.S
578	V* V999 Tau	123± 6	Ta	0.64	2012.1.00350.S
579	EM* LkHA 332	160± 12	Ta	0.14	2013.1.00105.S
580	V* GO Tau	145± 1	Ta	0.10	2016.1.01164.S
581	Haro 6-36	171± 4	Ta	0.14	2013.1.00105.S
582	IRAS S04414+2506	141± 3	Ta	0.42	2011.0.00259.S
583	V* DR Tau	196± 2	Ta	0.16	2016.1.00158.S
584	V* DS Tau	159± 1	Ta	0.09	2016.1.01164.S
585	V* UY Aur	156± 1	Ta	0.47	2011.0.00150.S
586	V* GM Aur	160± 2	Ta	0.02	2017.1.01151.S
587	J04554535+3019389	155± 2	Ta	0.14	2013.1.00105.S
588	V* AB Aur	163± 2	Ta	0.14	2012.1.00303.S
589	J04554801+3028050	165± 5	Ta	0.14	2013.1.00105.S
590	J04554969+3019400	156± 5	Ta	0.14	2013.1.00105.S
591	J04560118+3026348	159± 9	Ta	0.14	2013.1.00105.S
592	V* SU Aur	158± 1	Ta	0.13	2013.1.00426.S
593	HD 31648	162± 2	Ta	0.10	2016.1.01164.S
594	J05062332+2432199	151± 10	Ta	0.14	2013.1.00105.S
595	J05075496+2500156	165± 2	Ta	0.24	2012.1.00743.S

Table A.1: - continued.

ID #	Name†	Distance (pc)	SFR††	Res. (")	Project Code
596	V* CQ Tau	163± 2	Ta	0.21	2013.1.00498.S
597	HD31648	162± 2	Ta	0.11	2016.1.01164.S
598	LDN 1489	140**	Ta	0.65	2011.0.00210.S
599	V* CZ Tau	140**	Ta	0.14	2013.1.00105.S
600	V* FQ Tau	140**	Ta	0.47	2011.0.00150.S
601	J04202144+2813491	140**	Ta	0.06	2016.1.00460.S
602	J04220069+2657324	140**	Ta	0.06	2016.1.00460.S
603	V* FS Tau	140**	Ta	0.14	2013.1.00105.S
604	V* FV Tau	140**	Ta	0.47	2011.0.00150.S
605	J04270266+2605304	140**	Ta	0.11	2016.1.01042.S
606	J04284263+2714039	140**	Ta	0.23	2012.1.00743.S
607	IRAS F04262+2654	140**	Ta	0.25	2012.1.00743.S
608	V* DH Tau B	140**	Ta	0.14	2015.1.00773.S
609	V* UX Tau	140**	Ta	0.14	2013.1.00105.S
610	V* FX Tau	140**	Ta	0.47	2011.0.00150.S
611	V* DK Tau	140**	Ta	0.47	2011.0.00150.S
612	V* V1213 Tau	140**	Ta	0.02	2017.1.01701.S
613	V* HL Tau	140**	Ta	0.09	2013.1.00355.S
614	V* XZ Tau	140**	Ta	0.14	2013.1.00105.S
615	NAME HK Tau B	140**	Ta	0.06	2016.1.00460.S
616	V* V710 Tau	140**	Ta	0.47	2011.0.00150.S
617	V* GG Tau	140**	Ta	0.14	2013.1.00105.S
618	V* GH Tau	140**	Ta	0.14	2013.1.00105.S
619	IRAS 04302+2247	140**	Ta	0.06	2016.1.00460.S
620	V* IT Tau	140**	Ta	0.47	2011.0.00150.S
621	NAME CoKu Tau 3	140**	Ta	0.47	2011.0.00150.S
622	Haro 6-28	140**	Ta	0.14	2013.1.00105.S
623	V* HV Tau C	140**	Ta	0.06	2016.1.00460.S
624	V* GN Tau	140**	Ta	0.14	2013.1.00105.S
625	IRAS 04365+2535	140**	Ta	0.75	2011.0.00210.S

Table A.1: - continued.

ID #	Name†	Distance (pc)	SFR††	Res. (")	Project Code
626	[BCK99] HCl 2 NW-7a	140**	Ta	0.42	2011.0.00259.S
627	LDN 1527	140**	Ta	0.75	2011.0.00210.S
628	ITG 40	140**	Ta	0.14	2013.1.00105.S
629	V* DP Tau	140**	Ta	0.14	2013.1.00105.S
630	Haro 6-37	140**	Ta	0.14	2013.1.00105.S
631	J04555605+3036209	140**	Ta	0.24	2012.1.00743.S
632	IRAS 05022+2527	140**	Ta	0.47	2011.0.00150.S
633	HD 282276	492± 12***	Ta	0.64	2012.1.00350.S
634	V* V1322 Tau	463± 13***	Ta	0.64	2012.1.00350.S
635	RY Tau	442± 47***	Ta	0.02	2017.1.01460.S
636	J10455263-2819303	84± 1	TWH	1.04	2013.1.00457.S
637	V* TW Hya	60± 1	TWH	0.04	2017.1.00520.S
638	J11064461-3715115	101± 4	TWH	1.03	2013.1.00457.S
639	TWA 37	50± 1	TWH	1.04	2013.1.00457.S
640	TWA 30	48± 1	TWH	1.04	2013.1.00457.S
641	TWA 30B	46± 1	TWH	1.04	2013.1.00457.S
642	TWA 33	49± 1	TWH	1.03	2013.1.00457.S
643	TWA 38	80± 1	TWH	0.99	2013.1.00457.S
644	TWA 31	81± 1	TWH	1.04	2013.1.00457.S
645	TWA 27	64± 1	TWH	0.28	2013.1.01016.S
646	TWA 40	67± 4	TWH	0.99	2013.1.00457.S
647	HD 109573	72± 1	TWH	0.17	2015.1.00032.S
648	HD 109832	108± 1	TWH	0.67	2015.1.01243.S
649	TWA 29	83± 3	TWH	0.92	2013.1.00457.S
650	J12474428-3816464	85± 3	TWH	0.99	2013.1.00457.S
651	J12520989-4948280	116± 4	TWH	0.92	2013.1.00457.S
652	J13265348-5022270	107± 7	TWH	0.92	2013.1.00457.S
653	EC 13436-1335	88± 1	TWH	0.69	2015.1.00783.S
654	HE 1350-1612	109± 2	TWH	0.69	2015.1.00783.S
655	TWA 32	50**	TWH	0.99	2013.1.00457.S

Table A.1: - continued.

ID #	Name†	Distance (pc)	SFR††	Res. (")	Project Code
656	HD 98800	50**	TWH	0.10	2016.1.01042.S
657	TWA 34	61± 1	TWH	1.04	2013.1.00457.S
658	V* CE Ant	34± 1	TWH	0.10	2015.1.01015.S
659	V* CE Ant	34± 1	TWH	0.10	2015.1.01015.S
660	V* V419 Hya	22± 1	TWH	0.40	2016.1.00104.S
661	* eps Eri	3± 1	UM	1.04	2013.1.00645.S
662	UCAC2 23646111	136± 3	US	0.30	2013.1.00395.S
663	ScoPMS 8b	125± 2	US	0.28	2013.1.00395.S
664	HD 142506	144± 1	US	0.28	2013.1.00395.S
665	DENIS J155556.0-204518	146± 5	US	0.37	2012.1.00743.S
666	UScoCTIO 113	140± 5	US	0.37	2012.1.00743.S
667	[PBB2002] USco J155624.8-222555	141± 2	US	0.46	2011.0.00526.S
668	HD 142666	148± 1	US	0.20	2013.1.00498.S
669	[PBB2002] USco J155706.4-220606	158± 3	US	0.46	2011.0.00526.S
670	CD-23 12602	143± 1	US	0.28	2013.1.00395.S
671	RX J155829.5-231026	148± 3	US	0.46	2011.0.00526.S
672	HD 143006	166± 4	US	0.40	2015.1.00964.S
673	J15584772-1757595	139± 1	US	0.30	2013.1.00395.S
674	UScoCTIO 128	140± 7	US	0.37	2012.1.00743.S
675	J16001330-2418106	146± 1	US	0.28	2013.1.00395.S
676	UCAC3 135-174588	149± 2	US	0.28	2013.1.00395.S
677	[PBB2002] USco J160018.4-223011	138± 8	US	0.28	2013.1.00395.S
678	J16014157-2111380	145± 2	US	0.30	2013.1.00395.S
679	RX J1602.0-2221	145± 2	US	0.28	2013.1.00395.S
680	[PBB2002] USco J160207.5-225746	140± 1	US	0.28	2013.1.00395.S
681	EPIC 204607034	142± 3	US	0.29	2013.1.00395.S

Table A.1: - continued.

ID #	Name†	Distance (pc)	SFR††	Res. (")	Project Code
682	UScoCTIO 45	96± 3	US	0.37	2012.1.00743.S
683	RX J1602.8-2401B	144± 1	US	0.28	2013.1.00395.S
684	UScoCTIO 59	144± 3	US	0.29	2013.1.00395.S
685	J16031329-2112569	143± 2	US	0.29	2013.1.00395.S
686	J16032225-2413111	144± 3	US	0.28	2013.1.00395.S
687	J16035767-2031055	143± 1	US	0.50	2011.0.00526.S
688	[PGZ2001] J160357.9-194210	158± 2	US	0.30	2013.1.00395.S
689	EPIC 205037578	161± 2	US	0.30	2013.1.00395.S
690	J16042165-2130284	150± 1	US	0.16	2015.1.00888.S
691	[PGZ2001] J160439.1-194245	151± 2	US	0.30	2013.1.00395.S
692	J16050231-1941554	158± 3	US	0.30	2013.1.00395.S
693	J16052459-1954419	153± 2	US	0.30	2013.1.00395.S
694	[PGZ2001] J160525.5-203539	143± 3	US	0.46	2011.0.00526.S
695	[PGZ2001] J160532.1-193315	154± 3	US	0.46	2011.0.00526.S
696	[PGZ2001] J160545.4-202308	145± 2	US	0.30	2013.1.00395.S
697	J16055863-1949029	149± 2	US	0.30	2013.1.00395.S
698	DENIS J160603.9-205644	137± 5	US	0.37	2012.1.00743.S
699	J16061330-2212537	140± 2	US	0.29	2013.1.00395.S
700	[PGZ2001] J160622.8-201124	151± 2	US	0.43	2011.0.00526.S
701	J16063539-2516510	139± 3	US	0.28	2013.1.00395.S
702	J16064115-2517044	149± 2	US	0.28	2013.1.00395.S
703	J16064102-2455489	152± 3	US	0.28	2013.1.00395.S
704	[PGZ2001] J160643.8-190805	144± 7	US	0.50	2011.0.00526.S
705	[PGZ2001] J160700.1-203309	139± 2	US	0.30	2013.1.00395.S
706	1RXS J160708.6-192737	146± 2	US	0.30	2013.1.00395.S
707	[PGZ2001] J160719.7-202055	164± 3	US	0.30	2013.1.00395.S
708	EPIC 203889938	143± 2	US	0.28	2013.1.00395.S
709	[PGZ2001] J160739.4-191747	137± 1	US	0.30	2013.1.00395.S
710	EPIC 204830786	198± 8	US	0.29	2013.1.00395.S
711	J16080555-2218070	143± 1	US	0.29	2013.1.00395.S

Table A.1: - continued.

ID #	Name†	Distance (pc)	SFR††	Res. (")	Project Code
712	J16081566-2222199	140± 2	US	0.29	2013.1.00395.S
713	[T64] 3	138± 1	US	0.50	2011.0.00526.S
714	J16083455-2211559	136± 3	US	0.29	2013.1.00395.S
715	J16084894-2400045	145± 2	US	0.28	2013.1.00395.S
716	[PGZ2001] J160900.7-190852	138± 1	US	0.43	2011.0.00526.S
717	[PBB2002] USco J160900.0-190836	139± 3	US	0.43	2011.0.00526.S
718	[PBB2002] USco J160935.6-182822	165± 3	US	0.30	2013.1.00395.S
719	J16094098-2217594	146± 1	US	0.29	2013.1.00395.S
720	[PBB2002] USco J160953.6-175446	158± 5	US	0.30	2013.1.00395.S
721	[PGZ2001] J160954.4-190654	137± 1	US	0.30	2013.1.00395.S
722	[PGZ2001] J160959.4-180009	136± 2	US	0.46	2011.0.00526.S
723	DENIS J161005.4-191936	150± 7	US	0.37	2012.1.00743.S
724	K2-33	140± 2	US	0.30	2013.1.00395.S
725	EPIC 203756600	156± 4	US	0.28	2013.1.00395.S
726	ScoPMS 42b	134± 1	US	0.30	2013.1.00395.S
727	[PBB2002] USco J161028.1-191043	151± 3	US	0.30	2013.1.00395.S
728	[PGZ2001] J161039.5-191652	159± 2	US	0.30	2013.1.00395.S
729	GSC 06213-01459	140± 1	US	0.29	2013.1.00395.S
730	J16104636-1840598	143± 3	US	0.30	2013.1.00395.S
731	UCAC2 23893922	155± 2	US	0.30	2013.1.00395.S
732	1RXS J161115.1-175741	137± 1	US	0.30	2013.1.00395.S
733	ScoPMS 45	137± 1	US	0.30	2013.1.00395.S
734	J16115091-2012098	152± 4	US	0.30	2013.1.00395.S
735	J16122737-2009596	147± 4	US	0.30	2013.1.00395.S
736	[T64] 6	139± 2	US	0.30	2013.1.00395.S

Table A.1: - continued.

ID #	Name†	Distance (pc)	SFR††	Res. (")	Project Code
737	[PBB2002] USco J161248.9-180052	158± 2	US	0.30	2013.1.00395.S
738	HD 145655	152± 1	US	0.29	2013.1.00395.S
739	EPIC 205165965	137± 2	US	0.30	2013.1.00395.S
740	HD 145718	153± 2	US	0.72	2015.1.01600.S
741	[T64] 7	143± 3	US	0.43	2011.0.00526.S
742	EPIC 205188906	141± 2	US	0.30	2013.1.00395.S
743	[PGZ2001] J161433.6-190013	142± 2	US	0.30	2013.1.00395.S
744	RX J1614.6-1858	101± 1	US	0.39	2012.1.00350.S
745	J16145918-2750230	149± 1	US	0.28	2013.1.00395.S
746	EPIC 203770673	159± 3	US	0.29	2013.1.00395.S
747	EPIC 203938167	154± 3	US	0.29	2013.1.00395.S
748	GSC 06209-00747	132± 2	US	0.30	2013.1.00395.S
749	EPIC 203664569	163± 1	US	0.29	2013.1.00395.S
750	J16181904-2028479	138± 2	US	0.29	2013.1.00395.S
751	J16214199-2313432	139± 2	US	0.37	2012.1.00743.S
752	GSC 06214-00210	109± 1	US	0.29	2013.1.00395.S
753	J16220961-1953005	138± 2	US	0.64	2011.0.00733.S
754	J16223757-2345508	137± 1	US	0.39	2012.1.00350.S
755	CD-22 11523	140± 1	US	0.29	2013.1.00395.S
756	HD 147594	134± 1	US	0.29	2013.1.00395.S
757	J16251469-2456069	136± 1	US	0.39	2012.1.00350.S
758	GSS 31	138± 2	US	0.30	2015.1.00637.S
759	BKLT J162620-240854	136± 1	US	0.30	2015.1.00637.S
760	Elia 2-24	136± 2	US	0.20	2013.1.00498.S
761	GSS 39	116± 13	US	0.20	2013.1.00498.S
762	[GY92] 204	142± 3	US	0.42	2011.0.00259.S
763	J16270942-2148457	140± 3	US	0.29	2013.1.00395.S
764	YLW 58	137± 3	US	0.10	2016.1.01042.S
765	J16303390-2428062	151± 3	US	0.29	2013.1.00395.S

Table A.1: - continued.

ID #	Name†	Distance (pc)	SFR††	Res. (")	Project Code
766	HD 163296	101± 1	US	0.17	2015.1.00847.S
767	DoAr 25	138± 1	US	0.03	2016.1.00484.L
768	Elia 2-20	138± 4	US	0.02	2016.1.00484.L
769	EM* SR 4	135± 1	US	0.02	2016.1.00484.L
770	V* V1094 Sco	154± 1	US	0.24	2016.1.01239.S
771	UScoCTIO 13	140**	US	0.46	2011.0.00526.S
772	[PBB2002] USco J160140.8-225810	140**	US	0.28	2013.1.00395.S
773	[PBB2002] USco J160202.9-223613	140**	US	0.28	2013.1.00395.S
774	J16052661-1957050	140**	US	0.30	2013.1.00395.S
775	[PGZ2001] J160600.6-195711	140**	US	0.43	2011.0.00526.S
776	ScoPMS 31	140**	US	0.50	2011.0.00526.S
777	[PGZ2001] J160702.1-201938	140**	US	0.46	2011.0.00526.S
778	J16072747-2059442	140**	US	0.29	2013.1.00395.S
779	[PGZ2001] J160827.5-194904	140**	US	0.43	2011.0.00526.S
780	RX J1609.5-2105B	140**	US	0.15	2015.1.00773.S
781	ScoPMS 42a	140**	US	0.30	2013.1.00395.S
782	V* V866 Sco	140**	US	0.52	2011.0.00531.S
783	UCAC2 24372422	140**	US	0.39	2012.1.00350.S
784	EPIC 203750883	140**	US	0.28	2013.1.00395.S
785	J16135434-2320342	140**	US	0.29	2013.1.00395.S
786	CD-22 11432	140**	US	0.43	2011.0.00526.S
787	V* VV Sco	140**	US	0.29	2013.1.00395.S
788	DENIS J161816.2-261908	140**	US	0.29	2013.1.00395.S
789	WSB 4	140**	US	0.30	2015.1.00637.S
790	DENIS J161939.8-214535	140**	US	0.37	2012.1.00743.S
791	WSB 18	140**	US	0.30	2015.1.00637.S
792	GSS 26	140**	US	0.10	2016.1.01042.S
793	Haro 1-5	140**	US	0.30	2015.1.00637.S

Table A.1: - continued.

ID	Name†	Distance	SFR††	Res.	Project
#		(pc)		(")	Code
794	* zet02 Ret	12± 1	ζH	2.74	2017.1.00786.S

† Objects belonging to the Two Micron All-Sky Survey (2MASS) are displayed as 'J##+## or 'J##'–##' , where ## is its unique identity number. To query these objects in astronomical databases, such as `Simbad`, the prefix '*2MASS*' should be added.

†† The star forming region initials represent the following :

βP	β Pic Moving Group	Op	Ophiuchus
CA	Corona Australis	Or	Orion
Ch	Chamaeleon	Ori	Orionis
CN	Carina Nebula	Pe	Perseus
Co	Columba Association	PN	Pipe Nebula
DC	DC296.27.9	SC	Scorpius–Centaurus Association
ηC	η Chamaeleontis Association	Se	Serpens
Ge	Gemini	Ta	Taurus
Hy	Hydes	TWH	TW Hya Association
λO	λ Orionis Association	UM	Ursa Major Moving Group
LCC	Lower Centaurus Crux	US	Upper Scorpius
Lu	Lupus	ζH	ζ Herculis Moving Group
Lu 3	Lupus 3		

***** These sources have no associated Gaia DR2 distances. Their distances were obtained from: V* RW Aur, HD 98800, * Alf PsA and * Bet Leo (van Leeuwen 2007), EM* AS 220 (Gaia Collaboration et al. 2016).

****** These sources have no associated Gaia DR2 distance, nor individual distance estimate. We approximate the distance by using the distance to its association.

******* The updated Gaia DR2 distances put the associated SFR into question.

A.2 Ages of Star Forming Regions

The average age of nearby star–forming regions within which the protostars studied here are located is shown in Table A.2.

Table A.2: Average age of nearby star–forming regions used to compare the ages derived in Section 4.4 to.

SFR	Age	Reference
β Pic MG	22 ± 3	(1)
Chamaeleon	3-4	(2)
Corona Australis	9 ± 4	(3)
Lower Centaurus Crux	16	(4)
Lupus	3	(5)
Ophiuchus	2-5	(6)
Orion A	1-3	(7)
Orion OB1	5	(8)
Taurus	1-5	(9)
TW Hya	10 ± 3	(10)
Upper Scorpius	5	(4)

References : (1) Mamajek & Bell (2014) , (2) Luhman (2007), (3) James et al. (2006) , (4) Preibisch & Mamajek (2008), (5) Alcalá et al. (2017), (6) Wilking et al. (2008), (7) Da Rio et al. (2010), (8) Caballero & Solano (2008), (9) Kraus & Hillenbrand (2009), (10) Bell et al. (2015).